Synthesis and Properties of Porphyrin Nanotubes

Renée Haver

New College

University of Oxford

A thesis submitted for the degree of

Doctor of Philosophy

Hilary 2018

Synthesis and Properties of Porphyrin Nanotubes

DPhil Thesis, Trinity 2018

Renée Haver, New College, University of Oxford

Abstract

Porphyrins, with their planar aromatic cores, are suitable and versatile building blocks to form functional nanostructures. This thesis describes the synthesis and properties of atomically precise porphyrin nanostructures with a specific focus on porphyrin nanotubes.

Chapter 1 introduces the key properties of porphyrins and discusses the template-directed synthesis of (conjugated) porphyrin nanostructures. Furthermore, it explores the "bottom-up" synthesis of carbon nanotubes and its molecular analogues including those constructed from porphyrin building blocks.

Chapter 2 describes the assembly of a nested nanoring complex. Excitation energy is transferred from the inner nanoring to the outer nanoring. The inner porphyrin nanoring is used as a template to direct the synthesis of the outer nanoring from its linear precursor.

Chapter 3 explores different strategies for the synthesis of a nanotube consisting of 12 porphyrin subunits. An unprecedented method of ring-stacking of pre-formed 6-porphyrin nanorings is discussed as well as a template-directed procedure.

Chapter 4 describes the host-guest chemistry of a 12-porphyrin nanotube. C_{60} and C_{70} fullerenes are encapsulated in the cavity of the nanotube. Electron transfer from the nanotube host to the C_{60} guest is observed. The guests can be released when the molecular box is chemically opened.

Chapter 5 describes the synthesis and properties of porphyrin nanotubes with a mono-acetylene connection between the conjoined 6-porphyrin nanorings. This link enables the synthesis of an 18-porphyrin nanotube; the longest π-conjugated molecular nanotube to date. Enhanced conjugation is found compared to analogous bis-acetylene linked tubes.

Chapter 6 explores DFT calculations on large π-conjugated porphyrin nanostructures. Size-dependent bandgap oscillations in bis-acetylene linked porphyrin nanotubes are examined. TD-DFT studies on a 14-porphyrin nanoball provide insight into the electronic structure and agree with experimental observations.

Supplement to Statement of Authorship

Chapter 2: The design of the nested nanoring system and the synthetic methodology for the synthesis of the aluminium 6-porphyrin nanoring and ligand **L1** were developed by Dr. S. Rousseaux. The characterisation of the nested nanoring complex was performed by Dr. S. Rousseaux, Dr. B. Odell and Prof. T. D. W. Claridge. Photophysical measurements on the nested nanoring system were performed by Dr. J. Gong under the supervision of Prof. L. M. Herz.

Chapter 6: Most of the synthesis of porphyrin nanoballs ***b*-P14** and ***b*-P10** was performed by Jonathan Cremers. The author performed part of the synthesis and purification of these complexes. Photophysical measurements on the porphyrin nanoballs were performed by Dr. J. Gong under the supervision of Prof. L. M. Herz.

Acknowledgements

First of all, I would like to thank my supervisor Prof. Harry L. Anderson, for trusting me with this exciting and often challenging project. His knowledge, guidance and support have been essential and I am grateful for having had the opportunity to learn from such a brilliant chemist.

When I arrived in the HLA group I was lucky to find two very inspiring mentors; Dr. Dmitry Kondratiuk and Dr. Sophie Rousseaux. Their excellent teaching has been of great value throughout my DPhil.

Most of the work in this thesis was funded by the European Research Council. Additional funding came from the Department of Chemistry (Oxford) and New College. The Oxford Advanced Research Computing Facility generously provided computational time.

I have been very lucky to learn from and collaborate with numerous very bright people: Prof. Tim Claridge and Dr. Barbara Odell (Oxford Chemistry), Dr. Juliane Gong and Prof. Laura Herz (Oxford Physics), and Dr. Maria Lebedeva, Dr. Stuart Corners and Prof. Kyriakos Porfyrakis (Oxford Materials).

I was very fortunate to have the opportunity to supervise two fantastic summer students; Isabel Tomlinson and Joshua Sauer who kindly prepared starting materials for my projects.

The HLA group is known for its kind and supportive environment which is credited to its many group members, past and present. The wide variety in music that comes out of the lab's speakers is only one illustration of the diversity in the group. Thank you; Dmitry, Arjen, Julien, Sophie, Pablo, Ludovic, Levon, Johannes, Nuntaporn, Cécile, Dan, Andreas, Huawei, Isabell, Sabine, Michael, Will, James, Pernille, Lara, Lorel, Wenjun, Andrew and Keith. A particular thank you to: Martin, for your unlimited patience to answer questions (even when you moved to MIT); Anjul, for your incredibly entertaining group meeting presentations and motivational chats; Bart, biertje?; Michel, for running "slow" and Yaoyao for hugs. A special thank you to Dr. Przemek Gawel, Dr. Steffen Woltering, Dr. Martin Peeks and (soon to be Dr.) Jonathan Cremers for their meticulous proof-reading of this thesis.

Thank you to my friends in the Netherlands; Jody, Carmen, Martje and D'11 for your warm friendships that withstood the distance.

I am greatly indebted to you, Hessel, for your selfless encouragement to apply to Oxford. Thank you for your unwavering support and friendship.

I have been incredibly fortunate to have found amazing friends in Oxford that have provided me with love, friendship and a family away from home. Thank you, Lisa, Michael, Nir, James, George, Charlotte, Tomek, Lucy, Niamh, Fergus and Alex. Thank you, Zubin, for providing high-standard entertainment and welcome distractions during the final months of my DPhil. Thank you pals, Iona and Sam, for being better than the best.

My final and most profound thank you goes to my family; Papa, Mama, Pia, Fredie and Guusje, for your patience, support and unconditional love.

Table of Contents

List of Abbreviations

Abbreviations

Ar	Aryl
AFM	Atomic Force Microscopy
B3LYP	Becke, 3-parameter, Lee-Yang-Parr
BHT	2,6-Di-*tert*-butyl-4-methylphenol
CD	Circular Dichroism
COSY	Correlation Spectroscopy
CPDMS	Cyanopropyldimethylsilane
CPP	Cycloparaphenylene
CPPA	Cyclic Paraphenyleneacetylene
CNT	Carbon Nanotube
d	doublet (in NMR)
DABCO	1,4-diazabicyclo[2.2.2]octane
dba	dibenzylideneacetone
DCTB	*trans*-2-[3-(4-*tert*-Butylphenyl)-2-methyl-2-propenylidene]malononitrile
DDQ	2,3-Dichloro-5,6-dicyano-1,4-benzoquinone
DFT	Density Functional Theory
DIBODS	Diisopropyloctadecylsilane
DOSY	Diffusion-Ordered NMR Spectroscopy
EPR	Electron Paramagnetic Resonance
FP-TRMC	Flash-Photolysis Time-Resolved Microwave Conductivity
GPC	Gel Permeation Chromatography
h	Hours
HOMO	Highest Occupied Molecular Orbital
HPLC	High Performance Liquid Chromatography
HRTEM	High-Resolution Transmission Electron Microscopy
Hz	Herz
ITO	Indium Tin Oxide
LH	Light Harvesting
LiHMDS	Lithium bis(trimethylsilyl)amide
LUMO	Lowest Unoccupied Molecular Orbital
m	multiplet (in NMR)
MALDI-ToF	Matrix-Assisted Laser Desorption/Ionisation-Time of Flight
Me	Methyl

MM	Molecular Mechanics
Mw	Molecular weight
MWNT	Multi-Walled Carbon Nanotube
NBS	*N*-Bromosuccinimide
NMR	Nuclear Magnetic Resonance
NOESY	Nuclear Overhauser Effect Spectroscopy
OSC	Organic Solar Cell
PCE	Power Conversion Efficiency
PCP	Paracyclophane
PE 40-60	Petroleum Ether 40-60 °C
PL	Photoluminescence
ppm	Parts per million
RC	Reaction Centre
s	singlet (in NMR)
SEC	Size Exclusion Chromatography
STM	Scanning Tunneling Microscopy
SWNT	Single-Walled Carbon Nanotube
t	triplet (in NMR)
TAM	Transient Absorption Microscopy
TBAF	Tetra-*n*-butylammonium fluoride
TCSPC	Time-Correlated Single-Photon Counting
TD	Time-dependent
THF	Tetrahydrofuran
THS	Trihexylsilane
TIPS	Triisopropylsilane
TLC	Thin Layer Chromatography
TMS	Trimethylsilane
$TPPS_4$	*meso*-tetra(4-sulfonatophenyl)porphine
UV-vis-NIR	Ultra-violet, visible and near infra-red

Symbols

Å	Angstroms
δ	Chemical shift
ε	Molar absorption coefficient
λ	Wavelength
μ	Micro
θ	Angle

List of Publications and Awards

Publications

1. J. Cremers, **R. Haver**, M. Rickhaus, J. Q. Gong, L. Favereau, T. D. W. Claridge, L. M. H. Herz, H. L. A. Anderson. 'Template-Directed Synthesis of a Conjugated Zinc Porphyrin Nanoball'. *J. Am. Chem. Soc.,* **2018**, ASAP.

2. M. D. Peeks, C. E. Tait, P. Neuhaus, G. M. Fischer, M. Hoffmann, **R. Haver**, A. Cnossen, J. R. Harmer, C. R. Timmel, H. L. Anderson, 'Electronic delocalization in the radical cations of porphyrin oligomer molecular wires'. *J. Am. Chem. Soc.*, **2017**, *139*, 10461-10471

3. S. A. L. Rousseaux, J. Q. Gong, **R. Haver**, B. Odell, T. D. W. Claridge, L. M. Herz and H. L. Anderson, 'Self-Assembly of Russian Doll Concentric Porphyrin Nanorings'. *J. Am. Chem. Soc.*, **2015**, *137*, 12713-12718.

Awards

1. *Journal of Materials Chemistry B Poster Prize*, ISNA17 (International Symposium on Novel Aromatic Compounds), **2017**, Stony Brook NY, United States of America.

2. *Best 3-minute rapid-fire talk*, OSSC2016 (Oxford Synthesis Summer Conference), **2016**, Oxford, United Kingdom.

3. *Best Oral Presentation in the field of Macromolecular Chemistry*, ChemCYS2016 (Chemistry Conference for Young Scientists), **2016**, Blankenberge, Belgium.

Anything is Possible

-IronMan®-

1

Introduction

1.1 Abstract

This thesis describes the synthesis and properties of large porphyrin nanostructures. In this introductory chapter, a literature review is provided on the properties of porphyrins, the template-directed synthesis of cyclic porphyrin nanostructures, the bottom-up synthesis of carbon nanotubes (and their fragments) and the synthesis and properties of molecular nanotubes including ones constructed from porphyrin building blocks.

1.2 Porphyrins

1.2.1 Molecular Structure and Natural Abundance

Porphyrins – a class of macrocyclic compounds consisting of four pyrrole moieties connected by methine bridges – have been the topic of extensive research for decades. The wide abundance of porphyrins in natural systems has made these macrocycles the subject of numerous studies on synthetic analogues mimicking biological complexes. One example of the vital function porphyrins serve in natural systems is the transport of oxygen in blood (as haemoglobin and myoglobin).[1] Another example is the presence of numerous magnesium-containing porphyrin derivatives in the photosynthetic systems in plants and bacteria.[2–5] Their widespread abundance in natural processes as well as their colourful appearance, make porphyrins truly 'the colours of life'.[6,7]

The simplest porphyrin is porphine, in which the entire periphery of the macrocycle bears hydrogen substituents (Figure 1.1(left)). Porphyrins have a delocalised electronic system of 26 π-electrons and are aromatic according to Hückel's theory due to the presence of an 18 π-electron conjugated pathway around the cyclic system (Figure 1.1(centre)). ^{1}H NMR spectroscopy provides unambiguous evidence of the aromatic ring current in porphyrins, as the central N-*H* protons are strongly shielded (–1 to –4 ppm), while the protons on the periphery of the backbone are strongly deshielded (11 to 8 ppm).

The porphyrin backbone can readily be functionalised at the β- and *meso*-positions.[8] Further functionality can be induced *via* the coordination of a central metal atom. Numerous different metals are known to form so-called metalloporphyrins (Figure 1.1(right)). The broad range of functionalisation, combined with their unique electronic properties have accounted for widespread presence of porphyrins in natural systems and the consequent extensive interest in (chemistry) research.

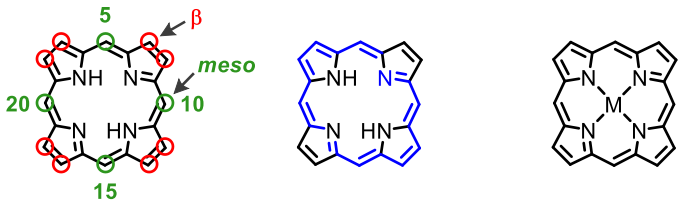

Figure 1.1: (left) Porphine, illustrating the positions of the *meso* (green, including IUPAC numbering) and β (red) positions. (centre) One of the conjugated 18 π-electron conjugated pathways rendering porphyrins aromatic. (right) Metalloporphyrin.

1.2.2 Photophysical Properties

The electronic absorption spectrum of a typical porphyrin monomer consists of a strong transition to the second excited state ($S_0 \rightarrow S_2$) at approximately 400 nm (denoted the Soret or B band), and a much weaker transition to the first excited state ($S_0 \rightarrow S_1$) at approximately 550 nm (denoted the Q band). Since there is rapid internal conversion from the S_2 to the S_1 state, fluorescence is only detected from the S_1 state.

The porphyrin absorption spectrum can be explained by considering the 'Gouterman four orbital model': two π orbitals (a_{1u} and a_{2u}) and a degenerate pair of π* orbitals (e_{gx} and e_{gy}). The B band and Q band both arise from π-π* transitions and since the two highest occupied π orbitals have nearly identical energies, intuitively one would expect that both $a_{1u} \rightarrow e_g$ and $a_{2u} \rightarrow e_g$ transitions have coincident absorption bands. However, their intensities and wavelengths are very different. This originates from a process known as configurational interaction: the $a_{1u} \rightarrow e_g$ and $a_{2u} \rightarrow e_g$ transitions mix together and constructive interference leads to the intense B band at higher energies, while the weak low energy Q band results from destructive interference (Figure 1.2).[7]

Substitution on the porphyrin backbone at one of the *meso*-positions results in stronger changes than substitution at the β-positions, since the orbital coefficients on the first positions are higher.[9] Linking multiple porphyrins *via* *meso*-linkages has received significant interest towards the formation of molecular wires. The nature of the link is crucial in this respect.[10] For example; a direct *meso-meso* bond,[11] or a phenylene link[11,12] between porphyrin monomers barely generates an increase in conjugation, as the *meso*-aryl twist impedes long range conjugation.

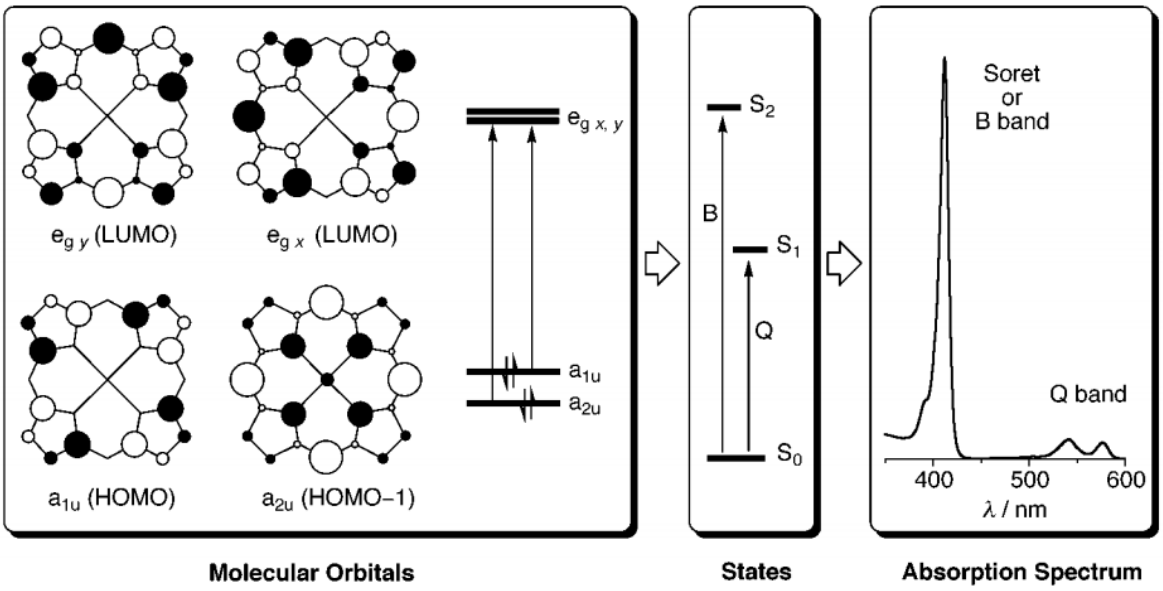

Figure 1.2: The four Gouterman molecular orbitals of a porphyrin monomer, used to explain the absorption spectra of a typical porphyrin monomer. Adapted with permission from ref. 7. Copyright 1999 Royal Society of Chemistry.

On the other hand, connecting porphyrin monomers *via meso*-(bis-acetylene) linkers was found to induce efficient electronic coupling between the porphyrin units,[13,14] which can be attributed to the predominantly co-planar conformation.[15] The extension of conjugation in these porphyrin-based molecular wires is apparent from the progressive bathochromic shift of the Q band (Figure 1.3).[16]

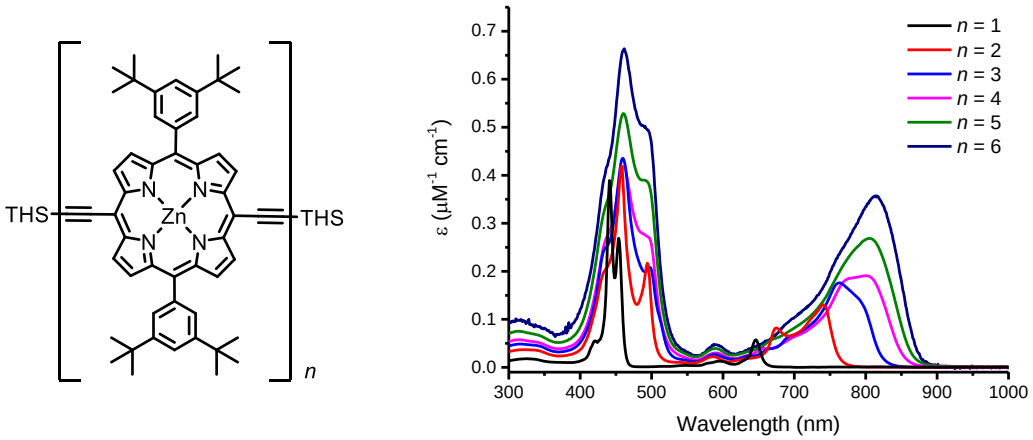

Figure 1.3: UV-vis-NIR absorption spectra of porphyrin-based molecular wires with *meso*-(bis-acetylene) linkages (measured in CH_2Cl_2/1% pyridine). Here shown; porphyrin monomer (n = 1) to porphyrin hexamer (n = 6) bearing 3,5-bis(*tert*-butyl)phenyl solubilising substituents. Adapted with permission from ref. 16. Copyright 1998 Royal Society of Chemistry.

The π-conjugation in *meso*-(bis-acetylene) linked porphyrin-based molecular wires can be enhanced by locking the torsion angle of the porphyrin units in a co-planar arrangement in supramolecular structures. This strongly narrows the distribution of conformers as well as securing a strictly co-planar conformation and hence, accounts for the narrowing and a bathochromic shift of the Q band.[17] This phenomenon has been extensively studied through the formation of ladder and sandwich complexes from linear and cyclic porphyrin structures, respectively, using bidentate ligands such as DABCO, 4,4'-bipyridine or 5,15-pyridyl functionalised porphyrins.[18–23] An analogous effect is observed in cyclic porphyrin nanostructures through the complexation with radial oligopyridine templates.[24]

1.2.3 Template-Directed Synthesis of Porphyrin Nanostructures

Complexation of a metal atom can introduce functionality to the porphyrin, and there are numerous examples of studies on such metalloporphyrins.[25–31] Besides altering the intrinsic properties of the molecule, a metal centre enables supramolecular directionality *via* non-covalent metal-ligand interactions.[32] Arguably the most commonly used metal-ligand interaction is that of the axial binding of zinc porphyrins to nitrogen-based ligands. This supramolecular strategy has been widely exploited in the template-directed synthesis of various porphyrin nanostructures by the Anderson group,[33–44] and other research groups such as the groups of Lindsey,[45–47] and Gossauer.[48,49] This thesis will primarily focus on the template-directed synthesis of zinc porphyrin nanostructures *via* nitrogen-based templating strategies. Different metals enable complementary metal-ligand interactions however, and in Chapter 2 of this thesis we exploit the orthogonal metal-ligand interactions of aluminium porphyrins to allow the assembly of a ring-in-ring complex.

The first template-directed synthesis of cyclic porphyrin nanostructures was reported by Anderson and Sanders (Figure 1.4).[33] In this work, coupling of a porphyrin monomer in the presence of the bidentate linear 4,4'-bipyridiyl template or the tridentate s-tri(4-pyridyl)-triazine ligand under Glaser-Hay coupling conditions, gave the cyclic porphyrin dimer (72% yield) and the cyclic porphyrin trimer (52% yield), respectively. The use of the nitrogen-based ligands in these reactions has a pronounced effect, as the coupling of the porphyrin monomer in the absence of a template gives a mixture of the cyclic porphyrin dimer (20-25% yield) and the cyclic porphyrin trimer (30-35% yield).

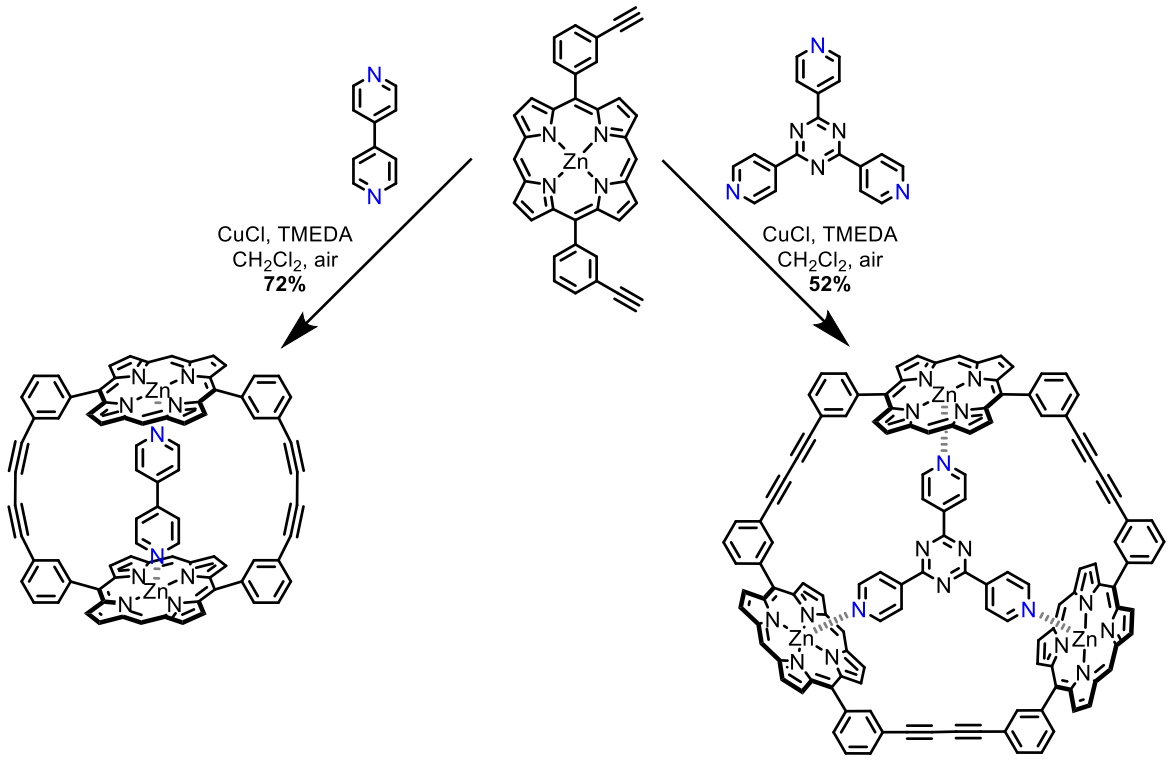

Figure 1.4: The first reported template-directed synthesis of porphyrin nanorings. Solubilising substituents on the β-positions of the porphyrins are omitted for clarity.[33]

After the pioneering work by Anderson and Sanders, several other groups have prepared cyclic zinc porphyrin nanostructures *via* nitrogen-based template-directed synthesis. The porphyrin units in many of these complexes are linked *via* an analogous combination of phenyl and acetylene linkages, as the *meta*-substitution of the phenyl ring offers a suitable geometry for nanoring formation.[45–49] For example, the group of Gossauer reported an elaborate study on the synthesis of a cyclic porphyrin hexamer, starting from either porphyrin monomer, linear dimer or hexamer, and using a variety of templates. A particularly aesthetically pleasing example from their study is the synthesis of a cyclic porphyrin hexamer from two different monomeric building blocks *via* template-directed synthesis using a C_3-symmetric porphyrin trimer as the template (Figure 1.5).[49]

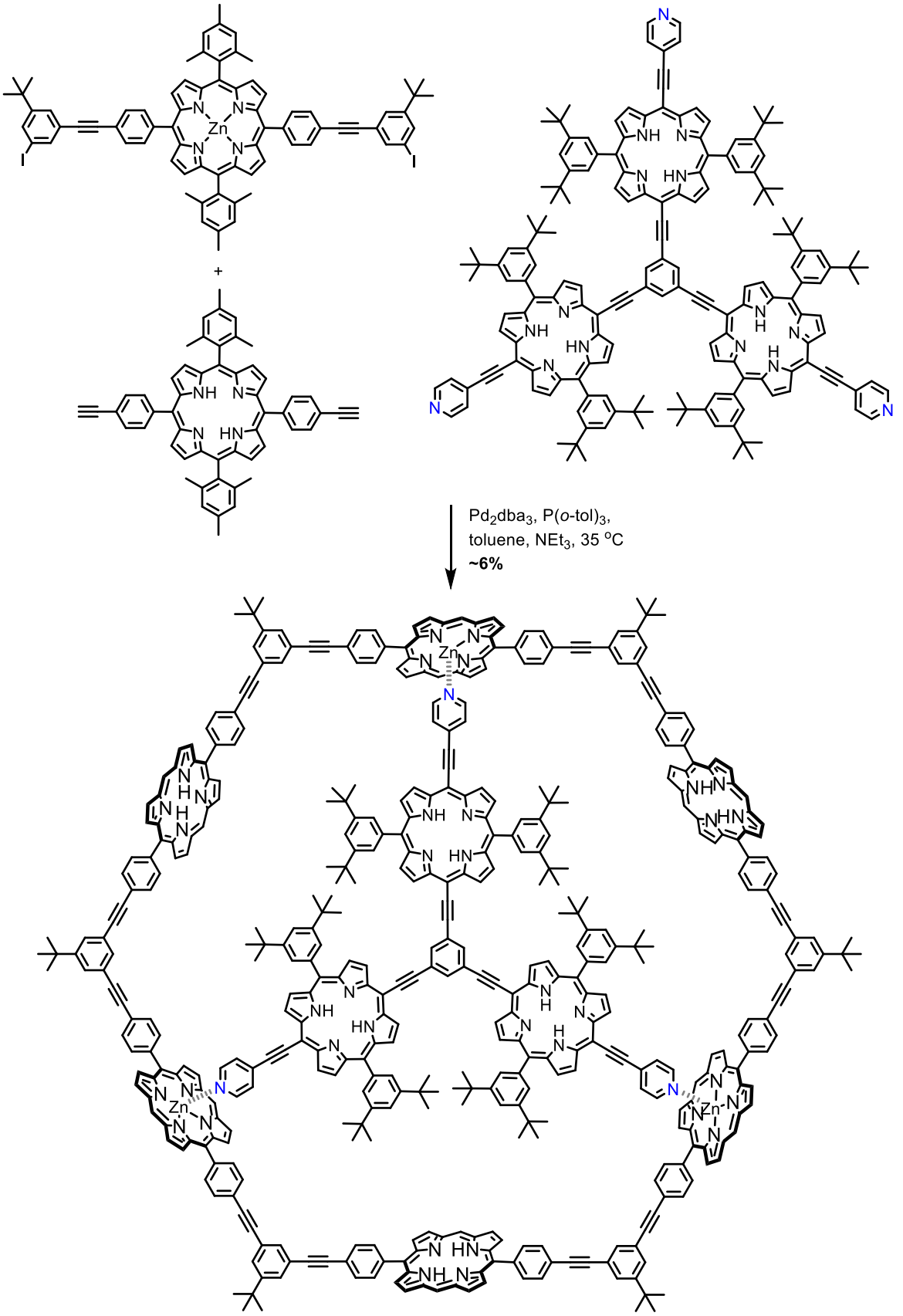

Figure 1.5: Synthesis of a cyclic porphyrin hexamer from monomeric building blocks using palladium-catalysed coupling conditions in the presence of a C_3-symmetric porphyrin trimer as template. The solubilising aryl substituents on the porphyrin units in the cyclic hexamer are omitted for clarity.[49]

Another strategy for the synthesis of covalent porphyrin nanostructures through nitrogen-based supramolecular interactions utilises olefin metathesis, and numerous literature examples on the formation of these more flexible porphyrin complexes are available.[50–53] One example of this synthetic strategy was reported by Inomata and Konishi.[54] Rather than using a molecular template, they functionalised a gold nanocluster with sixteen 4-pyridylmethyl appended thiolates, hence creating a spherical template. Upon complexation to a zinc porphyrin monomer with four terminal olefin functionalities, and subsequent cross-linking *via* olefin metathesis using Grubbs's second generation catalyst, a gold nanocluster entrapped hexa-porphyrin nanocage was formed (Figure 1.6).

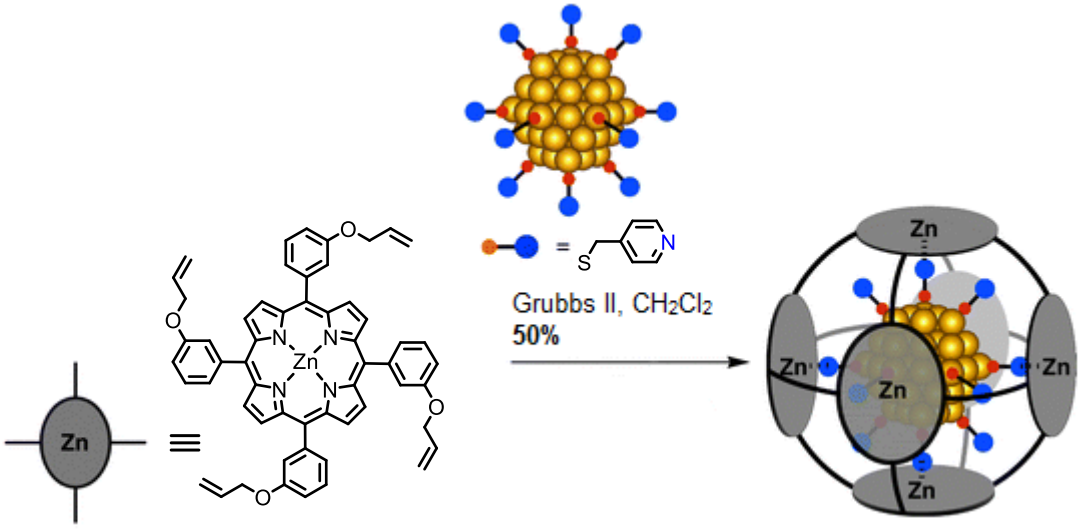

Figure 1.6: Template-directed synthesis of a hexaporphyrin nanocage using a functionalised gold nanocluster as the template. Adapted with permission from ref. 54. Copyright 2003 Royal Society of Chemistry.

Despite the variety of porphyrin nanostructures synthesised *via* template-directed methods, it was only in 2007 that the Anderson group prepared the first fully conjugated nanoring. This nanoring consisted of 8 porphyrin units connected through bis-acetylene linkages and was prepared from a linear porphyrin octamer precursor *via* templating around an 8-legged radial oligopyridine template.[34] In the decade that followed, the template-directed synthesis of π-conjugated porphyrin nanorings was extended to a comprehensive variety of nanorings with even and odd numbers of subunits.

Initially, the synthesis of porphyrin nanorings was achieved *via* classical templating which requires the synthesis of the desired radial oligopyridine template (**Tn**, with **T** denoting template and **n** denoting the number of binding sites) and subsequent coupling of porphyrin monomers or suitable linear precursors (***l*-Pm,** with ***l*** denoting a linear porphyrin

(**P**) oligomer consisting of **m** subunits, with **m** being a devisor of **n**). This classical templating strategy lead to the successful synthesis of ***c*-P5** (Figure 1.7),[43] ***c*-P6**,[35,38,55] ***c*-P7**,[38] ***c*-P8**,[34] and ***c*-P12** nanorings.[36]

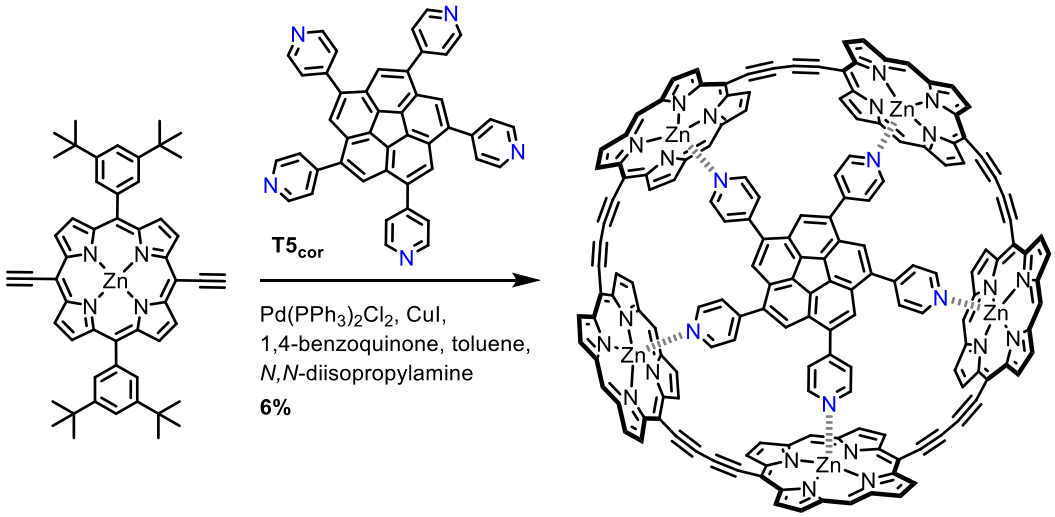

Figure 1.7: Classical template-directed synthesis of a 5-porphyrin nanoring (***c*-P5**) using a corannulene-based 5-legged oligopyridine template (**T5$_{cor}$**).[43] The solubilising aryl substituents on the porphyrin units in ***c*-P5** are omitted for clarity.

The synthesis of increasingly large porphyrin nanorings required the progressively laborious and challenging synthesis of large oligopyridine templates. To overcome this issue, a Vernier templating strategy was developed for porphyrin nanorings of 12-porphyrin subunits and more. Unlike the classical templating strategy discussed above, Vernier templating relies on the mismatch of the number of binding sites on the template, $\mathbf{n_T}$, and the number of binding sites on the porphyrin building block, $\mathbf{n_B}$. The number of binding sites of the product, $\mathbf{n_P}$, is the lowest common multiple of $\mathbf{n_T}$ and $\mathbf{n_B}$.[56,57] This strategy allows for the use of small templates in the synthesis of large porphyrin nanorings and resulted in the successful synthesis of large porphyrin nanorings starting from ***c*-P12** (Figure 1.8),[36,58] up to a nanoring containing 50-porphyrin subunits, ***c*-P50**.[37,40]

A third synthetic strategy used for the template-directed synthesis of π-conjugated porphyrin nanorings, relies on the formation of 2:1 caterpillar track complexes in which two small templates (each with n_T binding sites) direct the formation of one porphyrin nanoring (with $n_P = 2 \times n_T$ binding sites). This strategy was applied to prepare the zinc porphyrin nanorings ***c*-P8** and ***c*-P10**,[39] and a heterometallated 10-porphyrin nanoring with two orthogonal copper centres.[59]

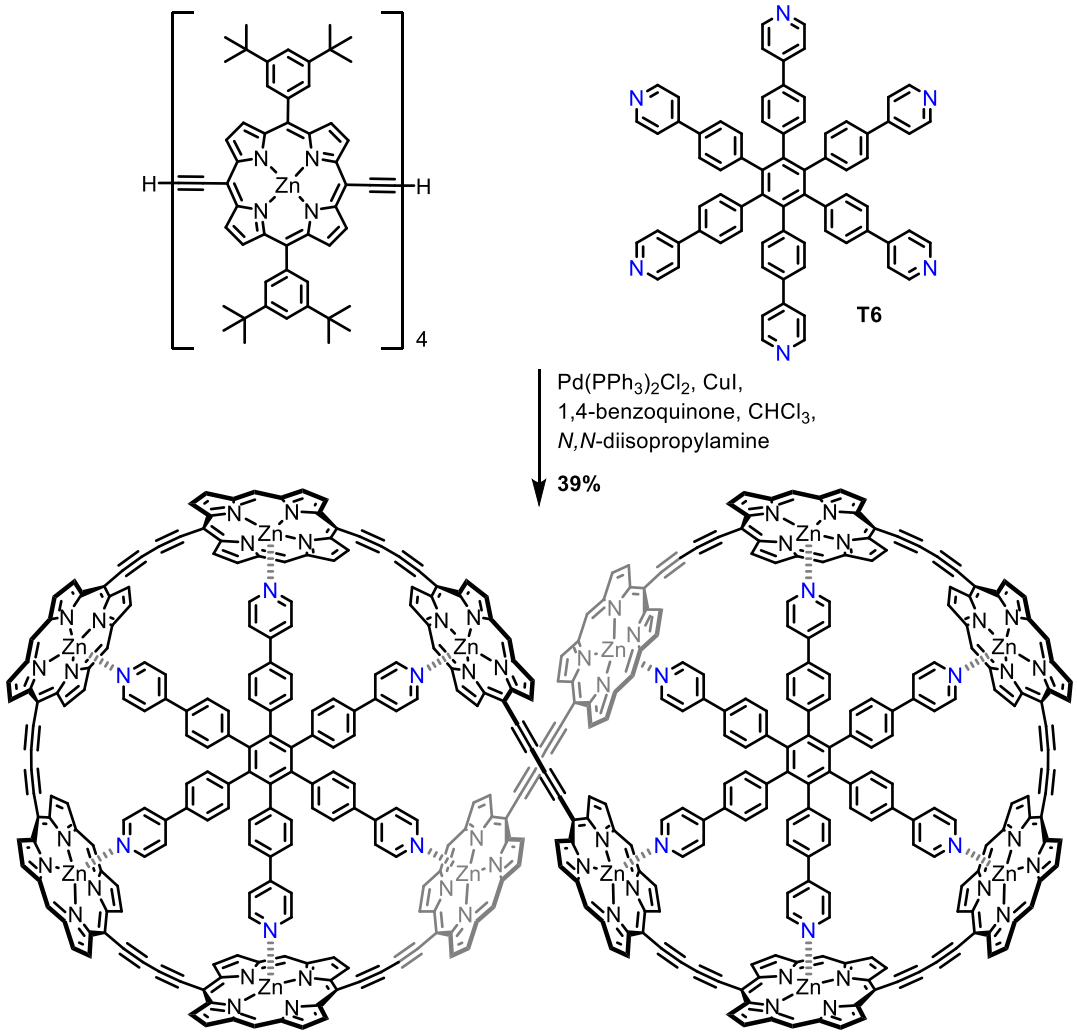

Figure 1.8: Vernier template-directed synthesis of a 12-porphyrin nanoring (***c*-P12**) from porphyrin tetramer building blocks, using a 6-legged oligopyridine template (**T6**).[36,58] The solubilising aryl substituents on the porphyrin units in ***c*-P12** are omitted for clarity.

Recently, zinc porphyrin nanostructures that extend beyond the two-dimensionality of the abovementioned nanorings have been prepared through nitrogen-based template-directed synthesis. The first example of a three-dimensional fully π-conjugated porphyrin nanostructure was a molecular nanotube consisting of 12-porphyrin units arranged in two conjoined 6-porphyrin nanorings, which is discussed in more detail in Chapter 3 of this thesis.[41]

Furthermore, a spiro-fused array of 11-porphyrin units was prepared. Notably, the porphyrin shared between two rings contains an unusual enforced pseudo-octahedral six-coordinate zinc centre. The final step in the synthesis of this complex involves the

coupling of a porphyrin cross-pentamer and two linear porphyrin trimers wrapped around two **T6** templates (Figure 1.9).[42]

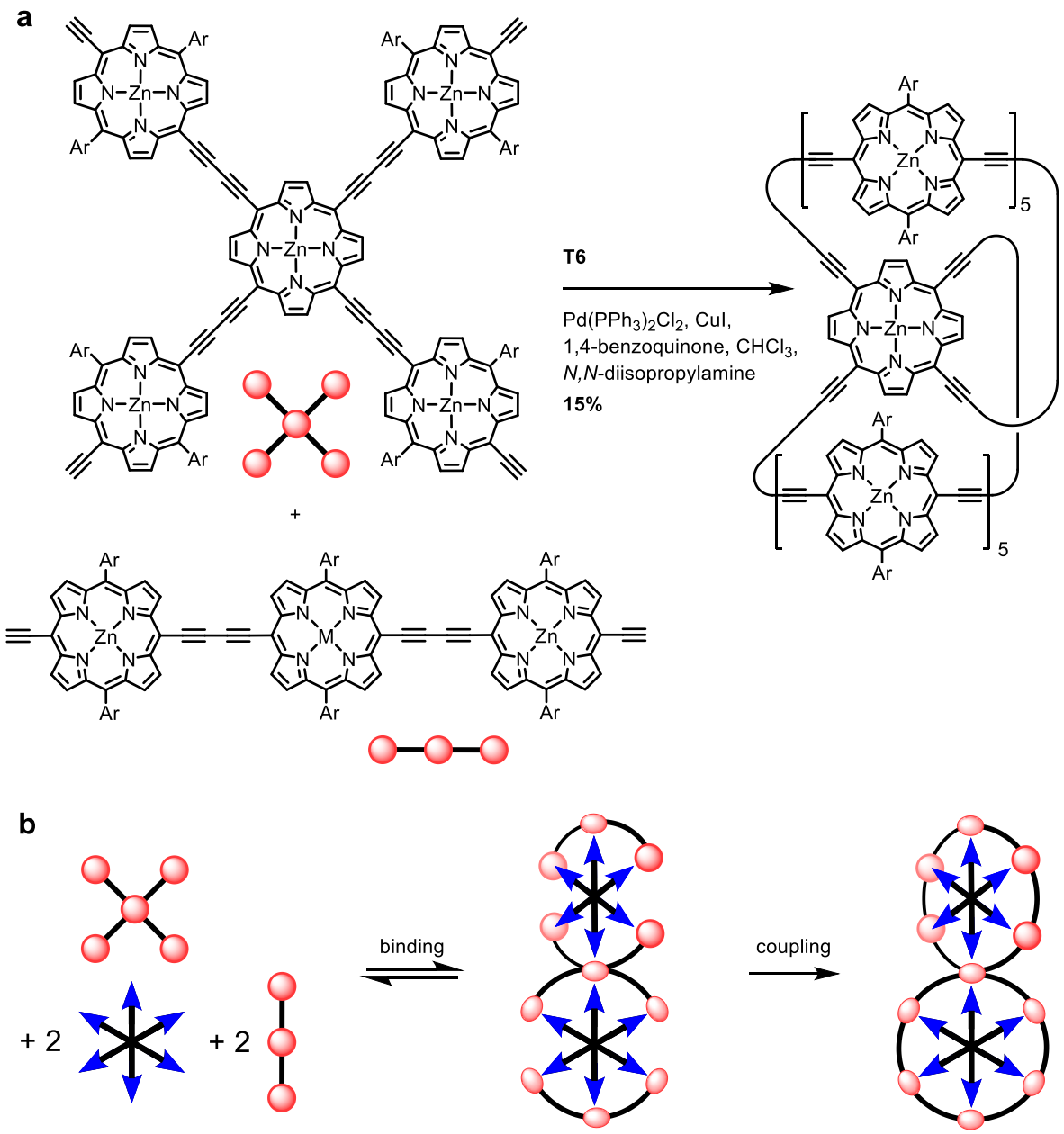

Figure 1.9: (a) Synthesis of a spiro-fused 11-porphyrin nanostructure *via* the template-directed coupling of a cross-pentamer and two porphyrin trimers in the presence of **T6** template. (Ar = 3,5-bis(trihexylsilyl)phenyl).[42] (b) Schematic representation of the synthetic route to the spiro-fused 11-porphyrin nanostructure.

Most recently, two fully π-conjugated porphyrin nanoballs with either 14-porphyrin subunits and 10-porphyrin subunits have been prepared. A manuscript on this work is currently in preparation.[60] In Chapter 6 of this thesis, DFT studies on these monodisperse spherical porphyrin nanostructures are discussed.

1.3 Carbon Allotropes and Carbon Nanotubes

1.3.1 Carbon Allotropes

Carbon, the sixth most abundant element in our universe, is the fundamental building block of all frameworks and backbones that are crucial to life on Earth. Out of the 118 elements currently included in the periodic table, carbon has the quintessential subatomic composition to be this versatile elemental building block.[61] One key feature is its ability to share electrons with up to four other atoms in order to fill its valence orbitals. This allows carbon to build complex chains and even three-dimensional molecular structures.

Until recently, the only allotropic forms of carbon that were available in macroscopic quantities were the natural modifications graphite and diamond (Figure 1.10).[62–64] Graphite (a sheet-like sp^2 carbon material), is amongst other applications, widely used as a reinforcement material in carbon fibre materials.[65–67] Diamond (a 3D network-like sp^3 carbon material) is known for its hardness and hence is used in drilling heads. Furthermore, diamond finds application in the jewellery industry due to its high refractive index.

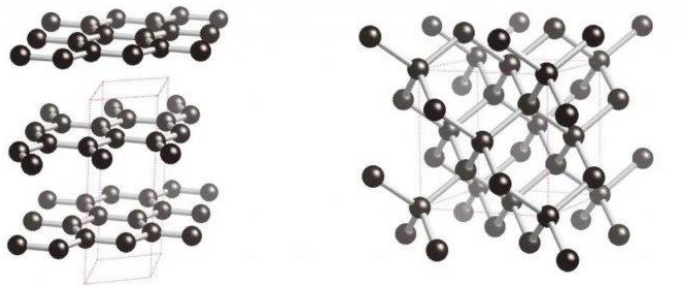

Figure 1.10: Network structures of graphite (left) and diamond (right).

The experimental identification of the third carbon allotrope; a geodesic dome of 60 carbon atoms (named C_{60} fullerene) by Kroto and co-workers in 1985 (ref. 68) who received the 1996 Noble prize in Chemistry for their work, was soon followed by its subsequent macroscopic preparation by Krätschmer and co-workers.[69] Since, the field of all-carbon based materials has exponentially expanded. In the past three decades, several new sp^2 carbon materials with remarkable properties have been discovered, such as the higher fullerenes,[68–73] carbon nanotubes,[74–76] and graphene.[77] However, *sp* carbon allotropes remain elusive, such as carbyne (an infinite polyyne; a one-dimensional rod constituted of alkyne units), and cycloc[*n*]carbons (monocyclic compounds constructed solely from *sp*-hybridised carbons).[78]

Fullerenes and their functionalised derivatives have found widespread application in, for example, different types of drugs,[79,80] and as electron-acceptor materials in organic solar cells (OSCs).[81–86] OSCs use organic semiconducting materials as photoactive molecules for light absorption and charge transport. Some of the advantages of these systems are the relatively low cost of the production of organic materials and their ability to be printed, *via* high throughput methods, on large-area, flexible substrates.[85] Currently the most efficient architecture to build OSCs is a bulk heterojunction structure, in which the photoactive layers comprise an interpenetrating network of a conjugated (polymer) donor and an acceptor such as a fullerene derivative. Blending the donor and acceptor accounts for higher charge photogeneration efficiencies and ambipolar transport properties when compared to a bilayer structure.[82,87]

The best performing polymer-fullerene single-junction OSC to date was reported by Zhao and co-workers in 2016 and exhibits a power conversion efficiency (PCE) of 11.7%.[88] The device uses a poly[(5,6-difluoro-2,1,3-benzothiadiazol-4,7-diyl)] polymer (PffBT4T-C_9C_{13}) as the donor material and phenyl-C_{71}-butyric acid methyl ester ($PC_{71}BM$) as the acceptor material (Figure 1.11). Recently also non-fullerene acceptor materials for OSCs have gained significant interest and the non-fullerene OSCs currently hold the record PCE of 13%.[89,90]

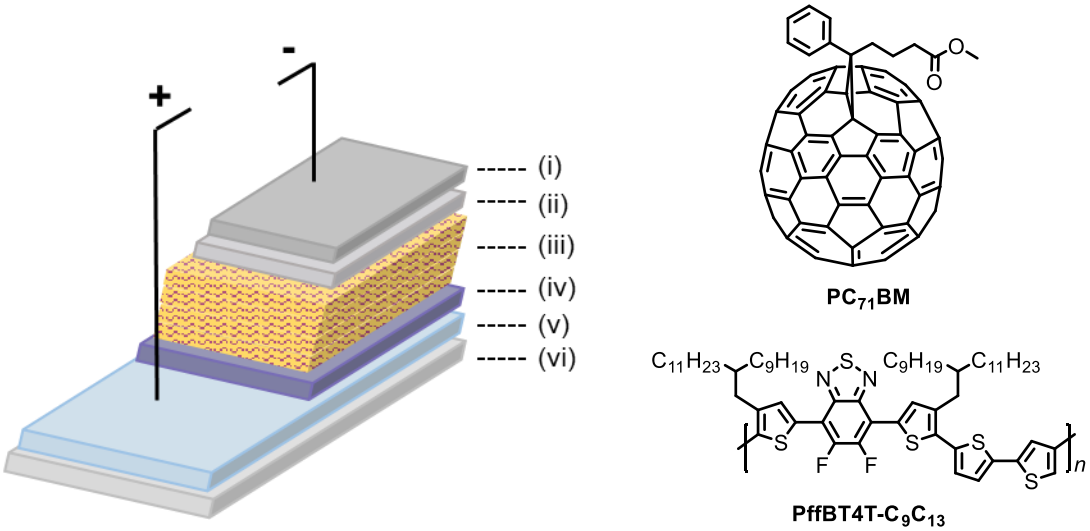

Figure 1.11: The best-performing polymer-fullerene single-junction OSC to date.[88] (left) Schematic representation of the OSC; (i) Al, (ii) V_2O_5, (iii) PffBT4T-C_9C_{13}/$PC_{71}BM$, (iv) ZnO, (v) ITO, (vi) glass. (right) Chemical structures of the active layer; donor polymer PffBT4T-C_9C_{13} and acceptor $PC_{71}BM$.

1.3.2 Carbon Nanotubes – Synthesis, Properties and Applications

Since the discovery of multi-walled carbon nanotubes (MWNTs) and single-walled carbon nanotubes (SWNTs) in 1991 and 1993 respectively, [74–76] these cylindrical sp^2-based carbon allotropes have received great interest from the scientific community. Carbon nanotubes have remarkable electronic transport properties and unusual mechanical properties which make them interesting materials for applications in electronics, mechanically reinforced materials, and various other applications.[91,92]

The current commercial application of these materials is predominantly in the form of bulk composite materials and thin films. Composites reinforced by CNTs,[93,94] are for example applied in lightweight wind turbine blades. A promising application of CNT-based materials is in transparent conducting films,[95] as an alternative to indium tin oxide (ITO) in thin film photovoltaics. Furthermore, MWNTs are widely used as additives to improve rate capability and cyclability for lithium ion batteries in small devices such as laptops and mobile phones.[96,97]

SWNTs hold great promise for their application in nanometer-sized electronics. SWNTs can be either semiconducting or metallic, depending on their diameter and chirality (Figure 1.12).[98,99] The structure of CNTs is designated by their (m,n) index; nanotubes with ($m = n$) are referred to as armchair and are metallic conductors; nanotubes with (m,0) are designated zigzag and all other CNTs are designated as chiral, of which the latter two can be either metallic or semiconducting depending on the specific (m,n) index.[100]

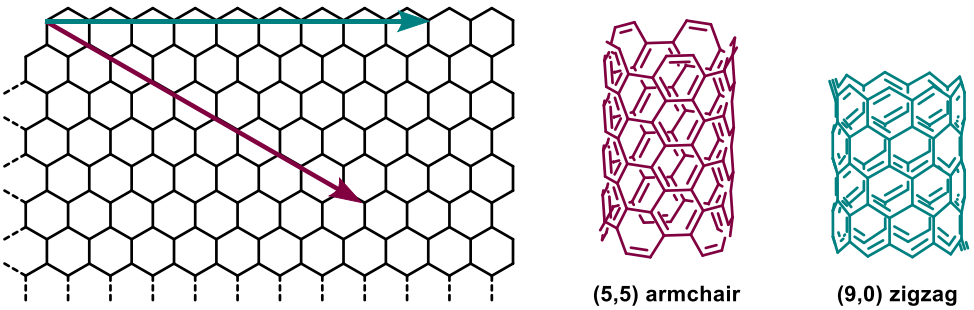

Figure 1.12: CNT structure visualised by imagining a carbon nanotube as a rolled-up sheet of graphene. The angle of rolling-up determines the CNT's structure, which can be designated by the (m,n) index. Depicted here as an example are an (5,5) armchair CNT (stemming from rolling up a graphene sheet along the purple arrow), and a (9,0) zigzag CNT (stemming from rolling up a graphene sheet along the teal arrow).

For their use in nanoscale electronics, the electronic properties of the CNTs must be precisely controlled. Hence, there is a demand for a synthetic method that gives structurally

uniform and atomically precise CNTs. Unfortunately, currently available synthetic procedures for CNT production, of which chemical vapour deposition is the dominant one,[101] still result in a mixture of nanotubes,[102,103] and hence a range of properties. Postprocessing methods have been developed to separate certain nanotube species, in particular metallic and semiconducting nanotubes, in order to obtain ultra-high purity SWNTs.[104–106] However, these postprocessing methods are still limited in their yield and selectivity and are furthermore very expensive. The inaccessibility of uniform-diameter single-chirality CNTs impedes the development of new CNT-based functional materials.

1.3.3 Bottom-up Synthetic Approaches Towards Atomically Precise CNTs

One of the approaches towards atomically precise CNTs is based on bottom-up organic synthesis. This approach requires the initial preparation of a small molecule, which includes the structural information of the nanotube. These small molecules, CNT structural segments (see Figure 1.13 for examples), can subsequently be used as templates to direct structurally uniform CNT growth.[107–110] In addition, these structural segments serve as finite models of CNTs, and provide fundamental insights into the properties of carbon nanotubess.[111–113]

[*n*]Cycloparaphenylenes present the shortest armchair (*n*,*n*)CNT segments. Since the first reported synthesis of [*n*]CPP (*n*=9,12,18) in 2008 by Bertozzi and co-workers,[114] a range of [*n*]CPPs (*n*=5-16,18) have been prepared.[115] Recently, Itami and co-workers reported the synthesis of the first closed loop of fully fused edge-sharing benzene rings.[109] The shortest zigzag (*n*,0)CNT segment, [*n*]cyclacene, has been proposed in 1954,[116] however synthesis of this nanobelt has so far been unsuccessful.[117] Another successfully prepared type of CNT segments are the end-caps (Figure 1.13).[118]

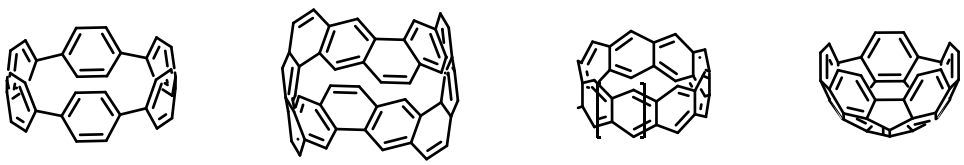

Figure 1.13: Synthesised and proposed CNT segments. From left to right; [6]CPP, carbon nanobelt (Itami, 2008), [*n*]cyclacene (not synthesised), (5,5)CNT end-cap.

A number of end-caps and [*n*]CPP CNT segments have been tested for their templating potential to direct the synthesis of structurally uniform CNTs.[107,119] In 2013, Omachi and

co-workers reported on [9]CPP- and [12]CPP-initiated CNT growth (Figure 1.14).[120] Under the reported reaction conditions in which the [*n*]CPP, coated on a C-plane sapphire substrate, was treated with flowing ethanol gas under vacuum at 500 °C, a narrow distribution of nanotube diameter and sidewall structure was obtained. Although promising, this strategy currently lacks absolute control over chirality and is furthermore only possible on a limited reaction scale.

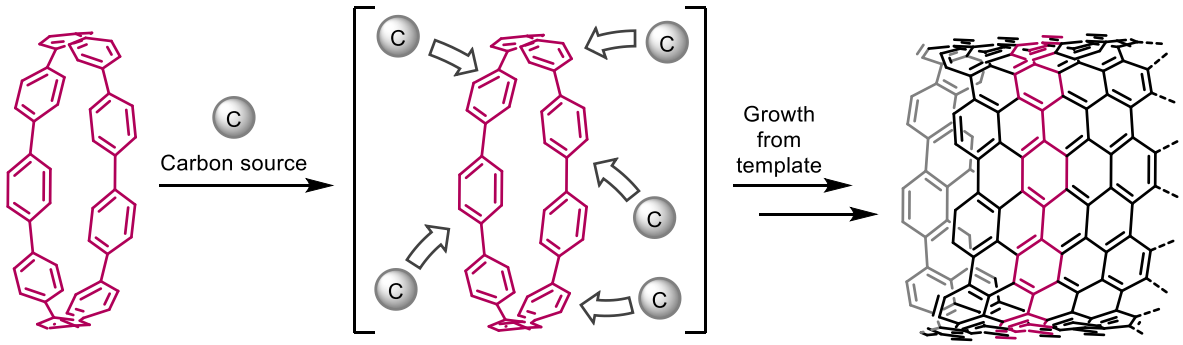

Figure 1.14: The 'growth-from-template' strategy for the bottom-up synthesis of structurally uniform CNTs. Here depicted the synthesis of (9,9)CNT from [9]CPP.[120]

1.4 Molecular Nanotubes and Nanobarrels

An alternative approach to the synthesis of atomically precise nanotubes comprises the synthesis of molecular nanotubular and belt-shaped structures.[115,121] The work discussed in this thesis comprises the construction of monodisperse, atomically precise π-conjugated nanotubes based on porphyrin building blocks. The field of molecular nanotubes constitutes a tremendous variety of both non-covalent and covalent structures. The introductory section of Chapter 3 of this thesis contains a concise review of covalent and non-covalent nanotubes obtained *via* ring-stacking strategies. In the following section, a comprehensive overview of reported π-conjugated molecular nanotubular structures is provided. These structures are, amongst other reasons, sought after for their potential as future seeds for CNT formation, and for the insight they might provide in the properties of CNTs. The section thereafter provides a comprehensive discussion of porphyrin based molecular nanobelts and tubes.

Sekiguchi and co-workers reported the preparation of a cyclic polyphenylene array that corresponds to a carbon array of a zigzag CNT segment. It was synthesised *via* a Diels-Alder reaction of a cyclic biphenylylene-acetylene derivative with tetraphenylcyclopentadienone (Figure 1.15).[113] The subsequent attempt towards the dehydrogenation and elimination of

the alkyl chains with excess $FeCl_3$ resulted in the formation of a complicated mixture analysed by MALDI-ToF spectrometry, which shows a broad signal that includes the mass of the presumed zigzag (18,0)CNT segment.

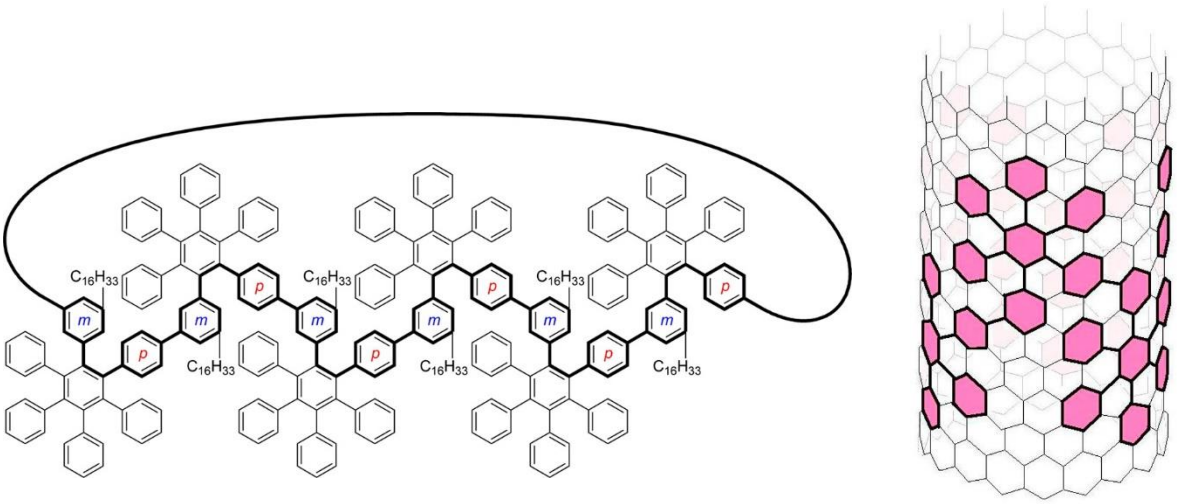

Figure 1.15: (left) Cyclic polyphenylene array, resembling a zigzag (18,0)CNT segment. (right) The same cyclic polyphenylene array, without the solubilising alkyl chains, superimposed on (18,0)CNT. Reprinted with permission from ref. 113. Copyright 2015 American Chemical Society.

Congeners of [*n*]CPP in the form of carbon nanohoops and nanobelts have been reported as finite models of SWNTs.[111,112,122,123] As structurally well-defined models of armchair (*n*,*n*)CNTs, Müllen and co-workers reported the synthesis of *para*-phenylene based 9- and 15-membered cylinders, as monodisperse models of (9,9) and (15,15)CNTs, respecitvely.[111] X-ray analysis of the 9-membered cylinder revealed an ellipsoid structure with large dihedral angels between adjacent phenyl rings. The large dihedral angle leads to a reduction in π-conjugation, which was indicated by hypsochromic shift in absorption. Cyclodehydrogenation with $FeCl_3$ resulted in mixtures of dehydrogenated products. ^{1}H NMR studies showed that upon cyclodehydrogenation, a 1,2-phenyl shift occurs to relieve ring strain.

Another model of armchair (*n*,*n*)CNTs was reported by Xia and co-workers. Rather than extending the backbone of [*n*]CPP itself, they formed a carbon nanobelt *via* the formation of arene-bridged cycloparaphenylene dimers.[124] The dimers were constructed from a [8]CPP precursors with a bromo-substituent as a versatile functional handle. Dimerisation in the presence of 1,4-benzenediboronic acid bis(pinacol) ester or 1,5-naphthalenediboronic acid bis(pinacol) ester followed by reductive elimination-aromatisation lead to 1,4-benzene and

1,5-naphthalene bridged CPP dimers respectively (Figure 1.16). DFT calculations suggested that the CPP dimers can adopt a desired (nanotube-like) cis-conformation in the gas phase and in solution, while in the solid state the trans configuration is lower in energy by 34 kcal/mol.

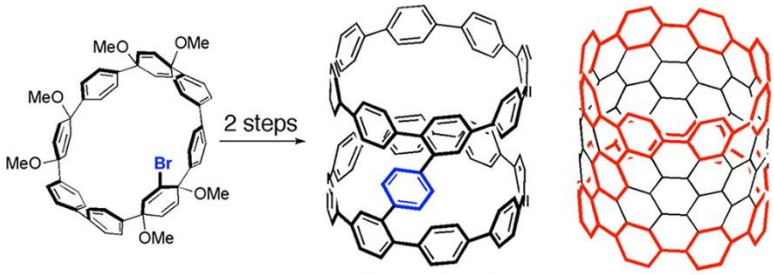

Figure 1.16: Synthesis of an 1,4-benzene bridged cycloparaphenylene dimer, a carbon nanobelt that can be considered a short segment of (8,8)CNTs. Reprinted with permission from ref. 124. Copyright 2012 American Chemical Society.

Examples of atomically precise carbon nanobelts are not limited to models of zigzag and armchair CNTs as discussed above. In 2015, the group of Isobe reported the first synthesis of a chiral hoop-shaped structure, which was based on single-bond linked cyclophenacenylenes. The assignment of the chiral indices of the obtained materials was achieved by Circular Dichroism (CD) spectroscopy and theoretical calculations.[112]

1.5 Porphyrin Nanotubes, Nanobelts and Nanobarrels

1.5.1 Supramolecular Assemblies

The formation of tubular architectures using porphyrin building blocks has been reported for both supramolecular assembled and covalently linked systems. A particularly well-studied building block for supramolecular porphyrin nanotubes is *meso*-tetra(4-sulfonatophenyl)porphine ($TPPS_4$).[125–129] In acidic aqueous solution, two protons bind to the central nitrogen atoms of the porphyrin ring, rendering the central part of the molecule positively charged. Strong intermolecular interactions of the negatively charged SO_3 groups of $TPPS_4$ molecules with the protonated nitrogen atoms at the centre of neighbouring molecules accounts for the formation of J-aggregates (Figure 1.17a).[130] Atomic force microscopy (AFM) studies demonstrated that the aggregates are straight nanotubes with a well-defined height.[127,131] Recent studies on the exciton transport in these supramolecular nanotubes with correlated AFM and transient absorption microscopy

(TAM) allowed imaging of exciton propagation (Figure 1.17b). Propagation was observed to occur exclusively along the long axis of the nanotubes, with a measured exciton diffusion constant of 3-6 $cm^2\ s^{-1}$. While it would evidently be interesting to compare this value to the exciton diffusion constants in CNTs, reported values cover a large range,[132,133] and hence no meaningful comparison can be made.

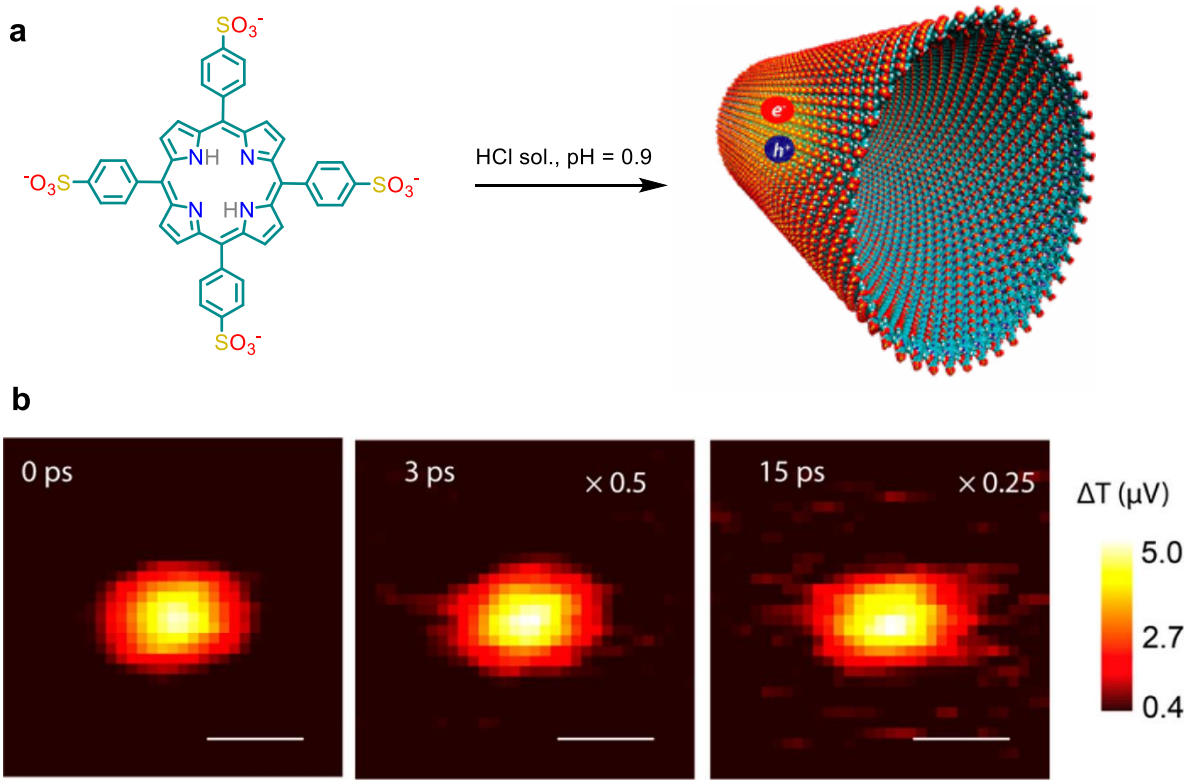

Figure 1.17: (a) Chemical structure of $TPPS_4$ and its assembly into tubular aggregates at pH 0.9. (b) TAM imaging of exciton transport showing the spatial distribution of exciton propagation at different pump-probe delay times as labelled. The colour scale represents the intensity of the differential transmission (ΔT) of the probe beam at 0 ps. For 3 and 15 ps, ΔT is plotted on a relative scale to the one at 0 ps, with the multiplication factor as labelled. Scale bar: 0.5 μm. Adapted with permission from ref. 129. Copyright 2017 American Chemical Society.

Another class of supramolecular porphyrin nanotubes relies on the self-assembly of metalloporphyrins bearing a coordinating side-arm.[134–136] In 2006, Kamada and co-workers reported on the self-assembly of a bis-cinchomeronimide substituted porphyrin dimer. Rotation of the cinchomeronimide group is restricted due to the steric hindrance of the two imide-carbonyl groups, resulting in three different stable atropisomers, in which the cinchomeronimide pyridyl nitrogen atoms either point in-in, in-out, or out-out (the latter is depicted in Figure 1.18). In addition, free rotation around the *meso-meso* linkage between the two porphyrins is severely prohibited. In noncoordinating solvents like $CHCl_3$, this

porphyrin dimer not only self-assembles into tubular aggregates, it performs rigorous homochiral self-sorting. The in-in dimer was found to form trimeric, the in-out dimer to form tetrameric, and the out-out dimer to form pentameric assemblies, respectively. The structure of the pentameric complex was confirmed by X-ray analysis and DFT studies (Figure 1.18).

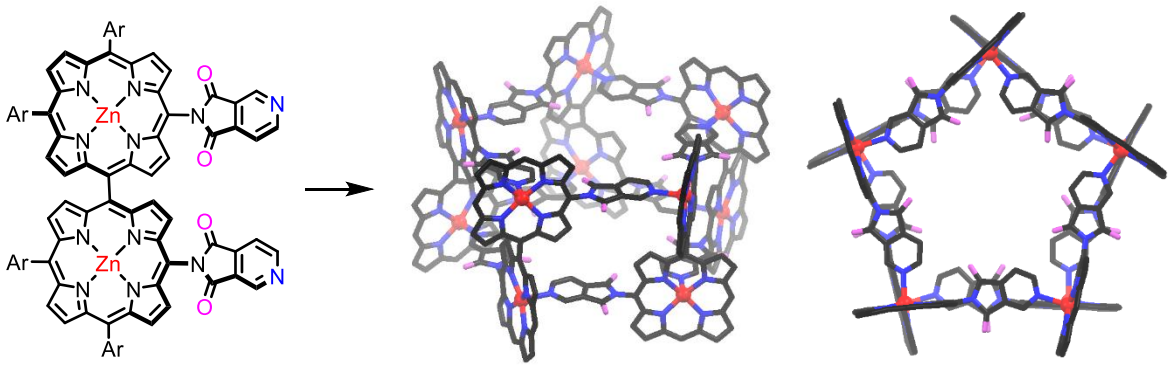

Figure 1.18: Self-assembly and homochiral self-sorting of a bis-cinchomeronimide substituted porphyrin dimer (Ar = 3,5-bis(*tert*-butyl)phenyl). Here depicted; the out-out atropisomer, which self-assembles into a pentameric assembly, of which the crystal structure is depicted. Solvent molecules, hydrogen atoms and *meso*-aryl groups are omitted for clarity. Adapted with permission from ref. 136. Copyright 2006 American Chemical Society.

Other examples include the self-assembly of an acyclic porphyrin dimer into a "supramolecular peapod" structure in the presence of C_{60} fullerene,[137] a supramolecular nanotube formed by hydrophobicity-driven self-assembly of a synthetic model of bacteriochlorophyll,[138] and the formation of supramolecular porphyrin prisms *via* the perpendicular arrangement of linear zinc porphyrin oligomers with tridentate nitrogen-based ligands.[139,140]

1.5.2 Covalent Structures

Compared to supramolecular assemblies, covalent systems benefit from shape-persistency and molecular integrity under various conditions.

Structures consisting of porphyrin-CNT frameworks have been prepared in which the MWNT surface act as template to direct the formation of an amorphous multi-layer covalent cobalt porphyrin coating around the nanotube sidewalls (Figure 1.19).[141,142] The cobalt porphyrin-MWNT complex was examined for its catalytic activity in the oxygen reduction reaction under acidic conditions,[141] and in the water oxidation reaction under basic

conditions.[142] In both cases, improved catalytic performance and catalytic stability was observed compared to a physisorbed analogous hybrid material. Furthermore, the optimal onset potential of the porphyrin-MWNT material in the water oxidation reaction was found to be much lower than those reported for other molecular and metal-oxide heterogeneous water oxidation catalysts, which makes it an attractive and efficient candidate for water oxidation using Earth-abundant elements.

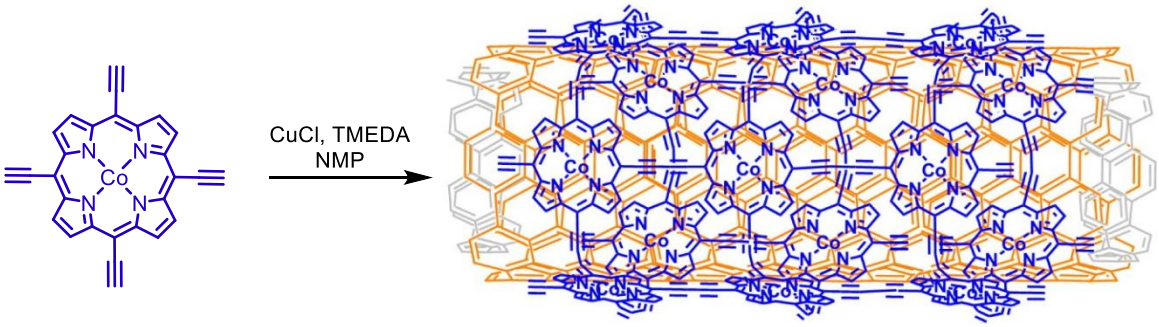

Figure 1.19: Synthesis of the covalent cobalt-porphyrin coated MWNT. The representation of the porphyrin polymer is an idealised view of the reality, as characterisation showed that the porphyrins form an amorphous polymer coating around the MWNT sidewalls. Adapted with permission from ref. 142. Copyright 2015 American Chemical Society.

Atomically precise, monodisperse porphyrin nanotubes were prepared by the groups of Osuka and Hupp. The latter reported the synthesis of a flexible porphyrin nanotube constructed from three porphyrin dimers which are held in a prismatic arrangement by a tridentate nitrogen-based template and subsequently covalently linked *via* olefin metathesis.[50]

The group of Osuka reported the synthesis of a nickel porphyrin nanobarrel *via* consecutive Suzuki-Miyaura cross-coupling reactions without the need of a template (Figure 1.20),[143] since the β,β'-double 2,6-pyridylene bridges between the individual porphyrin subunits account for a bent conformation. The authors claim that the pyridyl bridges serve as a conjugative mediator to cause overall moderate π-conjugation. Considering the pyridyl linkages between the porphyrin subunits that reside at the β-positions are *meta*-connected and have an average dihedral angle of 43.5°, the annotation 'moderate' seems appropriate. Interestingly, the porphyrin nanobarrel was found to be an excellent host for C_{60} as confirmed by X-ray analysis and ^{13}C NMR, with an estimated association constant in toluene of $(5.3 \pm 0.1) \times 10^5\ M^{-1}$.

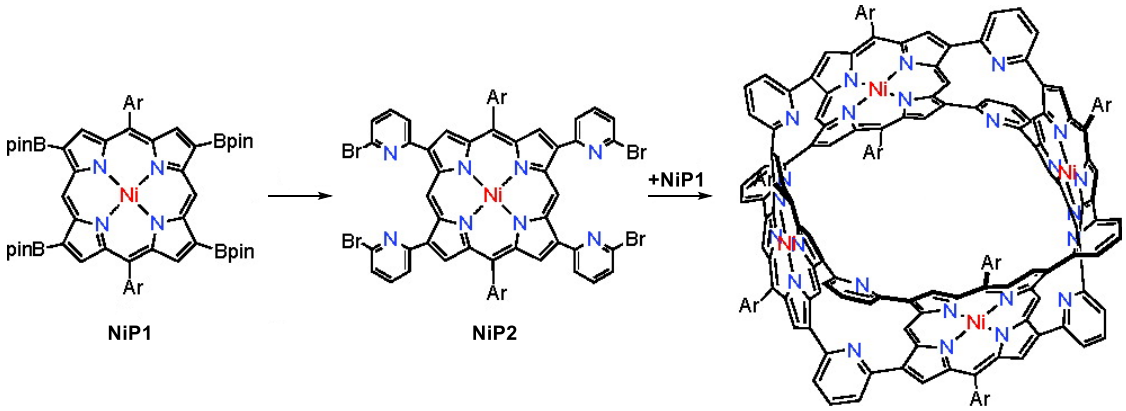

Figure 1.20: Synthesis of a nickel porphyrin nanobarrel *via* consecutive Suzuki-Miyaura cross-coupling reactions (Ar = 3,5-bis(*tert*-butyl)phenyl). Adapted with permission from ref. 143. Copyright 2010 American Chemical Society.

1.6 Prospective

Carbon nanotubes are promising materials for future nanotechnology applications. However, their current synthetic methods lack absolute synthetic control and produce mixtures of structures with inhomogeneous physical properties. Numerous research groups focus on the atomically precise construction of these carbon nanostructures. Others tend to a more molecular approach and a tremendous variety of exciting nanomaterials have been developed.

Porphyrins, with their planar aromatic cores, are suitable and versatile building blocks to construct functional nano-belts, barrels and tubes. Substitution of the porphyrin backbone as well as the compatibility with various metal atoms enables precise tuning of the molecular properties. High efficiencies in electron and energy transfer render porphyrins ideal candidates for the bottom-up "total" synthesis of atomically precise analogues of CNTs.

In 2015, the Anderson group reported the synthesis of a three-dimensional fully π-conjugated monodisperse molecular nanotube, resembling a molecular analogue to a short SWNT, constructed from 12 porphyrin subunits arranged in two conjoined 6-porphyrin nanorings; ***t*-P12·(T6)$_2$**.[41] Ultrafast time-resolved fluorescence spectroscopy demonstrated excited state delocalisation over the strongly π-conjugated system. A later study on the electronic delocalisation in the radical cation of this nanotube, ***t*-P12·(T6)$_2$$^{+\bullet}$**, revealed polaron delocalisation over 4-6 porphyrin units,[144] further highlighting the strong electronic coupling between the chromophores in this molecular nanotube.

This thesis aims to continue the exploration of π-conjugated porphyrin nanostructures with a special focus on porphyrin nanotubes. The first chapter (Chapter 2) investigates the supramolecular assembly of a ring-in-ring complex. Furthermore, it describes the synthesis of a 12-porphyrin nanoring, templated around a supramolecular 6-porphyrin nanoring-based template, and as such provides the first example of porphyrin nanoring synthesis *via* ring-around-ring templating.[145]

In Chapter 3, an unprecedented strategy towards porphyrin nanotube synthesis is described, using a ring-stacking approach of pre-formed 6-porphyrin nanorings. Furthermore, this chapter describes an improved template-directed procedure to the 12-porphyrin nanotube and a strategy to obtain the template-free nanotube. The latter enabled the exploration of the host-guest chemistry of this molecular box, which is described in Chapter 4. The 12-porphyrin nanotube proves to be an excellent fullerene-host, accommodating up to four C_{60} molecules, contained by the porphyrin "walls" and the template "lids". Upon addition of a strong competing ligand, the "lids" are displaced, liberating the encapsulated fullerenes from the nanotube cavity.

Chapter 5 describes the synthesis and properties of a new class of porphyrin nanotubes, in which the conjoined nanoring segments are connected *via* mono-acetylene linkages. This family exhibits enhanced electronic communication compared to their bis-acetylene linked analogues. Furthermore, this strategy enabled the bottom-up synthesis of an 18-porphyrin nanotube, the largest π-conjugated molecular nanotube to date.

The thesis concludes with a predominantly computational chapter (Chapter 6), including a DFT study on the odd-even effect in porphyrin nanotubes. Furthermore, it explores the electronic structure of an ellipsoidal 14-porphyrin nanoball, demonstrating excellent agreement with experimental observations.

1.7 References

(1) M. F. Perutz, M. G. Rossmann, A. F. Cullis, H. Muirhead, G. Will, A. C. T. North. 'Structure of Haemoglobin: A Three-Dimensional Fourier Synthesis at 5.5-Å. Resolution, Obtained by X-Ray Analysis'. *Nature*, **1960**, *185*, 416–422.

(2) G. McDermott, S. M. Prince, A. A. Freer, A. M. Hawthornthwaite-Lawless, M. Z. Papiz, R. J. Cogdell, N. W. Isaacs. 'Crystal Structure of an Integral Membrane Light-Harvesting Complex from Photosynthetic Bacteria'. *Nature*, **1995**, *374*, 517–521.

(3) M. Z. Papiz, S. M. Prince, T. Howard, R. J. Cogdell, N. W. Isaacs. 'The Structure and Thermal Motion of the B800-850 LH2 Complex from Rps. Acidophila at 2.0 Å Resolution and 100 K: New Structural Features and Functionally Relevant Motions'. *J. Mol. Biol.*, **2003**, *326*, 1523–1538.

(4) R. J. Cogdell, A. Gall, J. Köhler. 'The Architecture and Function of the Light-Harvesting Apparatus of Purple Bacteria: From Single Molecules to in Vivo Membranes'. *Q. Rev. Biophys.*, **2006**, *39*, 227–324.

(5) L. Luer, V. Moulisova, S. Henry, D. Polli, T. H. P. Brotosudarmo, S. Hoseinkhani, D. Brida, G. Lanzani, G. Cerullo, R. J. Cogdell. 'Tracking Energy Transfer between Light Harvesting Complex 2 and 1 in Photosynthetic Membranes Grown under High and Low Illumination'. *Proc. Natl. Acad. Sci.*, **2012**, *109*, 1473–1478.

(6) L. R. Milgrom. *The Colours of Life: Introduction to the Chemistry of Porphyrins and Related Compounds*, 1st ed.; Oxford University Press, **1997**.

(7) H. L. Anderson. 'Building Molecular Wires from the Colours of Life: Conjugated Porphyrin Oligomers'. *Chem. Comm.*, **1999**, 2323–2330.

(8) S. Hiroto, Y. Miyake, H. Shinokubo. 'Synthesis and Functionalization of Porphyrins through Organometallic Methodologies'. *Chem. Rev.*, **2017**, *117*, 2910–3043.

(9) V. S. Lin, S. G. Dimagno, M. J. Therien. 'Highly Conjugated, Acetylenyl Bridged Porphyrins: New Models for Light-Harvesting Antenna Systems'. *Science*, **1994**, *264*, 1105–1111.

(10) N. Aratani, A. Tsuda, A. Osuka. 'Discrete Giant Porphyrin Arrays: Challenges to Molecular Size, Length and the Extent of Electronic π-Conjugation'. *Synlett*, **2001**, 1663–1674.

(11) M. Terazima, H. Shimizu, A. Osuka. 'The Third-Order Nonlinear Optical Properties of Porphyrin Oligomers'. *J. Appl. Phys.*, **1997**, *81*, 2946–2951.

(12) A. Nakano, A. Osuka, I. Yamazaki, T. Yamazaki, Y. Nishimura. 'Windmill-like Porphyrin Arrays as Potent Light-Harvesting Antenna Complexes'. *Angew. Chem. Int. Ed.*, **1998**, *37*, 3023–3027.

(13) D. P. Arnold, A. W. Johnson, M. Mahendran. 'Some Reactions of *meso*-Formyloctaethylporphyrin'. *J. Chem. Soc. Perkin Trans. 1*, **1978**, *0*, 366–370.

(14) D. P. Arnold, L. J. Nitschinsk. 'Porphyrin Dimers Linked by Conjugated Butadiynes'. *Tetrahedron*, **1992**, *48*, 8781–8792.

(15) M. D. Peeks, P. Neuhaus, H. L. Anderson. 'Experimental and Computational Evaluation of the Barrier to Torsional Rotation in a Butadiyne-Linked Porphyrin Dimer'. *Phys. Chem. Chem. Phys.*, **2016**, *18*, 5264–5274.

(16) P. N. Taylor, J. Huuskonen, G. Rumbles, R. T. Aplin, E. Williams, H. L. Anderson. 'Conjugated Porphyrin Oligomers from Monomer to Hexamer'. *Chem. Comm.*, **1998**,

909–910.

(17) M. U. Winters, J. Kärnbratt, M. Eng, C. J. Wilson, H. L. Anderson, B. Albinsson. 'Photophysics of a Butadiyne-Linked Porphyrin Dimer: Influence of Conformational Flexibility in the Ground and First Singlet Excited State'. *J. Phys. Chem. C*, **2007**, *111*, 7192–7199.

(18) H. L. Anderson. 'Conjugated Porphyrin Ladders'. *Inorg. Chem.*, **1994**, *33*, 972–981.

(19) P. N. Taylor, H. L. Anderson. 'Cooperative Self-Assembly of Double-Strand Conjugated Porphyrin Ladders'. *J. Am. Chem. Soc.*, **1999**, *121*, 11538–11545.

(20) F. C. Grozema, C. Houarner-Rassin, P. Prins, L. D. A. Siebbeles, H. L. Anderson. 'Supramolecular Control of Charge Transport in Molecular Wires.'. *J. Am. Chem. Soc.*, **2007**, *129*, 13370–13371.

(21) S. G. Wilson, H. L. Anderson. 'A Conjugated Triple Strand Porphyrin Array'. *Chem. Comm.*, **1999**, *1*, 1539–1540.

(22) J. K. Sprafke, B. Odell, T. D. W. Claridge, H. L. Anderson. 'All-or-Nothing Cooperative Self-Assembly of an Annulene Sandwich'. *Angew. Chem. Int. Ed.*, **2011**, *50*, 5572–5575.

(23) P. Parkinson, C. E. I. Knappke, N. Kamonsutthipaijit, K. Sirithip, J. D. Matichak, H. L. Anderson, L. M. Herz. 'Ultrafast Energy Transfer in Biomimetic Multistrand Nanorings'. *J. Am. Chem. Soc.*, **2014**, *136*, 8217–8220.

(24) H. J. Hogben, J. K. Sprafke, M. Hoffmann, M. Pawlicki, H. L. Anderson. 'Stepwise Effective Molarities in Porphyrin Oligomer Complexes: Preorganization Results in Exceptionally Strong Chelate Cooperativity'. *J. Am. Chem. Soc.*, **2011**, *133*, 20962–20969.

(25) D. P. Arnold, G. A. Heath. 'Voltammetric and UV to Near-IR Spectroelectrochemical Characterization of the Meso,meso′-Buta- 1,3-Diyne-Bridged Octaethyiporphyrin Dimers {[M(OEP)](μ-C_4)[M(OEP)]} (M_2 = H_4, Co_2, Ni_2, Cu_2, Zn_2, Pd_2, Pt_2, Co/Ni, and Ni/Zn), in Their Neutral, Mononegative, and Dinegative Oxidation States'. *J. Am. Chem. Soc.*, **1993**, *115*, 12197–12198.

(26) S. Thies, H. Sell, C. Schütt, C. Bornholdt, C. Näther, F. Tuczek, R. Herges. 'Light-Induced Spin Change by Photodissociable External Ligands: A New Principle for Magnetic Switching of Molecules'. *J. Am. Chem. Soc.*, **2011**, *133*, 16243–16250.

(27) R. C. Bruce, R. Wang, J. Rawson, M. J. Therien, W. You. 'Valence Band Dependent Charge Transport in Bulk Molecular Electronic Devices Incorporating Highly Conjugated Multi-[(Porphinato)Metal] Oligomers'. *J. Am. Chem. Soc.*, **2016**, *138*, 2078–2081.

(28) T. V. Duncan, S. P. Wu, M. J. Therien. 'Ethyne-Bridged (Porphinato)Zinc(II)-(Porphinato)Iron(III) Complexes: Phenomenological Dependence of Excited-State Dynamics upon (Porphinato)Iron Electronic Structure'. *J. Am. Chem. Soc.*, **2006**, *128*, 10423–10435.

(29) M. Otte, P. F. Kuijpers, O. Troeppner, I. Ivanović-Burmazović, J. N. H. Reek, B. de Bruin. 'Encapsulation of Metalloporphyrins in a Self-Assembled Cubic M_8L_6 Cage: A New Molecular Flask for Cobalt-Porphyrin-Catalysed Radical-Type Reactions'. *Chem. - Eur. J.*, **2013**, *19*, 10170–10178.

(30) T. Tanaka, A. Osuka. 'Conjugated Porphyrin Arrays: Synthesis, Properties and Applications for Functional Materials'. *Chem. Soc. Rev.*, **2015**, *44*, 943–969.

(31) K. Tashiro, T. Aida. 'Metalloporphyrin Hosts for Supramolecular Chemistry of Fullerenes'. *Chem. Soc. Rev.*, **2007**, *36*, 189–197.

(32) S. Anderson, H. L. Anderson, J. K. M. Sanders. 'Expanding Roles for Templates in Synthesis'. *Acc. Chem. Res.*, **1993**, *26*, 469–475.

(33) H. L. Anderson, J. K. M. Sanders. 'Amine-Template-Directed Synthesis of Cyclic Porphyrin Oligomers'. *Angew. Chem. Int. Ed.*, **1990**, *29*, 1400–1403.

(34) M. Hoffmann, C. J. Wilson, B. Odell, H. L. Anderson. 'Template-Directed Synthesis of a π-Conjugated Porphyrin Nanoring'. *Angew. Chem. Int. Ed.*, **2007**, *46*, 3122–3125.

(35) M. Hoffmann, J. Kärnbratt, M. H. Chang, L. M. Herz, B. Albinsson, H. L. Anderson. 'Enhanced π Conjugation Around a Porphyrin[6] Nanoring'. *Angew. Chem. Int. Ed.*, **2008**, *47*, 4993–4996.

(36) M. C. O'Sullivan, J. K. Sprafke, D. V Kondratuk, C. Rinfray, T. D. W. Claridge, A. Saywell, M. O. Blunt, J. N. O'Shea, P. H. Beton, M. Malfois, H. L. Anderson. 'Vernier Templating and Synthesis of a 12-Porphyrin Nano-Ring'. *Nature*, **2011**, *469*, 72–75.

(37) D. V. Kondratuk, L. M. A. Perdigao, M. C. O'Sullivan, S. Svatek, G. Smith, J. N. O'Shea, P. H. Beton, H. L. Anderson. 'Two Vernier-Templated Routes to a 24-Porphyrin Nanoring'. *Angew. Chem. Int. Ed.*, **2012**, *51*, 6696–6699.

(38) P. Liu, P. Neuhaus, D. V. Kondratuk, T. S. Balaban, H. L. Anderson. 'Cyclodextrin-Templated Porphyrin Nanorings'. *Angew. Chem. Int. Ed.*, **2014**, *53*, 7770–7773.

(39) S. Liu, D. V. Kondratuk, S. A. L. Rousseaux, G. Gil-Ramírez, M. C. O'Sullivan, J. Cremers, T. D. W. Claridge, H. L. Anderson. 'Caterpillar Track Complexes in Template-Directed Synthesis and Correlated Molecular Motion'. *Angew. Chem. Int. Ed.*, **2015**, *54*, 5355–5359.

(40) D. V. Kondratuk, L. M. A. Perdigão, A. M. S. Esmail, J. N. O'Shea, P. H. Beton, H. L. Anderson. 'Supramolecular Nesting of Cyclic Polymers'. *Nat. Chem.*, **2015**, *7*, 317–322.

(41) P. Neuhaus, A. Cnossen, J. Q. Gong, L. M. Herz, H. L. Anderson. 'A Molecular Nanotube with Three-Dimensional π-Conjugation'. *Angew. Chem. Int. Ed.*, **2015**, *54*, 7344 –7348.

(42) L. Favereau, A. Cnossen, J. B. Kelber, J. Q. Gong, R. M. Oetterli, J. Cremers, L. M. Herz, H. L. Anderson. 'Six-Coordinate Zinc Porphyrins for Template-Directed Synthesis of Spiro-Fused Nanorings'. *J. Am. Chem. Soc.*, **2015**, *137*, 14256–14259.

(43) P. Liu, Y. Hisamune, M. D. Peeks, B. Odell, J. Q. Gong, L. M. Herz, H. L. Anderson. 'Synthesis of Five-Porphyrin Nanorings by Using Ferrocene and Corannulene Templates'. *Angew. Chem. Int. Ed.*, **2016**, *55*, 8358–8362.

(44) M. Rickhaus, A. Vargas Jentzsch, L. Tejerina, I. Gruebner, M. Jirasek, T. D. W. Claridge, H. L. Anderson. 'Single-Acetylene Linked Porphyrin Nanorings'. *J. Am. Chem. Soc.*, **2017**, *139*, 16502–16505.

(45) J. Li, A. Ambroise, S. I. Yang, J. R. Diers, J. Seth, C. R. Wack, D. F. Bocian, D. Holten, J. S. Lindsey. 'Template-Directed Synthesis, Excited-State Photodynamics, and Electronic Communication in a Hexameric Wheel of Porphyrins'. *J. Am. Chem. Soc.*, **1999**, *121*, 8927–8940.

(46) L. Yu, J. S. Lindsey. 'Rational Syntheses of Cyclic Hexameric Porphyrin Arrays for

Studies of Self-Assembling Light-Harvesting Systems'. *J. Org. Chem.*, **2001**, *66*, 7402–7419.

(47) K. Y. Tomizaki, L. Yu, L. Wei, D. F. Bocian, J. S. Lindsey. 'Synthesis of Cyclic Hexameric Porphyrin Arrays. Anchors for Surface Immobilization and Columnar Self-Assembly'. *J. Org. Chem.*, **2003**, *68*, 8199–8207.

(48) O. Mongin, A. Schuwey, M. A. Vallot, A. Gossauer. 'Synthesis of a Macrocyclic Porphyrin Hexamer with a Nanometer-Sized Cavity as a Model for the Light-Harvesting Arrays of Purple Bacteria'. *Tetrahedron Lett.*, **1999**, *40*, 8347–8350.

(49) S. Rucareanu, A. Schuwey, A. Gossauer. 'One-Step Template-Directed Synthesis of a Macrocyclic Tetraarylporphyrin Hexamer Based on Supramolecular Interactions with a C_3-Symmetric Tetraarylporphyrin Trimer'. *J. Am. Chem. Soc.*, **2006**, *128*, 3396–3413.

(50) K.-T. Youm, S. T. Nguyen, J. T. Hupp. 'Hollow Porphyrin Prisms: Modular Formation of Permanent, Torsionally Rigid Nanostructures via Templated Olefin Metathesis'. *Chem. Comm.*, **2008**, 3375–3377.

(51) R. K. Totten, P. Ryan, B. Kang, S. J. Lee, L. J. Broadbelt, R. Q. Snurr, J. T. Hupp, S. T. Nguyen. 'Enhanced Catalytic Decomposition of a Phosphate Triester by Modularly Accessible Bimetallic Porphyrin Dyads and Dimers'. *Chem. Comm.*, **2012**, *48*, 4178–4180.

(52) B. Zhu, H. Chen, W. Lin, Y. Ye, J. Wu, S. Li. 'Template-Directed Synthesis of Flexible Porphyrin Nanocage and Nanorings via One-Step Olefin Metathesis'. *J. Am. Chem. Soc.*, **2014**, *136*, 15126–15129.

(53) J. Taesch, V. Heitz, F. Topić, K. Rissanen. 'Templated Synthesis of a Large and Flexible Covalent Porphyrinic Cage Bearing Orthogonal Recognition Sites'. *Chem. Comm.*, **2012**, *48*, 5118–5120.

(54) T. Inomata, K. Konishi. 'Gold Nanocluster Confined within a Cage: Template-Directed Formation of a Hexaporphyrin Cage and Its Confinement Capability'. *Chem. Comm.*, **2003**, 1282–1283.

(55) J. K. Sprafke, D. V. Kondratuk, M. Wykes, A. L. Thompson, M. Hoffmann, R. Drevinskas, W. H. Chen, C. K. Yong, J. Kärnbratt, J. E. Bullock, M. Malfois, M. R. Wasielewski, B. Albinsson, L. M. Herz, D. Zigmantas, D. Beljonne, H. L. Anderson. 'Belt-Shaped π-Systems: Relating Geometry to Electronic Structure in a Six-Porphyrin Nanoring'. *J. Am. Chem. Soc.*, **2011**, *133*, 17262–17273.

(56) T. R. Kelly, R. L. Xie, C. K. Weinreb, T. Bregant. 'A Molecular Vernier'. *Tetrahedron Lett.*, **1998**, *39*, 3675–3678.

(57) C. A. Hunter, S. Tomas. 'Accurate Length Control of Supramolecular Oligomerization: Vernier Assemblies'. *J. Am. Chem. Soc.*, **2006**, *128*, 8975–8979.

(58) D. V. Kondratuk, J. K. Sprafke, M. C. O'Sullivan, L. M. A. Perdigao, A. Saywell, M. Malfois, J. N. O'Shea, P. H. Beton, A. L. Thompson, H. L. Anderson. 'Vernier-Templated Synthesis, Crystal Structure, and Supramolecular Chemistry of a 12-Porphyrin Nanoring'. *Chem. - Eur. J.*, **2014**, *20*, 12826–12834.

(59) J. Cremers, S. Richert, D. V. Kondratuk, T. D. W. Claridge, C. R. Timmel, H. L. Anderson. 'Nanorings with Copper(II) and Zinc(II) Centers: Forcing Copper Porphyrins to Bind Axial Ligands in Heterometallated Oligomers'. *Chem. Sci.*, **2016**, *7*, 6961–6968.

(60) J. Cremers, R. Haver, M. Rickhaus, J. Q. Gong, L. Favereau, T. D. W. Claridge, L. M.

H. Herz, H. L. A. Anderson. 'Template-Directed Synthesis of a Conjugated Zinc Porphyrin Nanoball'. *J. Am. Chem. Soc.*, **2018**, ASAP.

(61) S. Kean. *The Disappearing Spoon; and Other True Tales from the Periodic Table*; Black Swan, **2011**.

(62) A. T. Balaban. 'Carbon and Its Nets'. *Computers Math. Applic.*, **1989**, *17*, 397–416.

(63) F. P. Bundy, W. A. Bassett, M. S. Weathers, R. J. Hemley, H. K. Mao, A. F. Goncharov. 'The Pressure-Temperature Phase and Transformation Diagram for Carbon; Updated through 1994'. *Carbon N. Y.*, **1996**, *34*, 141–153.

(64) W. Grochala. 'Diamond: Electronic Ground State of Carbon at Temperatures Approaching 0 K'. *Angew. Chem. Int. Ed.*, **2014**, *53*, 3680–3683.

(65) E. Fitzer. 'Pan-Based Carbon Fibers-Present State and Trend of the Technology from the Viewpoint of Possibilities and Limits to Influence and to Control the Fiber Properties by the Process Parameters'. *Carbon N. Y.*, **1989**, *27*, 621–645.

(66) S. Chand. 'Carbon Fibers for Composites'. *J. Mater. Sci.*, **2000**, *35*, 1303–1313.

(67) L. Feng, N. Xie, J. Zhong. 'Carbon Nanofibers and Their Composites: A Review of Synthesizing, Properties and Applications'. *Materials*, **2014**, *7*, 3919–3945.

(68) H. W. Kroto, J. R. Heath, S. C. O'Brien, R. F. Curl, R. E. Smalley. 'C_{60}: Buckminsterfullerene'. *Nature*, **1985**, *318*, 162–163.

(69) W. Kratschmer, L. D. Lamb, K. Fostiropoulos, D. R. Huffman. 'Solid C_{60}: A New Form of Carbon'. *Nature*, **1990**, *347*, 354–358.

(70) F. Diederich, R. Ettl, Y. Rubin, R. L. Whenren, R. Beck, M. Alvarez, S. Anz, D. Sensharma, F. Wudl, K. C. Khemani, A. Koch. 'The Higher Fullerenes : Isolation and Characterization'. *Science*, **1991**, *252*, 3–6.

(71) D. H. Parker, P. Wurz, K. Chatterjee, K. R. Lykke, J. E. Hunt, M. J. Pellin, J. C. Hemminger, D. M. Gruen, L. M. Stock. 'High-Yield Synthesis, Separation, and Mass-Spectrometric Characterization of Fullerenes C_{60} to C_{266}'. *J. Am. Chem. Soc.*, **1991**, *113*, 7499–7503.

(72) F. Diederich, R. L. Whetten, C. Thilgen, R. Ettl, I. Chao, M. M. Alvarez. 'Fullerene Isomerism: Isolation of C_{2v}-C_{78} and D_3-C_{78}'. *Science*, **1991**, *254*, 1768–1771.

(73) R. Ettl, I. Chao, F. Diederich, R. L. Whetten. 'Isolation of C_{76}, a Chiral (D_2) Allotrope of Carbon'. *Nature*, **1991**, *353*, 149–153.

(74) S. Iijima. 'Helical Microtubules of Graphitic Carbon'. *Nature*, **1991**, *354*, 56–58.

(75) S. Iijima, T. Ichihashi. 'Single-Shell Carbon Nanotubes of 1-nm Diameter'. *Nature*, **1993**, *363*, 603–605.

(76) D. S. Bethune, C. H. Kiang, M. S. de Vries, G. Gorman, R. Savoy, J. Vazquez, R. Beyers. 'Cobalt-Catalysed Growth of Carbon Nanotubes with Single-Atomic-Layer Walls'. *Nature*, **1993**, *363*, 605–607.

(77) K. S. Novoselov, A. K. Geim, S. V. Morozov, D. Jiang, Y. Zhang, S. V. Dubonos, I. V. Grigorieva, A. A. Firsov. 'Electric Field Effect in Atomically Thin Carbon Films'. *Science*, **2004**, *306*, 666–669.

(78) F. Diederich, Y. Rubin. 'Synthetic Approaches toward Molecular and Polymeric Carbon Allotropes'. *Angew. Chem. Int. Ed.*, **1992**, *31*, 1101–1123.

(79) S. V Prylutska, A. P. Burlaka, Y. I. Prylutskyy, U. Ritter, P. Scharff. 'Pristine C_{60}

Fullerenes Inhibit the Rate of Tumor Growth and Metastasis'. *Exp. Oncol.*, **2011**, *2011*, 162–164.

(80) E. Castro, A. H. Garcia, G. Zavala, L. Echegoyen. 'Fullerenes in Biology and Medicine'. *J. Mater. Chem. B*, **2017**, *5*, 6523–6535.

(81) G. Dennler, M. C. Scharber, C. J. Brabec. 'Polymer-Fullerene Bulk-Heterojunction Solar Cells'. *Adv. Mater.*, **2009**, *21*, 1323–1338.

(82) C. J. Brabec, S. Gowrisanker, J. J. M. Halls, D. Laird, S. Jia, S. P. Williams. 'Polymer-Fullerene Bulk-Heterojunction Solar Cells'. *Adv. Mater.*, **2010**, *22*, 3839–3856.

(83) L. Lu, T. Zheng, Q. Wu, A. M. Schneider, D. Zhao, L. Yu. 'Recent Advances in Bulk Heterojunction Polymer Solar Cells'. *Chem. Rev.*, **2015**, *115*, 12666–12731.

(84) J. Brebels, J. Manca, L. Lutsen, D. Vanderzande, W. Maes. 'High Dielectric Constant Conjugated Materials for Organic Photovoltaics'. *J. Mater. Chem. A*, **2017**, *5*, 24037–24050.

(85) S. M. Ryno, M. K. Ravva, X. Chen, H. Li, J. L. Brédas. 'Molecular Understanding of Fullerene – Electron Donor Interactions in Organic Solar Cells'. *Adv. Energy Mater.*, **2017**, *7*, 1601370–1601391.

(86) D. Zhu, X. Bao, D. Ouyang, J. Wang, X. Yuan, Q. Wang, D. Zhou, S. Wen, R. Yang. 'Single-Junction Fullerene Solar Cells with 10% Efficiency and High Open-Circuit Voltage Approaching 1 V'. *Nano Energy*, **2017**, *40*, 495–503.

(87) A. A. Popov, S. Yang, L. Dunsch. 'Endohedral Fullerenes'. *Chem. Rev.*, **2013**, *113*, 5989–6113.

(88) J. Zhao, Y. Li, G. Yang, K. Jiang, H. Lin, H. Ade, W. Ma, H. Yan. 'Efficient Organic Solar Cells Processed from Hydrocarbon Solvents'. *Nat. Energy*, **2016**, *1*, 1–7.

(89) W. T. Hadmojo, F. T. A. Wibowo, D. Y. Ryu, I. H. Jung, S. Y. Jang. 'Fullerene-Free Organic Solar Cells with an Efficiency of 10.2% and an Energy Loss of 0.59 eV Based on a Thieno[3,4-c]Pyrrole-4,6-Dione-Containing Wide Band Gap Polymer Donor'. *ACS Appl. Mater. Interfaces*, **2017**, *9*, 32939–32945.

(90) W. Zhao, S. Li, H. Yao, S. Zhang, Y. Zhang, B. Yang, J. Hou. 'Molecular Optimization Enables over 13% Efficiency in Organic Solar Cells'. *J. Am. Chem. Soc.*, **2017**, *139*, 7148–7151.

(91) M. F. L. De Volder, S. H. Tawfick, R. H. Baughman, A. J. Hart. 'Carbon Nanotubes: Present and Future Commercial Applications'. *Science*, **2013**, *339*, 535–539.

(92) X. Jia, F. Wei. 'Advances in Production and Applications of Carbon Nanotubes'. *Top. Curr. Chem.*, **2017**, *375*, 1–35.

(93) T. W. Chou, L. Gao, E. T. Thostenson, Z. Zhang, J. H. Byun. 'An Assessment of the Science and Technology of Carbon Nanotube-Based Fibers and Composites'. *Compos. Sci. Technol.*, **2010**, *70*, 1–19.

(94) J. N. Coleman, U. Khan, W. J. Blau, Y. K. Gun'ko. 'Small but Strong: A Review of the Mechanical Properties of Carbon Nanotube-Polymer Composites'. *Carbon N. Y.*, **2006**, *44*, 1624–1652.

(95) Z. Wu, Z. Chen, X. Du, J. M. Logan, J. Sippel, M. Nikolou, K. Kamaras, J. R. Reynolds, D. B. Tanner, A. F. Hebard, A. G. Rinzler. 'Transparent, Conductive Carbon Nanotube Films'. *Science*, **2004**, *305*, 1273–1276.

(96) C. Sotowa, G. Origi, M. Takeuchi, Y. Nishimura, K. Takeuchi, I. Y. Jang, Y. J. Kim, T.

Hayashi, Y. A. Kim, M. Endo, M. S. Dresselhaus. 'The Reinforcing Effect of Combined Carbon Nanotubes and Acetylene Blacks on the Positive Electrode of Lithium-Ion Batteries'. *ChemSusChem*, **2008**, *1*, 911–915.

(97) L. Dai, D. W. Chang, J.-B. Baek, W. Lu. 'Carbon Nanomaterials for Advanced Energy Conversion and Storage'. *Small*, **2012**, *8*, 1130–1166.

(98) T. W. Odom, J. L. Huang, P. Kim, C. M. Lieber. 'Atomic Structure and Electronic Properties of Single-Walled Carbon Nanotubes'. *Nature*, **1998**, *391*, 62–64.

(99) M. S. Dresselhaus, G. Dresselhaus, P. Avouris, (Eds.). *Carbon Nanotubes: Synthesis, Structure, Properties, and Applications*; Springer-Verlag: Heidelberg, Germany, **2001**.

(100) R. Jasti, C. R. Bertozzi. 'Progress and Challenges for the Bottom-up Synthesis of Carbon Nanotubes with Discrete Chirality'. *Chem. Phys. Lett.*, **2010**, *494*, 1–7.

(101) M. Endo, T. Hayashi, Y.-A. Kim. 'Large-Scale Production of Carbon Nanotubes and Their Applications'. *Pure Appl. Chem.*, **2006**, *78*, 1703–1713.

(102) S. M. Bachilo, L. Balzano, J. E. Herrera, F. Pompeo, D. E. Resasco, R. B. Weisman. 'Narrow (n,m)-Distribution of Single-Walled Carbon Nanotubes Grown Using a Solid Supported Catalyst'. *J. Am. Chem. Soc.*, **2003**, *125*, 11186–11187.

(103) T. Kato, R. Hatakeyama. 'Direct Growth of Short Single-Walled Carbon Nanotubes with Narrow-Chirality Distribution by Time-Programmed Plasma Chemical Vapor Deposition'. *ACS Nano*, **2010**, *4*, 7395–7400.

(104) A. Nish, J. Y. Hwang, J. Doig, R. J. Nicholas. 'Highly Selective Dispersion of Single-Walled Carbon Nanotubes Using Aromatic Polymers'. *Nat. Nanotechnol.*, **2007**, *2*, 640–646.

(105) J. Gu, J. Han, D. Liu, X. Yu, L. Kang, S. Qiu, H. Jin, H. Li, Q. Li, J. Zhang. 'Solution-Processable High-Purity Semiconducting SWCNTs for Large-Area Fabrication of High-Performance Thin-Film Transistors'. *Small*, **2016**, *12*, 4993–4999.

(106) T. Lei, I. Pochorovski, Z. Bao. 'Separation of Semiconducting Carbon Nanotubes for Flexible and Stretchable Electronics Using Polymer Removable Method'. *Acc. Chem. Res.*, **2017**, *50*, 1096–1104.

(107) B. Liu, J. Liu, H. B. Li, R. Bhola, E. A. Jackson, L. T. Scott, A. Page, S. Irle, K. Morokuma, C. Zhou. 'Nearly Exclusive Growth of Small Diameter Semiconducting Single-Wall Carbon Nanotubes from Organic Chemistry Synthetic End-Cap Molecules'. *Nano Lett.*, **2015**, *15*, 586–595.

(108) Y. Segawa, H. Ito, K. Itami. 'Structurally Uniform and Atomically Precise Carbon Nanostructures'. *Nat. Rev. Mater.*, **2016**, *1*, 1–14.

(109) G. Povie, Y. Segawa, T. Nishihara, Y. Miyauchi, K. Itami. 'Synthesis of a Carbon Nanobelt'. *Science*, **2017**, *356*, 172–175.

(110) J. S. Siegel. 'Allotropy by design—Carbon Nanohoops'. *Science*, **2017**, *356*, 135–136.

(111) F. E. Golling, M. Quernheim, M. Wagner, T. Nishiuchi, K. Müllen. 'Concise Synthesis of 3D π-Extended Polyphenylene Cylinders'. *Angew. Chem. Int. Ed.*, **2014**, *53*, 1525–1528.

(112) S. Hitosugi, W. Nakanishi, T. Yamasaki, H. Isobe. 'Bottom-up Synthesis of Finite Models of Helical (*n*,*m*)-Single-Wall Carbon Nanotubes'. *Nat. Commun.*, **2011**, *2*, 492–495.

(113) R. Sekiguchi, K. Takahashi, J. Kawakami, A. Sakai, H. Ikeda, A. Ishikawa, K. Ohta, S. Ito. 'Preparation of a Cyclic Polyphenylene Array for a Zigzag-Type Carbon Nanotube Segment'. *J. Org. Chem.*, **2015**, *80*, 5092–5110.

(114) R. Jasti, J. Bhattacharjee, J. B. Neaton, C. R. Bertozzi. 'Synthesis, Characterization, and Theory of [9]-, [12]-, and [18]Cycloparaphenylene: Carbon Nanohoop Structures'. *J. Am. Chem. Soc.*, **2008**, *130*, 17646–17647.

(115) H. Omachi, Y. Segawa, K. Itami. 'Synthesis of Cycloparaphenylenes and Related Carbon Nanorings: A Step toward the Controlled Synthesis of Carbon Nanotubes'. *Acc. Chem. Res.*, **2012**, *45*, 1378–1389.

(116) E. Heilbronner. 'Molecular Orbitals in Homologen Reihen Mehrkerniger Aromatischer Kohlenwasserstoffe: I. Die Eigenwerte von LCAO-MO's in Homologen Reihen'. *Helv. Chim. Acta*, **1954**, *37*, 921–935.

(117) F. H. Kohnke, A. M. Z. Slawin, J. F. Stoddart, D. J. Williams. 'Molecular Belts and Collars in the Making: A Hexaepoxyoctacosahydro[12]cyclacene Derivative'. *Angew. Chem. Int. Ed.*, **1987**, *26*, 892–894.

(118) L. T. Scott, E. A. Jackson, Q. Zhang, B. D. Steinberg, M. Bancu, B. Li. 'A Short, Rigid, Structurally Pure Carbon Nanotube by Stepwise Chemical Synthesis'. *J. Am. Chem. Soc.*, **2012**, *134*, 107–110.

(119) J. R. Sanchez-Valencia, T. Dienel, O. Gröning, I. Shorubalko, A. Mueller, M. Jansen, K. Amsharov, P. Ruffieux, R. Fasel. 'Controlled Synthesis of Single-Chirality Carbon Nanotubes'. *Nature*, **2014**, *512*, 61–64.

(120) H. Omachi, T. Nakayama, E. Takahashi, Y. Segawa, K. Itami. 'Initiation of Carbon Nanotube Growth by Well-Defined Carbon Nanorings'. *Nat. Chem.*, **2013**, *5*, 572–576.

(121) K. Tahara, Y. Tobe. 'Molecular Loops and Belts'. *Chem. Rev.*, **2006**, *106*, 5274–5290.

(122) S. Hitosugi, T. Yamasaki, H. Isobe. 'Bottom-up Synthesis and Thread-in-Bead Structures of Finite (n,0)-Zigzag Single-Wall Carbon Nanotubes'. *J. Am. Chem. Soc.*, **2012**, *134*, 12442–12445.

(123) D. Lu, G. Zhuang, H. Wu, S. Wang, S. Yang, P. Du. 'A Large π-Extended Carbon Nanoring Based on Nanographene Units: Bottom-Up Synthesis, Photophysical Properties, and Selective Complexation with Fullerene C_{70}'. *Angew. Chem. Int. Ed.*, **2017**, *56*, 158–162.

(124) J. Xia, M. R. Golder, M. E. Foster, B. M. Wong, R. Jasti. 'Synthesis, Characterization, and Computational Studies of Cycloparaphenylene Dimers'. *J. Am. Chem. Soc.*, **2012**, *134*, 19709–19715.

(125) R. F. Pasternack, P. R. Huber, P. Boyd, G. Engasser, L. Francesconi, E. Gibbs, P. Fasella, G. C. Venturo, L. D. Hinds. 'On the Aggregation of Meso-Substituted Water-Soluble Porphyrins'. *J. Am. Chem. Soc.*, **1972**, *94*, 4511–4517.

(126) Z. Wang, C. J. Medforth, J. A. Shelnutt. 'Porphyrin Nanotubes by Ionic Self-Assembly'. *J. Am. Chem. Soc.*, **2004**, *126*, 15954–15955.

(127) R. Rotomskis, R. Augulis, V. Snitka, R. Valiokas, B. Liedberg. 'Hierarchical Structure of TPPS4 J-Aggregates on Substrate Revealed by Atomic Force Microscopy'. *J. Phys. Chem. B*, **2004**, *108*, 2833–2838.

(128) V. Gulbinas, R. Karpicz, R. Augulis, R. Rotomskis. 'Exciton Relaxation in Nanotubular TPPS4 Aggregates in Water Solution and in Polymeric Matrix'. *Chem. Phys.*, **2007**,

332, 255–261.

(129) Y. Wan, A. Stradomska, J. Knoester, L. Huang. 'Direct Imaging of Exciton Transport in Tubular Porphyrin Aggregates by Ultrafast Microscopy'. *J. Am. Chem. Soc.*, **2017**, *139*, 7287–7293.

(130) O. Ohno, Y. Kaizu, H. Kobayashi. 'J-aggregate Formation of a Water-soluble Porphyrin in Acidic Aqueous Media'. *J. Chem. Phys.*, **1993**, *99*, 4128–4139.

(131) A. D. Schwab, D. E. Smith, C. S. Rich, E. R. Young, W. F. Smith, J. C. de Paula. 'Porphyrin Nanorods'. *J. Phys. Chem. B*, **2003**, *107*, 11339–11345.

(132) L. Lüer, S. Hoseinkhani, D. Polli, J. Crochet, T. Hertel, G. Lanzani. 'Size and Mobility of Excitons in (6, 5) Carbon Nanotubes'. *Nat. Phys.*, **2009**, *5*, 54–58.

(133) B. A. Ruzicka, R. Wang, J. Lohrman, S. Ren, H. Zhao. 'Exciton Diffusion in Semiconducting Single-Walled Carbon Nanotubes Studied by Transient Absorption Microscopy'. *Phys. Rev. B*, **2012**, *86*, 205417–205422.

(134) A. Tsuda, T. Nakamura, S. Sakamoto, K. Yamaguchi, A. Osuka. 'A Self-Assembled Porphyrin Box from *meso* - *meso*-Linked bis[5-P-Pyridyl-15-(3,5-Di-Octyloxyphenyl)Porphyrinato Zinc(II)}'. *Angew. Chem. Int. Ed.*, **2002**, *41*, 2817–2821.

(135) A. Tsuda, H. Hu, R. Tanaka, T. Aida. 'Planar or Perpendicular? Conformational Preferences of π-Conjugated Metalloporphyrin Dimers and Trimers in Supramolecular Tubular Arrays'. *Angew. Chem. Int. Ed.*, **2005**, *44*, 4884–4888.

(136) T. Kamada, N. Aratani, T. Ikeda, N. Shibata, Y. Higuchi, A. Wakamiya, S. Yamaguchi, K. S. Kim, Z. S. Yoon, D. Kim, A. Osuka. 'High Fidelity Self-Sorting Assembling of Meso-Cinchomeronimide Appended *meso-meso* Linked Zn(II) Diporphyrins'. *J. Am. Chem. Soc.*, **2006**, *128*, 7670–7678.

(137) T. Yamaguchi, N. Ishii, K. Tashiro, T. Aida. 'Supramolecular Peapods Composed of a Metalloporphyrin Nanotube and Fullerenes'. *J. Am. Chem. Soc.*, **2003**, *125*, 13934–13935.

(138) S. Shoji, T. Ogawa, T. Hashishin, S. Ogasawara, H. Watanabe, H. Usami, H. Tamiaki. 'Nanotubes of Biomimetic Supramolecules Constructed by Synthetic Metal Chlorophyll Derivatives'. *Nano Lett.*, **2016**, *16*, 3650–3654.

(139) S. J. Lee, K. L. Mulfort, J. L. O'Donnell, X. Zuo, A. J. Goshe, P. J. Wesson, S. T. Nguyen, J. T. Hupp, D. M. Tiede. 'Supramolecular Porphyrinic Prisms: Coordinative Assembly and Solution Phase X-Ray Structural Characterization'. *Chem. Comm.*, **2006**, *3*, 4581–4583.

(140) R. F. Kelley, J. L. Suk, T. M. Wilson, Y. Nakamura, D. M. Tiede, A. Osuka, J. T. Hupp, M. R. Wasielewski. 'Intramolecular Energy Transfer within Butadiyne-Linked Chlorophyll and Porphyrin Dimer-Faced, Self-Assembled Prisms'. *J. Am. Chem. Soc.*, **2008**, *130*, 4277–4284.

(141) I. Hijazi, T. Bourgeteau, R. Cornut, A. Morozan, A. Filoramo, J. Leroy, V. Derycke, B. Jousselme, S. Campidelli. 'Carbon Nanotube-Templated Synthesis of Covalent Porphyrin Network for Oxygen Reduction Reaction'. *J. Am. Chem. Soc.*, **2014**, *136*, 6348–6354.

(142) H. Jia, Z. Sun, D. Jiang, P. Du. 'Covalent Cobalt Porphyrin Framework on Multiwalled Carbon Nanotubes for Efficient Water Oxidation at Low Overpotential'. *Chem. Mater.*, **2015**, *27*, 4586–4593.

(143) J. Song, N. Aratani, H. Shinokubo, A. Osuka. 'A Porphyrin Nanobarrel That Encapsulates C_{60}'. *J. Am. Chem. Soc.*, **2010**, *132*, 16356–16357.

(144) M. D. Peeks, C. E. Tait, P. Neuhaus, G. M. Fischer, M. Hoffmann, R. Haver, A. Cnossen, J. R. Harmer, C. R. Timmel, H. L. Anderson. 'Electronic Delocalization in the Radical Cations of Porphyrin Oligomer Molecular Wires'. *J. Am. Chem. Soc.*, **2017**, *139*, 10461–10471.

(145) S. A. L. Rousseaux, J. Q. Gong, R. Haver, B. Odell, T. D. W. Claridge, L. M. Herz, H. L. Anderson. 'Self-Assembly of Russian Doll Concentric Porphyrin Nanorings'. *J. Am. Chem. Soc.*, **2015**, *137*, 12713–12718.

2

Nested Nanorings: Russian Doll Templated Synthesis of a 12-Porphyrin Nanoring

Parts of this chapter were published in:

S. A. L. Rousseaux, J. Q. Gong, R. Haver, B. Odell, T. D. W. Claridge, L. M. Herz and H. L. Anderson, 'Self-Assembly of Russian Doll Concentric Porphyrin Nanorings'. *J. Am. Chem. Soc.,* **2015**, *137*, 12713-12718.

2.1 Abstract

This chapter describes the assembly and characterisation of a nested nanoring complex consisting of an aluminium 6-porphyrin nanoring and a zinc 12-porphyrin nanoring.[1] Excitation energy is transferred from the inner 6-porpyhyrin nanoring to the outer 12-porphyrin nanoring within 40 ps. The inner porphyrin nanoring is used as a template to direct the synthesis of the outer nanoring from its linear precursor.

2.2 Introduction

Russian doll nested assemblies are complexes of self-similar objects such that the layers form a homologous series (see Figure 2.2 for examples).[2–12] Such assemblies are not only the outcome of chemists' imagination and curiosity, but are found in natural systems as well. The natural light harvesting system in purple bacteria consists of light harvesting complexes, LH1 and LH2, which are circular arrangements of chlorophyll molecules. Excitation energy is funnelled between individual LH2 units and then from LH2 to LH1 on a picosecond time-scale (3-5 ps). It is subsequently transferred within approximately 35 picoseconds to the reaction centre (RC) which contains chlorophyll molecules as well and is nested within the LH1 in a non-covalent manner (Figure 2.1).[13–15]

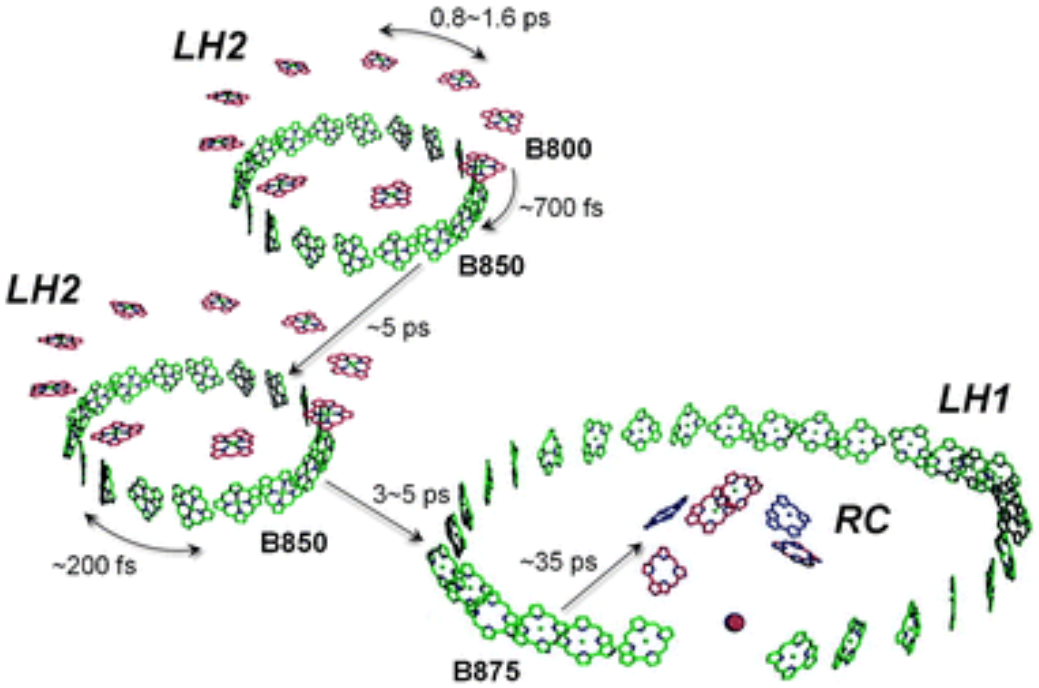

Figure 2.1: Schematic of the bacteriochlorophylls in LH2 and LH1/RC complexes from Rhodopseudomonas palustris and the excitation energy transfer (EET) times within and between them. Reprinted with permission from ref. 15. Copyright 2012 National Academy of Sciences.

There are numerous examples of synthetic Russian doll nested assemblies; C_{60} fullerene was found to nest within cyclic benzo-paraphenyleneacetylenes (CPPAs) to form a double inclusion (onion-type) complex (Figure 2.2a).[9] Paracyclophane ([2^3]PCP) was found to nest inside a pyromellitic diimide-based cyclophane through a charge transfer interaction between the electron deficient host and the π-electron donating PCP-guest (Figure 2.2b).[6]

Strong charge transfer has been observed for a complex of $Li^+@C_{60}$ nested in cycloparaphenylene ([10]CPP), where the positive charge was found to be delocalised over the entire supramolecular complex.[16] Not only can encapsulation of the inner shell fundamentally change its properties, the inner shell can also act as a template to aid the assembly of the outer shell(s),[17] creating increasingly complex supramolecular structures.

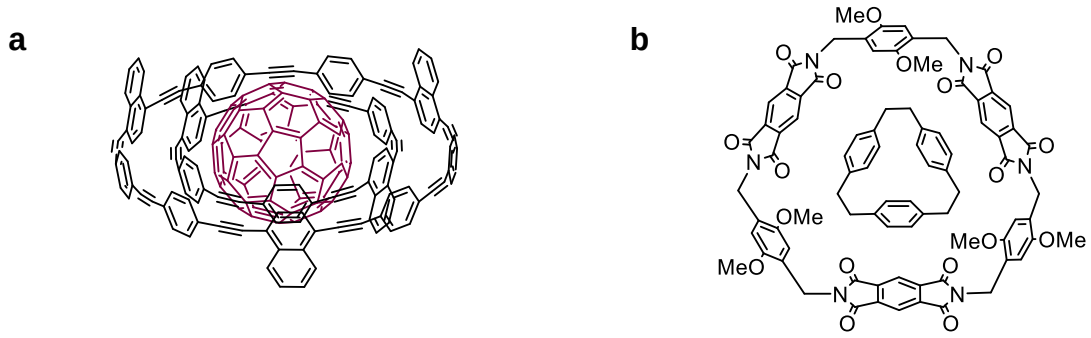

Figure 2.2: Examples of molecular Russian doll nested assemblies. (a) C_{60}@[6]CPPA@[9]CPPA; C_{60} nested inside CPPAs.[9] (b) [2^3]PCP nested inside pyromellitic diimide-based cyclophane.[6]

Synthetic porphyrin-based π-conjugated macrocycles showing ultrafast energy migration around the nanoring have been reported as a mimic to the natural photosynthetic antenna systems, LH2 and LH1.[18–26] Systems that show energy transfer from a porphyrin macrocycle to a central moiety mimicking the LH1/RC assembly have been less frequently reported. In one example, Kobuke and co-workers describe the assembly of a porphyrin macrocycle and a central acceptor ligand, consisting of C_{60}, a zinc porphyrin and a tripyridyl tripod.[26,27] The tripod binds strongly to the porphyrin macrocycle. Excitation energy collected by the nine porphyrins of the macrocyclic assembly was efficiently transferred to the tripod-porphyrin. Subsequent electron transfer from the tripod-porphyrin to C_{60} resulted in a stable charge-separated state with a total energy conversion efficiency from the excited cyclic porphyrin array to C_{60} of 85%.

2.3 Design, Synthesis and Characterisation of a Nested Nanoring System

2.3.1 Design of a Nested Nanoring System

Previously it was shown that bis-acetylene linked porphyrin nanorings (larger than 29 porphyrin units) form supramolecular stacked and nested assemblies on a gold surface.[28] Rings were found to fold and nest inside open rings. For both the nested and open rings, stacking was observed of up to three molecules (Figure 2.3). However, the on-surface nature of this study did not allow for energy-transfer studies between the nested nanorings.

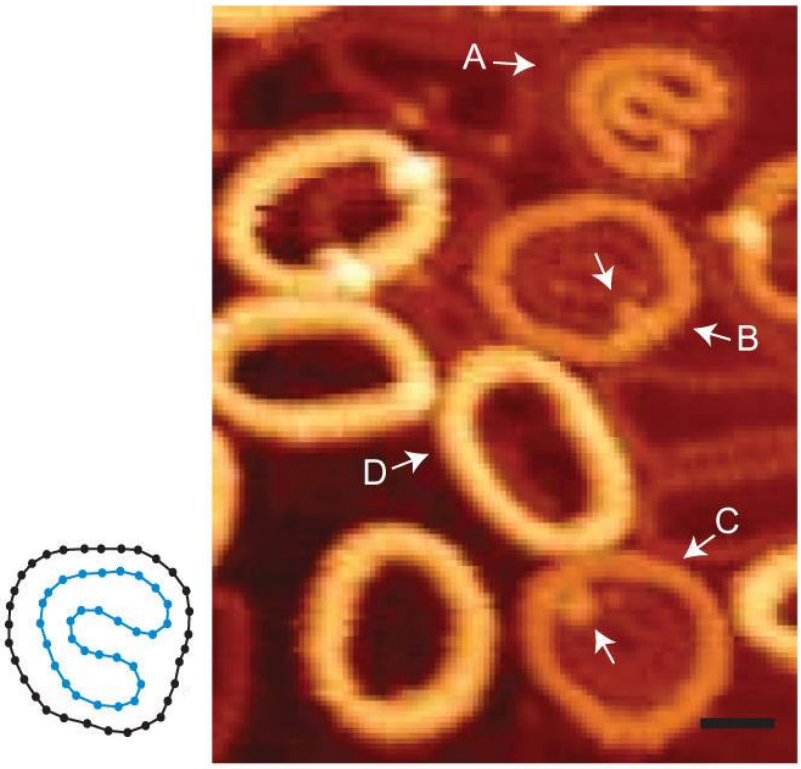

Figure 2.3: Schematic and STM images of nested nanoring complexes of ***c*-P30** (scale bar 5 nm). A is a 2-in-1 nested structure consisting of two stacked folded rings inside a single open ring. B and C are nested 1-in-2 structures that contain a single folded ring inside a two-layer stack of open rings. D is a triple-stack nanoring. The arrows indicate small sections where the nested nanoring adopts a conformation where, locally, the porphyrin groups are either non-parallel to the substrate, or there is a region of self-overlapping. Reprinted with permission from ref. 28. Copyright 2015 Nature Publishing Group.

To study the photophysical properties of a nested nanoring system in solution, we designed and studied the assembly of a 6-porphyrin nanoring[29] within a 12-porphyrin nanoring[18] reminiscent of the natural LH1/RC architecture (Figure 2.4a). Nesting of the two rings is achieved through a bridging Y-shaped ligand that contains one carboxylate moiety and two imidazole groups. The structure of the Russian doll complex as well as the schematic representation of the individual components are depicted in Figure 2.4.

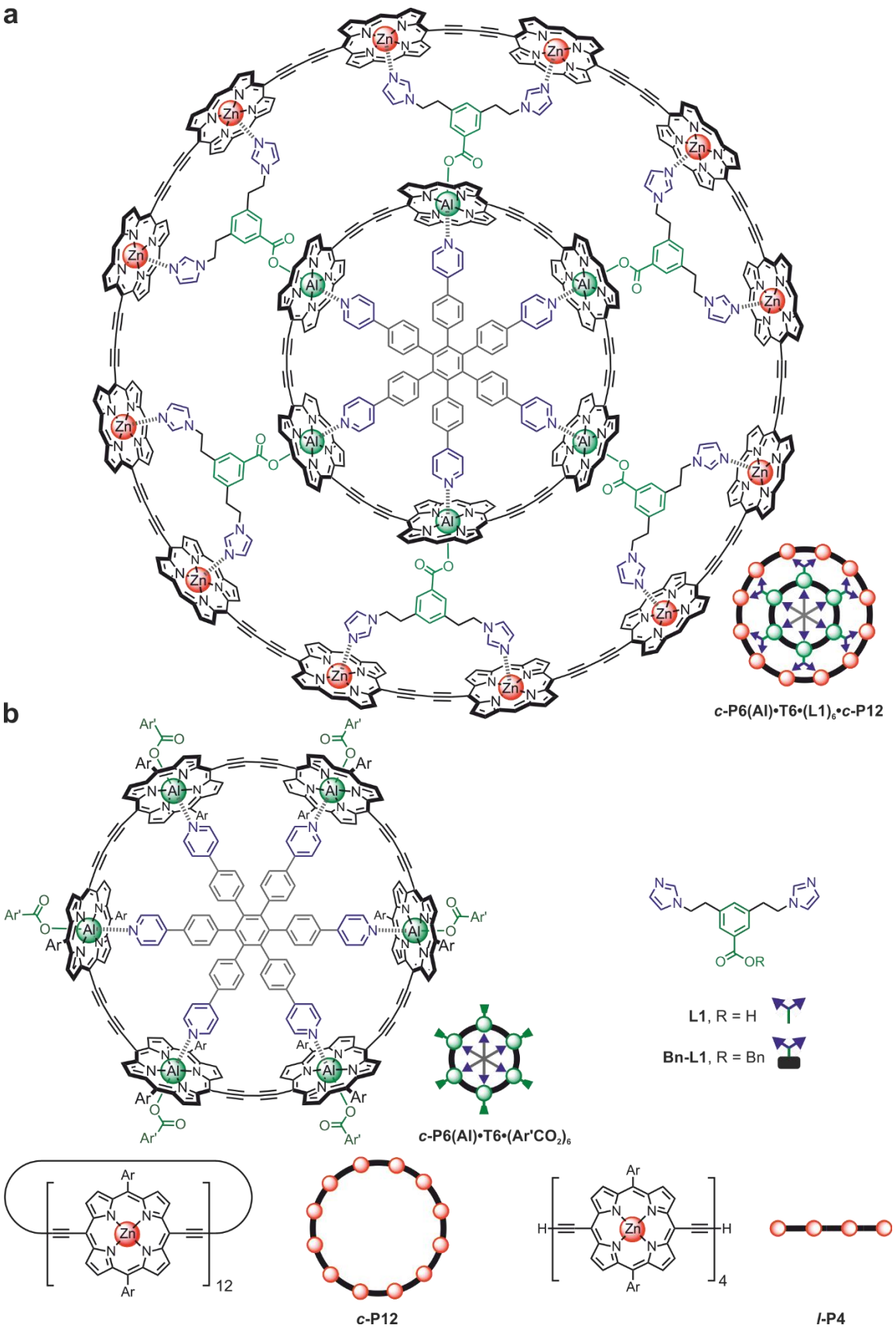

Figure 2.4: (a) Chemical structure of the Russian doll complex (*meso*-aryl groups are omitted for clarity). (b) Schematic representation of the individual components as used throughout this chapter. Ar = 3,5-bis(*tert*-butyl)phenyl (for ***c*-P6(Al)·T6·(Ar'CO$_2$)$_6$**) or 2,3-bis(octyloxy)phenyl (for ***l*-P4** and ***c*-P12**); Ar' = 3,5-dimethylphenyl.

The use of nanorings containing specific metals with a different coordination number was essential to the successful assembly of the nested nanoring system. The aluminium porphyrins in the inner 6-porphyrin nanoring can form hexacoordinate complexes, binding simultaneously pyridine and carboxylate ligands.[30,31] The zinc porphyrins of the outer 12-porphyrin nanoring can form pentacoordinate complexes and bind nitrogen-based ligands such as pyridine or imidazole (Figure 2.5). The hexacoordination of aluminium porphyrins allows the radial oligopyridine template **T6** to stay bound inside the ring. This forces the Y-shaped ligand **L1**, which binds to the aluminium centres *via* the carboxylate moiety, to reside externally, simultaneously pre-arranging its imidazole moieties for coordination to the zinc 12-porphyrin nanoring.

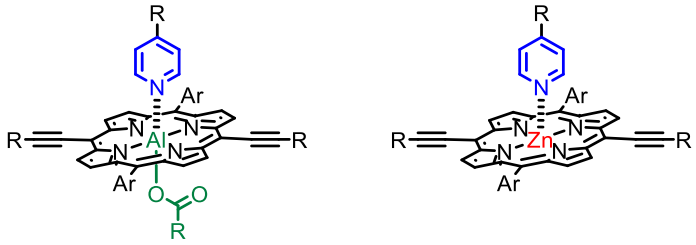

Figure 2.5: Complementary metal-ligand interactions in aluminium porphyrins and zinc porphyrins. Aluminium(III) in porphyrins is hexacoordinate, binding simultaneously nitrogen-based and carboxylate-based ligands. Zinc(II) in porphyrins is pentacoordinate and binds nitrogen-based ligands.

2.3.2 Synthesis of an Aluminium 6-Porphyrin Nanoring

The hexacoordination of aluminium porphyrins that allows the use of both nitrogen and carboxylate containing ligands, makes them interesting building blocks for supramolecular chemistry. Despite this, examples of aluminium porphyrins in the literature are rare,[32,33] especially compared to zinc, iron, and cobalt porphyrins.[34] This can be attributed to their challenging synthesis and purification. The hydroxy-derivative **P(Al)(OH)** exhibits a tendency to polymerise in solution, presumably *via* the formation of Al-O-Al connections.

To avoid a multistep synthesis with aluminium-porphyrin building blocks, the aluminium 6-porphyrin nanoring was prepared in three steps from the corresponding zinc nanoring. The zinc 6-porphyrin nanoring was demetallated followed by aluminium insertion. We found it crucial to treat the aluminium 6-porphyrin nanoring with a capping carboxylate ligand (3,5-dimethylbenzoate) and to re-introduce the six-legged template **T6** to avoid the abovementioned polymerisation and to enable purification by size-exclusion chromatography.

2.3.3 Assembly and Characterisation of a Nested Nanoring System

Assembly of the nested nanoring system was achieved by mixing the aluminium 6-porphyrin nanoring (***c*-P6(Al)·T6·(Ar'CO$_2$)$_6$**), Y-shaped ligand **L1** and zinc 12-porphyrin nanoring (***c*-P12**) in CD_2Cl_2. The Y-shaped ligand was prepared according to the procedure discussed in Section 2.8.1.[1] The zinc 12-porphyrin nanoring was prepared through template-directed synthesis according to previously published procedures.[18] The properties of the ring-in-ring complex were compared to a control mixture in which ligand **L1** had been replaced with ligand **Bn-L1** (see Figure 2.4b). The latter contains a benzyl ester-protecting group which therefore cannot bind to the aluminium porphyrins and hence prevents the formation of a ring-in-ring complex (Figure 2.6).

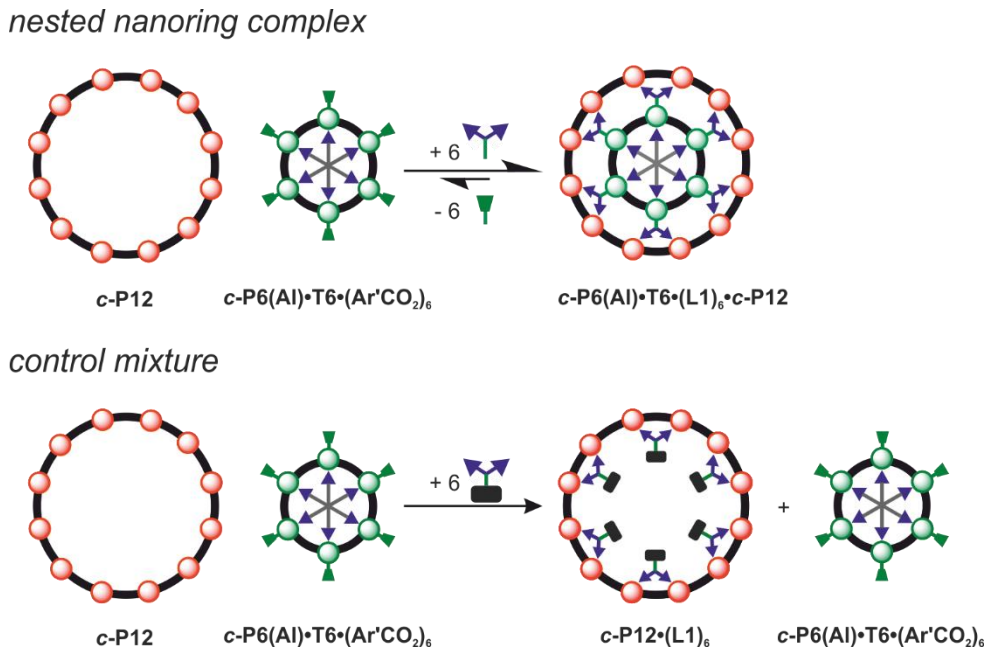

Figure 2.6: (top) Assembly of the nested nanoring complex from a 1:1 mixture of ***c*-P12** and ***c*-P6(Al)·T6·(Ar'CO$_2$)$_6$** in the presence of ligand **L1**. (bottom) Assembly of the control mixture from a 1:1 mixture of ***c*-P12** and ***c*-P6(Al)·T6·(Ar'CO$_2$)$_6$** in the presence of ligand **Bn-L1**.

The nested nanoring complex was characterised with NMR techniques. After mixing the components of the Russian doll complex, ^{1}H NMR showed the expected upfield shift of the aluminium 6-porphyrin nanoring protons (Figure 2.7a). Furthermore, a path of nuclear Overhauser effects connecting the inner 6-porphyrin nanoring and the outer 12-porphyrin nanoring were observed (Figure 2.7b). In the equivalent ^{1}H NMR titration experiment of the control mixture, no upfield shift of the aluminium 6-porphyrin nanoring protons or NOE pathway were observed. Additional confirmation of the successful formation of the

ring-in-ring complex was obtained with diffusion-ordered NMR spectroscopy (DOSY) experiments where the nested nanorings diffuse as a single species, while in the control mixture the two rings diffuse at different rates.

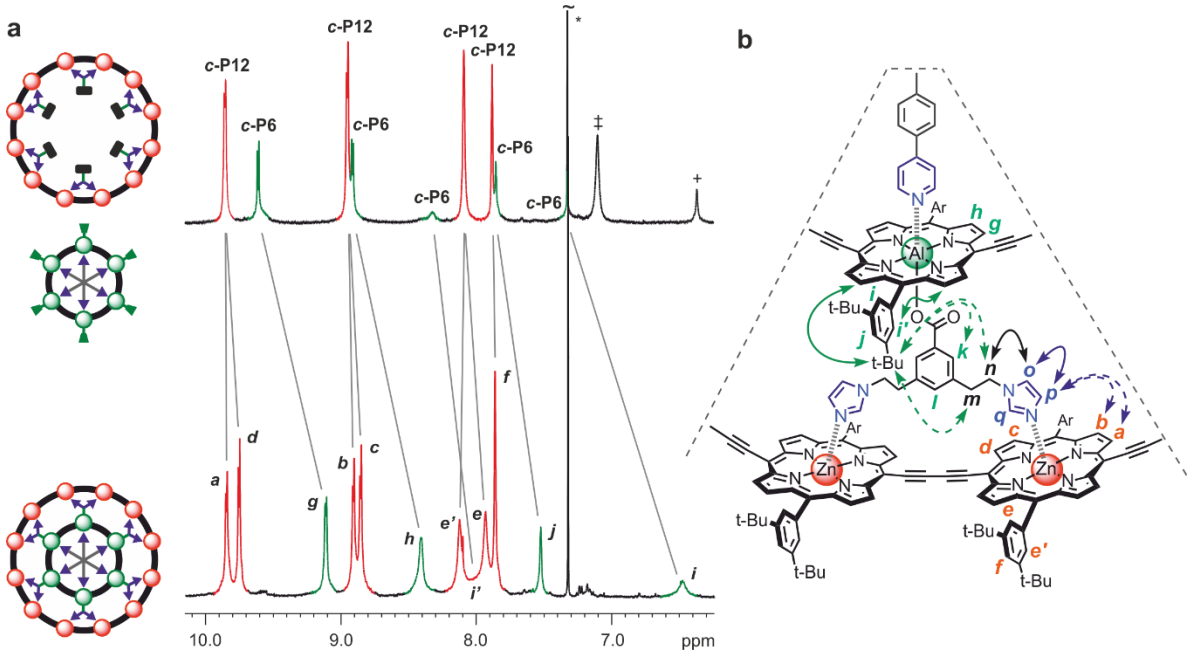

Figure 2.7: (a) Region of the ^{1}H NMR spectrum (CD_2Cl_2, 400 MHz, 298 K) of the control mixture (top) and the Russian doll nested nanoring complex (bottom) showing the upfield shift of the aluminium 6-porphyrin nanoring protons. (b) Signal assignment for the Russian doll nested nanoring complex showing selected NOEs between the nanorings and ligand protons (dotted arrows indicate weak NOEs; full arrows indicate strong NOEs).

2.4 Energy Migration in Russian Doll Nested Nanorings

2.4.1 Absorption Spectra

The absorption spectrum of the Russian doll nested nanorings (in $CHCl_3$) was measured and compared to those of reference compounds (i.e. the separate components as well as the control mixture). All spectra show characteristic absorption bands; Soret (400-550 nm) and Q (700-950 nm). The Q band of ***c*-P12·(Bn-L1)$_6$** is slightly red-shifted compared to ***c*-P6(Al)·T6·(Ar'CO$_2$)$_6$** due to an increased conjugation length (Figure 2.8a,b). The absorption spectrum of the control mixture resembles the sum of the contribution from its components, ***c*-P6(Al)·T6·(Ar'CO$_2$)$_6$** and ***c*-P12·(Bn-L1)$_6$** (Figure 2.8c). The Russian doll however, shows a stronger red-shift in the Q band (compared to ***c*-P12·(Bn-L1)$_6$**), which presumably originates form the increased rigidity of the 12-porphyrin nanoring component in the assembled complex (Figure 2.8d).

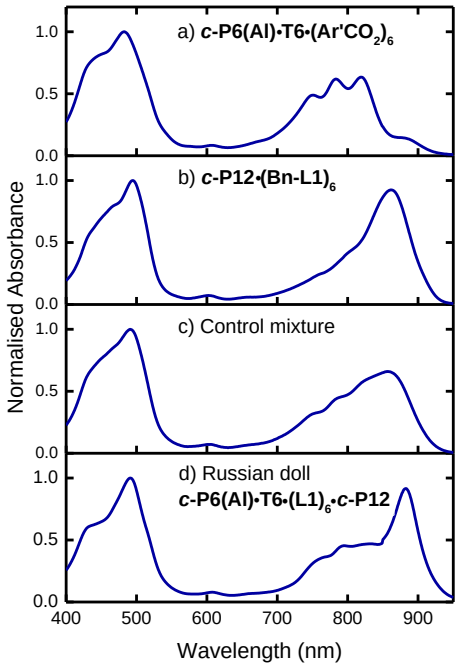

Figure 2.8: Normalised absorption spectra (recorded in $CHCl_3$ at 295 K) of (a) ***c*-P6(Al)·T6·(Ar'CO₂)₆**, (b) ***c*-P12·(Bn-L1)₆**, (c) Control mixture; 1:1 ***c*-P12·(Bn-L1)₆** and ***c*-P6(Al)·T6·(Ar'CO₂)₆**, and (d) Russian doll complex, ***c*-P6(Al)·T6·(L1)₆·*c*-P12**.

2.4.2 Fluorescence Studies

Similar to the absorption spectra discussed above, the fluorescence spectrum of the Russian doll complex exhibits a strong bathochromic shift compared to its individual constituent components due to the increased rigidity of the system.

Fluorescence excitation measurements show that the control mixture comprises two emitting species. For these emitters, ***c*-P6(Al)·T6·(Ar'CO₂)₆** and ***c*-P12·(Bn-L1)₆**, the fluorescence excitation spectrum resembles its absorption spectrum. However, due to the difference in fluorescence quantum yield between the components (φ_F = 2.1% for ***c*-P6(Al)·T6·(Ar'CO₂)₆**; φ_F = 8.4 % for ***c*-P12·(Bn-L1)₆**), the excitation spectrum of the control mixture is not reflecting its absorption spectrum (Figure 2.9a) but rather shows a larger contribution in emission from the ***c*-P12·(Bn-L1)₆** component. For the Russian doll complex, the excitation spectrum matches very well with the absorption spectrum, indicating that the complex acts as a single emitter (Figure 2.9b). This is a clear indication of electronic communication between the two porphyrin rings in the Russian doll complex.

The communication between the components of the Russian doll complex was further confirmed by fluorescence lifetime measurements using the time-correlated single-photon

(TCSPC) technique. In the control mixture, the fluorescence lifetime is dependent on the excitation wavelength as the contribution from ***c*-P6(Al)·T6·(Ar'CO$_2$)$_6$** and ***c*-P12·(Bn-L1)$_6$** to the fluorescence changes with excitation wavelength. On the other hand, fluorescence of the Russian doll complex exhibits no dependence on excitation wavelength, which confirms that emission occurs from a single emitter, and that there is efficient energy transfer between the components. The lifetime of the Russian doll complex (364 ps when detected at 760 nm; 375 ps when detected at 860 nm) suggest that the emitting species in the Russian doll is most likely the outer ***c*-P12** (fluorescence lifetime of 376 ps), indicating fast energy transfer from the inner ***c*-P6** within the time-resolution of the TCSPC system, which is 40 ps.

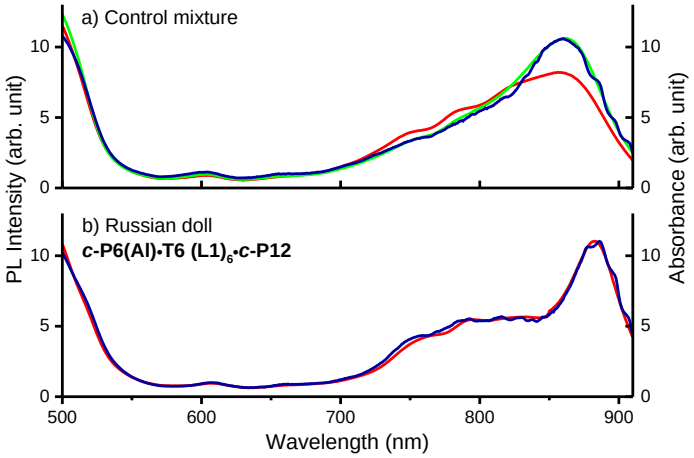

Figure 2.9: A comparison between the fluorescence excitation spectra detected at 929 nm (blue) and the absorption spectra (red) for (a) control mixture; 1:1 ***c*-P12·(Bn-L1)$_6$** and ***c*-P6(Al)·T6·(Ar'CO$_2$)$_6$** and (b) Russian doll complex, ***c*-P6(Al)·T6·(L1)$_6$·*c*-P12**. The green curve in (a) is a simulation of the excitation spectrum calculated from the excitation-dependent fluorescence intensity using the absorption spectra of ***c*-P6(Al)·T6·(Ar'CO$_2$)$_6$** and ***c*-P12·(Bn-L1)$_6$**, weighted by the fluorescence quantum yields of the components.

2.5 Russian Doll Templating

A 12-porphyrin nanoring (***c*-P12**) has previously been prepared *via* classical- and Vernier-templating.[18,35] In classical templating, a 12-legged radial oligopyridine template is used to direct the assembly of three linear porphyrin tetramers (***l*-P4**) giving ***c*-P12·T12** in a 35% yield after threefold homocoupling reaction. Vernier-templating relies on the principle of the lowest-common-multiple between 4 in ***l*-P4** and 6 in a 6-legged oligopyridine template (**T6**), which gives 12 as ***c*-P12·(T6)$_2$** in a 39% yield after threefold homocoupling reaction (see Chapter 1, Figure 1.8).

The successful self-assembly of the Russian doll nested porphyrin nanorings, as discussed above, led us to wonder whether the aluminium 6-porphyrin nanoring, in combination with the butterfly-shaped ligand **L1**, could template the formation of zinc 12-porphyrin nanoring from a linear precursor (linear porphyrin tetramer, ***l*-P4**). This would demonstrate the viability of porphyrin nanoring synthesis from a linear precursor using a template that is itself an eight-component noncovalent assembly. This supramolecular layer-by-layer approach could potentially lead to new ways of templating the synthesis of giant porphyrin nanostructures.

2.5.1 Reaction Design of the Russian Doll Templating and Control Reaction

To examine the viability of ring-around-ring templating, linear porphyrin tetramer (***l*-P4**) was added to a solution containing the aluminium 6-porphyrin nanoring (***c*-P6(Al)·T6·(Ar'CO$_2$)$_6$**) and the butterfly-shaped ligand (**L1**). The mixture was submitted to standard palladium-catalysed oxidative alkyne coupling conditions.[18,19,28,36–40] As a control reaction, ***l*-P4** was coupled in the presence of ***c*-P6(Al)·T6·(Ar'CO$_2$)$_6$** and the blocked butterfly-ligand (**Bn-L1**). In **Bn-L1**, the presence of a benzyl ester protecting group prevents the binding of the ligand to aluminium and hence, blocks the formation of a supramolecular Russian doll complex (Figure 2.10). We expected the Russian doll templated synthesis to yield ***c*-P12** and the control reaction to yield (insoluble) polymer *via* the linear (statistical) coupling of ***l*-P4**.

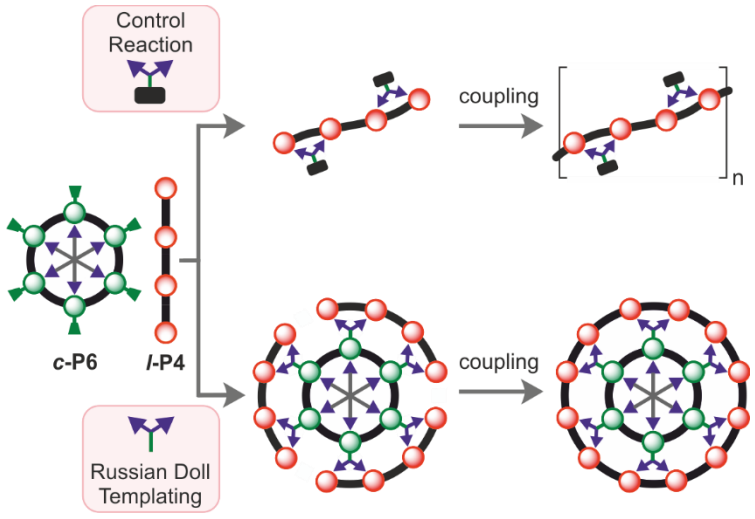

Figure 2.10: Schematic representation of the Russian doll templated synthesis of ***c*-P12** around ***c*-P6(Al)·T6·(Ar'CO$_2$)$_6$** and the control reaction.

Reaction progress of the Russian doll templating and control reaction were monitored by UV-vis-NIR spectroscopy. Upon completion, the Russian doll templating reaction and the control reaction were subjected to the same work-up procedure. The reaction mixtures were passed over a short Al_2O_3 column to remove insoluble polymers. Subsequently, the zinc porphyrin components were separated from ***c*-P6(Al)·T6·(L1)$_6$** or ***c*-P6(Al)·T6·(Ar'CO$_2$)$_6$, 6(Bn-L1)** by size-exclusion chromatography in $CHCl_3$/10% pyridine. The high pyridine concentration outcompetes the binding of **L1** or **Bn-L1** to the zinc centres after which the individual components separate according to size. This separation was performed to unambiguously demonstrate that we cyclised the 12-porphyrin nanoring. If the template had not been removed, it would have been hard to distinguish between a successful preparation of the 12-porphyrin nanoring and a supramolecular complex in which three porphyrin tetramers are bound to ***c*-P6(Al)·T6·(L1)$_6$**.

2.5.2 Reaction Analysis of the Russian Doll Templating and Control Reaction

Analysis and separation of the product mixtures from the Russian doll templating reaction and the control reaction were performed by recycling GPC (Figure 2.11). The collected materials were analysed by GPC retention times,[28] MALDI-ToF analysis and ^{1}H NMR. For both reactions, all obtained Zn-porphyrin material was injected onto the GPC. From the absolute scale of the respective GPC traces it is evident that from the control reaction little material was obtained, as most of the material was lost as insoluble polymer. The material that was obtained shows a statistical distribution of linear oligomers, demonstrating the lack of supramolecular control but rather the statistical coupling of linear ***l*-P4**. On the other hand, the Russian doll templating reaction formed ***c*-P12** in 12% yield (determined by GPC calibration[41]). Besides the formation of ***c*-P12**, also products from Vernier-templating (***c*-P24**)[36] and caterpillar-track templating[39] (***c*-P16** and ***c*-P20**) were observed (see Chapter 1 for an explanation of Vernier and caterpillar-track templating).

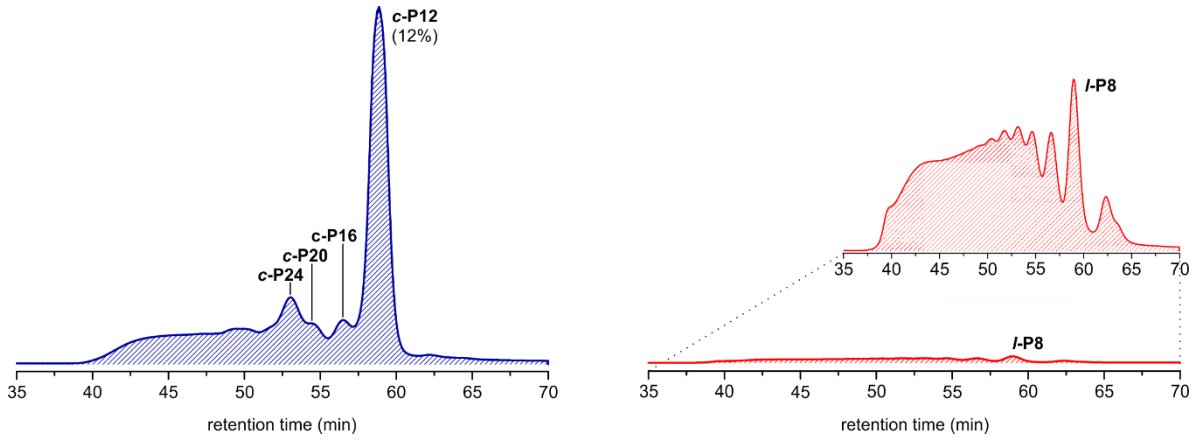

Figure 2.11: GPC traces (toluene/1% pyridine) of the Russian doll templated reaction of ***c*-P12** (left trace) and the control reaction (right trace). The GPC traces are depicted at their absolute scale (i.e. both have the same range on the y-axis).

2.6 Conclusion

In this chapter we demonstrated the assembly of nested nanorings into a supramolecular complex reminiscent of the chlorophyll arrays in photosynthetic bacteria, with a molecular weight of 17kDa. In resemblance to the natural LH1/RC architecture, there is rapid energy migration (within 40 picoseconds) between the nanoring components in the Russian doll complex. The fluorescence excitation spectrum of the nested nanoring complex matches perfectly with its absorption spectrum and its fluorescence lifetime is independent of excitation wavelength. This indicates that the complex behaves as a single emitter and that rapid energy migration occurs between the two nanorings of the complex.

Additionally, we performed templated synthesis of the outer 12-porphyrin nanoring around the inner 6-porphyrin nanoring. This is the first example of a Russian doll templating strategy to aid the covalent assembly of the outer shell. Thus far, porphyrin nanoring synthesis has been achieved by using radial oligopyridine templates of covalent nature. Russian doll templating provides a novel way of preparing ***c*-P12** in addition to the previously developed methods of classical- and Vernier-templating (Figure 2.12). The Russian doll templated strategy provides a new approach to amplify the size of covalent nanostructures and could in theory be extended to three-dimensional architectures such as porphyrin nanotubes and porphyrin nanoballs. This approach avoids the requirement of increasingly large and complicated templates and could provide a layer-by-layer approach of templating the synthesis of nanostructures of extraordinary sizes.

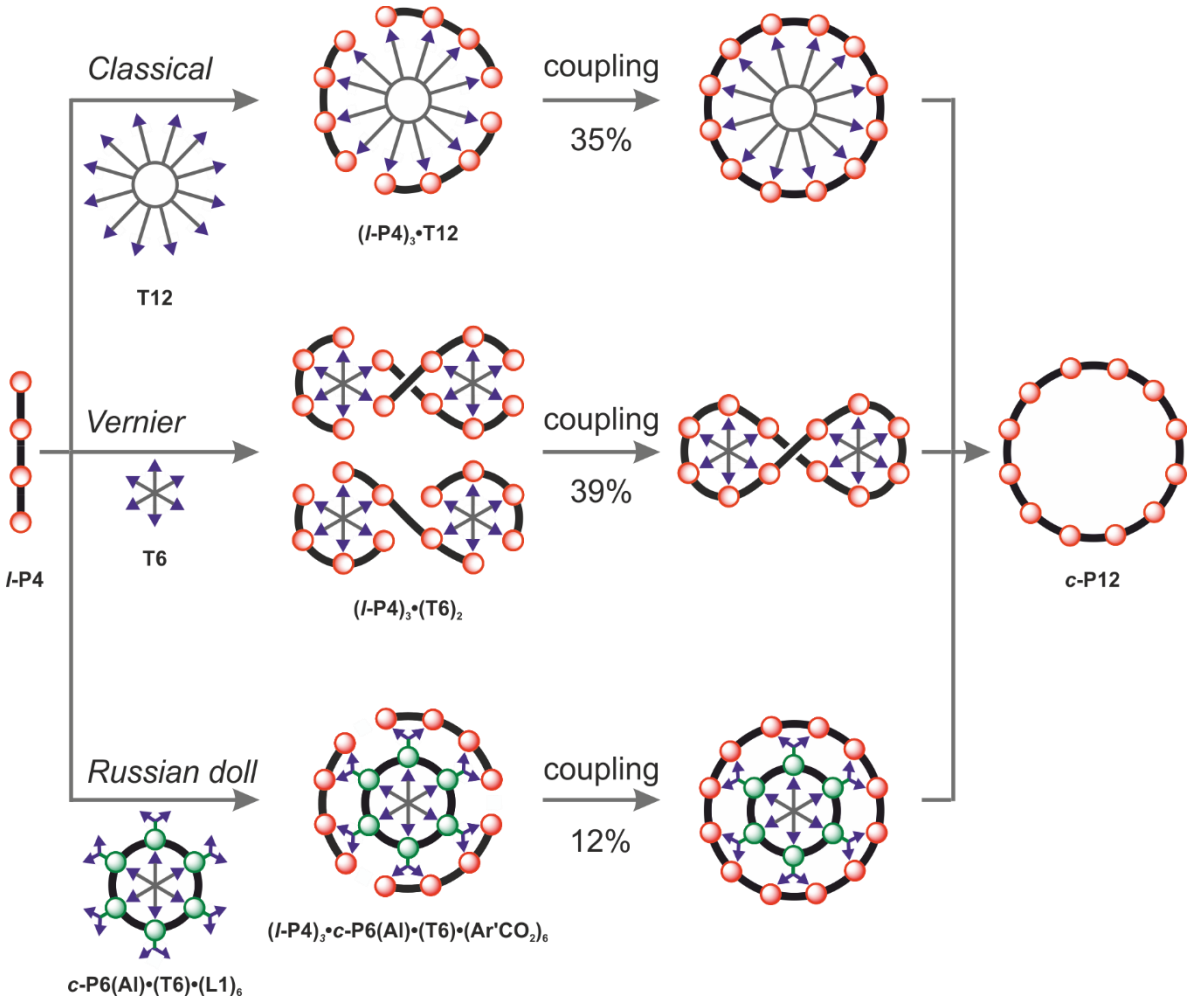

Figure 2.12: Three synthetic strategies towards the synthesis of a zinc 12-porphyrin nanoring, ***c*-P12**; Classical templating around a 12-legged oligopyridine template, Vernier-templating around two 6-legged oligopyridine templates and Russian doll templating around an aluminium 6-porphyrin nanoring in combination with butterfly-shaped ligand **L1**.

2.7 General Synthetic Methods

For the work discussed in this thesis, the following general synthetic methods were used; Unless stated otherwise, all reagents were obtained from commercial sources and used as received without further purification. Diethyl ether, THF and toluene were dried by passing over activated alumina. *N,N*-Diisopropylamine was dried by distillation over CaH_2. *N*-Bromosuccinimide was recrystallised from boiling water.

Flash column chromatography was carried out on silica gel 60 under positive pressure. Where mixtures of solvents were used, ratios are reported by volume. Alumina columns were run using activated basic alumina (Brockmann I, standard grade, ~150 mesh, 58 Å, Sigma). Size exclusion chromatography (SEC) was carried out using Bio-Beads S-X1, 200-400 mesh (Bio Rad).

Analytical gel permeation chromatography (GPC) was performed on a VWR system equipped with a JAIGEL H-P pre-column, a JAIGEL 3H-A (8 mm × 500 mm) and a JAIGEL 4H-A column (8 mm × 500 mm) in series with THF/1% pyridine containing 0.1% BHT stabiliser as eluent with a flow rate of 1 mL/min.

Semi-preparative recycling GPC was performed on a Shimadzu recycling GPC system equipped with a JAIGEL H-P pre-column, a JAIGEL 3H (20 mm × 600 mm) and a JAIGEL 4H column (20 mm × 600 mm) in series with toluene/1% pyridine as eluent or equipped with a JAIGEL H-P pre-column, a JAIGEL 3H (20 mm × 600 mm) and a JAIGEL 4H column (20 mm × 600 mm) in series with THF/1% pyridine containing 0.1% BHT stabiliser as eluent with a standard flow rate of 3.5 mL/min.

HPLC analysis was performed on a Japan Analytical JC-9103 recycling preparative HPLC equipped with a Buckyprep-M Cosmosil column (20 X 250 mm) with toluene as eluent and a flow rate of 16 mL/min. Detection was done at 312 nm.

NMR spectra were recorded on a Bruker AVII400, Bruker AVIII400 (400 MHz) or Bruker DRX500 (500 MHz) spectrometer. The residual solvent peak was used as internal reference ($CHCl_3$, ^1H δ = 7.27 ppm, ^{13}C δ = 77.2 ppm). Multiplicity (s = singlet, d = doublet, t = triplet, and m = multiplet) and coupling constant(s) were reported whenever possible

MALDI-ToF spectra were measured using a Bruker Microflex™ LRF, a Waters MALDI Micro MX, or were measured at the EPSRC National Mass Spectrometry service (Swansea) using the Applied Biosystems Voyager DE-STR. The MALDI-ToF mass spectra were

recorded using (*trans*-2-[3-(4-*tert*-butylphenyl)-2-methyl-2-propenylidene]malononitrile) (DCTB) as the matrix.

Steady-state UV-vis-NIR absorption spectra were recorded at 25 °C with a Perkin-Elmer Lambda 20 photospectrometer using quartz 1 cm cuvettes and temperature was controlled by a PTP-1 peltier unit from Perkin Elmer. Fluorescence measurements were carried out using a calibrated Edinburgh Instruments FS5 spectrofluorometer equipped with double monochromators, with different wavelength-adapted gratings, and two detectors: a photomultiplier tube (PMT) R13456 from Hamamatsu for 250 – 950 nm, an analogue detector for 850 – 1700 nm, and if required an integrating sphere (SC-30, Edinburgh Instruments). The exciting power of the xenon lamp after the monochromator was typically under 1 mW for the slits used. The calibration for wavelength accuracy, linearity of the detection system and determination of the spectral responsivity (spectral emission correction) was performed by Edinburgh Instrument and was not older than 12 months.

Molecular modelling was carried out using the MM+ force field (molecular mechanics) integrated in the HyperChemTM 8.0 (Hypercube Inc.) package.

2.8 Experimental Procedures

Porphyrin tetramer ***l*-P4**,[42] template **T6**[29] and nanoring ***c*-P6(Zn)·T6**[19] were prepared using previously reported procedures. The precursor to ligand **L1** and ***c*-P12**[18] for GPC calibration were kindly provided by Dr. S. Rousseaux.

2.8.1 Synthesis of Ligand **L1**

Benzyl 3,5-bis(2-(1*H*-imidazol-1-yl)ethyl)benzoic acid – L1

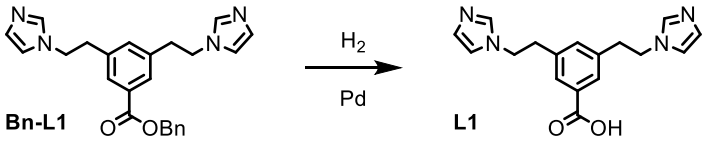

A solution of benzyl 3,5-bis(2-(1*H*-imidazol-1-yl)ethyl)benzoate (13 mg, 0.025 mmol, 1.0 equiv.) in MeOH (1.0 mL) was added to Pd/C (10 wt %, 3.0 mg) under nitrogen. Under vigorous stirring, H_2 was bubbled through the solution for 15 min. At this point the reaction was stirred vigorously under an atmosphere of H_2 for 16 h (by which time the reaction was judged to be complete by MS). The mixture was filtered over a pad of celite eluted with MeOH and concentrated under reduced pressure to afford **L1** (6.3 mg, 80%) as a pale yellow oil.

^{1}H NMR (500 MHz, CD_3OD, 298 K): δ_H 7.73 (br s, 2H), 7.65 (d, J = 1.0 Hz, 2H), 7.21 (br s, 2H), 7.08 (br s, 2H), 6.94 (br s, 1H), 4.29 (t, J = 7.0 Hz, 4H), 3.08 (t, J = 6.8 Hz, 4H).

2.8.2 Synthesis of Aluminium 6-Porphyrin Nanoring **c-P6(Al)·T6·(Ar'CO$_2$)$_6$**

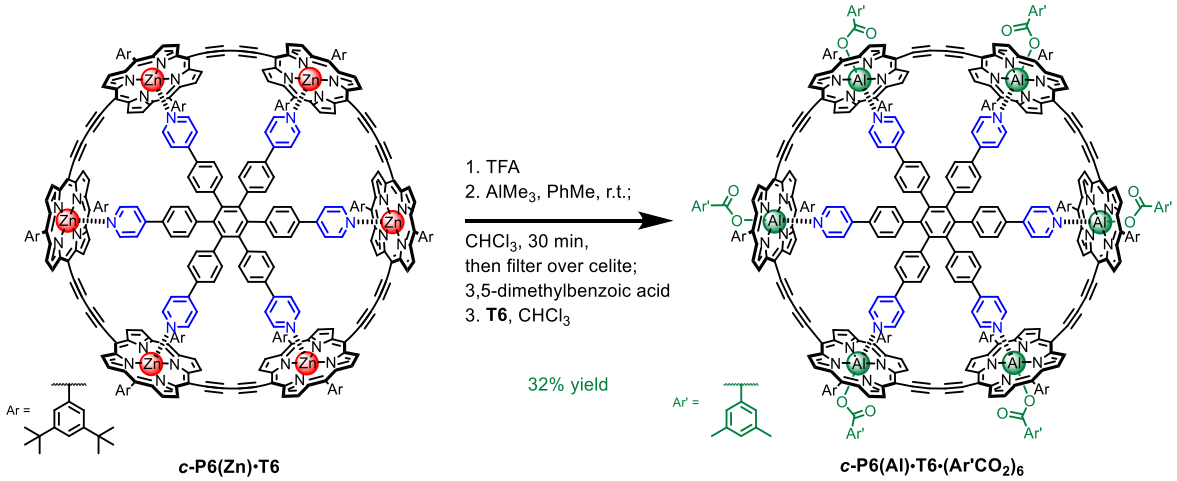

Free-base cyclic porphyrin hexamer – *c*-P6[2H]

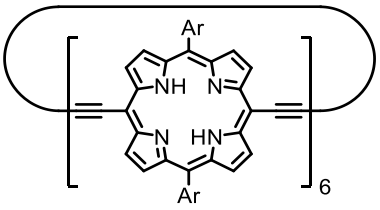

***c*-P6[2H]**

TFA (167 μL, 2.18 mmol, 600 equiv) was added dropwise to a solution of ***c*-P6(Zn)·T6** (21.0 mg, 3.6 μmol, 1.00 equiv) in $CHCl_3$ (4.0 mL, 0.9 mM). The reaction mixture was stirred at room temperature and the reaction progress was monitored by UV-vis-NIR spectroscopy. Upon completion (after 10 min), the reaction was quenched by the addition of pyridine (0.4 mL, 5.0 mmol, 1.4×10^3 equiv) and immediately passed through a short SiO_2 plug eluted with $CHCl_3$/1% pyridine. Solvents were removed *in vacuo* to afford ***c*-P6[2H]** (11.7 mg, 74%) as a brown solid.

^{1}H NMR (400 MHz, $CDCl_3$, 298 K): δ_H 9.63 (d, J = 4.7 Hz, 24H, *β-H*), 8.82 (d, J = 4.7 Hz, 24H, *β-H*), 7.98 (d, J = 1.4 Hz, 24H, Ar-H_{ortho}), 7.81 (br t, J = 1.5 Hz, 12H, Ar-H_{para}), 1.52 (s, 216H, *t*-Bu*H*), –1.31 (s, 12H, -N*H*).

Aluminum cyclic porphyrin hexamer – *c*-P6(Al)·(Ar'CO_2)$_6$

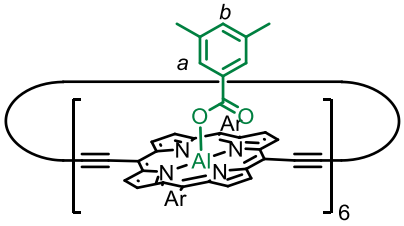

***c*-P6(Al)·(Ar'CO_2)$_6$**

$AlMe_3$ (2.0 M in hexanes, 5.8 μL, 11.7 μmol, 6.6 equiv) was added dropwise to a solution of ***c*-P6(H2)** (7.8 mg, 1.78 μmol, 1.00 equiv) in dry toluene (0.35 mL, 5.0 mM), under an atmosphere of argon. The reaction mixture was stirred at room temperature for 30 min, after which point the UV-vis-NIR spectrum indicated full conversion of the starting material. $CHCl_3$ was then added (approx. 1.5 mL). The mixture was stirred for 20–30 minutes until a precipitate formed, then filtered over celite into a flask containing 3,5-dimethylbenzoic acid (1.60 mg, 10.7 μmol, 6.00 equiv). After stirring at room temperature for 30 min, the ^{1}H NMR spectrum of the material indicated clean conversion to ***c*-P6(Al)·(Ar'CO_2)$_6$**. This material was used without further purification.

^{1}H NMR (400 MHz, $CDCl_3$, 298 K): δ_H 9.78 (d, J = 4.7 Hz, 24H, *β-H*), 9.00 (d, J = 4.7 Hz, 24H, *β-H*) 7.85 (br s, 24H, Ar-H_{ortho}), 7.80 (br s, 12H, Ar-H_{para}), 6.13 (s, 6H, Ar-H_b), 4.88 (s, 12H, Ar-H_a), 1.51 (s, 36 H, CH_3), 1.49 (s, 216 H, *t*-Bu*H*).

c-P6(Al)·T6·(Ar'CO_2)$_6$

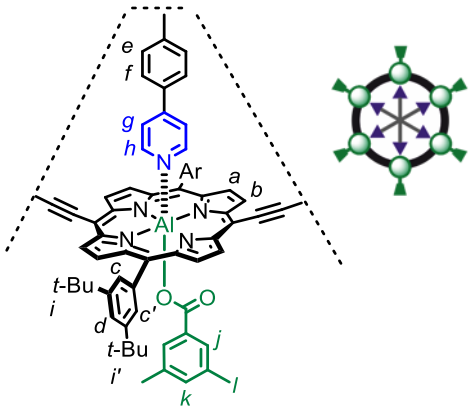

c-P6(Al)·T6·(Ar'CO_2)$_6$

Hexakis-(4-[4- phenylpyridine])benzene **T6** (1.78 mg, 1.78 μmol) was added to the sample of **c-P6(Al)·(Ar'CO_2)$_6$** in dry $CHCl_3$ (1.2 mL). The solution was stirred at room temperature for 90 minutes, at which point the reaction was complete (monitored by UV-vis-NIR spectroscopy). The reaction mixture was purified by size exclusion chromatography on Biobeads SX-1 using $CHCl_3$ to yield **c-P6(Al)·T6·(Ar'CO_2)$_6$** (4.9 mg, 43% yield from **c-P6[2H]**) as a brown solid.

^{1}H NMR (400 MHz, $CDCl_3$, 298 K): δ_H 9.58 (d, J = 4.6 Hz, 24H, *β-*H_a), 8.87 (d, J = 4.6 Hz, 24H, *β-*H_b), 8.22 (br s, 12H, Ar-H_c or Ar-$H_{c'}$), 7.79 (br s, 12H, Ar-H_d), 7.29 (br s, 12H, Ar-H_c or Ar-$H_{c'}$), 6.31 (s, 6H, Ar-H_k), 5.52–5.47 (m, 24 H, Ar-H_e and Ar-H_f), 4.84 (d, J = 4.8 Hz, 12H, Ar-H_g), 4.50 (s, 12H, Ar-H_j), 1.68 (m, 12H, Ar-H_h), 1.64 (s, 36 H, Me-H_l), 1.62 (br s, 108 H, *t*-Bu-H_i or *t*-Bu-$H_{i'}$), 1.35 (br s, 108 H, *t*-Bu-H_i or *t*-Bu-$H_{i'}$).

MALDI-TOF m/z 5445 (calculated for $C_{438}H_{402}Al_6N_{30}O_{12}$: 5443 (-**T6** template).

UV-vis-NIR ($CHCl_3$) λ_{max} (log ε): 483 (5.79), 752 (5.48), 784 (5.58), 820 (5.59).

MALDI-ToF and UV-vis-NIR data were recorded by Dr. S. Rousseaux.

2.8.3 Russian Doll Templated Synthesis of ***c*-P12** *and the Control Reaction*

Russian Doll Templated Synthesis of *c*-P12

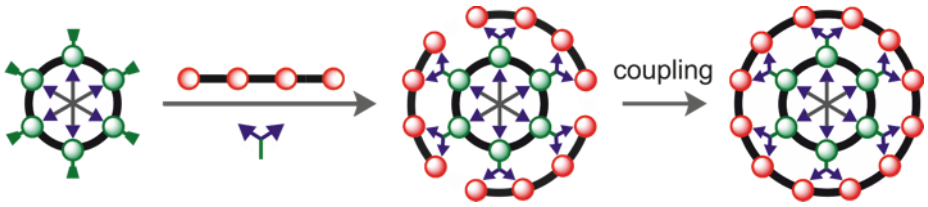

Ligand **L1** (0.43 mg, 1.4 µmol, 6.0 equiv, from a 0.19 M solution in MeOH) and ***l*-P4** (3.0 mg, 0.7 µmol, 3.0 equiv) were added to a solution of ***c*-P6(Al)·T6·(Ar'CO$_2$)$_6$** (1.5 mg, 0.23 µmol) in dry $CHCl_3$ (830 µL, 0.28 mM). After 1 h of stirring at room temperature, catalyst mixture was added ($Pd(PPh_3)_2Cl_2$ (0.25 mg, 0.35 µmol, 1.5 equiv), CuI (0.33 mg, 1.8 µmol, 7.5 equiv), and 1,4-benzoquinone (0.38 mg, 3.5 µmol, 15 equiv) in dry $CHCl_3$ (0.21 mL) and dry DIPA (8.5 µL)) and the reaction progress was monitored by UV-vis-NIR spectroscopy. After stirring for 2.5 h, no more spectroscopic changes were observed, after which half an equivalent of the above described catalyst mixture was added. After further stirring for 1 h, the reaction mixture was dried under a stream of N_2 and passed over a short plug of Al_2O_3 using $CHCl_3$. Solvents were removed *in vacuo* and the material was purified by size exclusion chromatography on Biobeads SX-1 using $CHCl_3$/10% pyridine to separate the zinc porphyrin material from the ***c*-P6(Al)·T6·(Ar'CO$_2$)$_6$**. Three of these SEC columns were required to separate all zinc porphyrin material from ***c*-P6(Al)·T6·(Ar'CO$_2$)$_6$**. Separation of the zinc porphyrin products by recycling GPC (toluene/1% pyridine) yielded ***c*-P12** (12%, GPC yield) and ***c*-P24** (2.5%, GPC yield) as brown solids.

***c*-P12**

^{1}H NMR (400 MHz, $CDCl_3$ + 1% pyridine-d$_5$, 298 K): δ_H 9.82 (d, J = 4.5 Hz, 24H, *β-H*), 9.03 (d, J = 4.5 Hz, 24H, *β-H*), 7.37 (d, J = 1.7 Hz, 48H, Ar-H_{ortho}), 6.90 (t, 24H, Ar-H_{para}), 4.16 (t, 96 H, -OCH_2-), 1.93–1.83 (m, 96H, -CH_2-), 1.57–1.46 (m, 96H, -CH_2-), 1.42–1.20 (m, 384H, -CH_2-), 0.84 (t, J = 6.8 Hz, 144H, -CH_3).

MALDI-ToF m/z 13004 (calculated for $C_{816}H_{984}N_{48}O_{48}Zn_{12}$: 13018).

As lit.[18]

***c*-P24**

^{1}H NMR (400 MHz, $CDCl_3$ + 1% pyridine-d$_5$, 298 K): δ_H 9.88 (d, J = 4.5 Hz, 96H, *β-H*), 9.07 (d, J = 4.2 Hz, 96H, *β-H*), 7.41 (m, 96H, Ar-H_{ortho}), 6.93 (m, 48H, Ar-H_{para}), 4.19

(s br, 192, -OCH_2-), 1.95–1.87 (m, 192H, -CH_2-), 1.59–1.50 (m, 192H, -CH_2-), 1.44–1.18 (m, 768H, -CH_2-), 0.91–0.78 (m, 288H, -CH_3)

MALDI-ToF m/z 26170 (calculated for $C_{1632}H_{1968}N_{96}O_{96}Zn_{24}$: 26035).

As lit.[21,36]

Control Reaction

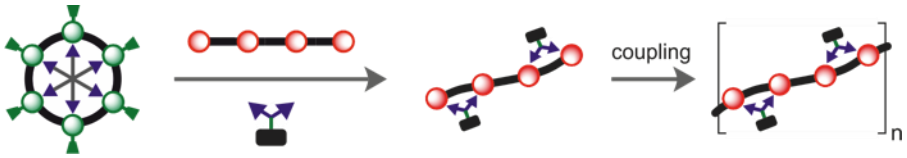

Protected ligand **Bn-L1** (0.56 mg, 1.4 µmol, 6.0 equiv, from a 0.16 M solution in MeOH) and ***l*-P4** (3.0 mg, 0.7 µmol, 3.0 equiv) were added to a solution of ***c*-P6(Al)·T6·(Ar'CO_2)$_6$** (1.5 mg, 0.23 µmol) in dry $CHCl_3$ (830 µL, 0.28 mM). After 1 h of stirring at room temperature, catalyst mixture was added ($Pd(PPh_3)_2Cl_2$ (0.25 mg, 0.35 µmol, 1.5 equiv), CuI (0.33 mg, 1.7 µmol, 7.5 equiv), and 1,4-benzoquinone (0.38 mg, 3.5 µmol, 15 equiv) in dry $CHCl_3$ (0.21 mL) and dry DIPA (8.5 µL)) and the reaction progress was monitored by UV-vis-NIR spectroscopy. After stirring for 2.5 h, half a portion of the above described catalyst mixture was added. After further stirring for 1 h, the reaction was dried under a stream of N_2 and passed over a short plug of Al_2O_3 using $CHCl_3$. The majority of ***l*-P4** starting material had polymerised. Therefore, after the Al_2O_3 plug only very little material was left. The resulting mixture was concentrated under reduced pressure and purified by size exclusion chromatography on Biobeads SX-1 using $CHCl_3$/10% pyridine to separate the zinc porphyrin material from the ***c*-P6(Al)·T6·(Ar'CO_2)$_6$**. An additional SEC column was required to separate all zinc porphyrin material from ***c*-P6(Al)·T6·(Ar'CO_2)$_6$**. The zinc porphyrin fraction was concentrated under reduced pressure and analysed by analytical recycling GPC (toluene/1%pyridine). The resulting GPC trace is depicted in Figure 2.11.

2.9 References

(1) S. A. L. Rousseaux, J. Q. Gong, R. Haver, B. Odell, T. D. W. Claridge, L. M. Herz, H. L. Anderson. 'Self-Assembly of Russian Doll Concentric Porphyrin Nanorings'. *J. Am. Chem. Soc.*, **2015**, *137*, 12713–12718.

(2) Y. Han, T.-L. Liang, X. Hao, C.-F. Chen. 'Solid-State "Russian Doll"-like Capsules Based on a Triptycene-Derived Macrotricyclic Host with Paraquat Derivative and Polycyclic Aromatic Hydrocarbons'. *CrystEngComm*, **2016**, *18*, 4900–4904.

(3) W. Gong, X. Yang, P. Y. Zavalij, L. Isaacs, Z. Zhao, S. Liu. 'From Packed Sandwich" to Russian Doll": Assembly by Charge-Transfer Interactions in Cucurbit[10]uril'. *Chem. - Eur. J.*, **2016**, *22*, 17612–17618.

(4) T. Beck, S. Tetter, M. Künzle, D. Hilvert. 'Construction of Matryoshka-Type Structures from Supercharged Protein Nanocages'. *Angew. Chem. Int. Ed.*, **2015**, *54*, 937–940.

(5) A. I. Day, R. J. Blanch, A. P. Arnold, S. Lorenzo, G. R. Lewis, I. Dance. 'A Cucurbituril-Based Gyroscane: A New Supramolecular Form'. *Angew. Chem. Int. Ed.*, **2002**, *41*, 275–277.

(6) T. Iwanaga, R. Nakamoto, M. Yasutake, H. Takemura, K. Sako, T. Shinmyozu. 'Cyclophanes within Cyclophanes: The Synthesis of a Pyromellitic Diimide-Based Macrocycle as a Structural Unit in a Molecular Tube and Its Inclusion Phenomena'. *Angew. Chem. Int. Ed.*, **2006**, *45*, 3643–3647.

(7) H. Danjo, Y. Hashimoto, Y. Kidena, A. Nogamine, K. Katagiri, M. Kawahata, T. Miyazawa, K. Yamaguchi. 'Nestable Tetrakis(spiroborate) Nanocycles'. *Org. Lett.*, **2015**, *17*, 2154–2157.

(8) T. Iwamoto, Z. Slanina, N. Mizorogi, J. Guo, T. Akasaka, S. Nagase, H. Takaya, N. Yasuda, T. Kato, S. Yamago. 'Partial Charge Transfer in the Shortest Possible Metallofullerene Peapod, La@C_{82}⊂[11]cycloparaphenylene'. *Chem. - Eur. J.*, **2014**, *20*, 14403–14409.

(9) T. Kawase, K. Tanaka, N. Shiono, Y. Seirai, M. Oda. 'Onion-Type Complexation Based on Carbon Nanorings and a Buckminsterfullerene'. *Angew. Chem. Int. Ed.*, **2004**, *43*, 1722–1724.

(10) M. Hervieu, B. Mellène, R. Retoux, S. Boudin, B. Raveau. 'The Route to Fullerenoid Oxides'. *Nat. Mater.*, **2004**, *3*, 269–273.

(11) R. S. Forgan, C. Wang, D. C. Friedman, J. M. Spruell, C. L. Stern, A. A. Sarjeant, D. Cao, J. F. Stoddart. 'Donor-Acceptor Ring-in-Ring Complexes'. *Chem. - Eur. J.*, **2012**, *18*, 202–212.

(12) W. Xie, R. J. Cava, G. J. Miller. 'Packing of Russian Doll Clusters to Form a Nanometer-Scale CsCl-Type Compound in a Cr-Zn-Sn Complex Metallic Alloy'. *J. Mater. Chem. C*, **2017**, *5*, 7215–7221.

(13) R. J. Cogdell, A. Gall, J. Köhler. 'The Architecture and Function of the Light-Harvesting Apparatus of Purple Bacteria: From Single Molecules to in Vivo Membranes'. *Q. Rev. Biophys.*, **2006**, *39*, 227–324.

(14) J. Strümpfer, M. Şener, K. Schulten. 'How Quantum Coherence Assists Photosynthetic Light-Harvesting'. *J. Phys. Chem. Lett.*, **2012**, *3*, 536–542.

(15) L. Luer, V. Moulisova, S. Henry, D. Polli, T. H. P. Brotosudarmo, S. Hoseinkhani, D. Brida, G. Lanzani, G. Cerullo, R. J. Cogdell. 'Tracking Energy Transfer between Light Harvesting Complex 2 and 1 in Photosynthetic Membranes Grown under High and

Low Illumination'. *Proc. Natl. Acad. Sci.*, **2012**, *109*, 1473–1478.

(16) H. Ueno, T. Nishihara, Y. Segawa, K. Itami. 'Cycloparaphenylene-Based Ionic Donor-Acceptor Supramolecule: Isolation and Characterization of Li+@C_{60}⊂[10]CPP'. *Angew. Chem. Int. Ed.*, **2015**, *54*, 3707–3711.

(17) Z. Liu, C. Tian, J. Yu, Y. Li, W. Jiang, C. Mao. 'Self-Assembly of Responsive Multilayered DNA Nanocages'. *J. Am. Chem. Soc.*, **2015**, *137*, 1730–1733.

(18) M. C. O'Sullivan, J. K. Sprafke, D. V Kondratuk, C. Rinfray, T. D. W. Claridge, A. Saywell, M. O. Blunt, J. N. O'Shea, P. H. Beton, M. Malfois, H. L. Anderson. 'Vernier Templating and Synthesis of a 12-Porphyrin Nano-Ring'. *Nature*, **2011**, *469*, 72–75.

(19) J. K. Sprafke, D. V. Kondratuk, M. Wykes, A. L. Thompson, M. Hoffmann, R. Drevinskas, W. H. Chen, C. K. Yong, J. Kärnbratt, J. E. Bullock, M. Malfois, M. R. Wasielewski, B. Albinsson, L. M. Herz, D. Zigmantas, D. Beljonne, H. L. Anderson. 'Belt-Shaped π-Systems: Relating Geometry to Electronic Structure in a Six-Porphyrin Nanoring'. *J. Am. Chem. Soc.*, **2011**, *133*, 17262–17273.

(20) P. Parkinson, C. E. I. Knappke, N. Kamonsutthipaijit, K. Sirithip, J. D. Matichak, H. L. Anderson, L. M. Herz. 'Ultrafast Energy Transfer in Biomimetic Multistrand Nanorings'. *J. Am. Chem. Soc.*, **2014**, *136*, 8217–8220.

(21) C.-K. Yong, P. Parkinson, D. V. Kondratuk, W.-H. Chen, A. Stannard, A. Summerfield, J. K. Sprafke, M. C. O'Sullivan, P. H. Beton, H. L. Anderson, L. M. Herz. 'Ultrafast Delocalization of Excitation in Synthetic Light-Harvesting Nanorings'. *Chem. Sci.*, **2015**, *6*, 181–189.

(22) P. Parkinson, D. V. Kondratuk, C. Menelaou, J. Q. Gong, H. L. Anderson, L. M. Herz. 'Chromophores in Molecular Nanorings: When Is a Ring a Ring?'. *J. Phys. Chem. Lett.*, **2014**, *5*, 4356–4361.

(23) H. W. Jiang, T. Tanaka, H. Mori, K. H. Park, D. Kim, A. Osuka. 'Cyclic 2,12-Porphyrinylene Nanorings as a Porphyrin Analogue of Cycloparaphenylenes'. *J. Am. Chem. Soc.*, **2015**, *137*, 2219–2222.

(24) Y. Nakamura, N. Aratani, A. Osuka. 'Cyclic Porphyrin Arrays as Artificial Photosynthetic Antenna: Synthesis and Excitation Energy Transfer.'. *Chem. Soc. Rev.*, **2007**, *36*, 831–845.

(25) J. Yang, M.-C. Yoon, H. Yoo, P. Kim, D. Kim. 'Excitation Energy Transfer in Multiporphyrin Arrays with Cyclic Architectures: Towards Artificial Light-Harvesting Antenna Complexes'. *Chem. Soc. Rev.*, **2012**, *41*, 4808–4826.

(26) A. Satake, S. Azuma, Y. Kuramochi, S. Hirota, Y. Kobuke. 'Supramolecular Organization of Light-Harvesting Porphyrin Macrorings'. *Chem. - Eur. J.*, **2011**, *17*, 855–865.

(27) Y. Kuramochi, A. S. D. Sandanayaka, A. Satake, Y. Araki, K. Ogawa, O. Ito, Y. Kobuke. 'Energy Transfer Followed by Electron Transfer in a Porphyrin Macrocycle and Central Acceptor Ligand: A Model for a Photosynthetic Composite of the Light-Harvesting Complex and Reaction Center'. *Chem. - Eur. J.*, **2009**, *15*, 2317–2327.

(28) D. V. Kondratuk, L. M. A. Perdigão, A. M. S. Esmail, J. N. O'Shea, P. H. Beton, H. L. Anderson. 'Supramolecular Nesting of Cyclic Polymers'. *Nat. Chem.*, **2015**, *7*, 317–322.

(29) M. Hoffmann, J. Kärnbratt, M. H. Chang, L. M. Herz, B. Albinsson, H. L. Anderson. 'Enhanced π Conjugation Around a Porphyrin[6] Nanoring'. *Angew. Chem. Int. Ed.*, **2008**, *47*, 4993–4996.

(30) G. J. E. Davidson, L. A. Lane, P. R. Raithby, J. E. Warren, C. V Robinson, J. K. M. Sanders. 'Coordination Polymers Based on Aluminum(III) Porphyrins'. *Inorg. Chem.*, **2008**, *47*, 8721–8726.

(31) G. J. E. Davidson, L. H. Tong, P. R. Raithby, J. K. M. Sanders. 'Aluminium(III) Porphyrins as Supramolecular Building Blocks'. *Chem. Comm.*, **2006**, 3087–3089.

(32) S. Mathew, F. Kuttassery, Y. Gomi, D. Yamamoto, R. Kiyooka, S. Onuki, Y. Nabetani, H. Tachibana, H. Inoue. 'Photochemical Oxygenation of Cyclohexene with Water Sensitized by Aluminium(III) Porphyrins with Visible Light'. *J. Photochem. Photobiol. A Chem.*, **2015**, *313*, 137–142.

(33) A. Amati, P. Cavigli, A. Kahnt, M. T. Indelli, E. Iengo. 'Self-Assembled Ruthenium(II)Porphyrin-Aluminium(III)Porphyrin-Fullerene Triad for Long-Lived Photoinduced Charge Separation'. *J. Phys. Chem. A*, **2017**, *121*, 4242–4252.

(34) I. Beletskaya, V. S. Tyurin, A. Y. Tsivadze, R. Guilard, C. Stern. 'Supramolecular Chemistry of Metalloporphyrins'. **2009**, *109*, 1659–1713.

(35) D. V. Kondratuk, J. K. Sprafke, M. C. O'Sullivan, L. M. A. Perdigao, A. Saywell, M. Malfois, J. N. O'Shea, P. H. Beton, A. L. Thompson, H. L. Anderson. 'Vernier-Templated Synthesis, Crystal Structure, and Supramolecular Chemistry of a 12-Porphyrin Nanoring'. *Chem. - Eur. J.*, **2014**, *20*, 12826–12834.

(36) D. V. Kondratuk, L. M. A. Perdigao, M. C. O'Sullivan, S. Svatek, G. Smith, J. N. O'Shea, P. H. Beton, H. L. Anderson. 'Two Vernier-Templated Routes to a 24-Porphyrin Nanoring'. *Angew. Chem. Int. Ed.*, **2012**, *51*, 6696–6699.

(37) M. Hoffmann, C. J. Wilson, B. Odell, H. L. Anderson. 'Template-Directed Synthesis of a π-Conjugated Porphyrin Nanoring'. *Angew. Chem. Int. Ed.*, **2007**, *46*, 3122–3125.

(38) P. Liu, P. Neuhaus, D. V. Kondratuk, T. S. Balaban, H. L. Anderson. 'Cyclodextrin-Templated Porphyrin Nanorings'. *Angew. Chem. Int. Ed.*, **2014**, *53*, 7770–7773.

(39) S. Liu, D. V. Kondratuk, S. A. L. Rousseaux, G. Gil-Ramírez, M. C. O'Sullivan, J. Cremers, T. D. W. Claridge, H. L. Anderson. 'Caterpillar Track Complexes in Template-Directed Synthesis and Correlated Molecular Motion'. *Angew. Chem. Int. Ed.*, **2015**, *54*, 5355–5359.

(40) P. Neuhaus, A. Cnossen, J. Q. Gong, L. M. Herz, H. L. Anderson. 'A Molecular Nanotube with Three-Dimensional π-Conjugation'. *Angew. Chem. Int. Ed.*, **2015**, *54*, 7344 –7348.

(41) S. Liu. 'A Non-Vernier Approach to Cooperative Templating', University of Oxford, **2014**.

(42) P. N. Taylor, H. L. Anderson. 'Cooperative Self-Assembly of Double-Strand Conjugated Porphyrin Ladders'. *J. Am. Chem. Soc.*, **1999**, *121*, 11538–11545.

3

Ring-Stacking Synthesis and Template-Directed Synthesis of a 12-Porphyrin Nanotube

During this project, I've had the privilege to work with Joshua Sauer who optimised the synthesis of the 6-porphyrin nanoring for ring-stacking during his summer student project.

3.1 Abstract

This chapter describes two strategies for the synthesis of a nanotube consisting of 12 porphyrin subunits. The first strategy comprises the homo-coupling of pre-formed 6-porphyrin nanorings. This strategy can in theory be extended towards the synthesis of increasingly long porphyrin nanotubes. The second strategy involves a template-directed synthesis from porphyrin dimer around two 6-legged templates. The templates can be removed from this complex through knock-out with a competing ligand. After template-removal, the zinc centres in this 12-porphyrin nanotube can be removed by treatment with acid.

3.2 Introduction

3.2.1 Template-Directed Synthesis of a 12-Porphyrin Nanotube

A 12-porphyrin nanotube, a discrete molecular equivalent of a carbon nanotube, has been prepared previously in the Anderson group.[1] This nanotube consists of two 6-porphyrin nanorings connected at the rims but is – perhaps unexpectedly - prepared through the template-directed synthesis from a specifically designed porphyrin dimer, ***l*-P2** (Figure 3.1). In this templated synthesis, eight components (two **T6** templates and six ***l*-P2** units) are coming together, and 12 new carbon-carbon bonds are being formed. Yet the yield in this reaction is 32%, demonstrating the power of supramolecular self-assembly in the template-directed synthesis of large porphyrin nanostructures.[2–6] This 12-porphyrin nanotube has an effective internal volume of 4 nm^3 which has potential for interesting host-guest chemistry.[7] Additionally, ultrafast fluorescence spectroscopy demonstrated extensive excited state delocalisation over the extended π-system.

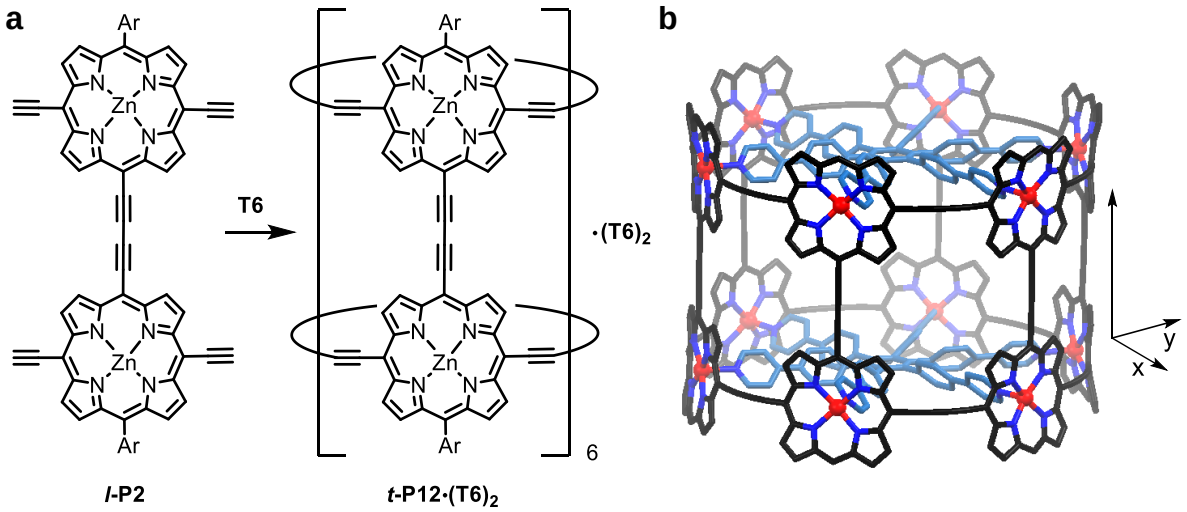

Figure 3.1: (a) Template-directed synthesis of a 12-porphyrin nanotube, ***t*-P12·(T6)$_2$**, from a specifically designed porphyrin dimer, ***l*-P2**. (b) Calculated structure of ***t*-P12·(T6)$_2$** (Modified MM2 forcefield, aryl groups were omitted to simplify calculations, hydrogen atoms omitted for clarity).

3.2.2 Molecular Nanotubes Through Ring-Stacking

Perhaps a more intuitive way of preparing molecular nanotubes is through the stacking of pre-formed rings. There are numerous examples in the literature of molecular, non-covalent, tubular assemblies. Popular methods include the hydrogen-bond directed stacking of cyclic peptide[8–13] (Figure 3.2a) and non-peptide[14–19] (Figure 3.2b) precursors. Other stacking strategies for molecular nanotube formation include; π-π stacking,[20] halogen bonding[21] and metal-ligand interactions.[22,23]

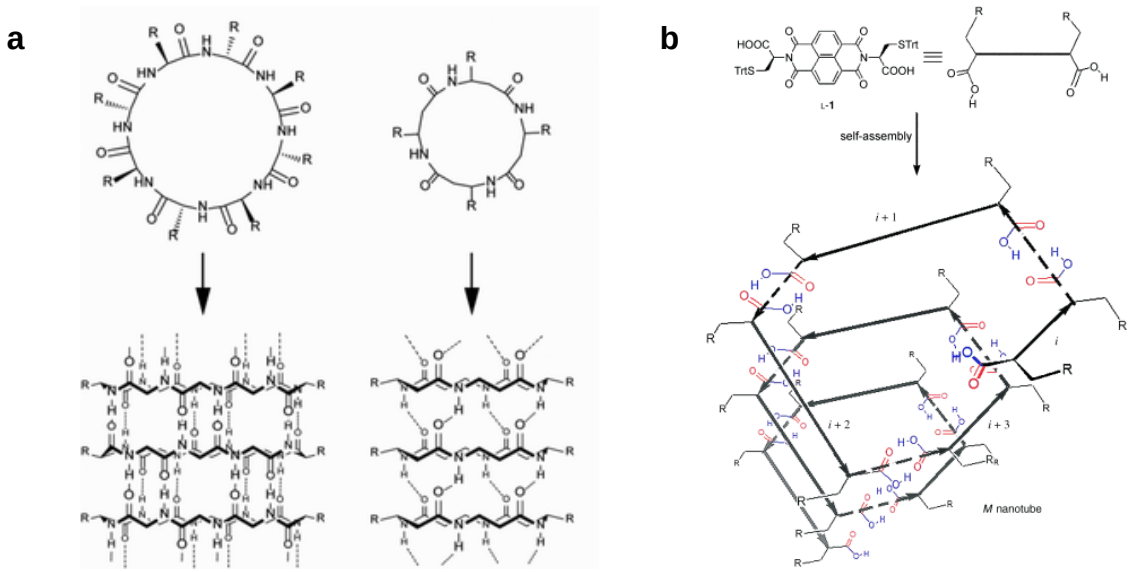

Figure 3.2: (a) Examples of cyclic peptides that assemble into nanotubes through β-sheet interactions. Reprinted with permission from ref. 8. Copyright 2012 The Royal Society of Chemistry. (b) Representation of a supramolecular self-assembled nanotube composed of naphthalenediimide units (STrt =S-trityl). The arrows indicate the direction of the nanotube assembly. Reprinted with permission from ref. 16. Copyright 2007 John Wiley and Sons.

Examples of the synthesis of a fully covalent molecular nanotube from pre-formed rings are less common. Over the last decade, the heat- or light-induced polymerisation of columnar stacked diacetylene-based macrocycles has been a popular strategy towards covalently linked molecular tubes.[24–28] In 2012, Hsu and co-workers reported the preparation of a molecular nanotube through solid-state polymerisation of a stacked column of diacetylene-based macrocycles (Figure 3.3). This approach provided excellent synthetic control over the diameter of the nanotubes. However, the obtained nanotubes were found to be indeterminately long and insoluble in a wide range of solvents.

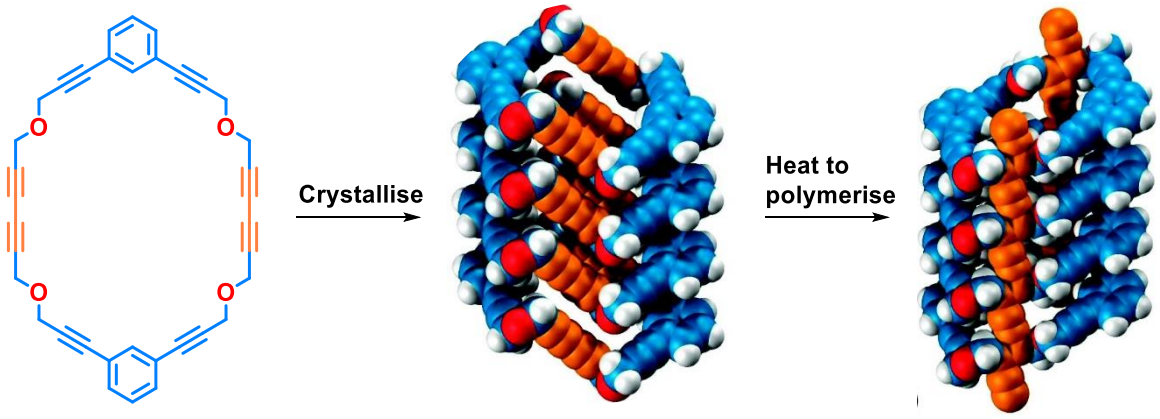

Figure 3.3: Schematic representation of the synthesis of a molecular nanotube. A diacetylene-containing macrocycle crystallised to form columnar stacks with a repeat distance of 4.84 Å. Slow annealing of the crystals at 40 °C *via* topochemical polymerisation resulted in the synthetic nanotube. Reprinted with permission from ref. 25. Copyright 2012 American Chemical Society.

3.2.3 Ring-Stacking Towards Porphyrin Nanotubes

The synthesis of increasingly longer porphyrin nanotubes through stacking of pre-formed nanorings is an appealing strategy. The template-directed method, as described above, is limited to the synthesis of 12-porphyrin nanotube. Due to the dynamic nature of template-directed synthesis, coupling of analogous oligomers longer than dimer would lead to mismatched coupling and polymer formation (Figure 3.4). Besides this, each increment in tube-length would require the laborious synthesis of the designated porphyrin oligomer.

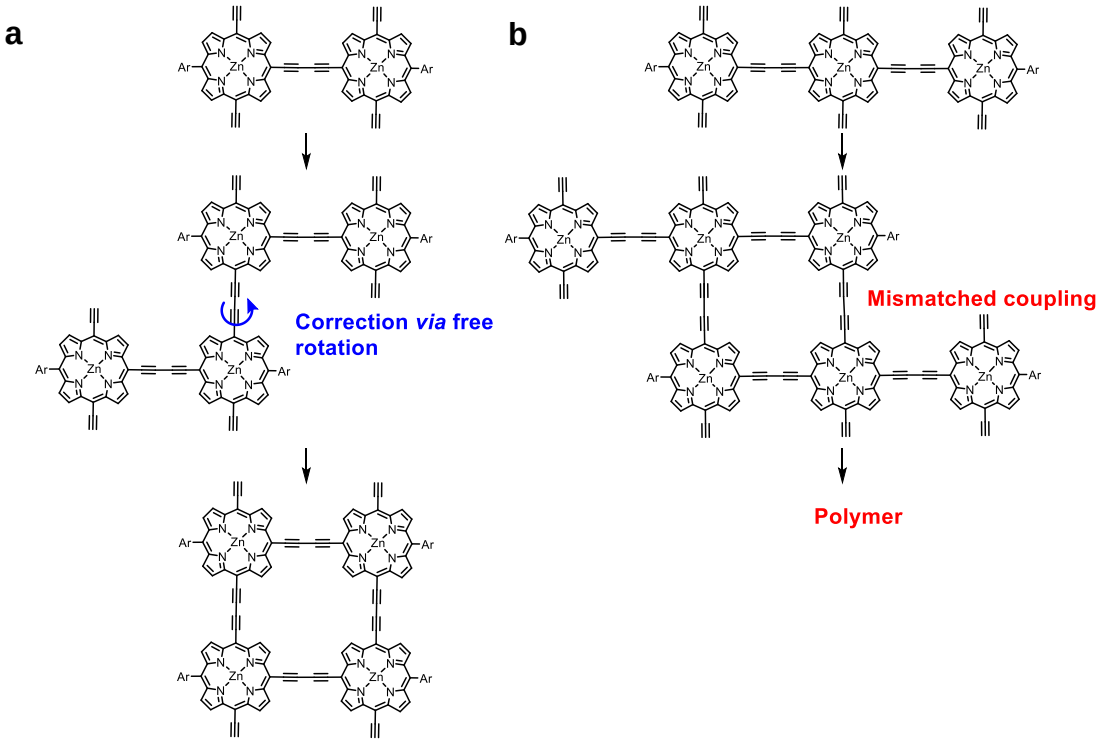

Figure 3.4: (a) Rotation around the bis-acetylene link allows the correction of initially staggered-coupled dimers. (b) Coupling of trimers leads to irreversible mismatched coupling and subsequent polymer formation.

Nanotube synthesis *via* the stacking of pre-formed porphyrin nanorings would require only two building blocks to access theoretically infinite extension in porphyrin nanotube length. The first building block is a *capping* ring with solubilising groups on one side of the porphyrin components and coupling moieties (e.g. free acetylenes) on the other, and the other a *central* ring with coupling moieties on both sides. Coupling of these two building blocks should lead to a statistical distribution of porphyrin nanotubes of various – but well defined – lengths with a monodisperse diameter of 2.5 nm (ref. 29) (Figure 3.5).

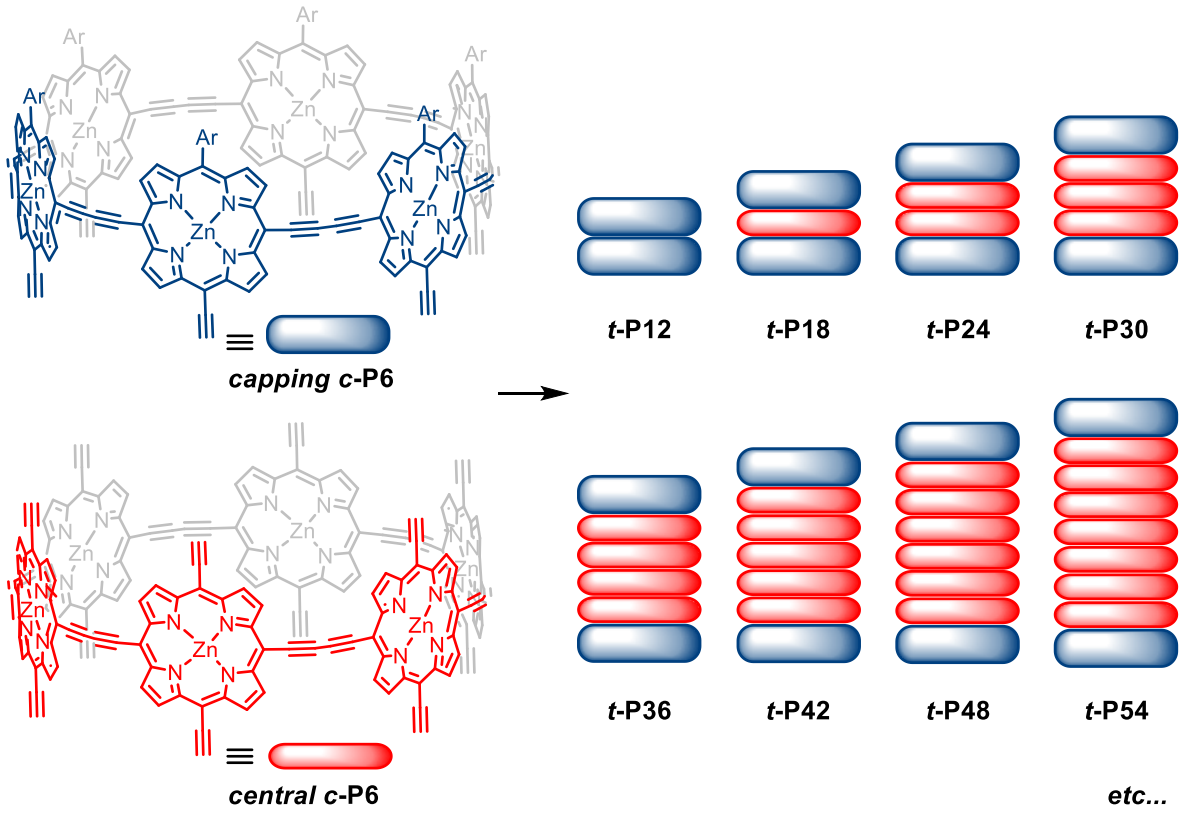

Figure 3.5: Ring-stacking approach towards the synthesis of 6-ring-based porphyrin nanotubes, in theory resulting in a statistical distribution of various-length porphyrin nanotubes with diameter 2.5nm.

In contrast to the abovementioned example of the polymerisation of columnar stacked diacetylene-based macrocycles, there is no initial, non-covalent pre-organisation of the 6-porpyrin nanorings prior to their coupling. We envision the stacking mechanism to involve an initial kinetic intermediate; two end-to-end connected rings. These rings can still freely rotate around the bis-acetylene bonds. Ring-ring inversion, followed by further covalent bis-acetylene bond formation will lead to the thermodynamic product; a 12-porphyrin nanotube (Figure 3.6).

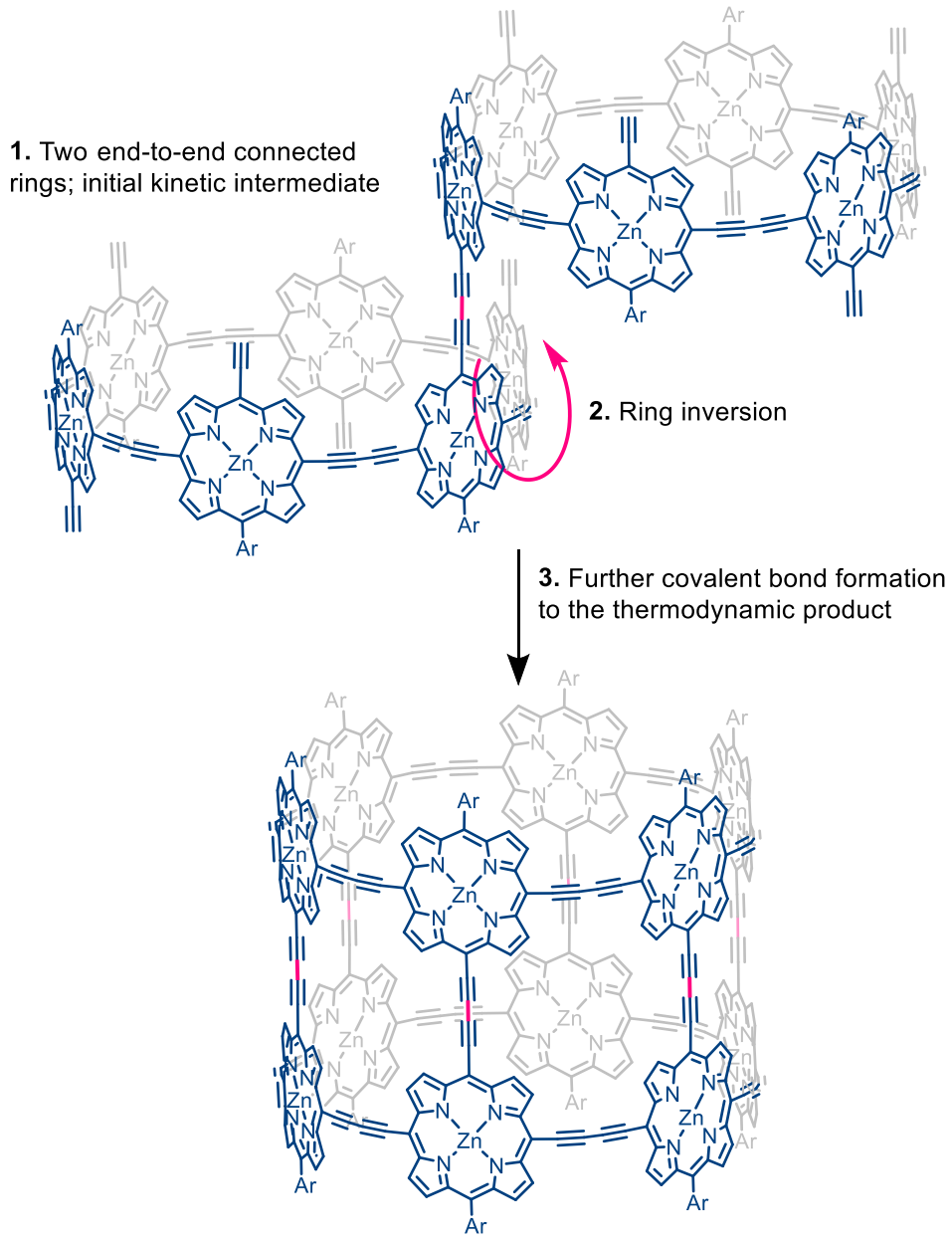

Figure 3.6: Proposed mechanism for the synthesis of a 12-porphyrin nanotube through ring-stacking of two 6-porphyrin nanorings.

The 12-porphyrin nanotube (***t*-P12**) is the simplest initial target to explore the ring-stacking strategy for porphyrin nanotube formation. To construct this nanotube through ring-stacking, the only building block required is the *capping* 6-porphyrin nanoring. This makes it a relatively simple first target. Furthermore, the previously discussed template-directed route to a 12-porphyrin nanotube delivers the reference compound, which makes the confirmation of 12-porphyrin nanotube formation through ring-stacking relatively straightforward.

3.3 Design and Synthesis of a 6-Porphyrin Nanoring for Ring-Stacking

3.3.1 First-Generation Design

As discussed above, the *capping* 6-porphyrin nanoring used for ring-stacking to ***t*-P12** requires a solubilising moiety on one side of the porphyrin components and coupling moieties on the other (Figure 3.5). Monomer **P1b** was prepared as an intermediate in the synthesis of 18-porphyrin nanotube (see Chapter 5), therefore, it was an attractive starting point for the synthesis of the *capping* 6-porphyrin nanoring. This porphyrin monomer contains two TIPS-acetylene moieties on *meso*-positions 10 and 20, a 1,3-bis(trihexylsilyl)-phenyl solubilising group on *meso* position 5 and a bromine on *meso*-position 15 (see Chapter 1, Figure 1.1, for *meso*-position numbering). **P1b** was prepared from porphyrin monomer **P1** via a lithium-mediated arylation reaction (**P1a[2H]**). After zinc insertion (**P1a[Zn]**), the porphyrin could be brominated to **P1b** (Scheme 3.1).

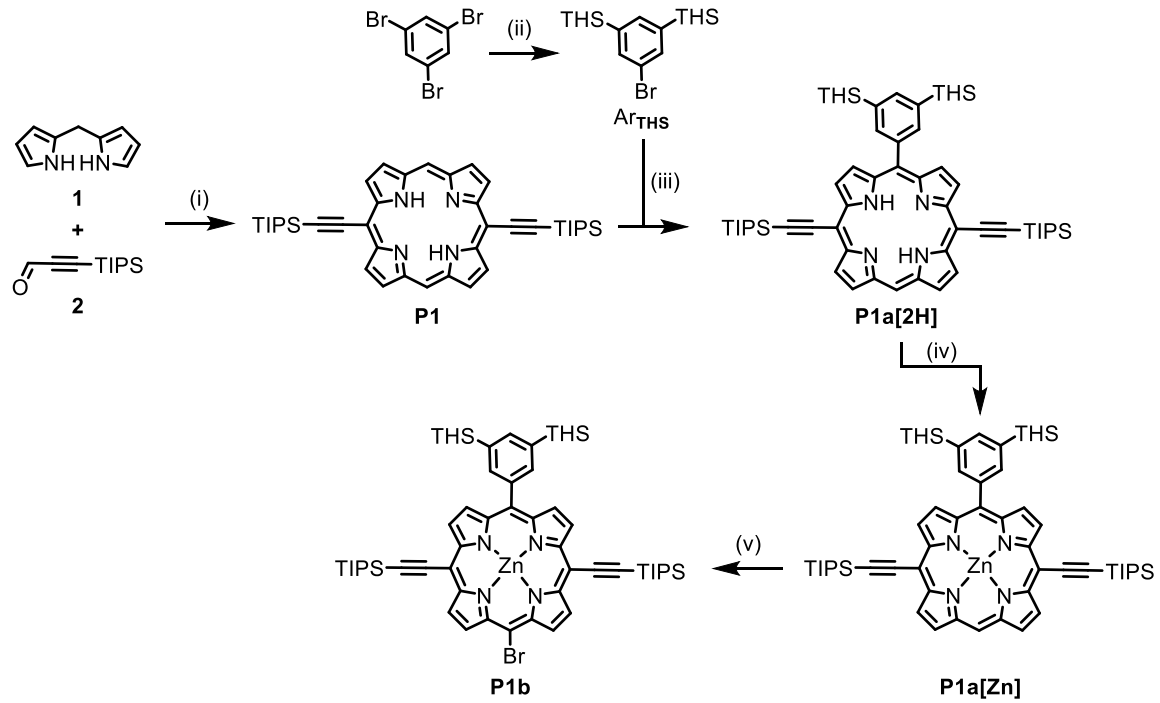

Scheme 3.1: (i) $BF_3{\cdot}Et_2O$, DDQ, CH_2Cl_2, 32%. (ii) *n*-butyl lithium, THS-chloride, Et_2O, (not isolated). (iii) *n*-butyl lithium, then H_2O, DDQ, Et_3N, Et_2O, THF, 74%. (iv) $Zn(OAc)_2{\cdot}2H_2O$, MeOH, $CHCl_3$, 100%. (v) NBS, $CHCl_3$, pyridine, 67%.

Deprotection of the TIPS groups in **P1b** using TBAF to form **P1c** and subsequent coupling in the presence of the 6-legged oligopyridine template **T6** led to the formation of a

6-porphyrin nanoring with *meso*-bromine substituents. However, unexpectedly polymerisation side reaction dominated and the *meso*-bromine nanoring could not be purified by recycling GPC. Sonogashira-coupling of CPDMS-acetylene onto the crude product resulted in a mixture that could be purified by recycling GPC and ***c*-P6$^{meso\text{-CPDMS}}$·T6** was successfully isolated. However, the losses in material due to polymer formation resulted in an overall yield of the desired ***c*-P6$^{meso\text{-CPDMS}}$·T6** from **P1c** of 5% (Scheme 3.2). Because of the relatively low yield and the encountered difficulties of working with the *meso*-bromine nanoring, this synthetic route was abandoned.

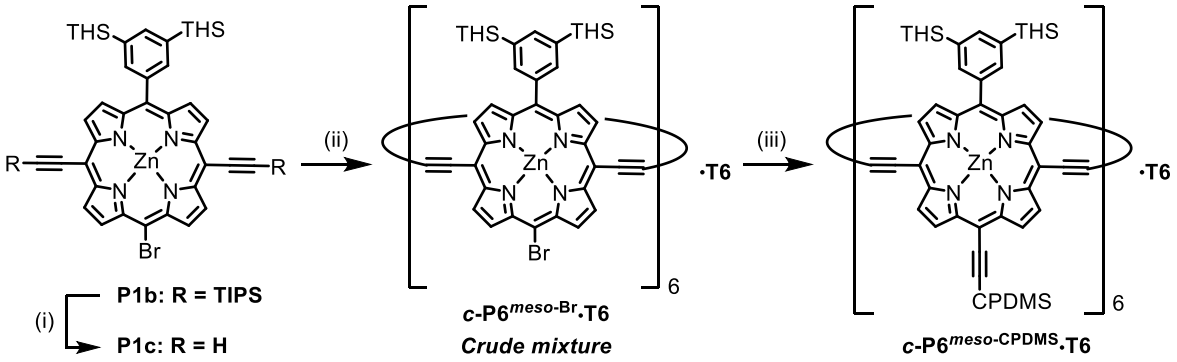

Scheme 3.2: (i) TBAF, CH_2Cl_2, 98%. (ii) **T6**, $Pd(PPh_3)_2Cl_2$, CuI, 1,4-benzoquinone, toluene, *N*,*N*-diisopropylamine, not isolated. (iii) Pd_2dba_3, CuI, PPh_3, toluene, *N*,*N*-diisopropylamine, CPDMS-acetylene, 5% from **P1c**.

3.3.2 Second-Generation Design

Due to the encountered difficulties with the *meso*-bromine ring an alternative synthetic strategy towards ***c*-P6$^{meso\text{-acetylene}}$** was adopted. Tri-acetylenic porphyrin building block **P1e** was prepared, containing orthogonal protecting groups that allow for selective deprotection of the acetylene groups on *meso*-positions 10 and 20. This strategy involved the deprotection of the TIPS-acetylene protecting groups of **P1b**, acetylene re-protection with TMS (**P1d**) and a Sonogashira coupling with THS-acetylene at *meso*-position 15 to obtain the desired orthogonal protecting-group distribution (Scheme 3.3). The relatively laborious sequence of deprotection and re-protection was required as bromination of the bis-acetylenic porphyrin **P1a[Zn]** (step (v) in Scheme 3.1), only works with TIPS-acetylenes on *meso*-positions 10 and 20 and hence TMS-acetylenes could not be installed at the beginning.

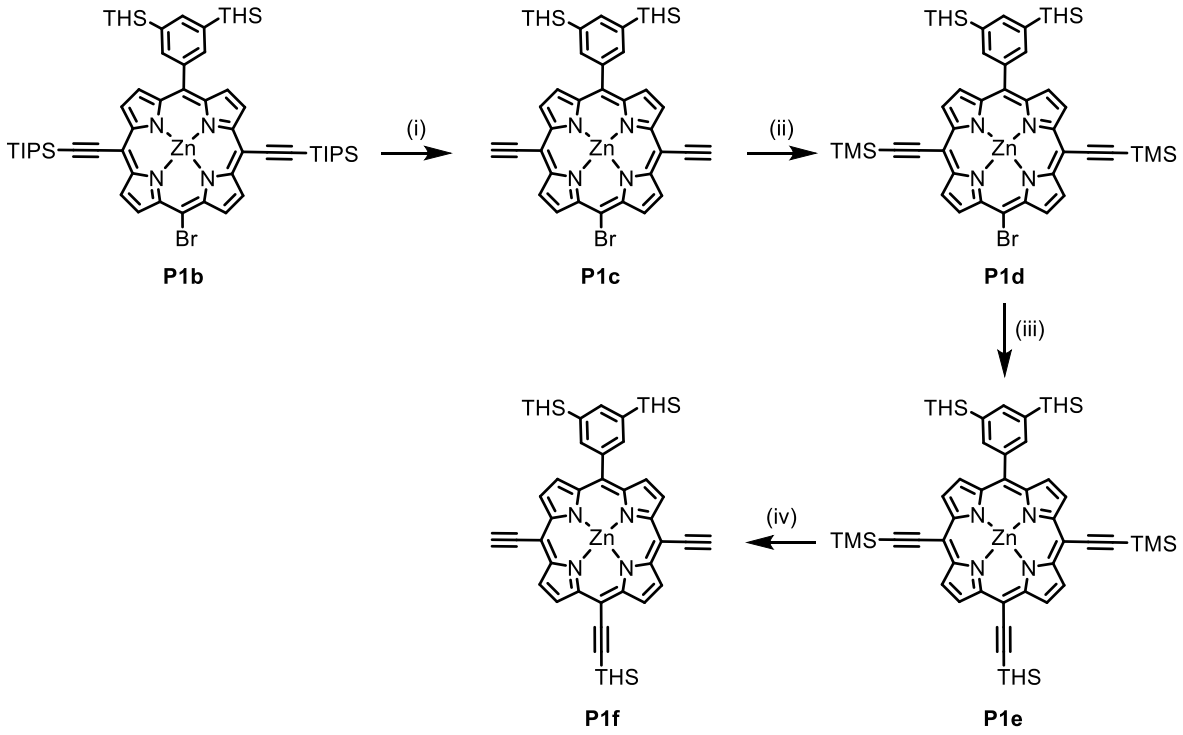

Scheme 3.3: (i) TBAF, CH_2Cl_2, 98%. (ii) LiHMDS, then TMS-chloride, THF, 82%. (iii) Pd_2dba_3, CuI, PPh_3, THS-acetylene, toluene, *N*,*N*-diisopropylamine, 90%. (iv) K_2CO_3, MeOH, THF, 98%.

Selective deprotection of the TMS protecting groups from **P1e** and coupling of **P1f** in the presence of **T6** gave the targeted 6-porphyrin nanoring in a 10% yield. Due to the asymmetric character of the obtained nanoring ***c*-P6$^{meso\text{-}THS}$•T6**, which inevitably exhibits a distribution in the directions of the *meso*-THS-acetylene substituents, it is crucial that the template is removed to allow for free rotation around the bis-acetylene links. Removal of the template was achieved by treating ***c*-P6$^{meso\text{-}THS}$•T6** with 1,4-diazabicyclo[2.2.2]octane (DABCO) combined with purification by a size-exclusion chromatography (SEC) column. DABCO acts as a competing ligand to the oligopyridine template and outcompetes the template in high concentrations, after which the significant difference in size causes ***c*-P6$^{meso\text{-}THS}$** and **T6** to separate. This 6-porphyrin nanoring was finally treated with TBAF to deprotect the remaining *meso*-THS-acetylene groups to give ***c*-P6$^{meso\text{-}acetylene}$**, a 6-porphyrin nanoring ready for ring-stacking (Scheme 3.4).

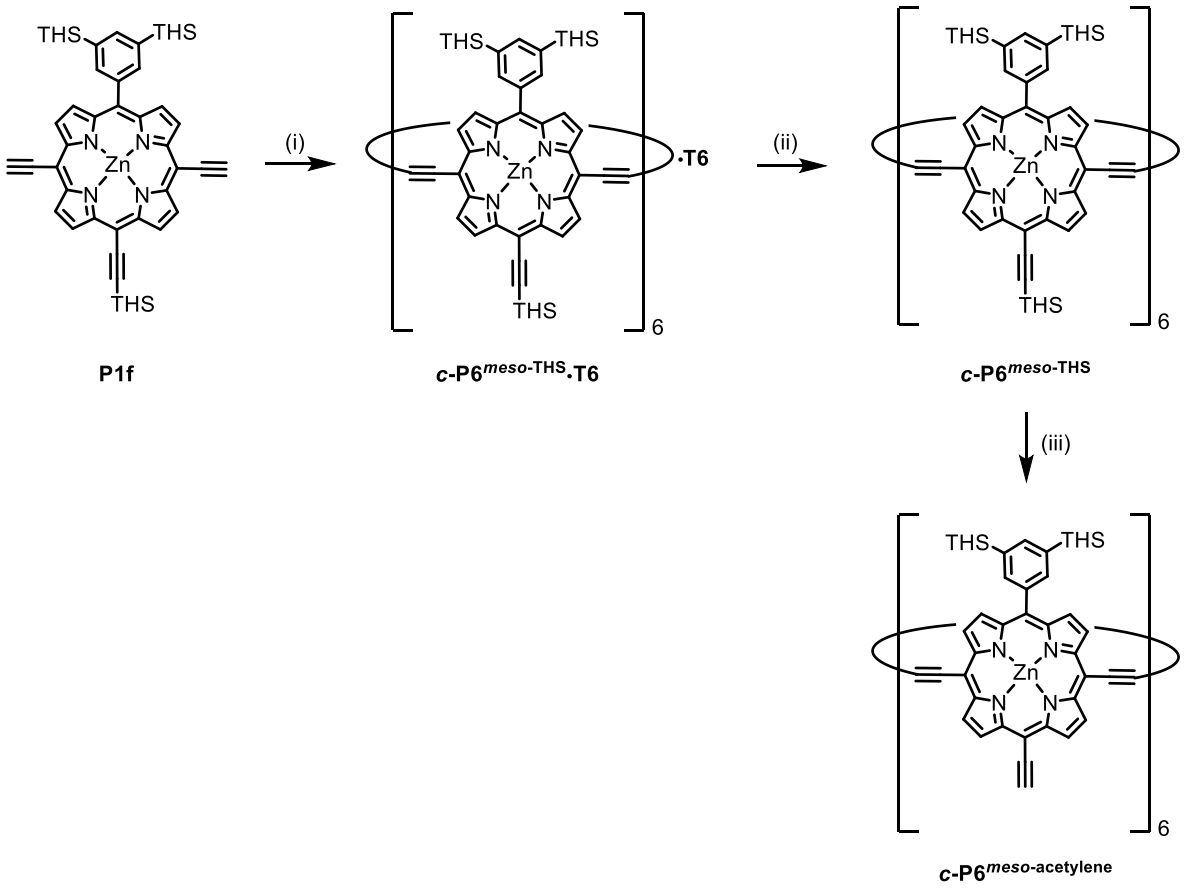

Scheme 3.4: (i) **T6**, $Pd(PPh_3)_2Cl_2$, CuI, 1,4-benzoquinone, toluene, *N*,*N*-diisopropylamine, 10%. (ii) DABCO, toluene, 89%. (iii) TBAF, toluene, pyridine, yield not determined.

3.4 Synthesis of *t*-P12 via Ring-Stacking

Porphyrin nanoring ***c*-P6*meso*-acetylene** was subjected to palladium catalysed oxidative alkyne coupling conditions.[2–5,29–31] The reaction was performed at a high dilution (45 μM) of porphyrin nanoring to prevent polymerisation, while maintaining the standard catalyst concentration. Reaction progress was monitored by UV-vis-NIR spectroscopy. After 24 h, the reaction mixture was passed through a short plug of Al_2O_3. The material was further purified by size-exclusion chromatography and finally subjected to recycling GPC (THF/1% pyridine) (Figure 3.7). The 12-porphyrin nanotube was obtained in 10% yield from its ***c*-P6*meso*-THS** precursor (Scheme 3.5).

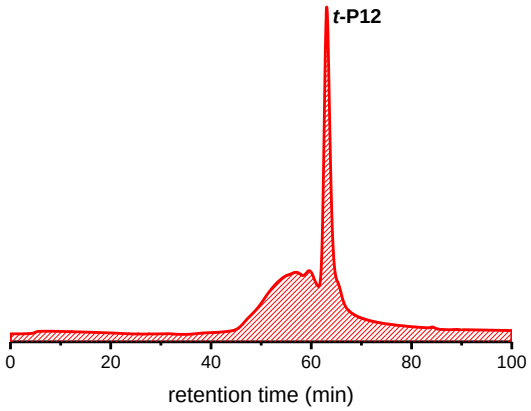

Figure 3.7: GPC trace (detection at 400 nm, THF/1% pyridine) of the product mixture from the synthesis of ***t*-P12** through ring-stacking.

As a proof of principle, **T6** template was inserted into the 12-porphyrin nanotube by mixing ***t*-P12** and **T6** in $CHCl_3$. The resulting complex, ***t*-P12·(T6)$_2$**, is identical by ^{1}H NMR, UV-vis-NIR spectroscopy and MALDI-ToF analysis to the 12-porphyrin nanotube prepared *via* template-directed synthesis from ***l*-P2$_{THS}$** as described in Section 3.2.1 and Section 3.5.

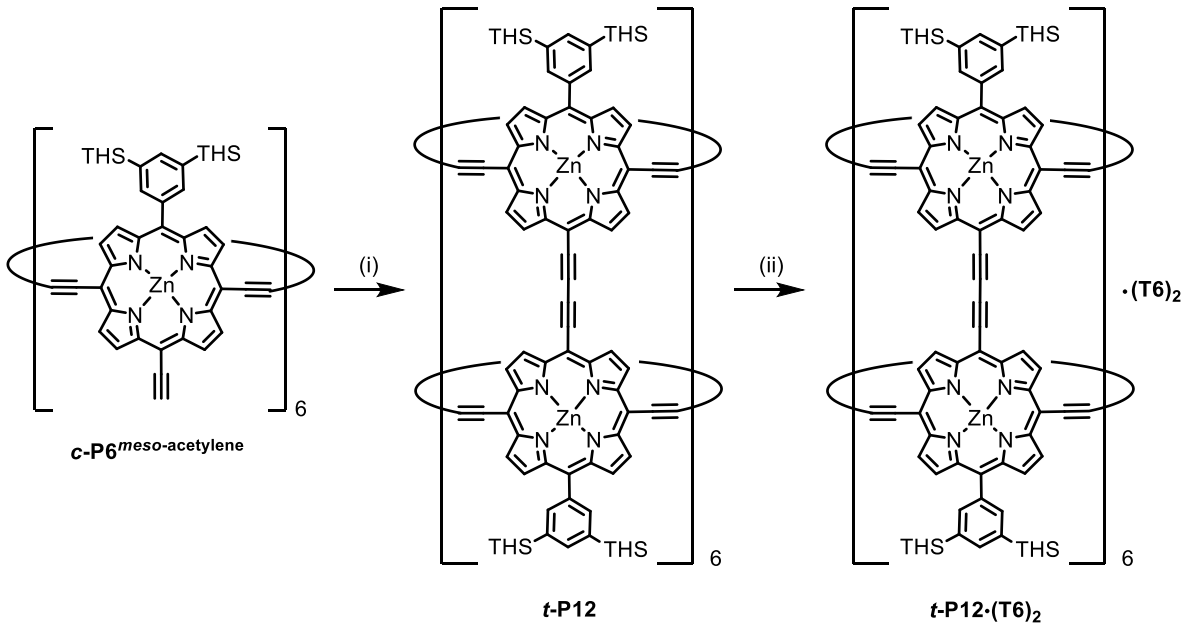

Scheme 3.5: (i) $Pd(PPh_3)_2Cl_2$, CuI, 1,4-benzoquinone, toluene, pyridine, *N*,*N*-diisopropylamine, 10% (two steps from ***c*-P6$^{meso\text{-}THS}$**); (ii) **T6**, $CHCl_3$, 100%.

3.5 Improved Template-Directed Synthetic Procedure to *t*-P12·(T6)$_2$

The template-directed procedure for the synthesis of ***t*-P12·(T6)$_2$** was optimised. The procedure as published[1] – although high yielding (32%) - was found to be unreliable and prone to random polymerisation. Extensive screening of reaction conditions indicated that using freshly distilled *N,N*-diisopropylamine in a concentration of 2 v/v % (versus the 33 v/v % reported), was crucial in securing reproducibility and prevention of polymer formation. The improved recipe allowed for a fourfold scale-up of the reaction without reducing the yield.

3.6 Synthesis of *t*-P12 via Template Knock-Out

When the synthesis and properties of ***t*-P12·(T6)$_2$** were first reported, efforts had been made to remove the **T6** templates from the nanotube cavity *via* either treatment with acid or with a competing ligand. However, these attempts were unsuccessful, and it was considered impossible to remove the **T6** templates from ***t*-P12·(T6)$_2$**.

We reinvestigated template removal from ***t*-P12·(T6)$_2$** which was prepared *via* template-directed synthesis. We found that outcompeting the template with high DABCO concentrations (200 mg/mL in toluene) in combination with size-exclusion chromatography efficiently removed the templates from the porphyrin nanotube cavity (Scheme 3.6).

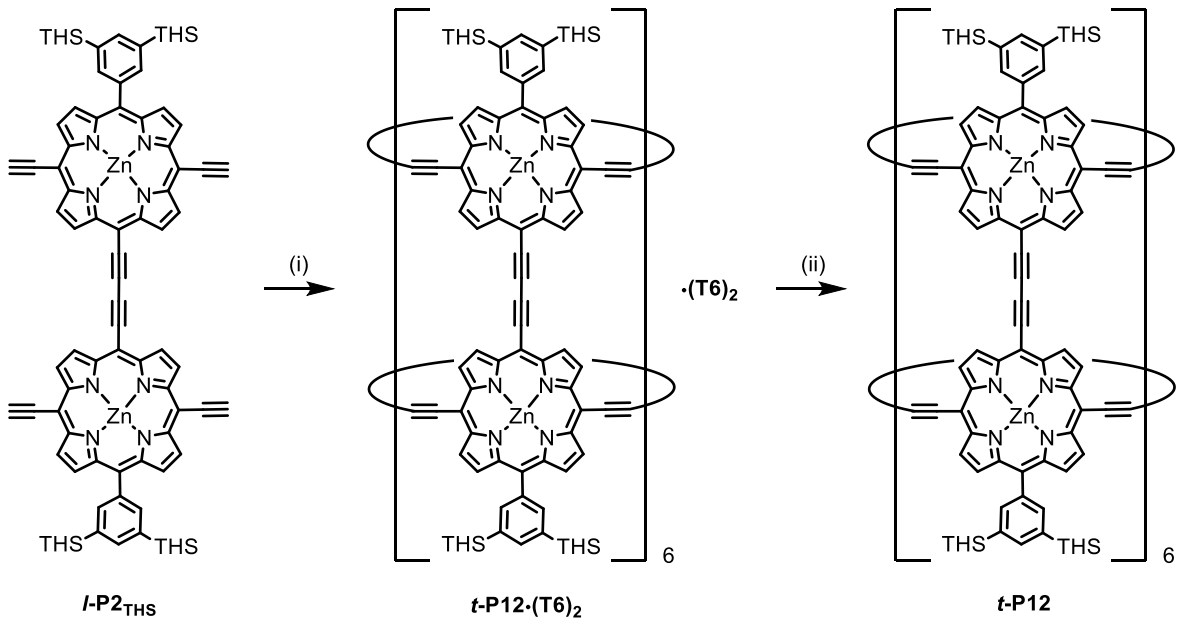

Scheme 3.6: (i) **T6**, $Pd(PPh_3)_2Cl_2$, CuI, 1,4-benzoquinone, toluene, *N,N*-diisopropylamine, 31%. (ii) DABCO, toluene, 86%.

3.7 Characterisation and Photophysical Properties of *t*-P12·(T6)$_2$ and *t*-P12

3.7.1 ^{1}H NMR

Full assignment of the β-protons, aryl-protons and template protons of ***t*-P12·(T6)$_2$** and ***t*-P12** was achieved *via* COSY and NOESY experiments. The template-containing and template-free porphyrin nanotubes show distinct differences in ^{1}H NMR. The *ortho*-protons on the *meso*-aryl groups are split in the ***t*-P12·(T6)$_2$** complex, indicating a difference in environment between the proton that is pointing to the centre of the tube and is in close proximity to the template (**b'** in Figure 3.8), and the proton that is pointing to the periphery of the complex (**b** in Figure 3.8). Once templates are removed from the complex, the *ortho*-protons become equivalent by ^{1}H NMR and appear as one singlet (Figure 3.8). Previously, for a 6-porphyrin nanoring system, the appearance of the *ortho*-protons as a single signal in the template-free nanoring was ascribed to fast rotation around the butadiyne links.[32,33] However, in the 12-porphyrin nanotube such rotation is not possible. Although fast rotation around the butadiyne links in 6-porphyrin nanoring should not be dismissed as an explanation for the change in *ortho*-proton signal, the observations on 12-porphyrin nanotube suggest that this phenomenon might need reinvestigating.

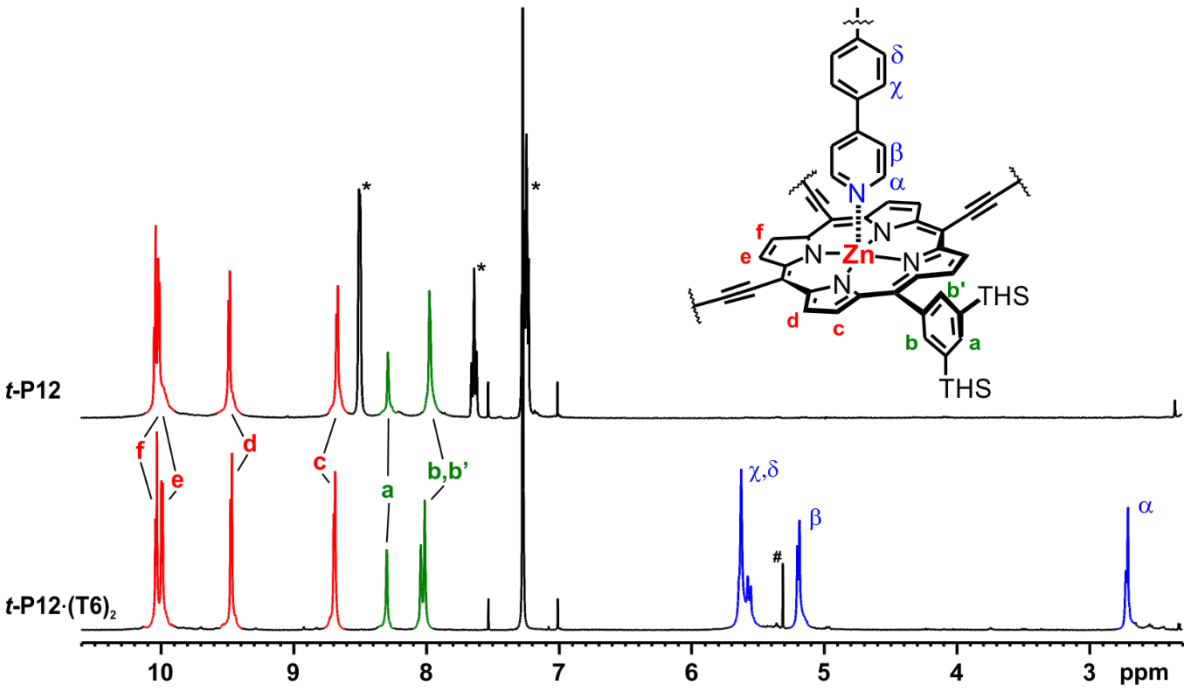

Figure 3.8: (top) Region of the ^{1}H NMR spectrum (400 MHz, $CDCl_3$ + 1% pyridine-d_5, 298K) of ***t*-P12** (*=pyridine residual signal). (bottom) Region of the ^{1}H NMR spectrum (400 MHz, $CDCl_3$, 298 K) of ***t*-P12·(T6)$_2$** (#=CH_2Cl_2 residual signal).

3.7.2 UV-vis-NIR Absorption

In Figure 3.9 the UV-vis-NIR absorption spectra of ***t*-P12·(T6)$_2$** versus ***t*-P12** and ***c*-P6$^{meso\text{-}THS}$·T6** versus ***c*-P6$^{meso\text{-}THS}$** are depicted. It is evident that, with the removal of the template, both systems become more dynamic, as can be deduced from the blue-shift and loss of fine vibronic structure in the Q band. Due to the higher intrinsic rigidity of the nanotube, this blue-shift and change in the Q band upon **T6** removal is lower for ***t*-P12** (18 nm blue-shift) than for ***c*-P6** (24 nm blue-shift).

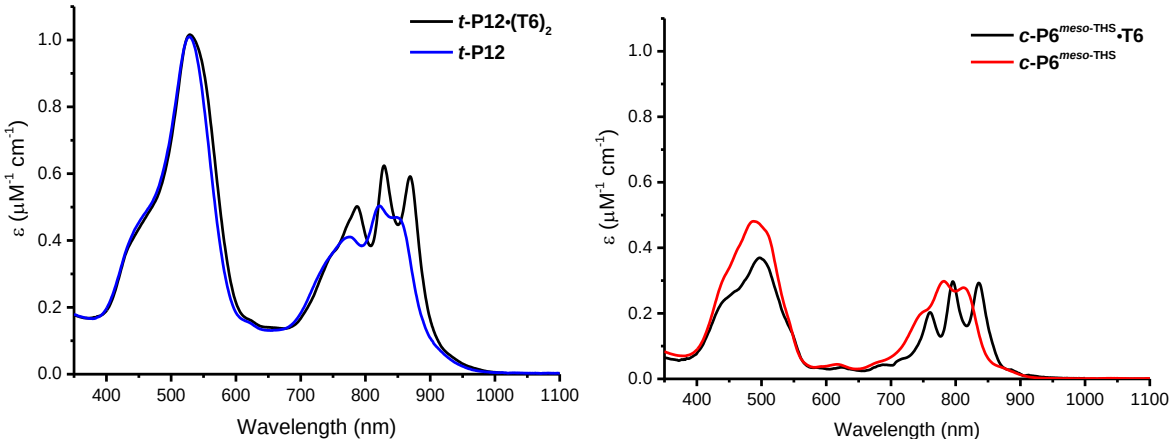

Figure 3.9: (left) UV-vis-NIR absorption spectra of ***t*-P12·(T6)$_2$** (black trace, measured in $CHCl_3$) and ***t*-P12** (blue trace, measured in $CHCl_3$ + 1% pyridine). (right) UV-vis-NIR absorption spectra of ***c*-P6$^{meso\text{-}THS}$·T6** (black trace, measured in $CHCl_3$) and ***c*-P6$^{meso\text{-}THS}$** (ted trace, measured in $CHCl_3$ + 1% pyridine). All traces were measured at 298 K.

3.7.3 Fluorescence Emission and Quantum Yield

In Figure 3.10 and Figure 3.11 the normalised absorbance and fluorescence emission spectra of ***t*-P12** and ***t*-P12·(T6)$_2$** are depicted, respectively. The high intrinsic rigidity of the 12-porphyrin nanotube accounts for a relatively small difference in fluorescence quantum yield between the template-complex and the template-free nanotube (***t*-P12**; φ_f = 0.26%, and ***t*-P12·(T6)$_2$**; φ_f = 0.22%).

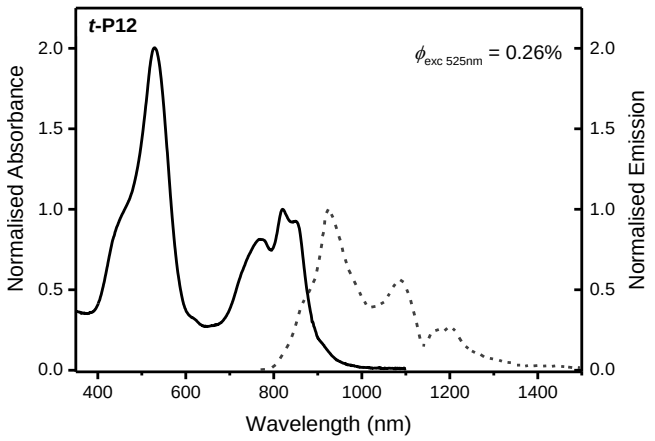

Figure 3.10: Normalised steady-state absorption (black line) and fluorescence (black dotted line) at 298 K of ***t*-P12** (λ_{exc} = 525 nm, measured in toluene/1% pyridine).

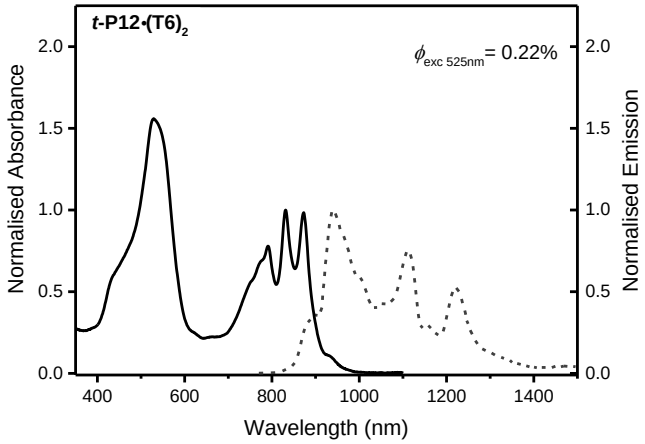

Figure 3.11: Normalised steady-state absorption (black line) and fluorescence (black dotted line) at 298 K of ***t*-P12·(T6)$_2$** (λ_{exc} = 525 nm, measured in toluene).

The rigid template-complex, ***t*-P12·(T6)$_2$**, has a smaller Stokes shift than ***t*-P12**. The Stokes shift difference between these two materials is slightly smaller than the change in Stokes shift for the 6-porphyrin nanoring with and without template ***c*-P6** and ***c*-P6·T6**, respectively (Table 3.1).[34]

The cancellation of the transition dipole moments in a symmetrical π-conjugated macrocyclic structure make the lowest electronic transition symmetry-forbidden. Emission from this first excited state becomes partially allowed through vibronic coupling with higher excited states.[29,35,36] This phenomenon is manifested in a low fluorescence quantum yield, as the slow radiative S_1-S_0 transition is competing with non-radiative decay pathways. Removing the templates from a cyclic porphyrin nanostructure allows more conformational freedom, decreases the symmetry and hence increases the fluorescence quantum yield.

Template removal from ***c*-P6·T6** allows for more conformational freedom, decreases the symmetry and hence increases the fluorescence quantum yield. Template removal from ***t*-P12·(T6)$_2$** on the other hand only induces a minor increase in fluorescence quantum yield as the intrinsic rigidity of this compound prevents desymmetrisation after template removal.

Table 3.1: Summary of absorption/emission, Stokes shifts and fluorescence quantum yields. The data on the 6-porphyrin nanoring was obtained from reference 34.

	$\lambda_{abs\ Q}$ (nm)	λ_{em} (nm)	Stokes shift (eV)	φ_f (%)
***c*-P6**[a]	822	890	0.11524	1.5
***c*-P6·T6**[b]	853	915	0.09849	0.42
***t*-P12**[c]	850	924	0.11682	0.26
***t*-P12·(T6)$_2$**[d]	873	941	0.10263	0.22

Fluorescence quantum yields were determined referenced to ***l*-P6** (φ_f = 28%). [a]measured in toluene/1% pyridine, λ_{exc} 770 nm. [b]measured in toluene, λ_{exc} 770 nm. [c]measured in toluene/1 % pyridine, λ_{exc} 525 nm. [d]measured in toluene/1% pyridine, λ_{exc} 525 nm.

3.8 Synthesis of a Free-Base 12-Porphyrin Nanotube

To date, template-directed synthesis of porphyrin nanostructures has relied on the Zn···N interaction between porphyrin zinc-centres and the template nitrogen-functionality. However, porphyrin nanostructures have been prepared that contain other metals than zinc.[37] An example is the synthesis of an aluminium 6-porphyrin nanoring (Chapter 2). This nanoring was prepared *via* template-directed synthesis of a zinc 6-porphyrin nanoring, demetallation of the zinc centres and subsequent re-metallation with aluminium.[6]

3.8.1 Demetallation of ***t*-P12[Zn]** *to* ***t*-P12[2H]**

Demetallation of zinc porphyrins can be achieved in acidic medium, which induces protonation of the central nitrogen atoms and hence loss of the coordinating zinc atom.[6,38] Demetallation of the zinc centres in the 12-porphyrin nanotube was found to be impossible in the presence of the **T6** templates, possibly due to the strong binding of the two templates. At very high acid concentrations, by UV-vis-NIR spectroscopy, a free-base peak was observed, but the complex decomposed under such conditions. However, after template removal *via* knock-out with DABCO, the zinc-centres could be demetallated under milder conditions and the free-base 12-porphyrin nanotube was obtained (Scheme 3.7). Full

demetallation was confirmed by MALDI-ToF analysis, in which a sharp single peak was observed at m/z 12266 (Figure 3.12) (***t*-P12[2H]** requires 12247.16).

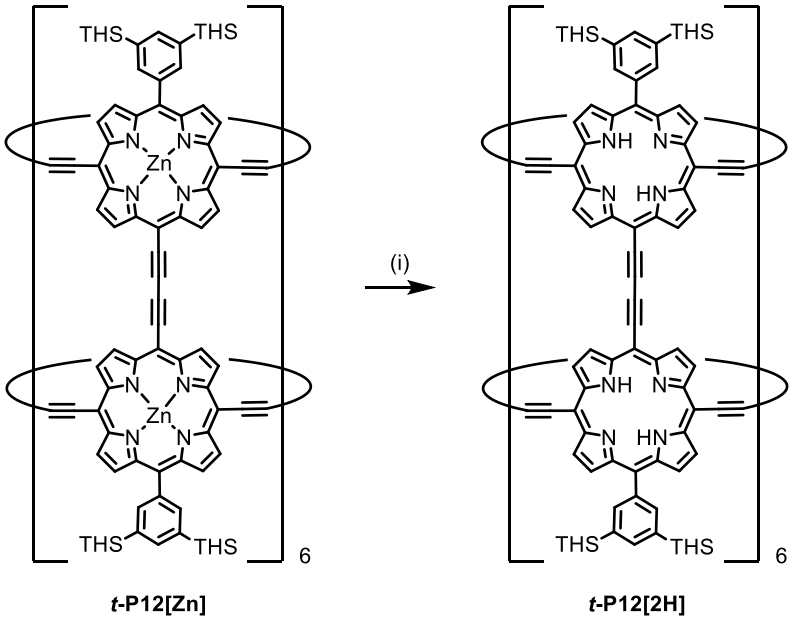

Scheme 3.7: (i) trifluoroacetic acid, CH_2Cl_2, 37%.

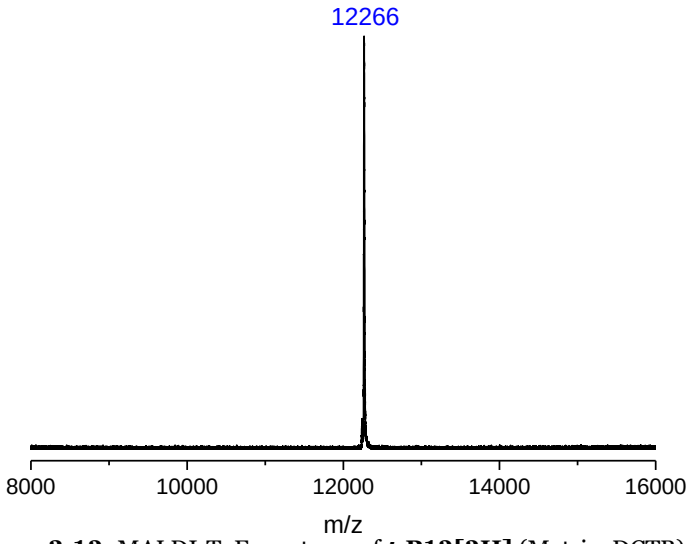

Figure 3.12: MALDI-ToF spectrum of ***t*-P12[2H]** (Matrix: DCTB).

3.8.2 UV-vis-NIR and ^{1}H NMR Spectroscopy Characterisation of ***t*-P12[2H]**

The UV-vis-NIR absorption spectrum of ***t*-P12[2H]** shows the characteristic vibronically coupled Q band with three distinct transitions,[1,35] while also showing the appearance of a characteristic broad free-base peak at 680 nm (Figure 3.13).

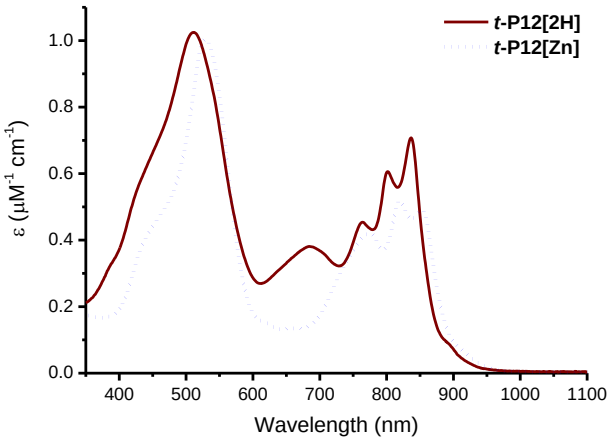

Figure 3.13: UV-vis-NIR absorption spectra of ***t*-P12[2H]** (burgundy trace, measured in toluene at 298 K) and ***t*-P12[Zn]** (blue dotted trace, measured in toluene/1% pyridine at 298 K).

The ^{1}H NMR spectrum of ***t*-P12[2H]** clearly shows the free-base proton signals at –0.6 ppm. The two β-proton signals that are furthest downfield overlap to form a broad singlet. Interestingly, the *ortho*-aryl protons appear as two well-defined singlets (Figure 3.14). These protons appeared as two singlets in the template-complex ***t*-P12·(T6)$_2$**, but as one singlet in the template-free nanotube ***t*-P12[Zn]**. This earlier observation lead to the suggestion that removal of the templates created a magnetically similar environment for the *ortho*-proton pointing towards the centre of the nanotube and the *ortho*-proton pointing towards the periphery (See Figure 3.8 and Section 3.7.1). From this point of view, it is therefore surprising that the *ortho*-protons are once more split in ***t*-P12[2H]**. The observed splitting in ***t*-P12·(T6)$_2$** and ***t*-P12[2H]** likely arises from low frequency aryl-rotation. In a previous study on molecular motion in a caterpillar track complex, aryl-rotation frequencies of 4 s^{-1} and 0.4 s^{-1} were measured giving rise to the observed *ortho*-proton splitting.[5] However, we are uncertain if the frequency of aryl-rotation can actually be high enough to account for the coalescence of the *ortho*-protons signals in ***t*-P12[Zn]**. It is therefore more likely that the *ortho*-protons in ***t*-P12[Zn]** are simply coincidentally isochronous.

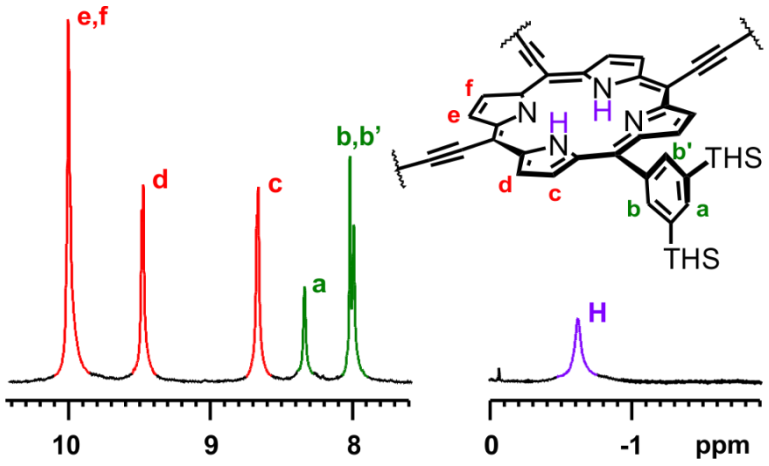

Figure 3.14: Regions of the ^{1}H NMR spectrum (400 MHz, $CDCl_3$, 298 K) of ***t*-P12[2H]**.

3.9 Conclusion

The procedure for the template-directed synthesis of a 12-porphyrin nanotube, ***t*-P12·(T6)$_2$**, was significantly improved, allowing for reproducible synthesis of this compound. Templates could be removed from this complex *via* knock-out with a competing ligand, an achievement that was previously considered to be impossible. After template knock-out, the zinc centres in the 12-porphyrin nanotube could be removed with acid. The ability to remove the zinc centres creates a range of opportunities for the incorporation of metals other than zinc. Multi-walled carbon nanotubes coated with an amorphous layer of cobalt porphyrins have shown potential in water oxidation catalysis.[44] Insertion of cobalt in the 12-porphyrin nanotube would create a monodisperse analogue of this system and could allow better understanding of structure-function relationships.

We have investigated the synthesis of the 12-porphyrin nanotube through the stacking of pre-formed 6-porphyrin nanorings. A design based on a tri-acetylenic porphyrin building block protected with two orthogonal trialkylsilyl groups in designated positions, proved an efficient route towards a 6-porphyrin nanoring decorated with aryl-solubilising groups on one side of the porphyrin components and acetylenes on the other. Removal of the protecting group from the *meso*-acetylene and subsequent coupling gave the 12-porphyrin nanotube in 10% yield. **T6** template could be inserted into the tube to close the nanotube cavity. This mechanism of molecular nanotube formation is fundamentally different to previously published methods where noncovalent binding between the building blocks was established

prior to covalent linkage. In our design the 12-porphyrin nanotube is formed as the thermodynamic product without preassembling of the components.

The synthesis of porphyrin nanotubes through ring-stacking could be a versatile strategy to increasingly longer porphyrin nanotubes. Extension of this strategy beyond the 12-porphyrin nanotube would require a porphyrin nanoring carrying acetylene groups on all its *meso*-positions. Such nanoring would most likely be insoluble. This issue could potentially be circumvented by the addition of solubilizing groups, such as ethyl, to the β-positions of the porphyrin (Figure 3.15).

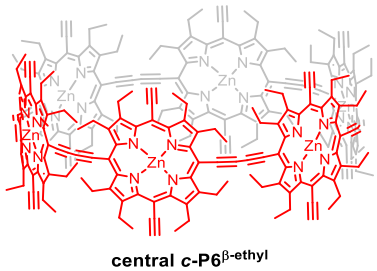

Figure 3.15: The central 6-porphyrin nanoring for ring-stacking carrying solubilising ethyl chains on its β-positions.

Alternatively, a stepwise approach could be employed. This would require a central 6-porphyrin nanoring with orthogonal acetylene protecting groups. However, this strategy would be relatively laborious and considering the synthesis of ***t*-P12** from ***c*-P6*meso*-acetylene** occurred in a 10% yield, we don't expect this strategy to be high yielding in long porphyrin nanotubes.

Although the synthesis of ***t*-P12** through ring-stacking was successful and we see the potential to extend this strategy to longer porphyrin nanotubes, we decided to focus on the bottom-up synthesis of an 18-porphyrin nanotube through template-directed synthesis instead (see Chapter 5). However, the knowledge gained during this project provided a better understanding of the synthetic challenges that arise while building longer porphyrin nanotubes. Furthermore, the synthetic route towards the asymmetrically substituted nanoring lead us to optimise synthetic procedures (such as the deprotection/reprotection sequence) that proved to be crucial in the synthesis of the 18-porphyrin nanotube (see Chapter 5) and in various other research projects that are currently being conducted in the group.

3.10 Experimental Procedures

3.10.1 Synthesis of Porphyrin Monomer

Dipyrromethane[39] (**1**) and triisopropylsilylpropynal[40] (**2**) were prepared according to literature procedures.

5,15-bis{[tri(propan-2-yl)silyl]ethynyl}porphyrin – P1

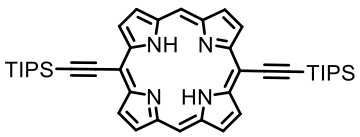

Dipyrromethane (**1**) (1.47 g, 10.1 mmol) was dissolved in CH_2Cl_2 (600 mL). The solution was degassed and kept under N_2 atmosphere. To this solution triisopropylsilylpropynal (**2**) (2.26 mL, 10.1 mmol) was added followed by $BF_3{\cdot}Et_2O$ (0.40 mL, 3.2 mmol). The mixture was stirred for 45 min in the dark under N_2 atmosphere. DDQ (3.44 g, 15.2 mmol) was then added and the mixture stirred for 10 min. The resulting brown solution was filtered through three consecutive SiO_2 plugs (CH_2Cl_2), to remove DDQ residues and tar. After removal of the volatiles *in vacuo*, recrystallization from CH_2Cl_2/MeOH yielded **P1** (1.1 g, 32%) as a purple solid.

^{1}H NMR (400 MHz, $CDCl_3$, 298 K): δ_H 10.14 (s, 2H, *meso-H*), 9.73 (d, *J* = 4.6 Hz, 4H, *βH*), 9.32 (d, *J* = 4.6 Hz, 4H, *βH*), 1.52-1.46 (m, 42H, TIPS-*H*), −2.62 (s, 2H, N*H*).

MALDI-ToF m/z 670.45 (calculated for $C_{42}H_{54}N_4Si_2$: 670.39).

As lit.[41,42]

(5-bromo-1,3-phenylene)bis(trihexylsilane)[43] – Ar_{THS}

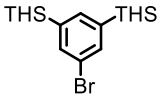

n-Butyl lithium (1.6 M in hexane, 10.4 mL, 16.6 mmol) was added dropwise by syringe to a solution (or suspension) of 1,3,5-tribromobenzene (2.5 g, 7.9 mmol) in Et_2O (62 mL) at −78 °C, under inert atmosphere. The solution was stirred for 90 min before THS-chloride (6.75 mL, 17.4 mmol) was added dropwise *via* a syringe. The solution was allowed to warm to room temperature. After stirring for another 90 min, the reaction mixture was washed with water, dried over $MgSO_4$ and filtered. The solution was concentrated and passed through a SiO_2 plug (PE 40-60). The solvent was removed to give 5.9 g of a 3:1 mixture of (5-bromo-1,3-phenylene)bis(trihexylsilane) and (benzene-1,3,5-triyl)tris(trihexylsilane).

This crude product was dried under high vacuum for several hours and was used without further purification in the next step.

10-[3,5-bis(trihexylsilyl)phenyl]-5,15-bis{[tri(propan-2-yl)silyl]ethynyl}porphyrin – P1a[2H]

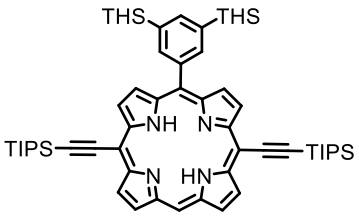

n-Butyl lithium (1.6 M in hexanes, 4.41 mL, 7.1 mmol) was added dropwise to a solution of (5-bromo-1,3-phenylene)bis(trihexylsilane) (5.1g, 7.1 mmol) in Et_2O (30 mL) at −78 °C, under N_2 atmosphere. The mixture was warmed to room temperature and stirred for 1 h. This solution was added dropwise to a solution of **P1** (600 mg, 0.89 mmol) in THF (30 mL). The mixture was stirred at room temperature overnight. Water (3.0 mL) was added, followed by DDQ (601 mg, 2.6 mmol). The reaction mixture was stirred for 20 min before addition of Et_3N (1.2 mL). The volatiles were removed *in vacuo* and the residue was taken up in CH_2Cl_2 (300 mL) and washed with H_2O (3 × 130 mL). The organic layer was dried over Na_2SO_4 and concentrated. Column chromatography (9:1 PE 40-60:CH_2Cl_2) afforded **P1a[2H]** (817 mg, 74 %) as a purple solid.

^{1}H NMR (400 MHz, $CDCl_3$, 298 K): δ_H 10.07 (s, 1H, *meso-H*), 9.75 (d, *J* = 4.6 Hz, 2H, *β-H*), 9.66 (d, *J* = 4.7 Hz, 2H, *β-H*), 9.29 (d, *J* = 4.6 Hz, 2H, *β-H*), 8.82 (d, *J* = 4.7 Hz, 2H, *β-H*), 8.23 (s, 2H, Ar-H_{ortho}), 8.01 (s, 1H, Ar-H_{para}), 1.55-1.45 (m, 54H), 1.43-1.35 (m, 12H), 1.35-1.28 (m, 24H), 0.97-0.90 (m, 12H), 0.90-0.86 (m, 18H), −2.35 (s, 2H, N*H*).

MALDI-ToF m/z 1312.64 (calculated for $C_{84}H_{134}N_4Si_4$: 1310.97).

As lit.[1]

Zinc 10-[3,5-bis(trihexylsilyl)phenyl]-5,15-bis{[tri(propan-2-yl)silyl]ethynyl}porphyrin – P1a[Zn]

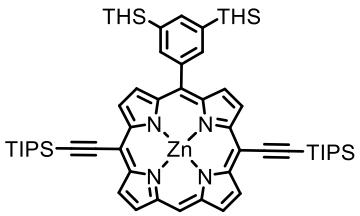

A solution of $Zn(OAc)_2 \cdot 2H_2O$ (484 mg, 2.2 mmol) in MeOH (4 mL) was added to a solution of **P1a[2H]** (643 mg, 0.49 mmol) in $CHCl_3$ (20 mL). The mixture was stirred at room temperature for 1 h before filtration over a short SiO_2 plug (100:1 CH_2Cl_2:pyridine). **P1a[Zn]** was obtained as a purple solid in 727 mg (100%) yield as a 1:1 complex with pyridine.

^{1}H NMR (400 MHz, $CDCl_3$, 298 K): δ_H 10.03 (s, 1H, *meso-H*), 9.80 (d, *J* = 4.4 Hz, 2H, *β-H*), 9.71 (d, *J* = 4.5 Hz, 2H, *β-H*), 9.30 (d, *J* = 4.4 Hz, 2H, *β-H*), 8.85 (d, *J* = 4.5 Hz, 2H, *β-H*), 8.20 (s, 2H, Ar-H_{ortho}), 7.97 (s, 1H, Ar-H_{para}), 1.52-1.44 (m, 54H), 1.42-1.33 (m, 12H), 1.33-1.26 (m, 24H) 0.96-0.90 (m, 12H), 0.90-0.84 (m, 18H).

MALDI-ToF m/z 1375.11 (calculated for $C_{84}H_{132}N_4Si_4Zn$: 1374.88).

As lit.[1]

Zinc 5-[3,5-bis(trihexylsilyl)phenyl]-15-bromo-10,20-bis{[tri(propan-2-yl)silyl]ethynyl}porphyrin – P1b

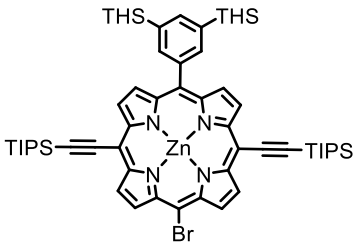

NBS (90 mg, 0.50 mmol) was added to a solution of **P1a[Zn]** (1:1 complex with pyridine, 727 mg, 0.50 mmol) in $CHCl_3$ (25 mL) and pyridine (2.5 mL). The mixture was stirred 14 h at room temperature. The reaction was monitored by TLC (in 4:1 PE 40-60:CH_2Cl_2, starting material is fluorescent while product is not). Additional NBS (34 mg (after 16 h) and further 20 mg (after 18 h), 7 mg (after 20 h) and 2 mg (after 21 h)) was added until the reaction was complete. Solvents were removed *in vacuo* and the residue was purified by column chromatography (4:1 PE 40-60:CH_2Cl_2, + 1% pyridine) yielding **P1b** as a 1:1 complex with pyridine (495 mg, 67%) as a purple solid.

^{1}H NMR (400 MHz, $CDCl_3$, 298 K): δ_H 9.73 (d, *J* = 4.6 Hz, 2H, *β-H*), 9.68 (d, *J* = 4.6 Hz, 2H, *β-H*), 9.63 (d, *J* = 4.6 Hz, 2H, *β-H*), 8.78 (d, *J* = 4.6 Hz, 2H, *β-H*), 8.16 (s, 2H, Ar-H_{ortho}), 7.96 (s, 1H, Ar-H_{para}), 1.51-1.42 (m, 54 H), 1.42-1.33 (m, 12H), 1.33- 1.26 (m, 24H), 0.96-0.89 (m, 12H), 0.89-0.84 (m, 18H).

MALDI-ToF m/z 1454.99 (calculated for $C_{84}H_{131}BrN_4Si_4Zn$: 1454.74).

As lit.[1]

Zinc 5-[3,5-bis(trihexylsilyl)phenyl]-15-bromo-10,20-diethynylporphyrin – P1c

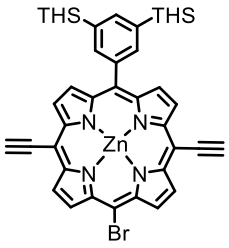

TBAF (1.0 M solution in THF, 0.98 mL, 0.98 mmol) was added to a solution of **P1b** (as a 1:1 complex with pyridine, 150 mg, 0.098 mmol) in CH_2Cl_2 (15 mL) and the reaction was stirred for 20 min before it was passed through a SiO_2 plug ($CHCl_3$/1% pyridine). Solvents were removed *in vacuo* and the material was dried under vacuum for 1 h yielding **P1c** (110 mg, 98%) as a green solid. This was used in the next step without further purification.

^{1}H NMR (400 MHz, $CDCl_3$, 298 K): δ_H 9.72 (d, J = 4.6 Hz, 2H, *β-H*), 9.69 (d, J = 4.6 Hz, 2H, *β-H*), 9.63 (d, J = 4.6 Hz, 2H, *β-H*), 8.83 (d, J = 4.6 Hz, 2H, *β-H*), 8.18 (s, 2H, Ar-H_{ortho}), 7.97 (s, 1H, Ar-H_{para}), 4.17 (s, 2H, C≡C*H*), 1.52-1.42 (m, 12 H), 1.41-1.32 (m, 12H), 1.32- 1.25 (m, 24H), 0.95-0.90 (m, 12H), 0.90-0.82 (m, 18H).

^{13}C NMR (100 MHz, $CDCl_3$, 298 K): δ_C 152.5 (2C), 151.2 (2C), 149.6 (2C), 143.2 (2C), 140.8 (2CH), 140.6 (C), 139.2 (CH), 136.0 (C), 135.0 (2C), 133.4 (2CH), 133.3 (2CH), 132.0 (2CH), 131.3 (2CH), 122.5 (2C), 99.9 (2C), 86.5 (C), 83.7 (2CH), 33.7, 31.8, 24.2, 22.8, 14.3, 12.8.

MALDI-ToF m/z 1141.18 (calculated for $C_{66}H_{91}BrN_4Si_2Zn$: 1140.52).

Zinc 5-[3,5-bis(trihexylsilyl)phenyl]-15-bromo-10,20-bis[(trimethylsilyl)ethynyl]porphyrin – P1d

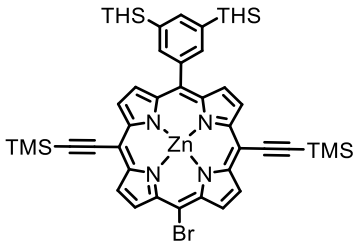

LiHMDS (1.0 M solution in THF, 0.36 mL, 0.36 mmol) was added to a solution of **P1c** (136 mg, 0.12 mmol) under nitrogen atmosphere in THF (20 mL) with vigorous stirring. The reaction was stirred for 10 min before TMS-chloride (66 µL, 0.48 mmol) was added and the reaction was monitored by TLC. After 2 h, a second batch of LiHMDS (0.18 mL, 0.18 mmol)

and TMS-chloride (66 μL, 0.48 mmol) was added and the reaction was stirred for a further 40 min. Upon reaction completion, $CHCl_3$:CH_2Cl_2 1:1 (60 mL) was added. The solution was washed with water and concentrated. Column chromatography (50:1:1 PE 40-60 :EtOAc:pyridine) afforded **P1d** (127 mg, 82%) as a purple solid with green lustre.

^{1}H NMR (400 MHz, $CDCl_3$, 298 K): δ_H 9.67 (d, J = 4.5 Hz, 2H, *β-H*), 9.64 (d, J = 4.6 Hz, 2H, *β-H*), 9.58 (d, J = 4.6 Hz, 2H, *β-H*), 8.80 (d, J = 4.5 Hz, 2H, *β-H*), 8.18 (s, 2H, Ar-H_{ortho}), 7.97 (s, 1H, Ar-H_{para}), 1.52-1.42 (m, 12H), 1.41-1.32 (m, 12H), 1.32-1.25 (m, 24H), 0.95-0.90 (m, 12H), 0.90-0.82 (m, 18H), 0.61 (s, 18H, TMS-*H*).

^{13}C NMR (100 MHz, $CDCl_3$, 298 K): δ_C 152.5 (4C), 151.1 (2C), 149.6 (2C), 140.7 (2CH), 140.6 (C), 139.2 (2C), 134.9 (CH), 133.2 (4CH), 132.1 (2CH), 131.4 (2CH), 124.6 (C), 108.1 (2C), 106.0 (C), 101.5 (2C), 101.3 (2C), 33.7, 31.8, 24.2, 22.8, 14.4, 12.8, 0.5 (6CH_3).

MALDI-ToF m/z 1285.18 (calculated for $C_{72}H_{107}BrN_4Si_4Zn$: 1284.60).

Zinc 5-[3,5-bis(trihexylsilyl)phenyl]-15-[(trihexylsilyl)ethynyl]-10,20-bis[(trimethylsilyl)ethynyl]porphyrin – P1e

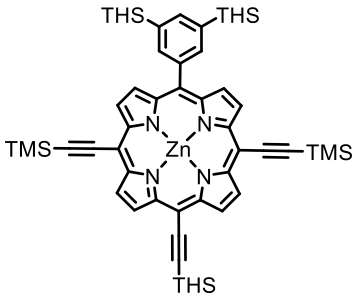

In a 25-mL two-necked flask **P1d** (68 mg, 53 μmol), Pd_2dba_3 (4.8 mg, 5.3 μmol), CuI (1.0 mg, 5.3 μmol) and PPh_3 (2.8 mg, 10.6 μmol) were placed. Toluene (3 mL) and *N,N*-diisopropylamine (1.5 mL) were added and the mixture was deoxygenated by 3 freeze-pump-thaw cycles. THS-acetylene (33 μL, 79 μmol) was added and the reaction mixture was stirred 14 h at room temperature. Solvents were removed *in vacuo* and the residue was purified by column chromatography (10:1 PE 40-60:CH_2Cl_2, + 1% pyridine) affording **P1e** (72 mg, 90%) as a green solid.

^{1}H NMR (400 MHz, $CDCl_3$ + 1% pyridine-d_5, 298 K): δ_H 9.65 (s, 4H, *β-H*), 9.53 (d, J = 4.5 Hz, 2H, *β-H*), 8.75 (d, J = 4.5 Hz, 2H, *β-H*), 8.15 (s, 2H, Ar-H_{ortho}), 7.95 (s, 1H, Ar-H_{para}), 1.85-1.75 (m, 6H), 1.63-1.53 (m, 6H), 1.51-1.39 (m, 24H), 1.39-1.31 (m, 12H), 1.31-1.29 (m, 36H), 1.09-1.01 (m, 9H), 0.98-0.90 (m, 12H), 0.90-0.83 (m, 12H), 0.59 (s, 18H, TMS-*H*).

^{13}C NMR (100 MHz, $CDCl_3$ + 1% pyridine-d_5, 298 K): δ_C 152.8 (2C), 152.3 (2C), 152.2 (2C), 150.3 (2C), 140.6 (2CH), 139.1 (CH), 134.8 (2C), 133.0 (2CH), 131.8 (2CH), 131.6 (2CH), 130.7 (2CH), 125.6 (C), 109.1 (C), 108.1 (2C), 101.5 (2C), 101.1 (2C), 100.8 (C), 99.3 (C), 88.5 (C), 33.7, 33.5, 33.2, 31.9, 31.8, 31.6, 24.5, 24.2, 23.9, 22.9, 22.8, 22.7, 14.4, 14.3, 14.2, 14.0, 13.2, 12.8, 0.4 (6CH3).

MALDI-ToF m/z 1513.57 (calculated for $C_{92}H_{146}N_4Si_5Zn$: 1512.97).

Zinc 5-[3,5-bis(trihexylsilyl)phenyl]-10,20-diethynyl-15-[(trihexylsilyl)ethynyl]porphyrin – P1f

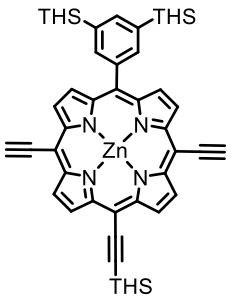

K_2CO_3 (150 mg, 1.08 mmol) was added to a solution of **P1e** (82 mg, 0.054 mmol) in THF (7 mL) and MeOH (7 mL). The suspension was stirred at room temperature for 30 min before it was passed through a SiO_2 plug (1:1 PE 40-60:CH_2Cl_2, + 1% pyridine). Solvents were removed *in vacuo* and the material was dried under high vacuum for 1 h to yield **P1f** (72.8 mg, 98%) as a purple solid with green lustre. This material was used in the next step without further purification.

^{1}H NMR (400 MHz, $CDCl_3$ + 1% pyridine-d_5, 298 K): δ_H 9.68 (dd, J = 4.6 Hz, J = 4.6 Hz, 4H, *β-H*), 9.58 (d, J = 4.6 Hz, 2H, *β-H*), 8.79 (d, J = 4.6 Hz, 2H, *β-H*), 8.17 (s, 2H, Ar-H_{ortho}), 7.96 (s, 1H, Ar-H_{para}), 4.15 (s, 2H, ≡*H*), 1.86-1.75 (m, 6H), 1.63-1.53 (m, 6H), 1.51-1.41 (m, 24H), 1.41-1.32 (m, 12H), 1.32-1.24 (m, 36H), 1.08-1.02 (m, 9H), 0.96-0.82 (m, 24H).

^{13}C NMR (100 MHz, $CDCl_3$ + 1% pyridine-d_5, 298 K): δ_C 153.0 (2C), 152.4 (2C), 152.3 (2C), 150.5 (2C), 140.7 (2CH), 139.2 (CH), 134.9 (2C), 133.2 (2CH), 131.8 (4CH), 130.8 (2CH), 125.6 (C), 109.0 (C), 100.9 (C), 100.3 (2C), 99.5 (C), 88.5 (C/2C), 86.5 (C/2C), 83.6 (2CH), 33.7, 33.5, 33.2, 31.9, 31.7, 31.6, 24.6, 24.2, 23.9, 22.9, 22.8, 22.7, 14.3, 14.2, 14.0 13.4, 13.2, 12.8.

MALDI-ToF m/z 1368.57 (calculated for $C_{86}H_{130}N_4Si_3Zn$: 1368.89).

3.10.2 Synthesis of First-Generation 6-Porphyrin Nanoring

Zinc 5-[3,5-bis(trihexylsilyl)phenyl]-15-bromo-10,20-diethynylporphyrin[6] nanoring-template complex

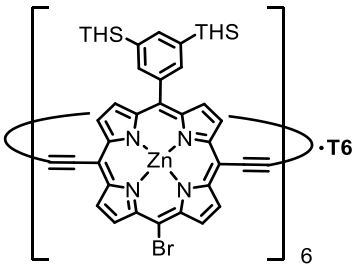

Hexadentate template **T6** (11 mg, 0.011 mmol) and **P1c** (crude from deprotection, ~0.65 mmol) were dissolved in dry $CHCl_3$ (100 mL) and sonicated for 2 h. A catalyst solution was added of $Pd(PPh_3)_2Cl_2$ (30 mg, 0.043 mmol), CuI (25 mg, 0.13 mmol), 1,4-benzoquinone (47 mg, 0.43 mmol) in dry $CHCl_3$ (11 mL) and dry *N,N*-diisopropylamine (0.5 mL) and the reaction was stirred 14 h at room temperature. The reaction mixture was passed through two short Al_2O_3 plugs (the first eluted with $CHCl_3$ and the second with toluene). The material was concentrated, dissolved in THF and the solution was centrifuged for 65 min at 1500 rpm. The solution was decanted, concentrated and then purified by size exclusion chromatography on Biobeads SX-1 (toluene/1% pyridine) to remove the benzoquinone. The crude reaction mixture (39.1 mg) was dried under vacuum for 1 h and used in the next step without further purification.

Zinc 4-[{15-[3,5-bis(trihexylsilyl)phenyl]-10,20-diethynylporphyrin-5-yl}(dimethyl)silyl]butanenitrile[6] nanoring-template complex

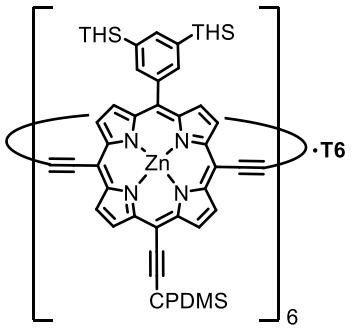

The crude reaction mixture from 6-ring formation (39.1 mg; ~34 μmol) was transferred to a 100 mL two-neck flask and Pd_2dba_3 (6.3 mg, 6.8 μmol), CuI (1.3 mg, 6.8 μmol) and PPh_3 (3.6 mg, 13.7 μmol) were added. Dry toluene (18 mL) and dry *N,N*-diisopropylamine (9 mL) were added and the solution was sonicated for 2 mins. The solution was degassed by 3 freeze pump thaw cycles before CPDMS-acetylene (40 mg, 0.13 mmol) was added. The reaction

was stirred for 3 h before it was slightly concentrated and passed through a short Al_2O_3 plug ($CHCl_3$). The material was concentrated and purified by size exclusion chromatography on Biobeads SX-1 (toluene/1% pyridine). Separation of the reaction products by recycling GPC (toluene/1% pyridine) yielded the product ***c*-P6$^{meso\text{-}CPDMS}$·T6** (4.1 mg, 5% over 3 steps from the monomer starting material) as a red solid.

MALDI-ToF m/z 8264.67 (calculated for $C_{516}H_{654}N_{36}Si_{18}Zn_6$: 8258.39).

3.10.3 Synthesis of Second-Generation 6-Porphyrin Nanoring

Zinc 5-[3,5-bis(trihexylsilyl)phenyl]-15-[(trihexylsilyl)ethynyl]porphyrin[6] nanoring-template complex – *c*-P6$^{meso\text{-}THS}$·T6

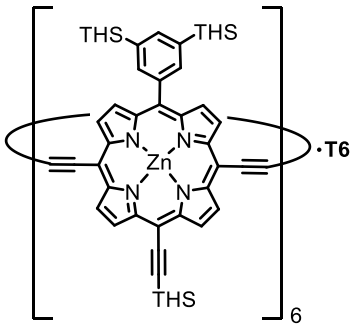

Hexadentate template **T6** (24.5 mg, 24.6 μmol) and **P1f** (112 mg, 82 μmol) were dissolved in dry $CHCl_3$ (51 mL) and sonicated for 20 mins. The solution was concentrated and the residue re-dissolved in dry toluene (46 mL) and *N,N*-diisopropylamine (23 mL). The solution was heated to 65 °C and subsequently a catalyst mixture was added of $Pd(PPh_3)_2Cl_2$ (11.5 mg, 16.4 μmol), CuI (15.6 mg, 81.9 μmol), and 1,4-benzoquinone (17.7 mg, 0.16 mmol) in dry toluene (6.8 mL) and dry *N,N*-diisopropylamine (3.3 mL). Heating was continued for 2.5 h, after which the reaction mixture was allowed to cool to room temperature, before it was passed through a SiO_2 plug eluted with toluene. After removal of the solvents *in vacuo*, the residue was passed through a second SiO_2 plug eluted with CH_2Cl_2. The material was further purified by size-exclusion chromatography (BioBeads SX-1, toluene/1% pyridine) and finally subjected to recycling GPC (toluene/1 % pyridine) to yield ***c*-P6$^{meso\text{-}THS}$·T6** (12.3 mg, 10%) as a red solid.

MALDI-ToF m/z 9210.14 (calculated for $C_{588}H_{816}N_{30}Si_{18}Zn_6$: 9202.65).

UV-vis-NIR ($CHCl_3$) λ_{max} (log ε): 497 (5.57), 760 (5.31), 796 (5.47), 836 (5.47).

Zinc 5-[3,5-bis(trihexylsilyl)phenyl]-15-[(trihexylsilyl)ethynyl]porphyrin[6] nanoring – *c*-P6*meso*-THS

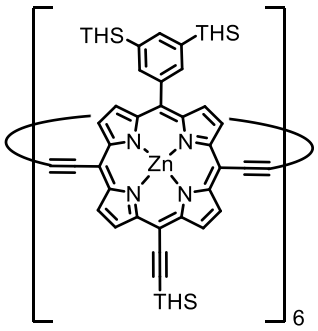

***c*-P6*meso*-THS•T6** (3.3 mg, 0.36 μmol) was dissolved in 0.5 mL of a 40 mg/mL DABCO in toluene solution. A size exclusion column (Biobeads SX-1) was loaded with ~10 mL of the same solvent system. The porphyrin solution was loaded onto the size exclusion column and eluted with another ~4 mL of the DABCO/toluene solution and further eluted with toluene/1% pyridine. Solvents were removed *in vacuo* and the material was passed over a second size exclusion column in toluene/40% pyridine to replace coordinating DABCO with pyridine. Solvents were removed *in vacuo* to yield ***c*-P6*meso*-THS** (2.6 mg, 89%) as a chestnut solid.

^{1}H NMR (400 MHz, $CDCl_3$ + 1% pyridine-d_5, 298K): δ_H 9.63 (d, *J* = 4.5 Hz, 12H, *β-H*), 9.56 (d, *J* = 4.5 Hz, 12H, *β-H*), 9.52 (d, *J* = 4.5 Hz, 12H, *β-H*), 8.67 (d, *J* = 4.5 Hz, 12H, *β-H*), 8.08 (s, 12H, -Ar*H*ortho), 7.93 (s, 6H, -Ar*H*para), 1.81-1.72 (m, 36H), 1.59-1.50 (m, 36H), 1.48-1.36 (m, 144H), 1.36-1.27 (m, 72H), 1.27-1.19 (m, 216H), 1.05-0.98 (m, 54H), 0.94-0.84 (m, 72H), 0.84-0.78 (m, 72H).

MALDI-ToF m/z 8211.17 (calculated for $C_{516}H_{768}N_{24}Si_{18}Zn_6$: 8205.25).

UV-vis-NIR ($CHCl_3$ + 1% pyridine) λ_{max} (log ε): 497 (5.70), 607 (4.67), 765 (5.45).

Zinc 5-[3,5-bis(trihexylsilyl)phenyl]-15-ethynylporphyrin[6] nanoring – *c*-P6*meso*-acetylene

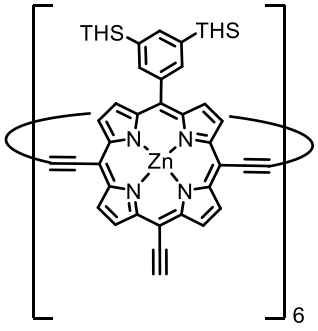

TBAF (1.0 M solution in THF, 33 µL, 33 µmol) was added to a solution of ***c*-P6$^{meso\text{-}THS}$** (9.1 mg, 1.1 µmol) in toluene (7 mL) and pyridine (0.7 mL). The reaction was stirred at room temperature for 20 min and then passed through a short SiO_2 plug eluted with toluene/40% pyridine yielding ***c*-P6$^{meso\text{-}acetylene}$** as a red solid. The material was used in the next step without further purification.

^{1}H NMR (400 MHz, $CDCl_3$ + 1% pyridine-d_5, 298K): δ_H 9.67 (d, *J* = 4.5 Hz, 12H, *β-H*), 9.58 (d, *J* = 4.5 Hz, 12H, *β-H*), 9.55 (d, *J* = 4.5 Hz, 12H, *β-H*), 8.71 (d, *J* = 4.5 Hz, 12H, *β-H*), 8.09 (s, 12H, -Ar*H*ortho), 7.94 (s, 6H, -Ar*H*para), 4.12 (s, 6H, ≡*H*), 1.48-1.38 (m, 72H), 1.38-1.20 (m, 216H), 0.92-0.79 (m, 108H), 0.62-0.55 (m, 72H).

MALDI-ToF m/z 6506.97 (calculated for $C_{408}H_{540}N_{24}Si_{12}Zn_6$: 6509.6).

3.10.4 Synthesis of ***t*-P12** *and* ***t*-P12·(T6)$_2$** *via Ring-Stacking*

Zinc 5-[3,5-bis(trihexylsilyl)phenyl]-15-ethynylporphyrin[12] nanotube – *t*-P12

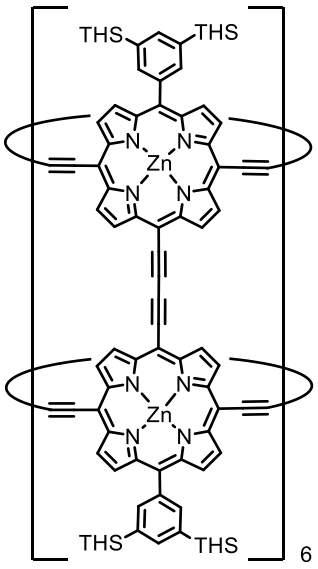

A catalyst mixture of $Pd(PPh_3)_2Cl_2$ (3.5 mg, 5.1 µmol), CuI (4.8 mg, 25.3 µmol) and 1,4-benzoquinone (5.5 mg, 50.6 µmol) in toluene (1.5 mL) and *N,N*-diisopropylamine (0.4 mL) was added to a solution of ***c*-P6$^{meso\text{-}acetylene}$** (crude material from deprotection of ***c*-P6$^{meso\text{-}THS}$**, assumed amount 1.1 µmol) in toluene (22 mL) and pyridine (2.6 mL). The reaction was stirred at room temperature and progress was monitored by UV-vis-NIR spectroscopy. Freshly prepared catalyst mixture (as above) was added after 2 h, 4.5 h and 18 h. After 24 h, the reaction mixture was passed through a short Al_2O_3 plug eluted with toluene/5% pyridine. The material was further purified by size-exclusion chromatography

(BioBeads SX-1, THF/1% pyridine) and finally subjected to recycling GPC (THF/1% pyridine) to yield ***t*-P12** (0.71 mg, 10%) as a pink solid.

^{1}H NMR (400 MHz, $CDCl_3$ + 1% pyridine-d_5, 298 K): δ_H 10.03 (d, J = 4.5 Hz, 24H, *β-H*), 10.01 (d, J = 4.5 Hz, 24H, *β-H*), 9.48 (d, J = 4.3 Hz, 24H, *β-H*), 8.66 (d, J = 4.3 Hz, 24H, *β-H*), 8.28 (s, 12H, Ar-H_{para}), 7.07 (s, 24H, Ar-H_{ortho}), 1.53–1.41 (m, 144H), 1.41–1.28 (m, 144H), 1.28–1.21 (m, 288H), 0.96–0.85 (m, 216H), 0.83–0.76 (m, 144H).

MALDI-ToF m/z 13023(calculated for $C_{816}H_{1068}N_{48}Si_{24}Zn_{12}$: 13008).

UV-vis-NIR ($CHCl_3$ + 1% pyridine) λ_{max} (log ε): 528 (6.00), 755 (5.61), 822 (5.70), 847 (5.67).

Zinc 5-[3,5-bis(trihexylsilyl)phenyl]-15-ethynylporphyrin[12] nanotube-templates complex – *t*-P12·(T6)$_2$

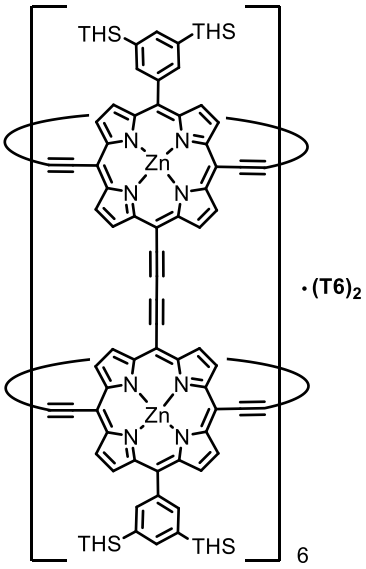

Hexadentate template **T6** (0.2 mg, 0.2 μmol) was added to a solution of ***t*-P12** (0.71 mg, 0.055 μmol) in $CHCl_3$ (0.6 mL). The solution was stirred for 1 h and purified by size-exclusion chromatography (BioBeads SX-1, toluene/1% pyridine) to yield ***t*-P12·(T6)$_2$** (0.82 mg, 0.055 μmol, 100%) as a pink solid.

^{1}H NMR (400 MHz, $CDCl_3$, 298 K): δ_H 10.03 (d, J = 4.3 Hz, 24H, *β-H*), 9.98 (d, J = 4.3 Hz, 24H, *β-H*), 9.46 (d, J = 4.3 Hz, 24H, *β-H*), 8.69 (d, J = 4.3 Hz, 24H, *β-H*), 8.29 (s, 12H, Ar-H_{para}), 8.04 (s, 12H, Ar-H_{ortho}), 8.01 (s, 12H, Ar-H_{ortho}), 5.66– 5.53 (m, 48H), 5.19 (d, J = 6.6 Hz, 24H), 2.72 (d, J = 6.6 Hz, 24H), 1.58–1.44 (m, 144H), 1.44–1.37 (m, 144H), 1.37–1.26 (m, 288H), 1.00–0.89 (m, 216H), 0.89–0.82 (m, 144H).

MALDI-ToF m/z 15012 (calculated for $C_{960}H_{1164}N_{60}Si_{24}Zn_{12}$: 15003).

As lit.[1]

3.10.5 Improved Procedure for the Synthesis of ***t*-P12·(T6)$_2$** *and Synthetic Procedure for* ***t*-P12** *by Template Knock-Out*

***l*-P2$_{THS}$[TIPS]$_4$** was obtained as a side-product in the synthesis of a linear porphyrin trimer (see Chapter 5).

Zinc 5-[3,5-bis(trihexylsilyl)phenyl]-15-ethynylporphyrin dimer – *l*-P2$_{THS}$

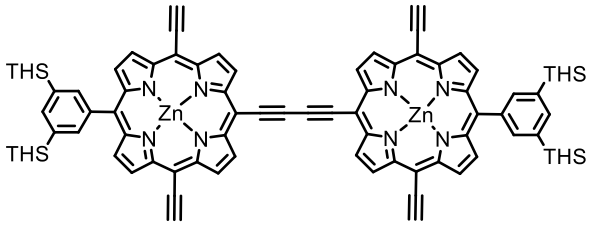

TBAF (1.0 M solution in THF, 1.13 mL, 1.13 mmol) was added to a solution of ***l*-P2$_{THS}$[TIPS]$_4$** (159 mg, 0.057 mmol) in CH_2Cl_2 (35 mL) and pyridine (0.5 mL). The solution was stirred at room temperature for 30 min and then passed through a short SiO_2 plug (CH_2Cl_2+1% pyridine). Solvents were removed *in vacuo* to yield ***l*-P2$_{THS}$** (124 mg, 100%) as a green solid.

^{1}H NMR (400 MHz, $CDCl_3$ + 1% pyridine-d$_5$, 298 K): δ_H 9.96 (d, *J*= 4.7 Hz, 4H, *β-H*), 9.81 (d, *J*=4.7 Hz, 4H, *β-H*), 9.63 (d, J= 4.6 Hz, 4H, *β-H*), 8.84 (d, *J*= 4.6 Hz, 4H, *β-H*), 8.23 (s, 4H, Ar-H_{ortho}), 8.01 (s, 2H, Ar-H_{para}), 4.20 (s, 4H, C≡*H*), 1.55–1.45 (m, 24H), 1.44–1.35 (m, 24H), 1.35–1.26 (m, 48H), 0.98–0.92 (m, 24H), 0.92–0.85 (m, 36H).

MALDI-ToF m/z 2170.22 (calculated for $C_{136}H_{182}N_8Si_4Zn_2$: 2171.22).

As lit.[1]

Zinc 5-[3,5-bis(trihexylsilyl)phenyl]-15-ethynylporphyrin[12] nanotube-templates complex – *t*-P12·(T6)$_2$

***l*-P2$_{THS}$** (124 mg, 0.057 mmol) was dissolved in $CHCl_3$ (45 mL) and hexadentate template **T6** (85.2 mg, 0.085 mmol) was added. The solution was stirred for 10 min after which UV-vis-NIR spectroscopy confirmed formation of the complex. The solution was concentrated and the residue re-dissolved in dry toluene (55 mL). The solution was heated to 45 °C and subsequently a catalyst mixture of $Pd(PPh_3)_2Cl_2$ (8.0 mg, 0.014 mmol), CuI (10.8 mg, 0.057 mmol) and 1,4-benzoquinone (12.3 mg, 0.11 mmol) in toluene (3 mL) and *N,N*-diisopropylamine (1 mL) was added. Heating was continued for 2 h (after 1 h, half an

equivalent of freshly prepared catalyst mixture was added). The reaction was allowed to cool down to room temperature, before it was passed through a SiO_2 plug and eluted with CH_2Cl_2. The material was further purified by size-exclusion chromatography (BioBeads SX-1, toluene/1% pyridine) and finally subjected to recycling GPC (toluene/1% pyridine) to yield ***t*-P12·(T6)$_2$** (44.5 mg, 3 μmol, 31%) as a pink solid.

^{1}H NMR and **MALDI-ToF m/z** as above.

Zinc 5-[3,5-bis(trihexylsilyl)phenyl]-15-ethynylporphyrin[12] nanotube – *t*-P12

A solution of freshly recrystallised DABCO in toluene (200 mg/mL) was prepared. A size exclusion column (BioBeads SX-1, toluene/1% pyridine) was eluted with ~15 mL DABCO solution such that the top of the column was saturated with DABCO. ***t*-P12·(T6)$_2$** was dissolved in 0.5 mL DABCO solution and loaded onto the size exclusion column. The column was eluted with ~5 mL DABCO solution and subsequently with toluene/1% pyridine. The collected material was diluted to ~30 mL in toluene and washed with a saturated potassium hydrogen phthalate solution (25 mL, 4x) and with water (25 mL, 4x). The toluene fraction was dried over $MgSO_4$ and concentrated. The material was purified on a short SiO_2 plug in $CHCl_3$/5% pyridine to yield ***t*-P12** (3.8 mg, 0.29 μmol, 86%) as a pink solid.

^{1}H NMR and **MALDI-ToF m/z** as above.

3.10.6 Synthesis of Free-Base Porphyrin Nanotube ***t*-P12[2H]**

5-[3,5-bis(trihexylsilyl)phenyl]-15-ethynylporphyrin[12] nanotube – *t*-P12[2H]

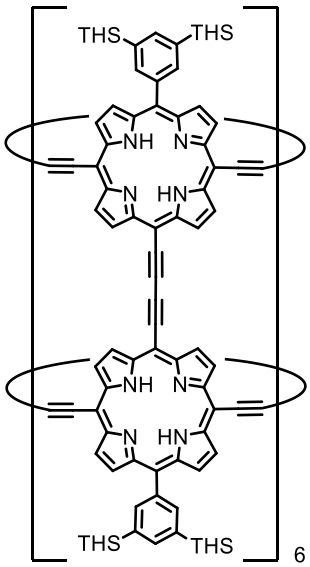

Trifluoroacetic acid (0.13 mL, 1.7 mmol) was added dropwise to a solution of ***t*-P12[Zn]** (3.4 mg, 0.26 μmol) in CH_2Cl_2 (4 mL), under magnetic stirring. The reaction was monitored by UV-vis-NIR spectroscopy. Upon completion (5 min), the reaction was quenched by the addition of pyridine (2 mL) and immediately passed through a SiO_2 plug ($CHCl_3$). Solvents were removed *in vacuo* to afford ***t*-P12[2H]** (1.2 mg, 37%) as a purple/brown solid.

^{1}H NMR (400 MHz, $CDCl_3$, 298 K): δ_H 10.00 (m, 48H, *β-H*), 9.48 (d, *J* = 4.3 Hz, 24H, *β-H*), 9.46 (d, *J* = 4.3 Hz, 24H, *β-H*), 8.67 (d, *J* = 4.3 Hz, 24H, *β-H*), 8.33 (s, 12H, Ar-H_{para}), 8.01 (s, 12H, Ar-H_{ortho}), 7.99 (s, 12H, Ar-H_{ortho}), 1.52–1.42 (m, 144H), 1.42–1.30 (m, 144H), 1.30–1.20 (m, 288H), 0.99–0.86 (m, 216H), 0.86–0.78 (m, 144H), –0.63 (s, 24H, N*H*).

MALDI-ToF m/z 12266.53 (calculated for $C_{816}H_{1092}N_{48}Si_{24}$: 12247.16).

UV-vis-NIR (toluene) λ_{max} (log ε): 512 (6.11), 684 (5.68), 764 (5.75), 802 (5.88), 837 (5.95).

3.11 References

(1) P. Neuhaus, A. Cnossen, J. Q. Gong, L. M. Herz, H. L. Anderson. 'A Molecular Nanotube with Three-Dimensional π-Conjugation'. *Angew. Chem. Int. Ed.*, **2015**, *54*, 7344 –7348.

(2) M. Hoffmann, C. J. Wilson, B. Odell, H. L. Anderson. 'Template-Directed Synthesis of a π-Conjugated Porphyrin Nanoring'. *Angew. Chem. Int. Ed.*, **2007**, *46*, 3122–3125.

(3) M. C. O'Sullivan, J. K. Sprafke, D. V Kondratuk, C. Rinfray, T. D. W. Claridge, A. Saywell, M. O. Blunt, J. N. O'Shea, P. H. Beton, M. Malfois, H. L. Anderson. 'Vernier Templating and Synthesis of a 12-Porphyrin Nano-Ring'. *Nature*, **2011**, *469*, 72–75.

(4) D. V. Kondratuk, L. M. A. Perdigão, A. M. S. Esmail, J. N. O'Shea, P. H. Beton, H. L. Anderson. 'Supramolecular Nesting of Cyclic Polymers'. *Nat. Chem.*, **2015**, *7*, 317–322.

(5) S. Liu, D. V. Kondratuk, S. A. L. Rousseaux, G. Gil-Ramírez, M. C. O'Sullivan, J. Cremers, T. D. W. Claridge, H. L. Anderson. 'Caterpillar Track Complexes in Template-Directed Synthesis and Correlated Molecular Motion'. *Angew. Chem. Int. Ed.*, **2015**, *54*, 5355–5359.

(6) S. A. L. Rousseaux, J. Q. Gong, R. Haver, B. Odell, T. D. W. Claridge, L. M. Herz, H. L. Anderson. 'Self-Assembly of Russian Doll Concentric Porphyrin Nanorings'. *J. Am. Chem. Soc.*, **2015**, *137*, 12713–12718.

(7) J. Song, N. Aratani, H. Shinokubo, A. Osuka. 'A Porphyrin Nanobarrel That Encapsulates C_{60}'. *J. Am. Chem. Soc.*, **2010**, *132*, 16356–16357.

(8) R. Chapman, M. Danial, M. L. Koh, K. A. Jolliffe, S. Perrier. 'Design and Properties of Functional Nanotubes from the Self-Assembly of Cyclic Peptide Templates'. *Chem. Soc. Rev.*, **2012**, *41*, 6023–6041.

(9) M. R. Ghadiri, J. R. Granja, R. A. Milligan, D. E. McRee, N. Khazanovich. 'Self-Assembling Organic Nanotubes Based on a Cyclic Peptide Architecture'. *Nature*, **1993**, *366*, 324–327.

(10) A. Fuertes, M. Juanes, J. R. Granja, J. Montenegro. 'Supramolecular Functional Assemblies: Dynamic Membrane Transporters and Peptide Nanotubular Composites'. *Chem. Comm.*, **2017**, *53*, 7861–7871.

(11) H. Lin, J. Fan, P. Weng, X. Si, X. Zhao. 'Molecular Dynamics Simulations on the Behaviors of Hydrophilic/Hydrophobic Cyclic Peptide Nanotubes at the Water/Hexane Interface'. *J. Phys. Chem. A*, **2017**, *121*, 6863–6873.

(12) I. W. Hamley. 'Peptide Nanotubes'. *Angew. Chem. Int. Ed.*, **2014**, *53*, 6866–6881.

(13) D. Gauthier, P. Baillargeon, M. Drouin, Y. L. Dory. 'Self-Assembly of Cyclic Peptides into Nanotubes and Then into Highly Anisotropic Crystalline Materials'. *Angew. Chem. Int. Ed.*, **2001**, *40*, 4635–4638.

(14) Q. Ji, H. T. M. Le, X. Wang, Y. S. Chen, T. Makarenko, A. J. Jacobson, O. Miljanic. 'Cyclotetrabenzoin: Facile Synthesis of a Shape-Persistent Molecular Square and Its Assembly into Hydrogen-Bonded Nanotubes'. *Chem. - Eur. J.*, **2015**, *21*, 17205–17209.

(15) Z. Liu, G. Liu, Y. Wu, D. Cao, J. Sun, S. T. Schneebeli, M. S. Nassar, C. A. Mirkin, J. F. Stoddart. 'Assembly of Supramolecular Nanotubes from Molecular Triangles and 1,2-Dihalohydrocarbons'. *J. Am. Chem. Soc.*, **2014**, *136*, 16651–16660.

(16) G. D. Pantoş, P. Pengo, J. K. M. Sanders. 'Hydrogen-Bonded Helical Organic Nanotubes'. *Angew. Chem. Int. Ed.*, **2007**, *46*, 194–197.

(17) Y. Zhong, Q. Wang, Y. Yang, Z. Lu, L. He, B. Gong. 'Hexakis(m-Phenylene Ethynylene) Macrocycles with Multiple H-Bonding Side Chains and Modified Cavities: Altered Stacking Strength and Persistent Tubular Assembly'. *Org. Lett.*, **2016**, *18*, 2094–2097.

(18) X. Wu, R. Liu, B. Sathyamoorthy, K. Yamato, G. Liang, L. Shen, S. Ma, D. K. Sukumaran, T. Szyperski, W. Fang, L. He, X. Chen, B. Gong. 'Discrete Stacking of Aromatic Oligoamide Macrocycles'. *J. Am. Chem. Soc.*, **2015**, *137*, 5879–5882.

(19) H. Nobukuni, Y. Shimazaki, F. Tani, Y. Naruta. 'A Nanotube of Cyclic Porphyrin Dimers Connected by Nonclassical Hydrogen Bonds and Its Inclusion of C_{60} in a Linear Arrangement'. *Angew. Chem. Int. Ed.*, **2007**, *46*, 8975–8978.

(20) D. Xiao, D. Zhang, B. Chen, D. Xie, Y. Xiang, X. Li, W. Jin. 'Size-Selective Recognition by a Tubular Assembly of Phenylene-Pyrimidinylene Alternated Macrocycle through Hydrogen-Bonding Interactions'. *Langmuir*, **2015**, *31*, 10649–10655.

(21) A. Bauza, A. Frontera. 'Supramolecular Nanotubes Based on Halogen Bonding Interactions: Cooperativity and Interaction with Small Guests'. *Phys. Chem. Chem. Phys.*, **2017**, *19*, 12936–12941.

(22) T. Fukino, H. Joo, Y. Hisada, M. Obana, H. Yamagishi, T. Hikima, M. Takata, N. Fujita, T. Aida. 'Manipulation of Discrete Nanostructures by Selective Modulation of Noncovalent Forces'. *Science*, **2014**, *344*, 499–504.

(23) G. L. Zhang, L. P. Zhou, D. Q. Yuan, Q. F. Sun. 'Bottom-Up Construction of Mesoporous Nanotubes from 78-Component Self-Assembled Nanobarrels'. *Angew. Chem. Int. Ed.*, **2015**, *54*, 9844–9848.

(24) Y. Xu, M. D. Smith, M. F. Geer, P. J. Pellechia, J. C. Brown, A. C. Wibowo, L. S. Shimizu. 'Thermal Reaction of a Columnar Assembled Diacetylene Macrocycle'. *J. Am. Chem. Soc.*, **2010**, *132*, 5334–5335.

(25) T. J. Hsu, F. W. Fowler, J. W. Lauher. 'Preparation and Structure of a Tubular Addition Polymer: A True Synthetic Nanotube'. *J. Am. Chem. Soc.*, **2012**, *134*, 142–145.

(26) J. M. Heo, Y. Kim, S. Han, J. F. Joung, S. hwa Lee, S. Han, J. Noh, J. Kim, S. Park, H. Lee, Y. M. Choi, Y. S. Jung, J. M. Kim. 'Chromogenic Tubular Polydiacetylenes from Topochemical Polymerization of Self-Assembled Macrocyclic Diacetylenes'. *Macromolecules*, **2017**, *50*, 900–913.

(27) S. Rondeau-Gagné, J. R. Néabo, M. Desroches, I. Levesque, M. Daigle, K. Cantin, J.-F. Morin. 'Rigid Organic Nanotubes Obtained from Phenylene-Butadiynylene Macrocycles'. *Chem. Comm.*, **2013**, *49*, 9546–9548.

(28) S. Rondeau-Gagné, J. R. Néabo, M. Desroches, J. Larouche, J. Brisson, J. F. Morin. 'Topochemical Polymerization of Phenylacetylene Macrocycles: A New Strategy for the Preparation of Organic Nanorods'. *J. Am. Chem. Soc.*, **2013**, *135*, 110–113.

(29) J. K. Sprafke, D. V. Kondratuk, M. Wykes, A. L. Thompson, M. Hoffmann, R. Drevinskas, W. H. Chen, C. K. Yong, J. Kärnbratt, J. E. Bullock, M. Malfois, M. R. Wasielewski, B. Albinsson, L. M. Herz, D. Zigmantas, D. Beljonne, H. L. Anderson. 'Belt-Shaped π-Systems: Relating Geometry to Electronic Structure in a Six-Porphyrin Nanoring'. *J. Am. Chem. Soc.*, **2011**, *133*, 17262–17273.

(30) D. V. Kondratuk, L. M. A. Perdigao, M. C. O'Sullivan, S. Svatek, G. Smith, J. N. O'Shea,

P. H. Beton, H. L. Anderson. 'Two Vernier-Templated Routes to a 24-Porphyrin Nanoring'. *Angew. Chem. Int. Ed.*, **2012**, *51*, 6696–6699.

(31) P. Liu, P. Neuhaus, D. V. Kondratuk, T. S. Balaban, H. L. Anderson. 'Cyclodextrin-Templated Porphyrin Nanorings'. *Angew. Chem. Int. Ed.*, **2014**, *53*, 7770–7773.

(32) M. Hoffmann. 'Nanosized Porphyrin Molecular Wires and Rings: Synthesis, Thermodynamics of Self-Assembly and Optoelectronic Properties', DPhil Thesis, University of Oxford, **2008**.

(33) J. K. Sprafke. 'Supramolecular Control of Synthesis and Electronic Structure of Porphyrin Oligomers', DPhil Thesis, University of Oxford, **2011**.

(34) C.-K. Yong, P. Parkinson, D. V. Kondratuk, W.-H. Chen, A. Stannard, A. Summerfield, J. K. Sprafke, M. C. O'Sullivan, P. H. Beton, H. L. Anderson, L. M. Herz. 'Ultrafast Delocalization of Excitation in Synthetic Light-Harvesting Nanorings'. *Chem. Sci.*, **2015**, *6*, 181–189.

(35) M. Hoffmann, J. Kärnbratt, M. H. Chang, L. M. Herz, B. Albinsson, H. L. Anderson. 'Enhanced π Conjugation Around a Porphyrin[6] Nanoring'. *Angew. Chem. Int. Ed.*, **2008**, *47*, 4993–4996.

(36) M. Rickhaus, A. Vargas Jentzsch, L. Tejerina, I. Gruebner, M. Jirasek, T. D. W. Claridge, H. L. Anderson. 'Single-Acetylene Linked Porphyrin Nanorings'. *J. Am. Chem. Soc.*, **2017**, *139*, 16502–16505.

(37) K.-T. Youm, S. T. Nguyen, J. T. Hupp. 'Hollow Porphyrin Prisms: Modular Formation of Permanent, Torsionally Rigid Nanostructures via Templated Olefin Metathesis'. *Chem. Comm.*, **2008**, 3375–3377.

(38) J. Cremers, S. Richert, D. V. Kondratuk, T. D. W. Claridge, C. R. Timmel, H. L. Anderson. 'Nanorings with Copper(II) and Zinc(II) Centers: Forcing Copper Porphyrins to Bind Axial Ligands in Heterometallated Oligomers'. *Chem. Sci.*, **2016**, *7*, 6961–6968.

(39) B. J. Littler, M. A. Miller, C.-H. Hung, R. W. Wagner, D. F. O'Shea, P. D. Boyle, J. S. Lindsey. 'Refined Synthesis of 5-Subsituted Dipyrromethanes'. *J. Org. Chem.*, **1999**, *64*, 1391–1396.

(40) N. Kerisit, L. Toupet, P. Larini, L. Perrin, J. C. Guillemin, Y. Trolez. 'Straightforward Synthesis of 5-Bromopenta-2,4-Diynenitrile and Its Reactivity Towards Terminal Alkynes: A Direct Access to Diene and Benzofulvene Scaffolds'. *Chem. - Eur. J.*, **2015**, *21*, 6042–6047.

(41) S. G. Wilson, H. L. Anderson. 'A Conjugated Triple Strand Porphyrin Array'. *Chem. Comm.*, **1999**, *1*, 1539–1540.

(42) T. E. O. Screen, K. B. Lawton, G. S. Wilson, N. Dolney, R. Ispasoiu, T. Goodson III, S. J. Martin, D. D. C. Bradley, H. L. Anderson. 'Synthesis and Third Order Nonlinear Optics of a New Soluble Conjugated Porphyrin Polymer'. *J. Mater. Chem.*, **2001**, *11*, 312–320.

(43) F. C. Grozema, C. Houarner-Rassin, P. Prins, L. D. A. Siebbeles, H. L. Anderson. 'Supramolecular Control of Charge Transport in Molecular Wires.'. *J. Am. Chem. Soc.*, **2007**, *129*, 13370–13371.

(44) H. Jia, Z. Sun, D. Jiang, P. Du. 'Covalent Cobalt Porphyrin Framework on Multiwalled Carbon Nanotubes for Efficient Water Oxidation at Low Overpotential'. *Chem. Mater.*, **2015**, *27*, 4586–4593.

4

Encapsulation of Fullerenes in a 12-Porphyrin Nanotube

4.1 Abstract

This chapter describes the host-guest chemistry of a 12-porphyrin nanotube. C_{60} and C_{70} fullerenes were successfully encapsulated in the cavity of the nanotube, trapped by the porphyrin "walls" and the **T6** templates that act as the "lids" of this molecular box. Encapsulation was confirmed by MALDI-ToF spectrometry and HPLC analysis. The latter showed the release of C_{60} from the porphyrin nanotube cavity after the **T6** templates had been removed *via* the addition of a competing ligand. In the C_{60}-nanotube complex, **$(C_{60})_n \subset$[*t*-P12·$(T6)_2$]**, fluorescence of the nanotube was quenched, indicative of electron transfer from the nanotube receptor to the fullerene guest. When encapsulation was performed from an equimolar solution of C_{60} and C_{70}, dominant encapsulation of C_{70} was observed.

4.2 Introduction

4.2.1 Carbon Peapods

The entrapment of fullerenes within carbon nanotubes has been studied extensively. The first carbon peapod of a linear array of C_{60} molecules encapsulated in a single-walled carbon nanotube (SWNT) was reported in 1998.[1] The complex was serendipitously discovered by high-resolution transmission electron microscopy (HRTEM) on purified nanotube material that had been synthesised by pulsed laser vaporisation (Figure 4.1).[2]

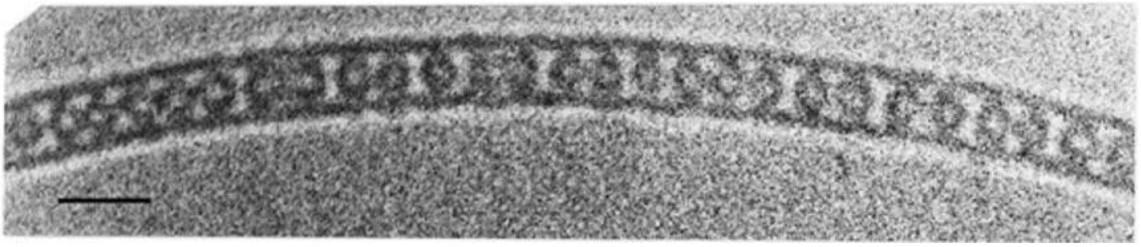

Figure 4.1: HRTEM micrograph of a 1.4 nm diameter SWCNTs that contains a self-assembled chain of C_{60} molecules; Scale bar 2 nm. Reprinted with permission from ref. 2. Copyright 1999 Elsevier Science.

Since this first report, multiple controlled methods to encapsulate (endo)fullerenes in SWNTs have been developed. The most common preparation method involves vacuum-annealing where end-opened SWNTs are heated together with fullerenes.[3] C_{60} encapsulation yields of up to 90% have been achieved with this method.[4]

The encapsulation of C_{60} in SWNTs affects the mechanical and electronic properties of the CNTs. For example; filling carbon nanotubes with fullerenes can increase their mechanical stiffness.[5] Furthermore, fullerene encapsulation can alter the optical bandgap,[6,7] which makes SWNTs peapods interesting structures as molecular wires and sensors. Encapsulation of C_{60} in SWNTs is also thought to lower the activation barrier for the polymerisation of C_{60} and peapods have been observed consisting of C_{60} *n*-mers (dimer, trimer, …, polymer).[3,8,9]

Studies on the encapsulation of fullerenes in SWNTs have not been limited to the inclusion of C_{60}. The inclusion of endofullerenes,[10] such as $N@C_{60}$ and $N@C_{70}$,[11–13] and metallofullerenes, such as $Sc@C_{82}$, $La@C_{82}$, and $Gd@C_{82}$, have sparked wide interest.[14–18] Metallofullerene peapods can act as a starting material for the fabrication of metal nanowires *via* high-vacuum high-temperature treatment. The nanowires are stabilised by the presence of the surrounding carbon walls, rendering them interesting materials for electronic nanodevices.[19,20]

4.2.2 Porphyrin-Fullerene Host-Guest Complexes

Evidence of the attraction between porphyrins and C_{60} was first provided in 1997,[21] and in the two decades since, many supramolecular porphyrin-fullerene inclusion complexes have been reported.[22–25] Most commonly, fullerene encapsulation is achieved through the strong π-π interaction of a porphyrin dimer or trimer with the fullerene.[26–31]

An example of such a complex was reported by Hernández-Eguía and co-workers in 2011. They examined the complexation of endofullerene $Sc_3N@C_{80}$ with cyclic zinc porphyrin dimers and confirmed the existence of strong π-π interactions between the fullerene and the porphyrin dimer *via* UV-vis and fluorescence titration experiments.[32]

Another example describes the allosteric cooperativity upon the binding of C_{60} fullerene to a dendritic porphyrin receptor with three rotational axes. Binding of the first fullerene to the porphyrin receptor suppresses the rotational freedom of the remaining porphyrin "tweezers" (Figure 4.2). This domino-effect accounts for the binding of three equivalents of C_{60} in a cooperative allosteric manner with high affinity for the C_{60} host molecule as was shown *via* UV-vis and ^{1}H NMR spectroscopy studies.[33]

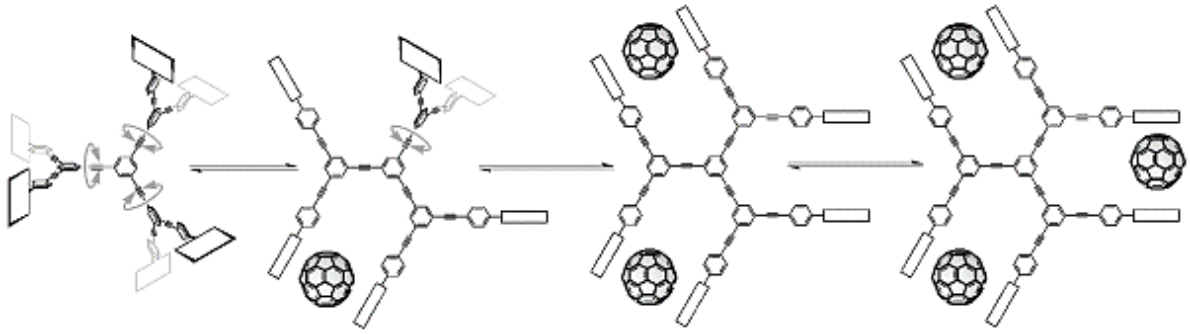

Figure 4.2: Rotational axes of a dendritic porphyrin receptor. When two porphyrins sandwich one C_{60} molecule, the complexation site successively suppresses the rotational freedom of the remaining porphyrin "tweezers". Reprinted with permission from ref. 33. Copyright 2002 John Wiley and Sons.

In the literature there are numerous examples on fullerene inclusion in (supramolecular) porphyrin nanotubes and porphyrin barrels.[34] A porphyrin-based supramolecular peapod was reported in 2007 by Nobukuni and co-workers. Cyclic porphyrin dimers that form nanotubular assemblies *via* C-H···N hydrogen-bonding and weak π-π interactions can host C_{60} molecules, as was observed *via* UV-vis absorption spectroscopy. X-ray crystallography showed a linear arrangement of the fullerene hosts (Figure 4.3).[35] Flash-photolysis time-resolved microwave conductivity (FP-TRMC) measurements on the inclusion complex showed an anisotropic high electron mobility along the crystallographic *b* axis (the linear array of C_{60} molecules).[36]

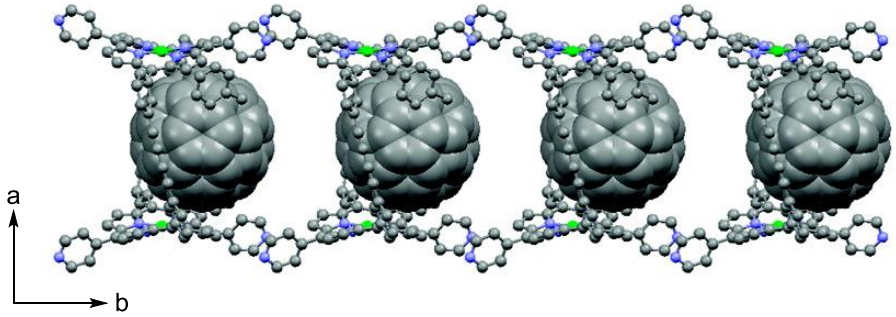

Figure 4.3: Crystal structure of the tubular assembly of nickel-porphyrin dimer and C_{60}, including the crystallographic axes. Hydrogen atoms are omitted for clarity. Reprinted with permission from ref. 36. Copyright 2009 American Chemical Society.

Furthermore, there are several reported studies in which fullerenes act as templates in the formation of covalent porphyrin nanostructures or supramolecular porphyrin assemblies. An example of the former was reported by Mulholland and co-workers in 2011. In the presence of C_{60} (or C_{70}), a covalently linked cyclic porphyrin trimer was formed from

a porphyrin monomer pre-cursor in 60% yield, using olefin metathesis. In the absence of the fullerene template, the major product is the cyclic dimer.[37]

An example of a non-covalent porphyrin-fullerene assembly, a porphyrin-based supramolecular peapod, was reported by Yamaguchi and co-workers.[38] In this study C_{60} pre-organises a porphyrin dimer for supramolecular assembly, while in the absence of C_{60} the porphyrin building blocks form an irregular assembly.

4.3 Synthesis and Properties of $(C_{60})_n \subset$[*t*-P12·$(T6)_2$]

The template-free 12-porphyrin nanotube (Chapter 3) is an attractive candidate for host-guest chemistry experiments.[39] Inspired by numerous studies on (supramolecular) carbon peapods and porphyrin-fullerene host-guest complexes, we explored the encapsulation of fullerenes in ***t*-P12·$(T6)_2$**.

4.3.1 Effective Internal Cavity Determination of ***t*-P12·$(T6)_2$**

To determine the effective internal cavity of ***t*-P12·$(T6)_2$** available for guest molecules, we estimated the cavity of the tube as a perfect cylinder. The cavity is determined by the confinement of the porphyrin units around the circumference, and the template units at the top and bottom. The Zn-Zn distance between two porphyrin units along the staves (*z*-axis) is 1.35 nm, while the Zn-Zn distance between two porphyrin centres across the tube (*xy*-plane) is 2.56 nm (Figure 4.4).

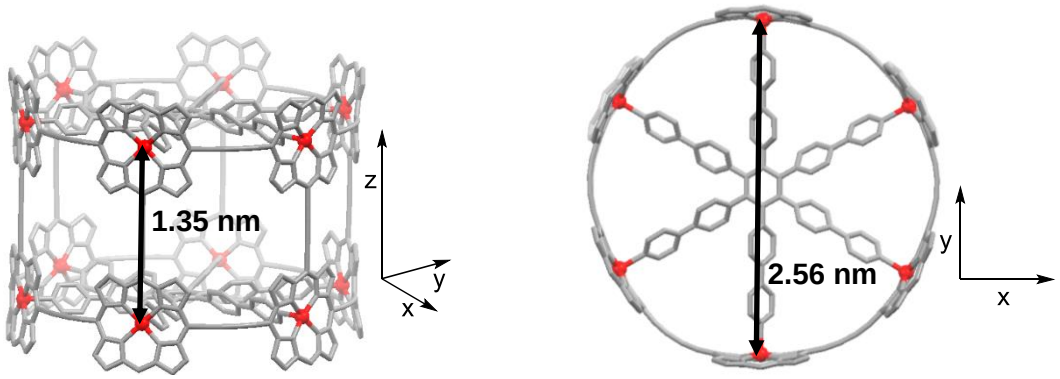

Figure 4.4: Side-view and top-view of ***t*-P12·$(T6)_2$**, indicating the Zn-Zn distances along the different dimensions of the nanotube. Calculated at the modified MM2 force field. Hydrogen atoms were omitted for clarity. Aryl groups bearing solubilising chains were omitted to simplify the calculation.

When taking the van der Waals radius of a carbon atom into account (0.17 nm, as stated by Bondi[40] in 1964, and confirmed by Rowland and Taylor[41] in 1996), the effective cavity volume of ***t*-P12·(T6)$_2$** is 3.91 nm^3. The volume of a C_{60} molecule is 0.6 nm^3 (assuming a radius of 3.53 Å[42] and a van der Waals radius of a carbon atom of 1.70 Å).

When the packing of fullerene hosts in the nanotube cavity is approached as resembling a hexagonally close-packed (hcp) lattice, with a theoretical packing coefficient of 0.74, maximum four C_{60} guests could bind inside the porphyrin nanotube cavity. Naturally, the shape of the cylindrical cavity of the nanotube is not a perfect match for the spherical fullerene guest molecules. Hence, Molecular Mechanics (MM) calculations were performed to provide scrutiny into this approximation. The calculations support that the maximum number of C_{60} fullerene molecules that geometrically fit in the porphyrin nanotube cavity is four (Figure 4.5). However, the quadruple occupancy complex leaves very little entropic freedom for the C_{60} guests and, as reported by Mecozzi and Rebek in 1998, host-guest complexes in the liquid state exhibit an optimal packing coefficient of 55%.[43] We therefore expected the single, double and triple occupancy complex to be entropically favoured over the quadruple occupancy complex.

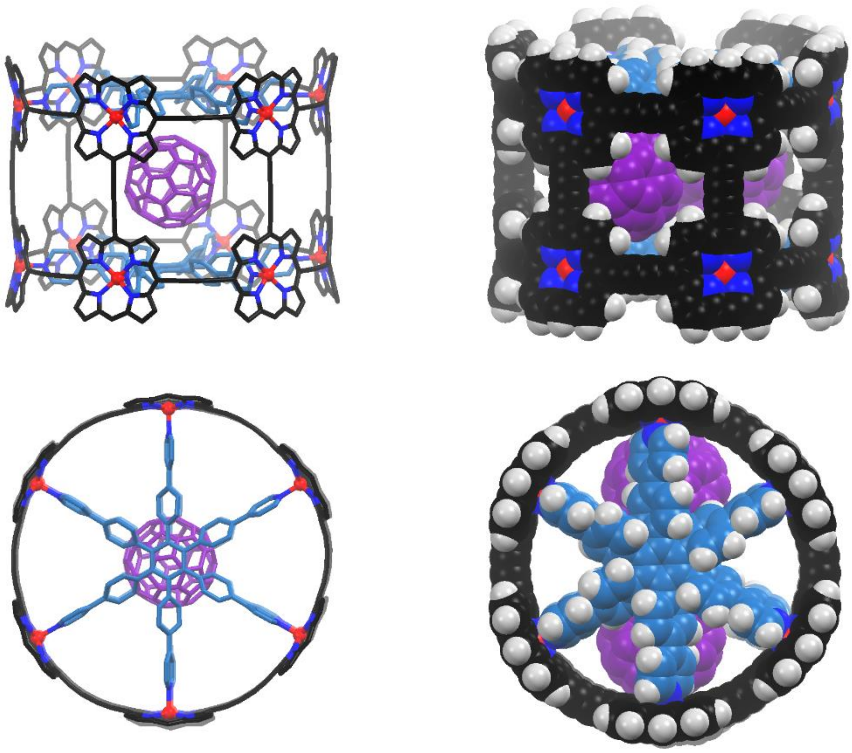

$C_{60}\subset$[*t*-P12·(T6)$_2$] **$(C_{60})_2\subset$[*t*-P12·(T6)$_2$]**

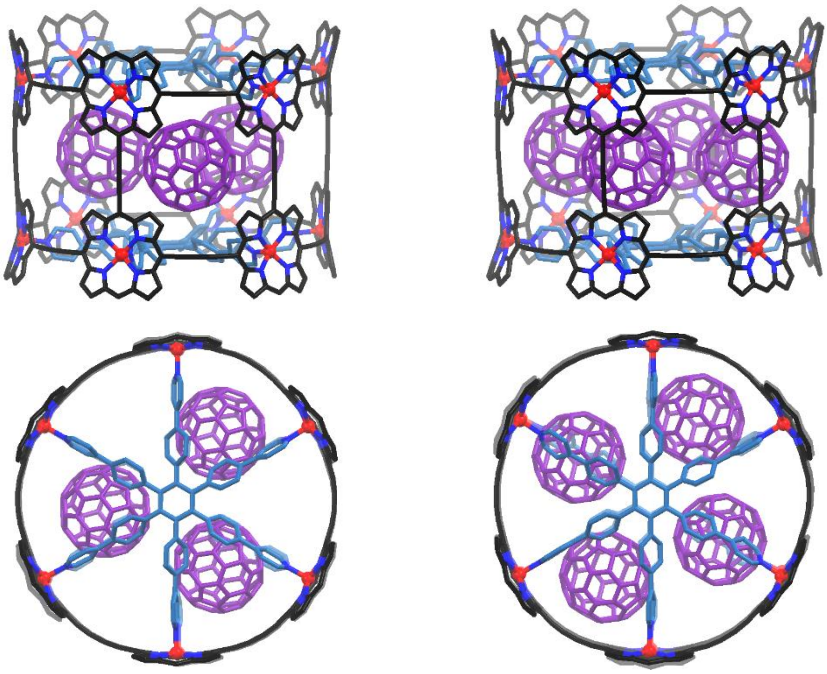

$(C_{60})_3\subset[t\text{-P12}\cdot(T6)_2]$ **$(C_{60})_4\subset[t\text{-P12}\cdot(T6)_2]$**

Figure 4.5: Optimised geometry of **$(C_{60})_n\subset[t\text{-P12}\cdot(T6)_2]$** calculated at the modified MM2 force field. Where applicable, hydrogen atoms are omitted for clarity. Aryl groups bearing solubilising chains were omitted to simplify the calculations.

4.3.2 Encapsulation of C_{60} *in* ***t*-P12·(T6)$_2$**

Entrapment of C_{60} within the 12-porphyrin nanotube was achieved by dissolving C_{60} and ***t*-P12** together under saturated conditions of C_{60}. Subsequent complexation of two **T6** templates traps any C_{60} molecules that reside inside the cavity of the nanotube (Figure 4.6). The strong binding of the **T6** template to the nanotube zinc-centres ensures that encapsulated C_{60} molecules are contained in the cavity. Molecular models show that the fullerenes cannot escape the cavity through the "windows" (Figure 4.5, **$(C_{60})_2\subset[t\text{-P12}\cdot(T6)_2]$**), hence secure entrapment of C_{60} in the nanotube cavity is achieved.

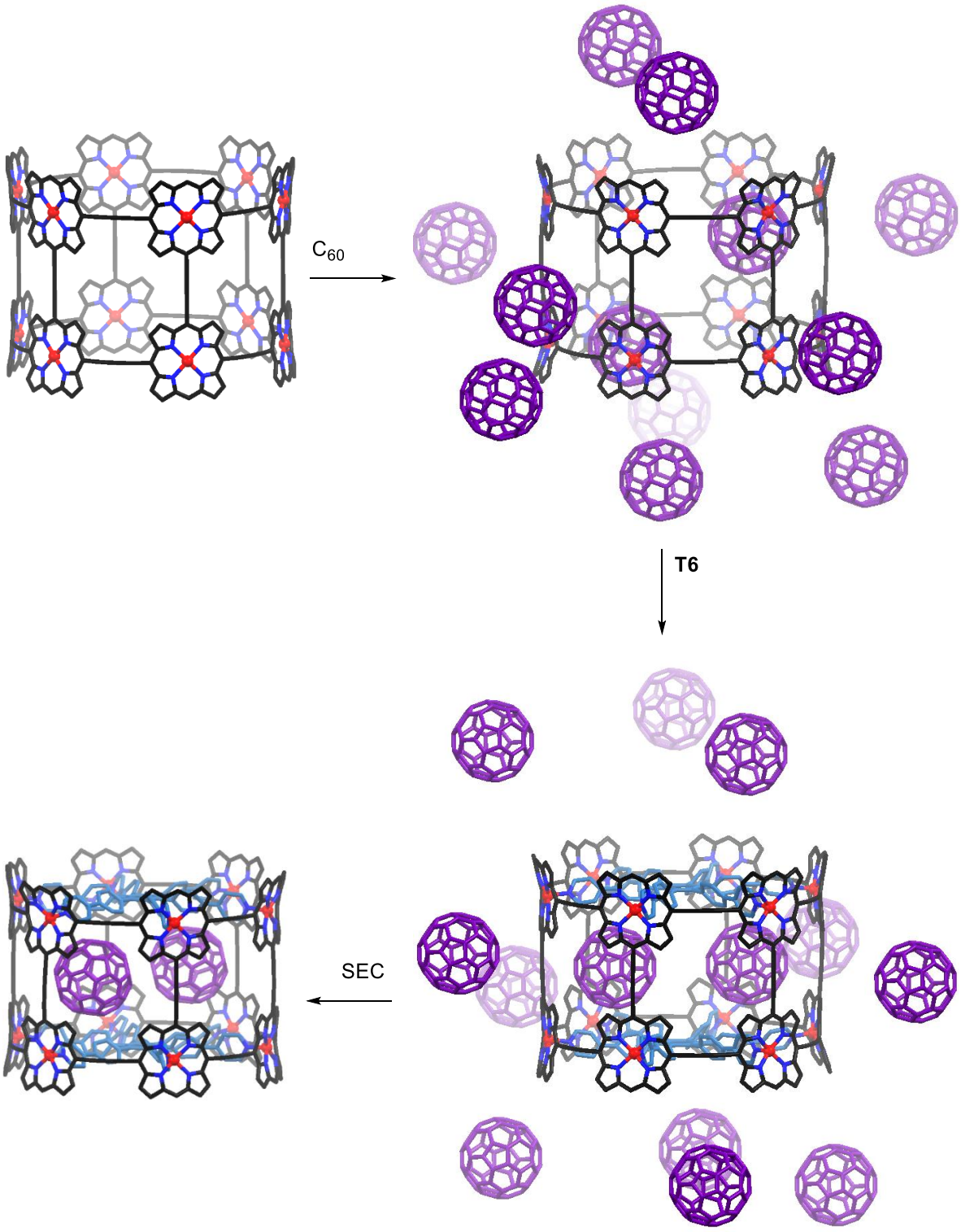

Figure 4.6: (Artistic impression) Experimental procedure for the encapsulation of C_{60} within ***t*-P12·(T6)$_2$**. Optimised geometry of ***t*-P12** calculated at the B3LYP/6-31G(d) level of theory. Hydrogen atoms omitted for clarity. Optimised geometry of C_{60} and **(C$_{60}$)$_2$⊂[*t*-P12·(T6)$_2$]** calculated at the modified MM2 force field with hydrogen atoms omitted. Aryl groups bearing solubilising chains were omitted to simplify calculations.

The highest extent of inclusion was achieved in saturated toluene of C_{60} (4.4 mg/mL). The solution of C_{60} was stirred in the dark before ***t*-P12** was added as a solution in toluene and the components were stirred for 25 minutes before **T6** was added. The reaction mixture was purified by size-exclusion chromatography in toluene/0.1% pyridine to separate **$(C_{60})_n$⊂[*t*-P12·$(T6)_2$]** from excess C_{60}. An efficient separation between the excess C_{60} and the 12-porphyrin nanotube component, containing **$(C_{60})_n$⊂[*t*-P12·$(T6)_2$]** was achieved by size-exclusion chromatography (Figure 4.7).

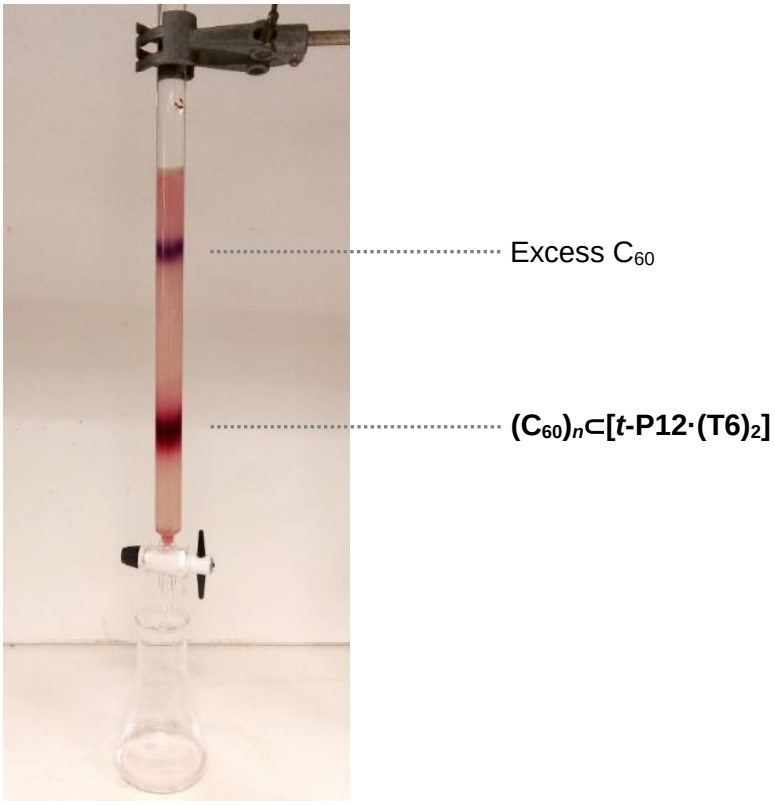

Figure 4.7: Size-exclusion chromatography (BioBeads SX-1, toluene/0.1% pyridine) of the reaction mixture of the encapsulation of C_{60} in ***t*-P12·$(T6)_2$**.

4.3.3 Characterisation of **$(C_{60})_n$⊂[*t*-P12·$(T6)_2$]**

Encapsulation of C_{60} within the cavity of ***t*-P12·$(T6)_2$** was confirmed by MALDI-ToF spectrometry and HPLC. The MALDI-ToF analysis shows a clear pattern with m/z values that correspond to ***t*-P12·$(T6)_2$** (at m/z 15001; expected 15003), **C_{60}⊂[*t*-P12·$(T6)_2$]** (at m/z 15722; expected 15723), **$(C_{60})_2$⊂[*t*-P12·$(T6)_2$]** (at m/z 16442; expected 16443), **$(C_{60})_3$⊂[*t*-P12·$(T6)_2$]** (at m/z 17164; expected 17163), and **$(C_{60})_4$⊂[*t*-P12·$(T6)_2$]** (at m/z 17883; expected 17883) (Figure 4.8), with the latter – being entropically disfavoured – in microscopic abundancy.

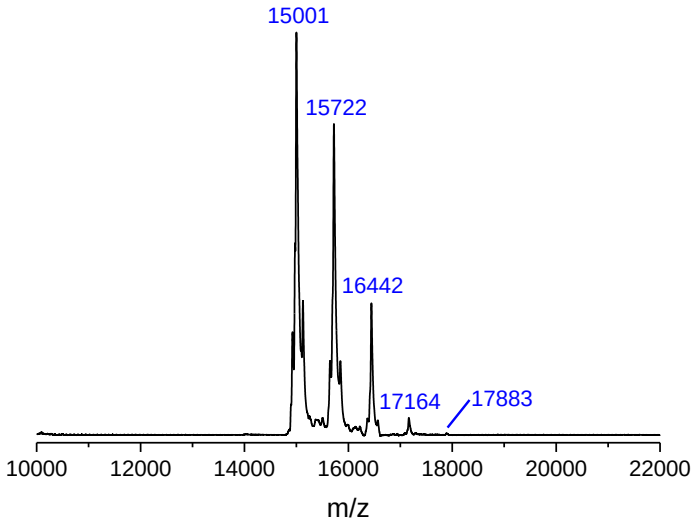

Figure 4.8: MALDI-ToF spectrum of **$(C_{60})_n$⊂[*t*-P12·(T6)$_2$]** (matrix: DCTB).

Although MALDI-ToF is not a quantitative analytical method, we might assume that the different **$(C_{60})_n$⊂[*t*-P12·(T6)$_2$]** complexes desorb and ionise similarly to one another and to ***t*-P12·(T6)$_2$**. Integration of the peaks in the MALDI-ToF spectrum gives an approximate encapsulation distribution (Table 4.1). According to this approximation, 48% of the tubes contain C_{60} in either single, double, triple or quadruple occupancy.

Table 4.1: Relative peak integrals of the MALDI-ToF spectrum of **$(C_{60})_n$⊂[*t*-P12·(T6)$_2$]**.

Species	Normalised MALDI-ToF peak area (%)
***t*-P12·(T6)$_2$**	52
C_{60}⊂[*t*-P12·(T6)$_2$]	35
$(C_{60})_2$⊂[*t*-P12·(T6)$_2$]	12
$(C_{60})_3$⊂[*t*-P12·(T6)$_2$]	1
$(C_{60})_4$⊂[*t*-P12·(T6)$_2$]	<0.1

Release of C_{60} from the nanotube cavity was analysed by HPLC. First, we determined the retention time of the individual components; C_{60} and ***t*-P12·(T6)$_2$** (Figure 4.9a and Figure 4.9b, respectively). The HPLC trace of **$(C_{60})_n$⊂[*t*-P12·(T6)$_2$]** shows a single peak with a similar retention time to ***t*-P12·(T6)$_2$** (Figure 4.9c). After addition of a competing ligand (DABCO) to remove the **T6** templates, the encapsulated C_{60} is released (Figure 4.9d).

From the calibrations of the individual components, an average C_{60} to ***t*-P12·(T6)$_2$** ratio of 0.91 was deduced (Section 4.7.2). This ratio is slightly higher than that obtained from MALDI-ToF analysis, also when double, triple and quadruple occupancy is considered (which would give a ratio of 0.61). However, the sensitivity of the HPLC detector at 312 nm for the nanotube is low, which could easily induce an error. On the other hand, as stated before, MALDI-ToF is not a quantitative analytical method.

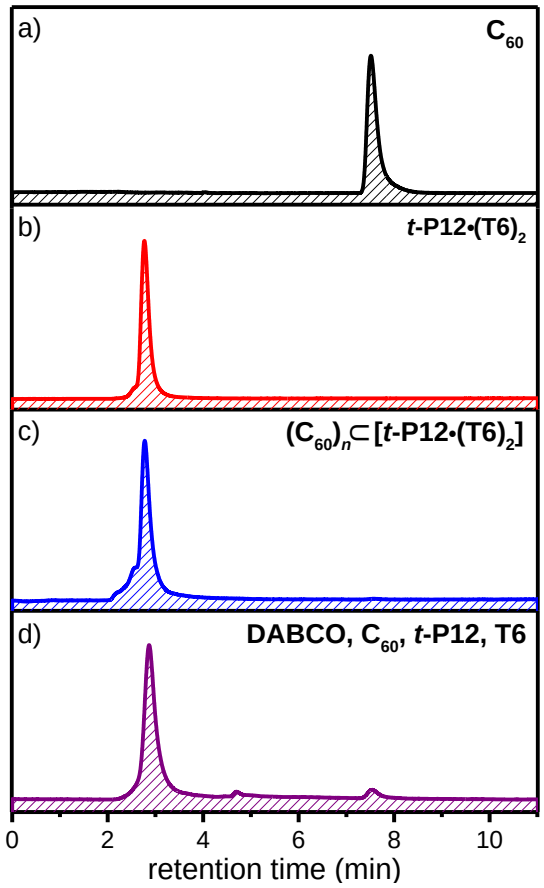

Figure 4.9: HPLC traces (detection at 312 nm, toluene; Japan Analytical JC-9103 recycling preparative HPLC with a Buckyprep-M Cosmosil column, 20 × 250 mm) of (a) C_{60}, (b) ***t*-P12·(T6)$_2$**, (c) **$(C_{60})_n$⊂[*t*-P12·(T6)$_2$]**, and (d) **$(C_{60})_n$⊂[*t*-P12·(T6)$_2$]** after the addition of DABCO.

4.3.4 Fluorescence Quenching in **$(C_{60})_n$⊂[*t*-P12·(T6)$_2$]**

C_{60} is known to quench the fluorescence of porphyrin receptors, generally *via* photoinduced electron transfer.[28,44–47] The fluorescence quantum yield of the porphyrin nanotube-fullerene complex was measured for excitation at 525 nm and 790 nm and compared to the quantum yield of the 12-porphyrin nanotube without encapsulated C_{60} molecules (Figure 4.10). After excitation at 525 nm, the fluorescence of **$(C_{60})_n$⊂[*t*-P12·(T6)$_2$]** is quenched by 55% compared to ***t*-P12·(T6)$_2$**. To ensure selective

excitation of the porphyrin chromophore system, fluorescence quantum yield measurements were also performed after the complex had been excited at 790 nm, since C_{60} does not absorb at this wavelength. At this wavelength, a fluorescence quenching of 48% was measured.

Assuming that any encapsulated C_{60} molecule will induce complete quenching of the fluorescence, these observations suggest that approximately 52% of the nanotubes contain C_{60} in either single, double, triple or quadruple occupancy, which is similar to the extent of encapsulation as was determined by MALDI-ToF spectrometry.

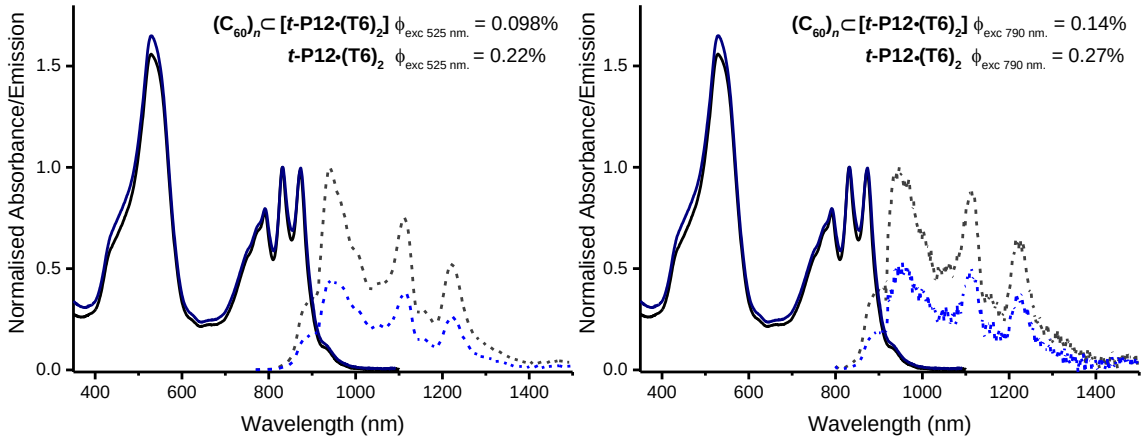

Figure 4.10: Normalised steady-state absorption (black line and blue line) and fluorescence (black dotted line and blue dotted line) at 298 K of ***t*-P12·(T6)$_2$** and **$(C_{60})_n$⊂[*t*-P12·(T6)$_2$]** respectively (right; λ_{exc} = 525 nm, left; λ_{exc} = 790 nm, measured in toluene).

4.4 Synthesis and Properties of $(C_{70})_n$⊂[*t*-P12·(T6)$_2$]

After the successful encapsulation of C_{60} in ***t*-P12·(T6)$_2$**, encapsulation of the next-largest fullerene, C_{70},[42,48,49] was examined. Using an analogous approach as was described above, we can approximate (supported by Molecular Modelling as depicted in Figure 4.11) that a maximum number of three C_{70} molecules can be encapsulated by ***t*-P12·(T6)$_2$**.

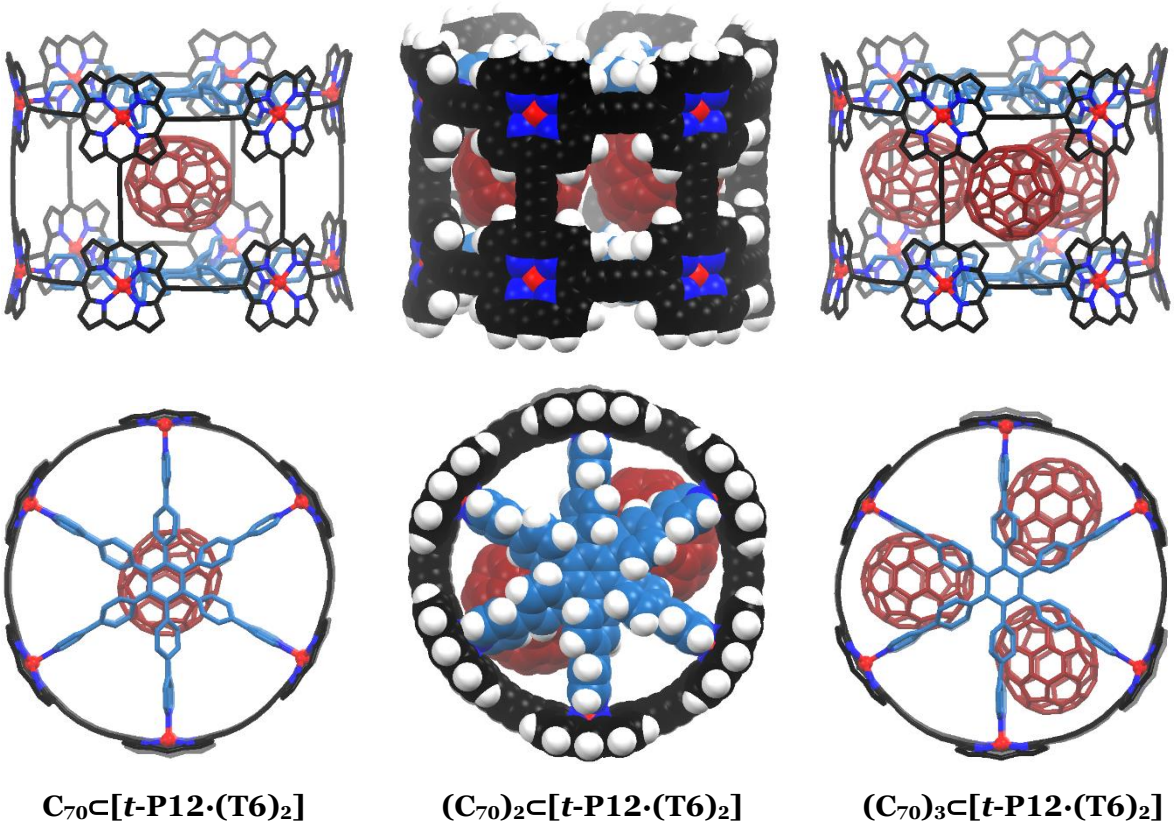

C_{70}⊂[*t*-P12·(T6)$_2$] **(C_{70})$_2$⊂[*t*-P12·(T6)$_2$]** **(C_{70})$_3$⊂[*t*-P12·(T6)$_2$]**

Figure 4.11: Optimised geometry of **(C_{70})$_n$⊂[*t*-P12·(T6)$_2$]** calculated at the modified MM2 force field. Hydrogen atoms were omitted in the left and right complexes for clarity. Aryl groups bearing solubilising chains were omitted to simplify the calculations.

4.4.1 Encapsulation and MALDI-ToF Characterisation of C_{70} *in* ***t*-P12·(T6)$_2$**

For the encapsulation of C_{70} in 12-porphyrin nanotube, an analogous procedure was used as for the encapsulation of C_{60}. A toluene solution of ***t*-P12** was added to a solution of C_{70} (1.6 mg/mL in toluene) and the components were stirred for 15 minutes before **T6** was added. After 1 hour, the reaction mixture was purified by size-exclusion chromatography in toluene/0.1% pyridine to separate **(C_{70})$_n$⊂[*t*-P12·(T6)$_2$]** from excess C_{70}. Successful encapsulation of C_{70} within the cavity of ***t*-P12·(T6)$_2$** was confirmed by MALDI-ToF analysis, which shows a clear pattern with m/z values that correspond to ***t*-P12·(T6)$_2$** (at m/z 15003; expected 15003), **C_{70}⊂[*t*-P12·(T6)$_2$]** (at m/z 15851; expected 15843), **(C_{70})$_2$⊂[*t*-P12·(T6)$_2$]** (at m/z 16693; expected 16683), and **(C_{70})$_3$⊂[*t*-P12·(T6)$_2$]** (at m/z 17534; expected 17523) (Figure 4.12).

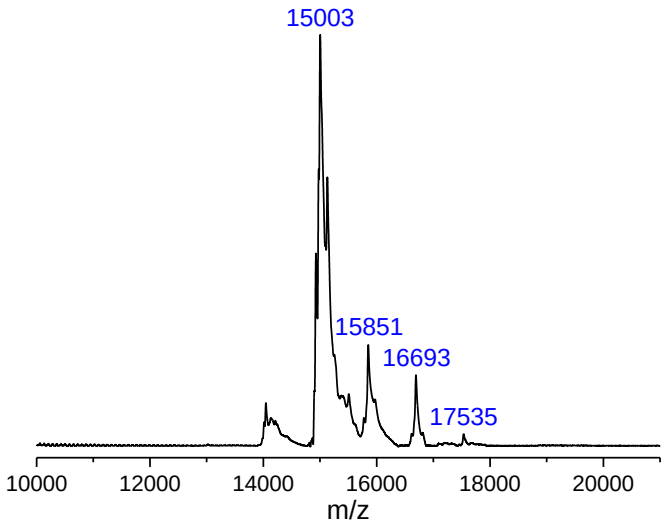

Figure 4.12: MALDI-ToF spectrum of **$(C_{70})_n$⊂[*t*-P12·(T6)$_2$]** (matrix: DCTB).

Encapsulation of C_{80} in ***t*-P12·(T6)$_2$** following an analogous procedure as for C_{60} and C_{70} showed negligible inclusion by MALDI-ToF analysis. Molecular Modelling on **C_{80}⊂[*t*-P12·(T6)$_2$]** demonstrated that the **T6** templates must adopt a domed conformation to accommodate the C_{80} molecule. Presumably, the rigidity of the templates renders complex formation with C_{80} unfavourable.

4.5 Selective Encapsulation

Various receptors, including porphyrin-based ones, have been studied for their potential to selectively extract particular fullerenes from a fullerene mixture.[31,47,50–53] In general, C_{70} was found to bind stronger to the porphyrin receptor than C_{60} due to the possible "side-on" binding of C_{70}. This maximises the van der Waals interaction between the flatter equatorial π-surface of this fullerene and the π-surface of the porphyrin.[31,47,52,54]

In a recent study by Mondal and Rath, an adaptable cyclic porphyrin dimer was found to bind C_{70} with a higher association constant than C_{60}.[47] Selective extraction from a 10:1 C_{60}:C_{70} mixture with the cyclic porphyrin dimer resulted in a C_{70} enriched sample with a C_{70}:C_{60} ratio of 3:1.

4.5.1 Selective Fullerene Encapsulation in ***t*-P12·(T6)$_2$**

To examine if the 12-porphyrin nanotube exhibits selective encapsulation, ***t*-P12** (as a solution in toluene) was added to an equimolar solution of C_{60} and C_{70}. The solution was stirred for 15 minutes before **T6** template was added. The solution was stirred for 45 minutes and then purified by size-exclusion chromatography eluted with toluene/0.1% pyridine to separate **$(C_{60})_n(C_{70})_m$⊂[*t*-P12·(T6)$_2$]** from excess C_{60} and C_{70}.

MALDI-ToF analysis of the product mixture shows preferred encapsulation of C_{70} over C_{60} (Figure 4.13). Singly occupied species are only present for C_{70}, while for the doubly and triply occupied complexes, a mixture of C_{60} and C_{70} is observed with a dominant contribution of C_{70}. The poor resolution of the MALDI-ToF spectrum renders it difficult to quantitatively determine the relative binding strengths. However, when the doubly occupied species are considered, a C_{70}/C_{60} binding ratio of approximately 4:1 can be deduced from integrating the MALDI-ToF spectrum, which is similar to the selectivity observed by Mondal and Rath.[47]

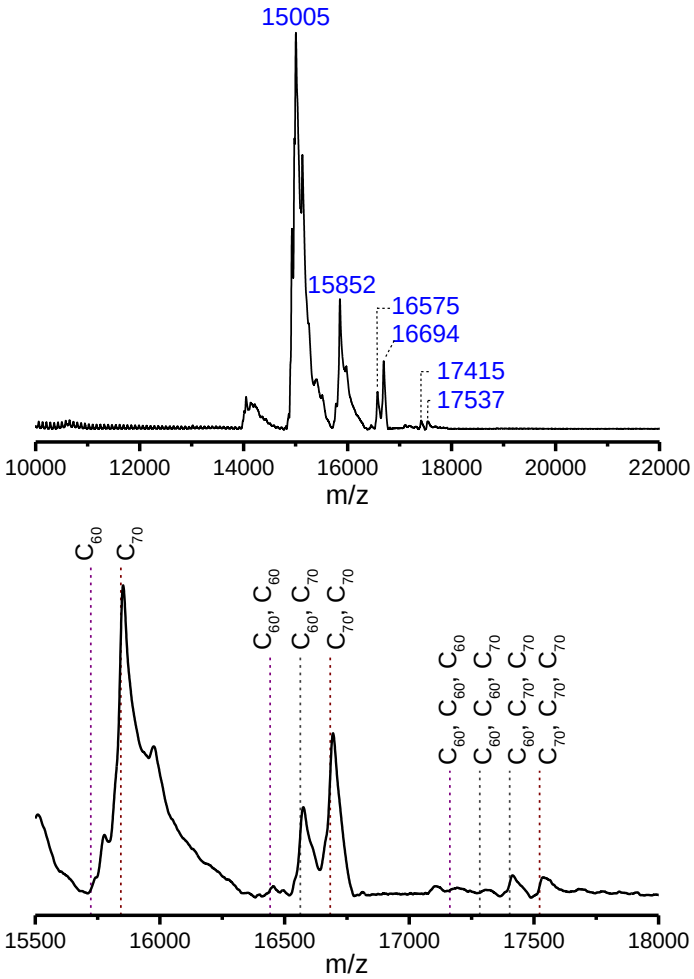

Figure 4.13: (top) MALDI-ToF spectrum of **$(C_{60})_n(C_{70})_m$⊂[*t*-P12·(T6)$_2$]**. (bottom) Region of the same MALDI-ToF spectrum, with added guidelines of expected m/z values for the different fullerene-nanotube complexes (matrix: DCTB).

4.6 Conclusion

Analogous to carbon nanotube peapods, we successfully encapsulated C_{60} and C_{70} fullerenes in a 12-porphyrin nanotube. Encapsulation was achieved by simply mixing the 12-porphyrin nanotube, ***t*-P12**, and the fullerene, C_{60} or C_{70}, together. Upon addition of **T6** template, the fullerene molecules were trapped in the nanotube cavity, forming a supramolecular choromophore/electron acceptor system in which the electron accepting fullerene resides "protected" in the cavity of the porphyrin nanotube.

HPLC analysis of **$(C_{60})_n$⊂[*t*-P12·$(T6)_2$]** confirms that the complex is stable and moves as a single species on the column. After the addition of a competing ligand, the templates were removed from the complex and C_{60} fullerenes were released from the cavity. This makes the porphyrin-nanotube complex an interesting candidate for a "molecular cargo" system, where the fullerene is picked-up, transported and eventually released.

Fluorescence quenching was observed for **$(C_{60})_n$⊂[*t*-P12·$(T6)_2$]**, indicative of electron transfer from the porphyrin chromophores to the encapsulated C_{60} acceptor, reminiscent of the natural LH1/RC assembly (Chapter 2, Figure 2.1).

Analysis of the fullerene-nanotube complexes by MALDI-ToF shows encapsulation of either none, one, two, three or four fullerenes per nanotube. Furthermore, when encapsulation was performed with an equimolar solution of C_{60} and C_{70}, preferred encapsulation of the latter fullerene was observed. The dimensions of the nanotube do not allow for significant inclusion of fullerenes larger than C_{70}. Therefore, the nanotube could act as a selective receptor for the smaller fullerenes (C_{60} and C_{70}) when a mixed-fullerene sample is used and hence could be used to extract the smaller fullerenes from fullerene soot.

4.7 Experimental Procedures

***t*-P12** was prepared as described in Chapter 3.

4.7.1 Preparation of Fullerene-Nanotube Complexes

$(C_{60})_n$⊂[*t*-P12·$(T6)_2$]

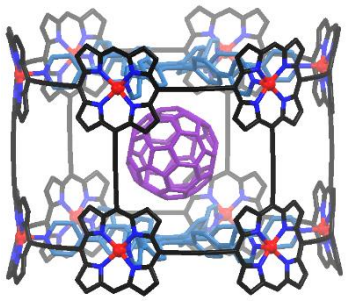

(an example of **$(C_{60})_n$⊂[*t*-P12·$(T6)_2$]**)

C_{60} fullerene (6.6 mg, 9.2 μmol) was dissolved in toluene (1.5 mL) and stirred for 30 min in the dark. ***t*-P12** (1.5 mg, 0.11 μmol) was dissolved in toluene (0.15 mL) and added to the C_{60} fullerene solution. The mixture was stirred for 25 min before **T6** template was added (0.5 mg, 0.5 μmol). The mixture was stirred for 2 h before it was purified by size-exclusion chromatography (BioBeads SX-1, toluene/0.1% pyridine).

MALDI-ToF m/z 15001 (***t*-P12·$(T6)_2$** expected at 15003); 15722 (**C_{60}⊂[*t*-P12·$(T6)_2$]** expected at 15723); 16442 (**$(C_{60})_2$⊂[*t*-P12·$(T6)_2$]** expected at 16443); 17164 (**$(C_{60})_3$⊂[*t*-P12·$(T6)_2$]** expected at 17163).

$(C_{70})_n$⊂[*t*-P12·$(T6)_2$]

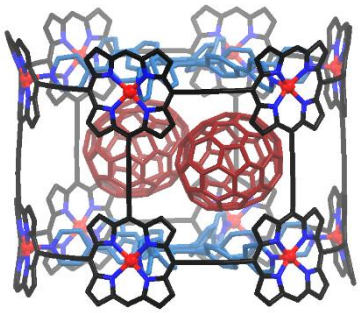

(an example of **$(C_{70})_n$⊂[*t*-P12·$(T6)_2$]**)

C_{70} fullerene (0.8 mg, 0.95 μmol) was dissolved in toluene (0.5 mL) and stirred for 10 min. ***t*-P12** (0.5 mg, 0.04 μmol) was dissolved in toluene (75 μL) and added to the C_{70} fullerene

solution. The mixture was stirred for 15 min before **T6** template was added (0.1 mg, 0.1 μmol). The mixture was stirred for 1 h before it was purified by size-exclusion chromatography (BioBeads SX-1, toluene/0.1% pyridine).

MALDI-ToF m/z 15003 (***t*-P12·(T6)$_2$** expected at 15003); 15851 (**C_{70}⊂[*t*-P12·(T6)$_2$]** expected at 15843); 16693 (**(C_{70})$_2$⊂[*t*-P12·(T6)$_2$]** expected at 16683); 17534 (**(C_{70})$_3$⊂[*t*-P12·(T6)$_2$]** expected at 17523).

(C_{60})$_n$(C_{70})$_m$⊂[*t*-P12·(T6)$_2$]

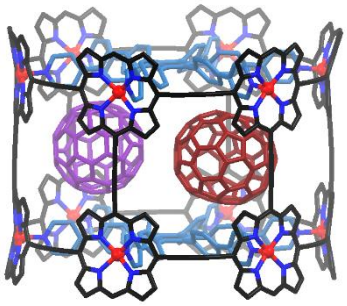

(an example of **(C_{60})$_n$(C_{70})$_m$⊂[*t*-P12·(T6)$_2$]**)

C_{60} fullerene (0.37 mg, 0.51 μmol) and C_{70} fullerene (0.47 mg, 0.55 μmol) were dissolved in toluene (0.5 mL) and stirred for 10 min. ***t*-P12** (0.5 mg, 0.04 μmol) was dissolved in toluene (75 μL) and added to the fullerene mixture. The mixture was stirred for 15 min before **T6** template was added (0.1 mg, 0.1 μmol). The mixture was stirred for 45 min before it was purified by size-exclusion chromatography (BioBeads SX-1, toluene/0.1% pyridine).

MALDI-ToF m/z 15005 (***t*-P12·(T6)$_2$** expected at 15003); 15852 (**C_{70}⊂[*t*-P12·(T6)$_2$]** expected at 15843); 16575 (**(C_{60})(C_{70})⊂[*t*-P12·(T6)$_2$]** expected at 16563); 16694 (**(C_{70})$_2$⊂[*t*-P12·(T6)$_2$]** expected at 16683); 17415 (**(C_{60})(C_{70})$_2$⊂[*t*-P12·(T6)$_2$]** expected at 17403); 17537 (**(C_{70})$_3$⊂[*t*-P12·(T6)$_2$]** expected at 17523).

4.7.2 HPLC Analysis of $(C_{60})_n \subset [t\text{-P12}\cdot(T6)_2]$

The calibration of C_{60} on the recycling preparative HPLC had previously been performed by Dr. Maria Lebedeva (University of Oxford, Department of Materials). In Figure 4.14 the calibration of ***t*-P12·(T6)$_2$** is depicted. From the HPLC trace of **$(C_{60})_n \subset [t\text{-P12}\cdot(T6)_2]$** obtained after the addition of DABCO (Figure 4.9d), we deduced the ratio of C_{60} to ***t*-P12·(T6)$_2$** to be 0.91 (Table 4.2).

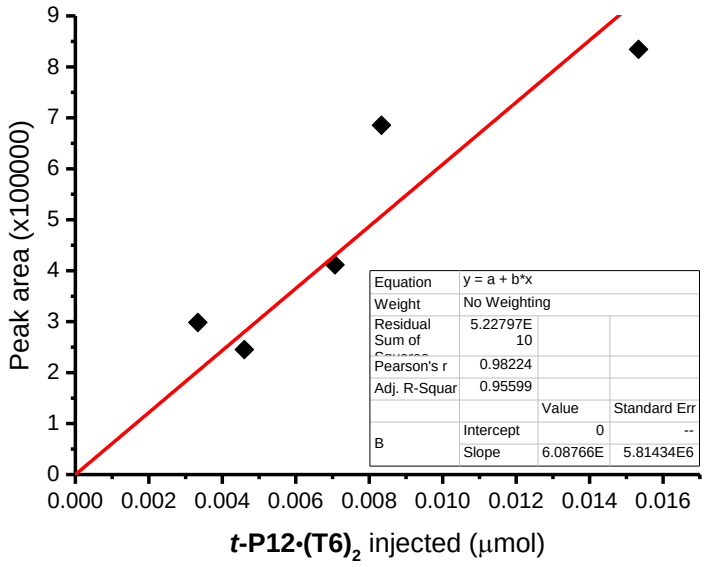

Figure 4.14: Calibration of the peak area to the injected amount of ***t*-P12·(T6)$_2$** on a Japan Analytical JC-9103 recycling preparative HPLC with a Buckyprep-M Cosmosil column (20 X 250 mm), detection at 312 nm, toluene.

Table 4.2: HPLC data from **$(C_{60})_n \subset [t\text{-P12}\cdot(T6)_2]$ + DABCO** and deduced amounts of C_{60} and ***t*-P12·(T6)$_2$**.

Species	Peak Area	Amount (μmol)
***t*-P12**	491650	8.08E-03
C_{60}	25779	7.37E-03
C_{60} to *t*-P12		**0.91**

4.8 References

(1) B. W. Smith, M. Monthioux, D. E. Luzzi. 'Encapsulated C_{60} in Carbon Nanotubes'. *Nature*, **1998**, *396*, 323–324.

(2) B. W. Smith, M. Monthioux, D. E. Luzzi. 'Carbon Nanotube Encapsulated Fullerenes: A Unique Class of Hybrid Materials'. *Chem. Phys. Lett.*, **1999**, *315*, 31–36.

(3) D. E. Luzzi, B. W. Smith. 'Carbon Cage Structures in Single Wall Carbon Nanotubes: A New Class of Materials'. *Carbon N. Y.*, **2000**, *38*, 1751–1756.

(4) B. W. Smith, R. M. Russo, S. B. Chikkannanavar, D. E. Luzzi. 'High-Yield Synthesis and One-Dimensional Structure of C_{60} Encapsulated in Single-Wall Carbon Nanotubes'. *J. Appl. Phys.*, **2002**, *91*, 9333–9340.

(5) P. Jaroenapibal, S. B. Chikkannanavar, D. E. Luzzi, S. Evoy. 'Nanomechanical Resonance Studies of Carbon Nanotube Peapod Bundles'. *J. Appl. Phys.*, **2005**, *98*, 44301–44306.

(6) S. Okada. 'Energetics of Carbon Peapods: Elliptical Deformation of Nanotubes and Aggregation of Encapsulated C_{60}'. *Phys. Rev. B* , **2008**, *77*, 1–7.

(7) D. J. Hornbaker. 'Mapping the One-Dimensional Electronic States of Nanotube Peapod Structures'. *Science*, **2002**, *295*, 828–831.

(8) A. Trave, F. J. Ribeiro, S. G. Louie, M. L. Cohen. 'Energetics and Structural Characterization of C_{60} Polymerization in BN and Carbon Nanopeapods'. *Phys. Rev. B* , **2004**, *70*, 1–7.

(9) J. Cambedouzou, S. Rols, R. Almairac, J. L. Sauvajol, H. Kataura, H. Schober. 'Low-Frequency Excitations of C_{60} Chains Inserted inside Single-Walled Carbon Nanotubes'. *Phys. Rev. B* , **2005**, *71*, 1–4.

(10) A. A. Popov, S. Yang, L. Dunsch. 'Endohedral Fullerenes'. *Chem. Rev.*, **2013**, *113*, 5989–6113.

(11) F. Simon, H. Kuzmany, H. Rauf, T. Pichler, J. Bernardi, H. Peterlik, L. Korecz, F. Fülöp, A. Jánossy. 'Low Temperature Fullerene Encapsulation in Single Wall Carbon Nanotubes: Synthesis of N@C_{60}@SWCNT'. *Chem. Phys. Lett.*, **2004**, *383*, 362–367.

(12) S. Tóth, D. Quintavalle, B. Náfrádi, L. Korecz, L. Forró, F. Simon. 'Enhanced Thermal Stability and Spin-Lattice Relaxation Rate of N@C_{60} inside Carbon Nanotubes'. *Phys. Rev. B* , **2008**, *77*, 1–5.

(13) B. Corzilius, A. Gembus, N. Weiden, K. P. Dinse, K. Hata. 'EPR Characterization of Catalyst-Free SWNT and N@C_{60}-Based Peapods'. *Phys. Stat. Sol.*, **2006**, *243*, 3273–3276.

(14) A. L. Cantone, M. R. Buitelaar, C. G. Smith, D. Anderson, G. A. C. Jones, S. J. Chorley, C. Casiraghi, A. Lombardo, A. C. Ferrari, H. Shinohara, A. Ardavan, J. Warner, A. A. R. Watt, K. Porfyrakis, G. A. D. Briggs. 'Electronic Transport Characterization of Sc@C_{82} Single-Wall Carbon Nanotube Peapods'. *J. Appl. Phys.*, **2008**, *104*, 1–7.

(15) K. Hirahara, K. Suenaga, S. Bandow, H. Kato, T. Okazaki, H. Shinohara, S. Iijima. 'One-Dimensional Metallofullerene Crystal Generated inside Single-Walled Carbon Nanotubes'. *Phys. Rev. Lett.*, **2000**, *85*, 5384–5387.

(16) J. H. Warner, A. A. R. Watt, L. Ge, K. Porfyrakis, T. Akachi, H. Okimoto, Y. Ito, A. Ardavan, B. Montanari, J. H. Jefferson, N. M. Harrison, H. Shinohara, G. A. D. Briggs. 'Dynamics of Paramagnetic Metallofullerenes in Carbon Nanotube Peapods'. *Nano*

Lett., **2008**, *8*, 1005–1010.

(17) T. Shimada, T. Okazaki, R. Taniguchi, T. Sugai, H. Shinohara, K. Suenaga, Y. Ohno, S. Mizuno, S. Kishimoto, T. Mizutani. 'Ambipolar Field-Effect Transistor Behavior of Gd@C_{82} Metallofullerene Peapods'. *Appl. Phys. Lett.*, **2002**, *81*, 4067–4069.

(18) T. Shimada, Y. Ohno, K. Suenaga, T. Okazaki, S. Kishimoto, T. Mizutani, R. Taniguchi, H. Kato, B. Cao, T. Sugai, H. Shinohara. 'Tunable Field-Effect Transistor Device with Metallofullerene Nanopeapods'. *Jpn. J. Appl. Phys.*, **2005**, *44*, 469–472.

(19) R. Kitaura, N. Imazu, K. Kobayashi, H. Shinohara. 'Fabrication of Metal Nanowires in Carbon Nanotubes via Versatile Nano-Template Reaction'. *Nano Lett.*, **2008**, *8*, 693–699.

(20) L. Guan, K. Suenaga, S. Okubo, T. Okazaki, S. Iijima. 'Metallic Wires of Lanthanum Atoms inside Carbon Nanotubes'. *J. Am. Chem. Soc.*, **2008**, *130*, 2162–2163.

(21) Y. Sun, T. Drovetskaya, R. D. Bolskar, R. Bau, P. D. W. Boyd, C. A. Reed. 'Fullerides of Pyrrolidine-Functionalized C_{60}'. *J. Org. Chem.*, **1997**, *62*, 3642–3649.

(22) F. J. Rizzuto, D. M. Wood, T. K. Ronson, J. R. Nitschke. 'Tuning the Redox Properties of Fullerene Clusters within a Metal-Organic Capsule'. *J. Am. Chem. Soc.*, **2017**, *139*, 11008–11011.

(23) P. D. W. Boyd, C. A. Reed. 'Fullerene - Porphyrin Constructs'. *Acc. Chem. Res.*, **2005**, *38*, 235–242.

(24) K. Tashiro, T. Aida. 'Metalloporphyrin Hosts for Supramolecular Chemistry of Fullerenes'. *Chem. Soc. Rev.*, **2007**, *36*, 189–197.

(25) J. S. Marois, K. Cantin, A. Desmarais, J. F. Morin. '[3]Rotaxane-Porphyrin Conjugate as a Novel Supramolecular Host for Fullerenes'. *Org. Lett.*, **2008**, *10*, 33–36.

(26) K. Tashiro, T. Aida, J. Y. Zheng, K. Kinbara, K. Saigo, S. Sakamoto, K. Yamaguchi. 'A Cyclic Dimer of Metalloporphyrin Forms a Highly Stable Inclusion Complex with C_{60}'. *J. Am. Chem. Soc.*, **1999**, *121*, 9477–9478.

(27) C. Zhang, Q. Wang, H. Long, W. Zhang. 'A Highly C_{70} Selective Shape-Persistent Rectangular Prism Constructed through One-Step Alkyne Metathesis'. *J. Am. Chem. Soc.*, **2011**, *133*, 20995–21001.

(28) G. Gil-Ramirez, S. D. Karlen, A. Shundo, K. Porfyrakis, Y. Ito, G. A. D. Briggs, J. J. L. Morton, H. L. Anderson. 'A Cyclic Porphyrin Trimer as a Receptor for Fullerenes'. *Org. Lett.*, **2010**, *12*, 3544–3547.

(29) A. Takai, M. Chkounda, A. Eggenspiller, C. P. Gros, M. Lachkar, J.-M. Barbe, S. Fukuzumi. 'Efficient Photoinduced Electron Transfer in a Porphyrin Tripod–Fullerene Supramolecular Complex via π–π Interactions in Nonpolar Media'. *J. Am. Chem. Soc.*, **2010**, *132*, 4477–4489.

(30) L. H. Tong, J. L. Wietor, W. Clegg, P. R. Raithby, S. I. Pascu, J. K. M. Sanders. 'Supramolecular Assemblies of Tripodal Porphyrin Hosts and C_{60}'. *Chem. - Eur. J.*, **2008**, *14*, 3035–3044.

(31) Y. Shoji, K. Tashiro, T. Aida. 'Selective Extraction of Higher Fullerenes Using Cyclic Dimers of Zinc Porphyrins'. *J. Am. Chem. Soc.*, **2004**, *126*, 6570–6571.

(32) L. P. Hernández-Eguía, E. C. Escudero-Adán, J. R. Pinzón, L. Echegoyen, P. Ballester. 'Complexation of $Sc_3N@C_{80}$ Endohedral Fullerene with Cyclic Zn-Bisporphyrins: Solid State and Solution Studies'. *J. Org. Chem.*, **2011**, *76*, 3258–3265.

(33) M. Ayabe, A. Ikeda, Y. Kubo, M. Takeuchi, S. Shinkai. 'A Dendritic Porphyrin Receptor for C_{60} Which Features a Profound Positive Allosteric Effect'. *Angew. Chem. Int. Ed.*, **2002**, No. 15, 2790–2792.

(34) J. Song, N. Aratani, H. Shinokubo, A. Osuka. 'A Porphyrin Nanobarrel That Encapsulates C_{60}'. *J. Am. Chem. Soc.*, **2010**, *132*, 16356–16357.

(35) H. Nobukuni, Y. Shimazaki, F. Tani, Y. Naruta. 'A Nanotube of Cyclic Porphyrin Dimers Connected by Nonclassical Hydrogen Bonds and Its Inclusion of C_{60} in a Linear Arrangement'. *Angew. Chem. Int. Ed.*, **2007**, *46*, 8975–8978.

(36) H. Nobukuni, F. Tani, Y. Shimazaki, Y. Naruta, K. Ohkubo, T. Nakanishi, T. Kojima, S. Fukuzumi, S. Seki. 'Anisotropic High Electron Mobility and Photodynamics of a Self-Assembled Porphyrin Nanotube Including C_{60} Molecules'. *J. Phys. Chem. C*, **2009**, *113*, 19694–19699.

(37) A. R. Mulholland, C. P. Woodward, S. J. Langford. 'Fullerene-Templated Synthesis of a Cyclic Porphyrin Trimer Using Olefin Metathesis'. *Chem. Comm.*, **2011**, *47*, 1494–1496.

(38) T. Yamaguchi, N. Ishii, K. Tashiro, T. Aida. 'Supramolecular Peapods Composed of a Metalloporphyrin Nanotube and Fullerenes'. *J. Am. Chem. Soc.*, **2003**, *125*, 13934–13935.

(39) P. Neuhaus, A. Cnossen, J. Q. Gong, L. M. Herz, H. L. Anderson. 'A Molecular Nanotube with Three-Dimensional π-Conjugation'. *Angew. Chem. Int. Ed.*, **2015**, *54*, 7344 –7348.

(40) A. Bondi. 'Van Der Waals Volumes and Radii'. *J. Phys. Chem.*, **1964**, *68*, 441–451.

(41) R. S. Rowland, R. Taylor. 'Intermolecular Nonbonded Contact Distances in Organic Crystal Structures'. *J. Phys. Chem.*, **1996**, *100*, 7384–7391.

(42) G. B. Adams, M. O'Keeffe, R. S. Ruoff. 'Van Der Waals Surface Areas and Volumes of Fullerenes'. *J. Phys. Chem.*, **1994**, *98*, 9465–9469.

(43) S. Mecozzi, J. Rebek. 'The 55% Solution: A Formula for Molecular Recognition in the Liquid State'. *Chem. - Eur. J.*, **1998**, *4*, 1016–1022.

(44) M. E. El-Khouly, O. Ito, P. M. Smith, F. D'Souza. 'Intermolecular and Supramolecular Photoinduced Electron Transfer Processes of Fullerene-Porphyrin/Phthalocyanine Systems'. *J. Photochem. Photobiol. C Photochem. Rev.*, **2004**, *5*, 79–104.

(45) B. Wang, S. Zheng, A. Saha, L. Bao, X. Lu, D. M. Guldi. 'Understanding Charge-Transfer Characteristics in Crystalline Nanosheets of Fullerene/(Metallo)Porphyrin Cocrystals'. *J. Am. Chem. Soc.*, **2017**, *139*, 10578–10584.

(46) P. O. Krasnov, A. A. Kuzubov, A. S. Kholtobina, E. A. Kovaleva, M. V. Kuzubova. 'Optical Charge Transfer Transitions in Supramolecular Fullerene and Porphyrin Compounds'. *J. Struct. Chem.*, **2016**, *57*, 681–687.

(47) P. Mondal, S. P. Rath. 'A Tunable Cyclic Container: Guest-Induced Conformational Switching, Efficient Guest Exchange, and Selective Isolation of C_{70} from a Fullerene Mixture'. *Chem. - Asian J.*, **2017**, *12*, 1824–1835.

(48) H. W. Kroto, J. R. Heath, S. C. O'Brien, R. F. Curl, R. E. Smalley. 'C_{60}: Buckminsterfullerene'. *Nature*, **1985**, *318*, 162–163.

(49) W. Kratschmer, L. D. Lamb, K. Fostiropoulos, D. R. Huffman. 'Solid C_{60}: A New Form of Carbon'. *Nature*, **1990**, *347*, 354–358.

(50) T. Andersson, K. Nilsson, M. Sunda, G. Westman, O. Wennerstrom. 'C_{60} Embedded in Y-Cyclodextrin: A Water-Soluble Fullerene'. *J. Chem. Soc. Chem. Commun.*, **1992**, 604–606.

(51) J. L. Atwood, G. A. Koutsantonis, C. L. Raston. 'Purification of C_{60} and C_{70} by Selective Complexation with Calixarenes'. *Nature*, **1994**, *368*, 229–231.

(52) D. Sun, F. S. Tham, C. A. Reed, L. Chaker, P. D. W. Boyd. 'Supramolecular Fullerene-Porphyrin Chemistry. Fullerene Complexation by Metalated "Jaws Porphyrin" Hosts'. *J. Am. Chem. Soc.*, **2002**, *124*, 6604–6612.

(53) D. Lu, G. Zhuang, H. Wu, S. Wang, S. Yang, P. Du. 'A Large π-Extended Carbon Nanoring Based on Nanographene Units: Bottom-Up Synthesis, Photophysical Properties, and Selective Complexation with Fullerene C_{70}'. *Angew. Chem. Int. Ed.*, **2017**, *56*, 158–162.

(54) D. Sun, F. S. Tham, C. A. Reed, L. Chaker, M. Burgess, P. D. W. Boyd. 'Porphyrin–Fullerene Host–Guest Chemistry'. *J. Am. Chem. Soc.*, **2000**, *122*, 10704–10705.

5

Synthesis and Properties of a π-Conjugated 12-Porphyrin Nanotube and 18-Porphyrin Nanotube

5.1 Abstract

This chapter describes the synthesis and properties of porphyrin nanotubes. A 12-porphyrin nanotube was prepared with a mono-acetylene connection between the conjoined 6-porphyrin nanorings. This molecular nanotube exhibits strong conjugation around the π-system with a bathochromic shift in absorption of 40 nm and a lower fluorescence quantum yield compared to the analogous complex connected by bis-acetylene linkages.

Furthermore, the synthesis of a nanotube consisting of 18-porphyrin subunits is discussed, for which different synthetic strategies were examined. Our second-generation synthetic strategy to this nanotube comprised the use of a mono-acetylene linked porphyrin trimer precursor. Remarkably, this strategy allowed us to prepare the 18-porphyrin nanotube in one step from porphyrin trimer, albeit with a low yield of the desired compound, presumably due to mismatched coupling. The target 18-porphyrin nanotube was successfully isolated after a step-wise approach *via* a pre-tube complex, confirmed by analytical GPC, MALDI-ToF, UV-vis-NIR and ^{1}H NMR.

5.2 Introduction

In contrast to the previously reported π-conjugated porphyrin nanorings,[1–5] π-conjugated porphyrin nanotubes exhibit strong intrinsic rigidity which enforces shape-persistency. In the case of porphyrin nanorings, it was demonstrated that as the diameter of the rings increases beyond ~10 nm, their electronic properties tend to resemble a similarly sized linear porphyrin oligomer.[6] This is a result of exciton delocalisation on a subsegment of the ring rather than around the entire π-system. A similar dependence of π-conjugation on conformational distortion was demonstrated for cycloparaphenylenes of different-sizes.[7,8]

To the best of our knowledge, the 12-porphyrin nanotube (as depicted in Figure 5.1 and discussed in Chapter 3 and Chapter 4) is the longest synthetic π-conjugated molecular nanotube to date.[9] Ultrafast exciton migration around the conjugated system of the nanotube was observed as a fluorescence anisotropy of –0.04 after excitation at 742 nm. Absorption at this wavelength is associated with the porphyrin dimer staves (*z*-plane) of the nanotube after which the excitation energy is transferred to states that emit from the *xy*-plane.

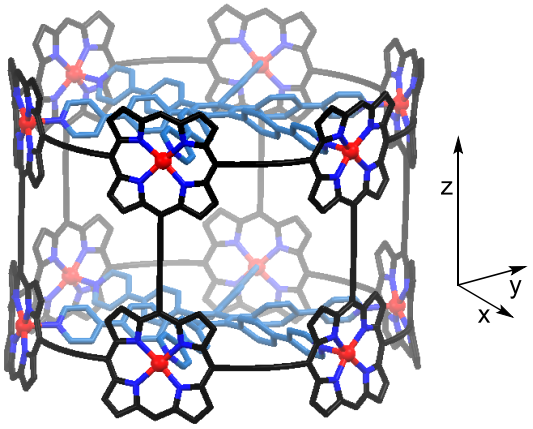

Figure 5.1: Optimised geometry of ***t*-P12·(T6)$_2$** calculated at the Modified MM2 forcefield. Hydrogen atoms are omitted for clarity. Aryl groups bearing solubilising chains were omitted to simplify the calculations.

For π-conjugated porphyrin nanotubes the longitudinal extension of the π-system from the 12-porphyrin nanotube to the 18-porphyrin nanotube is not compromised by an increase in flexibility. We therefore expect this compound to exhibit interesting optoelectronic properties. Naturally, we expect the 18-porphyrin nanotube to exhibit a further bathochromic shift in absorption and emission compared to the 12-porphyrin nanotube. Furthermore, we anticipate extensive excited-state delocalisation over the entire 18-porphyrin chromophore system. However, we are curious as to whether we will observe a similar transfer of exciton migration in the 18-porphyrin nanotube as was observed in its 12-porphyrin analogue (*i.e.* from the *z*-plane to the *xy*-plane), or whether after excitation of the trimer components emission will occur from the trimer component as well, rather than from the ring-entity in the *xy*-plane.

These potentially exciting properties, as well as the ambition to push the boundaries of supramolecular chemistry and construct increasingly large porphyrin nanostructures, inspired us to explore the synthesis and properties of a π-conjugated molecular nanotube constructed of 18-porphyrin units.

5.3 Towards a Bis-Acetylene Linked 18-Porphyrin Nanotube – *t*-P18

5.3.1 Synthesis of ***t*-P18·(T6)$_3$** *from* ***l*-P3**

Considering the efficient template-directed synthesis of ***t*-P12·(T6)$_2$** from ***l*-P2** (Chapter 3), it seems intuitive to employ a similar synthetic strategy towards longer porphyrin nanotubes such as ***t*-P18·(T6)$_3$**. This would involve direct coupling of a porphyrin trimer ***l*-P3**, in the

presence of 6-legged template **T6**. However, as was discussed previously, we expected this approach to lead to polymer formation *via* mismatched coupling (Chapter 3, Figure 3.4). To test this assumption, we submitted fully deprotected trimer ***l*-P3** to palladium catalysed oxidative coupling conditions in the presence of **T6** (Figure 5.2a).[1–4,10–12] The coupling was examined in chloroform and in toluene. Both reactions resulted mainly in polymeric materials that were removed during work-up. The small amount of material that was obtained after work-up, was subjected to analysis by analytical GPC (Figure 5.2b). The analytical GPC trace of the product mixture after work-up shows higher molecular weight materials and one major component which was identified as unreacted ***l*-P3** when referenced to fully protected ***l*-P3**.

This experiment confirmed our hypothesis that the template-directed synthesis of ***t*-P18·(T6)$_3$** is not viable directly from its linear precursor ***l*-P3**.

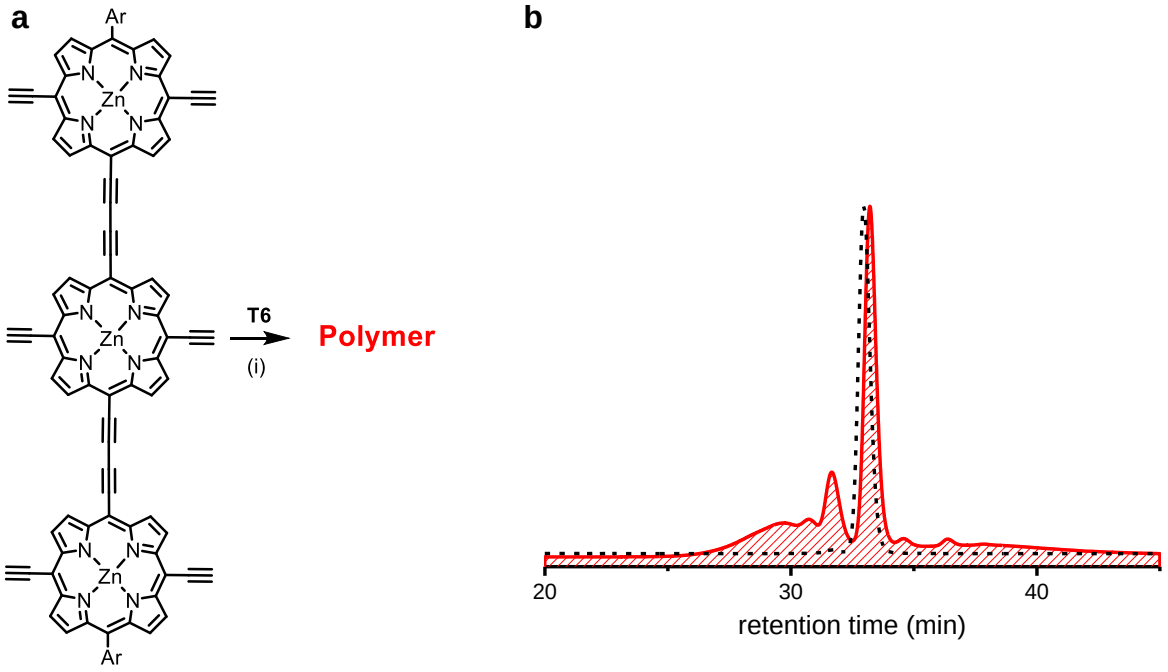

Figure 5.2: (a) Coupling of ***l*-P3** in the presence of **T6**; (i) **T6**, $Pd(PPh_3)_2Cl_2$, CuI, 1,4-benzoquinone, toluene or $CHCl_3$, *N*,*N*-diisopropylamine. (b) Analytical GPC traces (detection at 500 nm, THF/1% pyridine); (red trace) the reaction mixture from coupling of ***l*-P3** in the presence of **T6** (in $CHCl_3$ at 40 °C); (black dashed trace) ***l*-P3** (fully protected).

*5.3.2 A Synthetic Strategy to **t*-P18; The Pre-Tube Approach*

To circumvent the issue of mismatched coupling and consequential polymer formation, we designed a step-wise approach to the 18-porphyrin nanotube. This approach requires the synthesis of a porphyrin trimer containing orthogonal acetylene protecting groups on its

central and outer porphyrins. Selective deprotection of the acetylenes on the central porphyrin (R_1) and subsequent coupling in the presence of **T6** template was envisioned to result in a 6-porphyrin nanoring with 12 porphyrins on its *meso*-positions; a pre-tube complex (Figure 5.3). Removal of the acetylene protecting groups (R_2) on the outer porphyrins of this complex and subjecting the strongly pre-organised structure to coupling conditions should then lead to the formation of the 18-porphyrin nanotube.

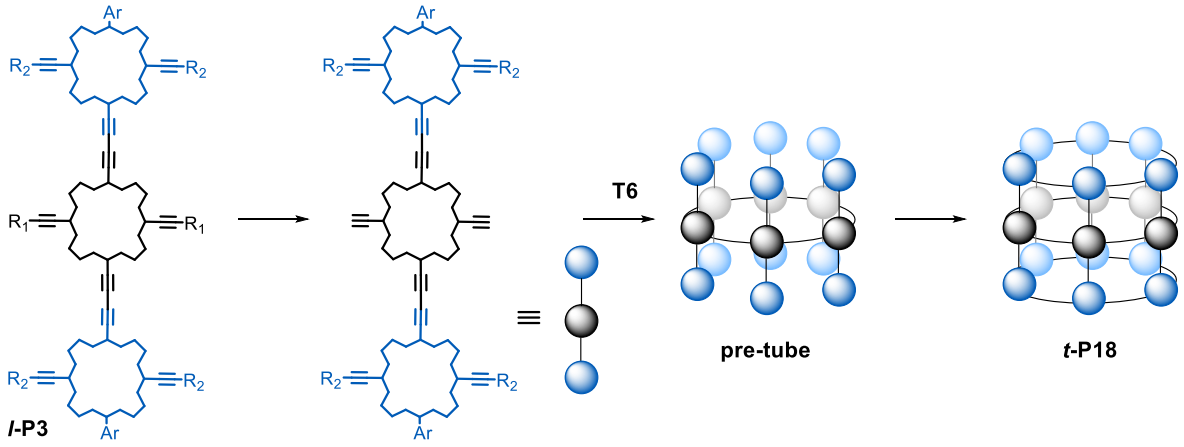

Figure 5.3: Schematic representation of the synthesis of an 18-porphyrin nanotube *via* the pre-tube approach.

5.3.3 Synthesis of a Bis-Acetylene Trimer with Orthogonal Protecting Groups

The porphyrin trimer for pre-tube synthesis requires orthogonal protecting groups on the central and outer porphyrins. This trimer can be prepared *via* the statistical coupling of an "outer porphyrin" bearing two TIPS-acetylene moieties on *meso*-positions 10 and 20, a solubilising group on *meso*-position 5 and an acetylene substituent on *meso*-position 15, and a "central porphyrin" bearing acetylene substituents on two opposing *meso*-positions and bromines on the other. The outer porphyrin monomer was prepared through a Sonogashira coupling with TMS-acetylene on **P1b** (synthesis of this compound was described in Chapter 3), to give **P1l**. Selective deprotection of the TMS acetylene protecting group gave **P1m** (Scheme 5.1).

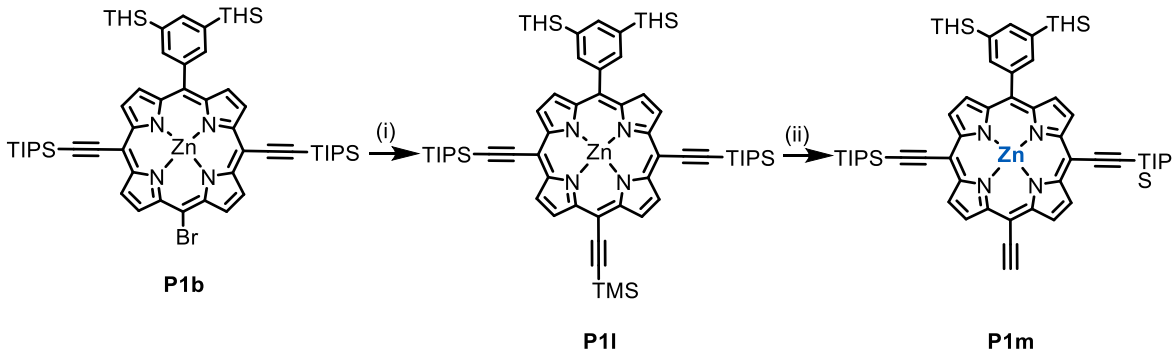

Scheme 5.1: (i) Pd_2dba_3, CuI, PPh_3, TMS-acetylene, toluene, *N,N*-diisopropylamine, 100%. (ii) K_2CO_3, THF, MeOH, 82%. The zinc atom in **P1m** is blue and bold according to the colour coding introduced in Figure 5.3.

The central porphyrin monomer was prepared in a 5-step synthesis from porphyrin **P1**, which was prepared according to literature procedures.[13,14] Magnesium insertion afforded **P1g**, which was brominated with NBS to afford **P1h**. Magnesium insertion was crucial for the bromination to occur. When the same reaction conditions were applied to the equivalent zinc porphyrin monomer, no bromination occurred. After bromination, demetallation afforded **P1i**. Re-metallation with zinc to **P1j** and subsequent deprotection of the TIPS acetylene protecting groups gave **P1k**, the central monomer for bis-acetylene trimer formation (Scheme 5.2).

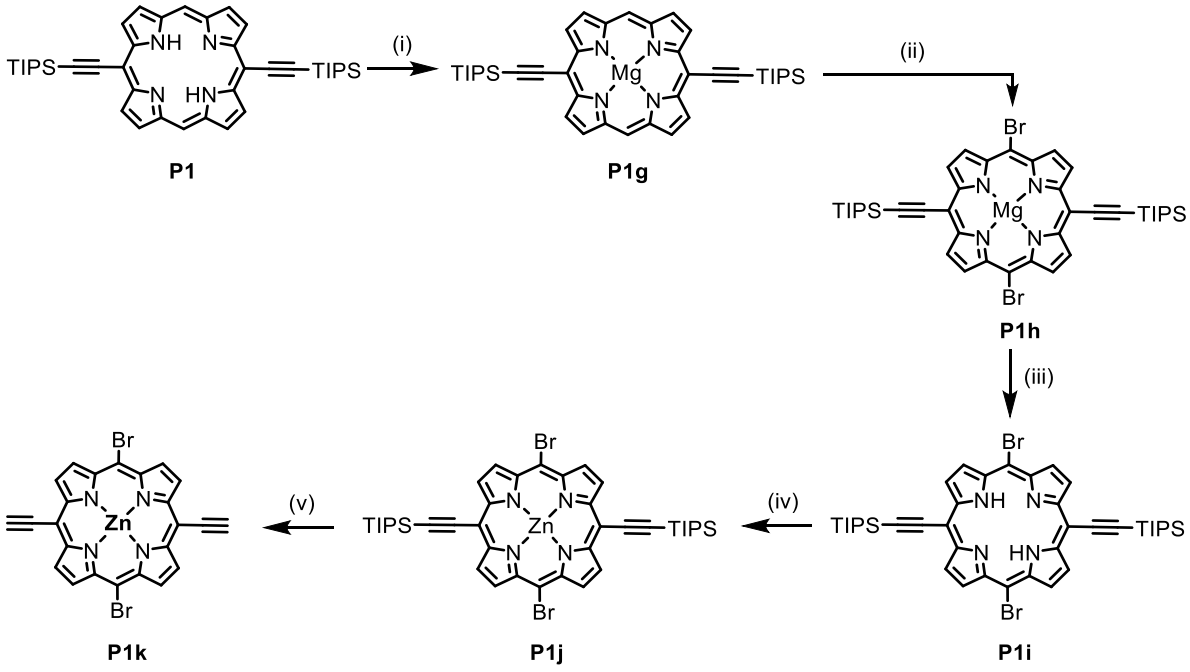

Scheme 5.2: (i) MgI_2, pyridine, Et_3N, reflux, 97%. (ii) NBS, $CHCl_3$, 63%. (iii) trifluoroacetic acid, $CHCl_3$, 91%. (iv) $Zn(OAc)_2{\cdot}2H_2O$, MeOH, $CHCl_3$, reflux, 100%. (v) TBAF, CH_2Cl_2, 93%. The zinc atom in **P1k** is black and bold, according to the colour coding introduced in Figure 5.3.

Trimer ***l*-P3$^{C\text{-}2Br}$** was prepared through a statistical coupling of the outer porphyrins (**P1m**) and central porphyrin (**P1k**). We found that a 3:1 outer to central porphyrin ratio gave the best yield of the desired trimer ***l*-P3$^{C\text{-}2CPDMS}$** (28% from **P1k**). Under these conditions a substantial amount of dimer, ***l*-P2$_{THS}$[TIPS]$_4$**, is formed *via* the homo-coupling of outer porphyrin **P1m** (50% from **P1m**). The different reaction products were separated by recycling GPC. ***l*-P2$_{THS}$[TIPS]$_4$** is a useful side-product as it is utilised for the template-directed synthesis of 12-porphyrin nanotube (Chapter 3).

To obtain the required orthogonal acetylene protecting group distribution, CPDMS-acetylene was coupled onto the central porphyrin monomer in ***l*-P3$^{C\text{-}2Br}$** *via* Sonogashira coupling to afford trimer ***l*-P3$^{C\text{-}2CPDMS}$** (Scheme 5.3).

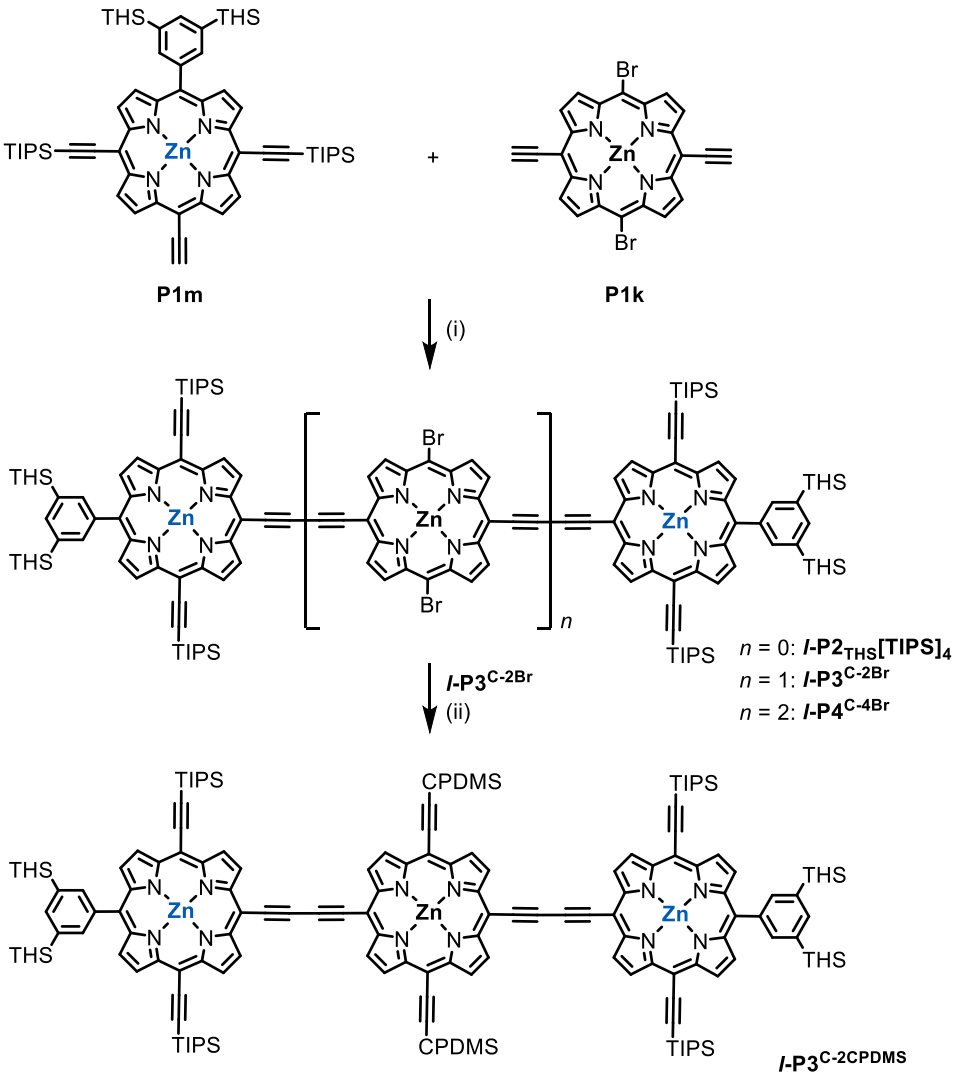

Scheme 5.3: (i) $Pd(PPh_3)_2Cl_2$, CuI, 1,4-benzoquinone, toluene, *N*,*N*-diisopropylamine, n = 0: 50% (from **P1m**), n = 1: 28% (from **P1k**), n = 3: 13% (from **P1k**) (ii) Pd_2dba_3, CuI, PPh_3, CPDMS-acetylene, toluene, *N*,*N*-diisopropylamine, 97%.

5.3.4 Synthesis of ***t*-P18·T6 pre-tube**

The CPDMS acetylene protecting groups in ***l*-P3$^{C\text{-}2CPDMS}$** were selectively removed using K_2CO_3 to give ***l*-P3$^{C\text{-}2acetylene}$**. Coupling of this centrally deprotected trimer in the presence of **T6** template gave the desired pre-tube in 7% yield (Scheme 5.4).

The yield of ***t*-P18·T6 pre-tube** from ***l*-P3$^{C\text{-}2acetylene}$** is significantly lower than that of ***c*-P6·T6** from porphyrin monomer (up to 36%),[15] while fundamentally, both reactions comprise the formation of a 6-porphyrin nanoring around **T6** from a monomeric building block. The recycling GPC trace of the reaction mixture from ***t*-P18·T6 pre-tube** synthesis shows that a large amount of higher molecular weight products is formed (Figure 5.4a). This might be caused by unfavourable wrapping of porphyrin trimer around the template (Figure 5.4b). This binding behaviour would disrupt the desired supramolecular arrangement of the trimer for ring-formation and explains the relative low yield of ***t*-P18·T6 pre-tube** formation.

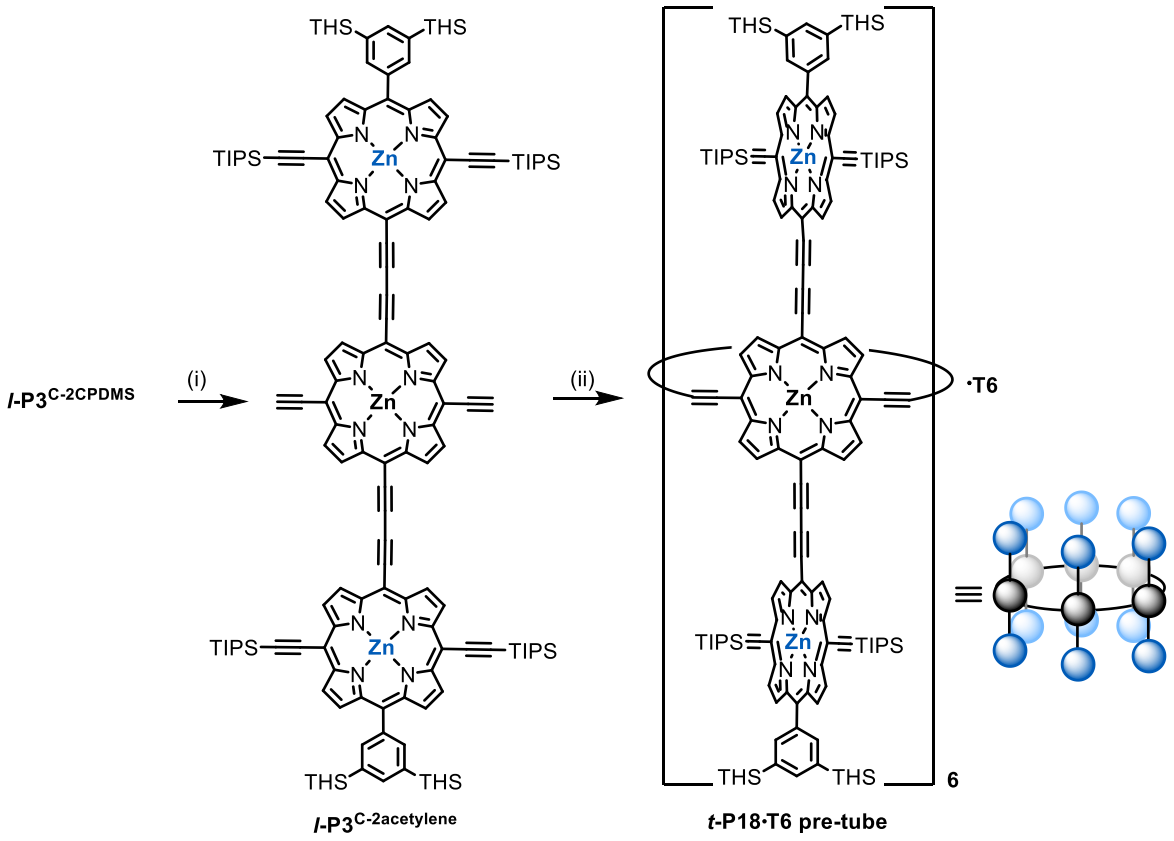

Scheme 5.4: (i) K_2CO_3, THF, MeOH, 100%. (ii) **T6,** $Pd(PPh_3)_2Cl_2$, CuI, 1,4-benzoquinone, toluene, *N*,*N*-diisopropylamine, 7%.

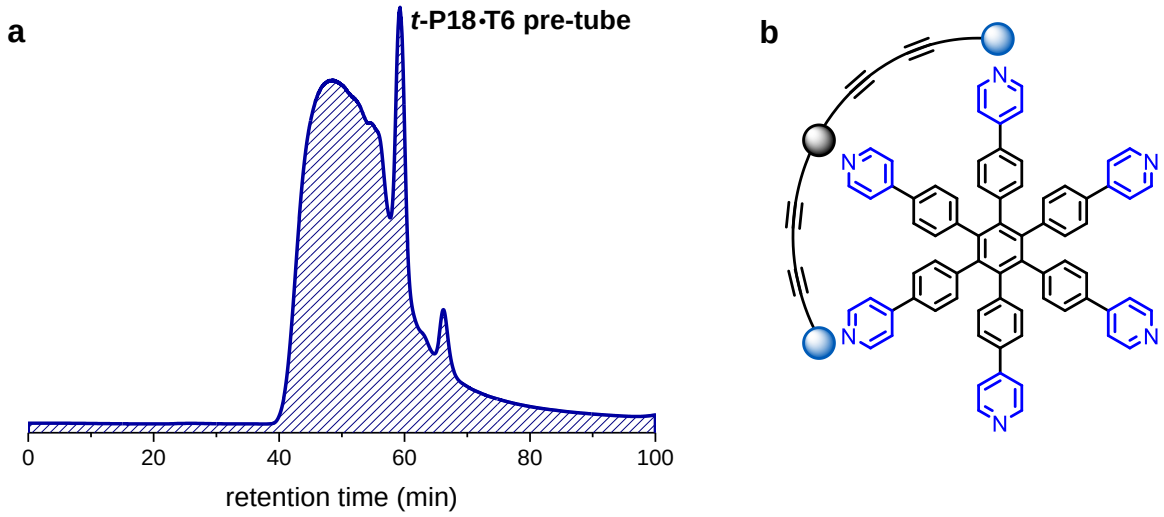

Figure 5.4: (a) Trace of the first round of recycling GPC (detection at 500 nm, toluene/1% pyridine) of the reaction mixture of ***t*-P18·T6 pre-tube** synthesis from ***l*-P3**$^{C\text{-}2acetylene}$. (b) Schematic representation of wrapping-mode binding of ***l*-P3** to **T6**.

The 18-porphyrin pre-tube was characterised by ^{1}H NMR and UV-vis-NIR spectroscopy. The ^{1}H NMR spectrum is relatively simple considering the size of the molecule (Mw: 20576 Da) due to its D_{6h} symmetry (Figure 5.5). The UV-vis-NIR absorption spectrum is different than simply the sum of its parts and shows a broad Q band consisting of three distinct peaks, which is characteristic for a 6-porphyrin nanoring.[9,16] The Soret band is broad as well and additionally, there is an unusual absorption at 658 nm which presumably originates from the trimer component (Figure 5.6).

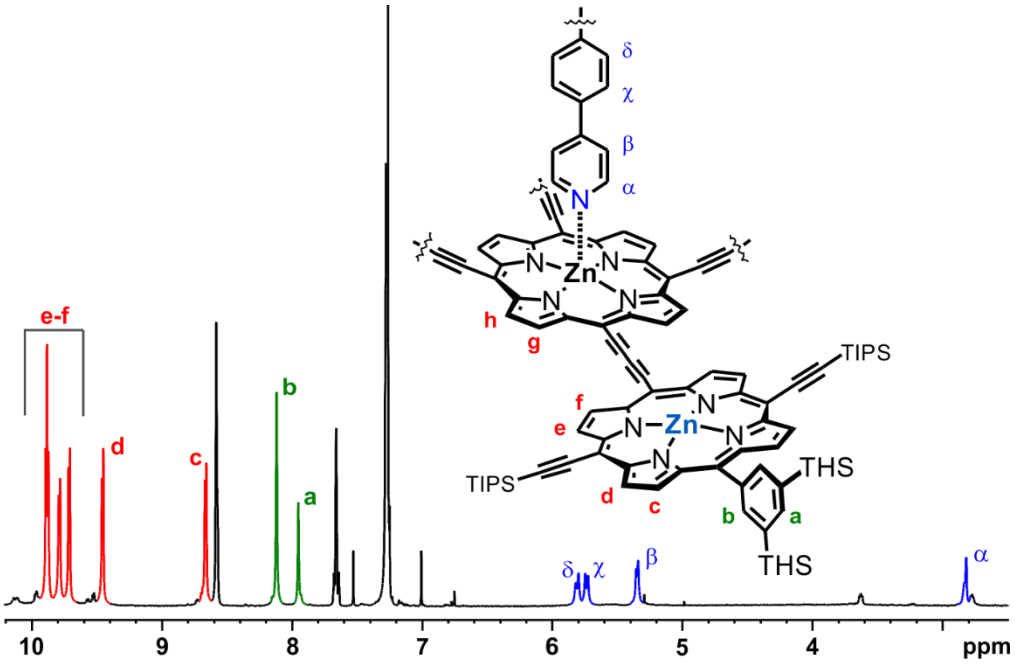

Figure 5.5: Region of the ^{1}H NMR spectrum (400 MHz, $CDCl_3$ + 1% pyridine-d_5, 298 K) of ***t*-P18·T6 pre-tube**.

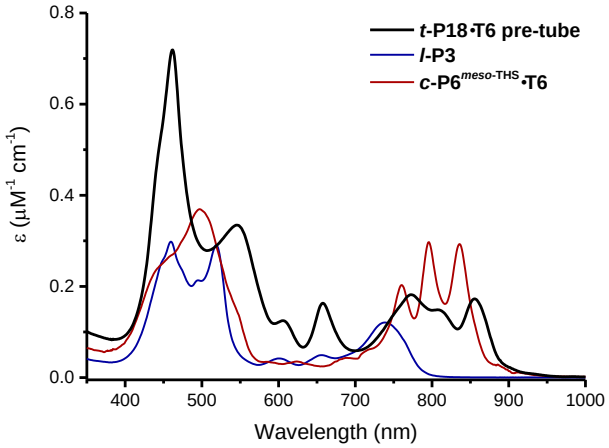

Figure 5.6: UV-vis-NIR absorption spectrum of ***t*-P18·T6 pre-tube** (black trace), ***l*-P3** (blue trace) and ***c*-P6$^{meso\text{-}THS}$·T6** (red trace) (all measured in $CHCl_3$ at 298 K).

5.3.5 Synthesis of ***t*-P18·(T6)$_3$** *from* ***t*-P18·T6 pre-tube**

Deprotection of the TIPS acetylene protecting groups on the outer porphyrins of ***t*-P18·T6 pre-tube** and subsequent coupling under palladium catalysed oxidative conditions was expected to lead to the 18-porphyrin nanotube (Scheme 5.5)

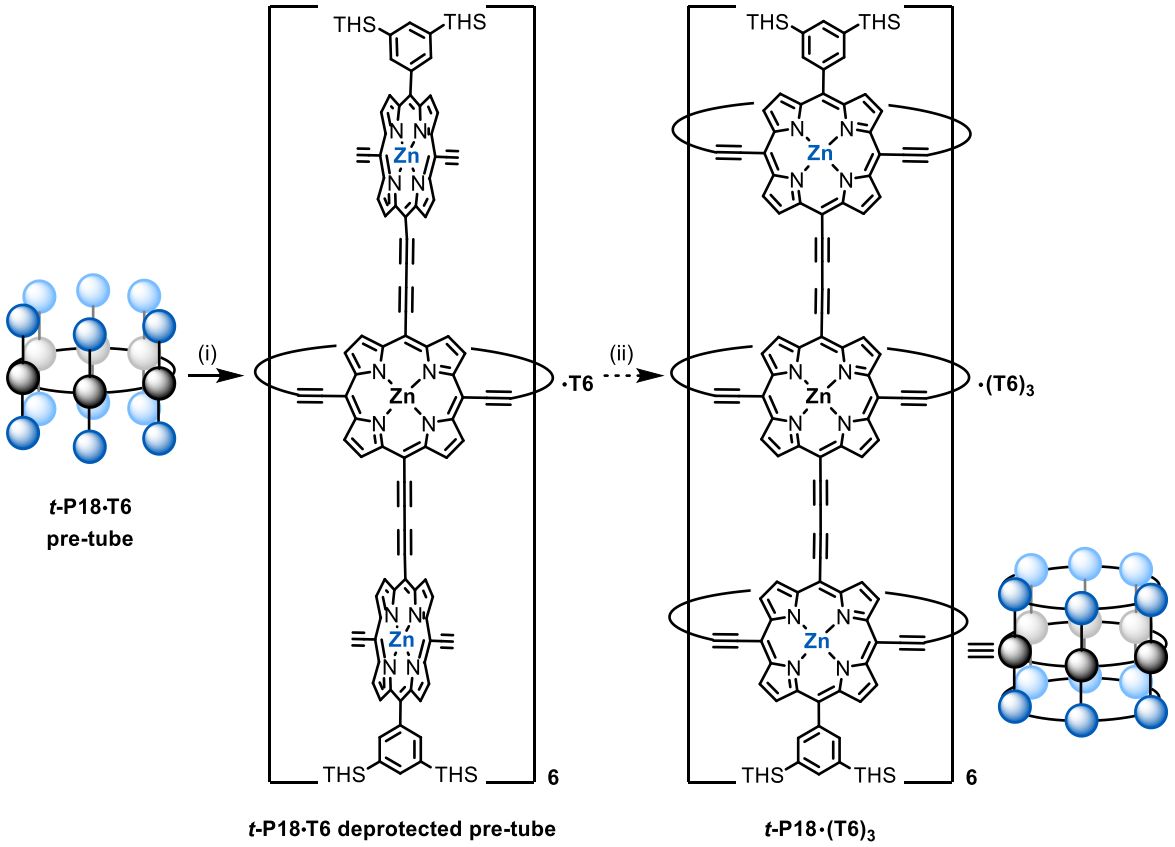

Scheme 5.5: (i) TBAF, toluene, pyridine, product not isolated. (ii) **T6,** $Pd(PPh_3)_2Cl_2$, CuI, 1,4-benzoquinone, toluene, *N*,*N*-diisopropylamine, product not isolated.

Deprotection of the pre-tube made the compound susceptible to polymerisation/decomposition upon drying. Therefore, after ***t*-P18·T6 pre-tube** was deprotected using TBAF in toluene/1% pyridine, and passed through a short SiO_2 plug, the material was directly proceeded to the next step. $CHCl_3$ and **T6** were added and the solution was stirred for 20 min to allow the complex to form, as confirmed by UV-vis-NIR spectroscopy. Subsequently, toluene and *N,N*-diisopropylamine were added and $CHCl_3$ was carefully removed under reduced pressure after which the mixture was subjected to palladium catalysed oxidative coupling conditions.

The reaction mixture changed colour over the course of the reaction from red to pink, indicating porphyrin nanotube formation. Upon completion, the material was passed through a short SiO_2 plug in toluene/1% pyridine. The product mixture was analysed by GPC (Figure 5.7), which shows the formation of a major product which is presumably ***t*-P18·(T6)$_3$** (with a retention time of 30.9 min) referenced to the fully protected ***t*-P18·T6 pre-tube** (retention time 30.5 min).

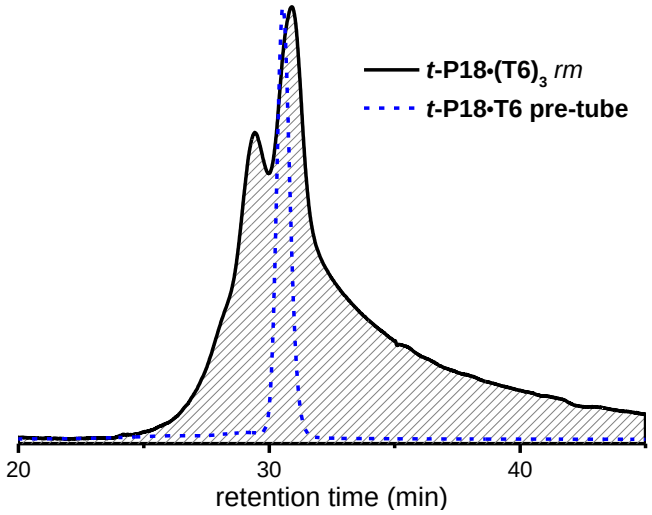

Figure 5.7: Analytical GPC traces (recorded at 500 nm, THF/1% pyridine) of the ***t*-P18·(T6)$_3$** reaction mixture (black solid trace), and ***t*-P18·T6 pre-tube** (blue dashed trace).

Unfortunately, the material was found to streak on the recycling GPC columns (toluene/1% pyridine) and ***t*-P18·(T6)$_3$** could not be isolated. Considering the relatively low yields in the statistical preparation of ***l*-P3$^{C\text{-}2Br}$** and the preparation of ***t*-P18·T6 pre-tube**, we decided to adjust our strategy to 18-porphyrin nanotube which will be discussed in the following sections.

5.4 Introducing a New Solubilising Group

One of the issues when building increasingly large porphyrin nanostructures is their limited solubility. Over the course of two decades of porphyrin research in the Anderson group, the increasing size of porphyrin nanostructures has required the development of progressively powerful solubilising substituents. In the synthesis of ***c*-P6·T6**, *tert*-butyl and octyloxy solubilising groups gave comparable yields.[10] For most of the subsequently prepared larger nanorings with up to 50-porphyrin units, the octyloxy moiety was used to ensure solubility.[2,3,11]

The trihexylsilyl (THS) solubilising aryl group was introduced in 2007 in a study of charge transport in porphyrin-based molecular wires. This solubilising substituent enabled the solubility of the porphyrin oligomers even in nonpolar solvents.[17] Hence, THS has been the solubilising group of choice for most of the recently synthesised porphyrin nanostructures such as spiro-fused nanorings,[18] copper-porphyrin systems,[19] mono-acetylene linked porphyrin nanorings,[20] and a 12-porphyrin nanotube.[9]

We suspected the insolubility after deprotection of the ***t*-P18·T6 pre-tube** and streaking on the GPC, as discussed above, to be a result of limited solubility. Hence, we deduced that the THS moiety does not provide sufficient solubilising power for this next-generation porphyrin nanostructure. Therefore, we designed a new solubilising group with an even longer alkyl chain; diisopropyloctadecylsilyl (DIBODS, Figure 5.8). This new solubilising group was utilized in our second-generation design to an 18-porphyrin nanotube.

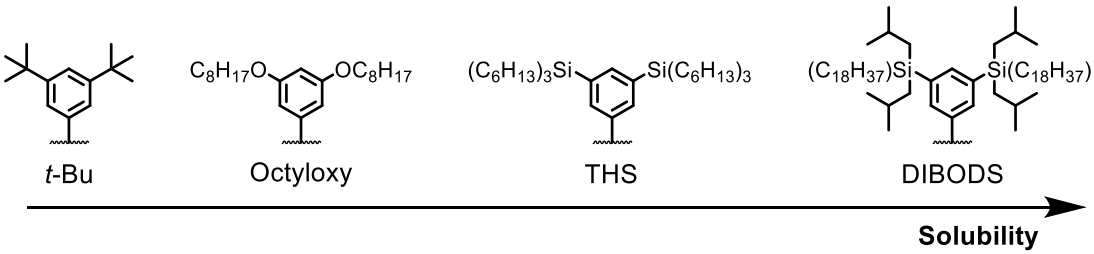

Figure 5.8: Aryl-substituents with progressively powerful solubilising substituents to allow for solubility of increasingly big porphyrin nanostructures.

5.5 Second-Generation Design; Mono-Acetylene Linked Porphyrin Nanotubes

The use of mono-acetylene linked porphyrin oligomers for nanotube formation provides a dual benefit. First, the synthesis of the oligomer itself can occur *via* a Sonogashira cross-coupling reaction. This allows a more efficient conversion of starting materials to the desired oligomer, compared to the statistical coupling required to prepare bis-acetylenic oligomers. Second, the mono-acetylenic oligomers do not possess a suitable geometry for binding around the **T6** template in an unfavourable wrapping-mode (Figure 5.9). Hence a perpendicular binding mode of the mono-acetylene linked trimer to the template is expected, which should improve the yield of the 18-porphyrin pre-tube complex.

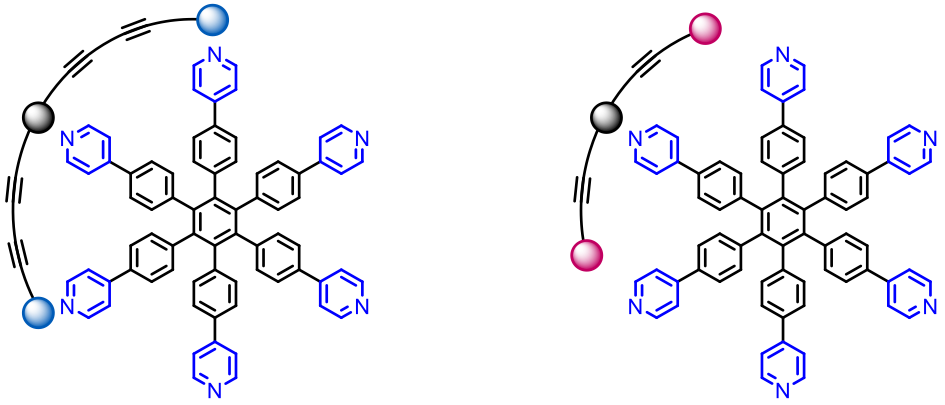

Figure 5.9: Schematic representation of the binding of bis-acetylenic porphyrin trimer (left) and mono-acetylenic porphyrin trimer (right) to **T6** template.

5.6 Synthesis of Mono-Acetylene Linked Porphyrin Dimer and Trimer

5.6.1 Synthesis of DIBODS-Aryl Substituted Porphyrin Monomer

As we wanted to incorporate the new DIBODS solubilising group in our second-generation design to an 18-porphyrin nanotube, we prepared porphyrin monomer **P1q** in an analogous way to its THS-solubilised counterpart **P1m** (see Scheme 5.1). **P1q** was prepared from porphyrin monomer **P1** *via* a lithium-mediated arylation reaction (**P1n[2H]**). After zinc insertion (**P1n[Zn]**), the porphyrin was brominated to give **P1o**. Sonogashira coupling with TMS-acetylene gave **P1p** which enabled selective deprotection to give **P1q** (Scheme 5.6).

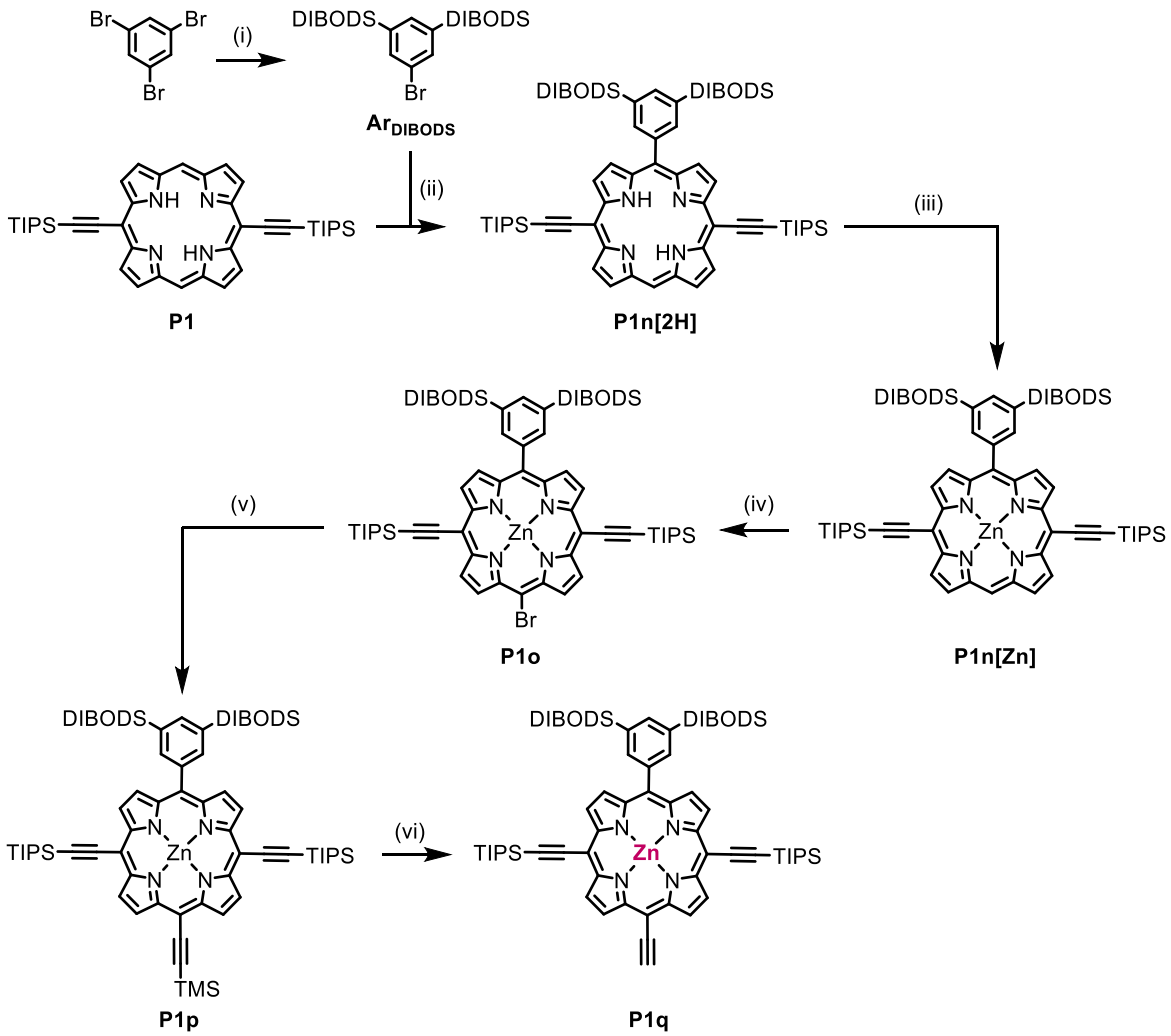

Scheme 5.6: (i) *n*-butyl lithium, DIBODS-chloride, Et_2O. (ii) *n*-butyl lithium, then H_2O, DDQ, Et_3N, Et_2O, THF, 63%. (iii) $Zn(OAc)_2{\cdot}2H_2O$, $CHCl_3$, MeOH, 100%. (iv) NBS, $CHCl_3$, pyridine, 52%. (v) Pd_2dba_3, CuI, PPh_3, toluene, *N*,*N*-diisopropylamine, TMS-acetylene, 98%. (vi) K_2CO_3, THF, MeOH, 100%. The zinc atom in **P1q** is pink and bold according to the colour coding introduced in Figure 5.9.

5.6.2 Synthesis of Mono-Acetylene Linked Porphyrin Dimer ***l*-P2*[TIPS]$_4$**

To examine the effect of the shorter inter-ring linkages on the properties of a porphyrin nanotube, we prepared a 12-porphyrin nanotube with mono-acetylene connections between the conjoined 6-porphyrin nanorings.

Sonogashira cross-coupling of porphyrin monomers **P1o** and **P1q** in a 3:1 ratio gave the mono-acetylene-connected porphyrin dimer ***l*-P2*[TIPS]$_4$** in 97% yield (Scheme 5.7). Of the excess **P1o**, 52% was recovered during the purification. As a minor side product, bis-acetylene porphyrin dimer, ***l*-P2$_{DIBODS}$[TIPS]$_4$**, was obtained *via* the homo-coupling of **P1q** (<1% from **P1q**). This material could be separated from the target molecule ***l*-P2*[TIPS]$_4$** *via* extensive recycling GPC.

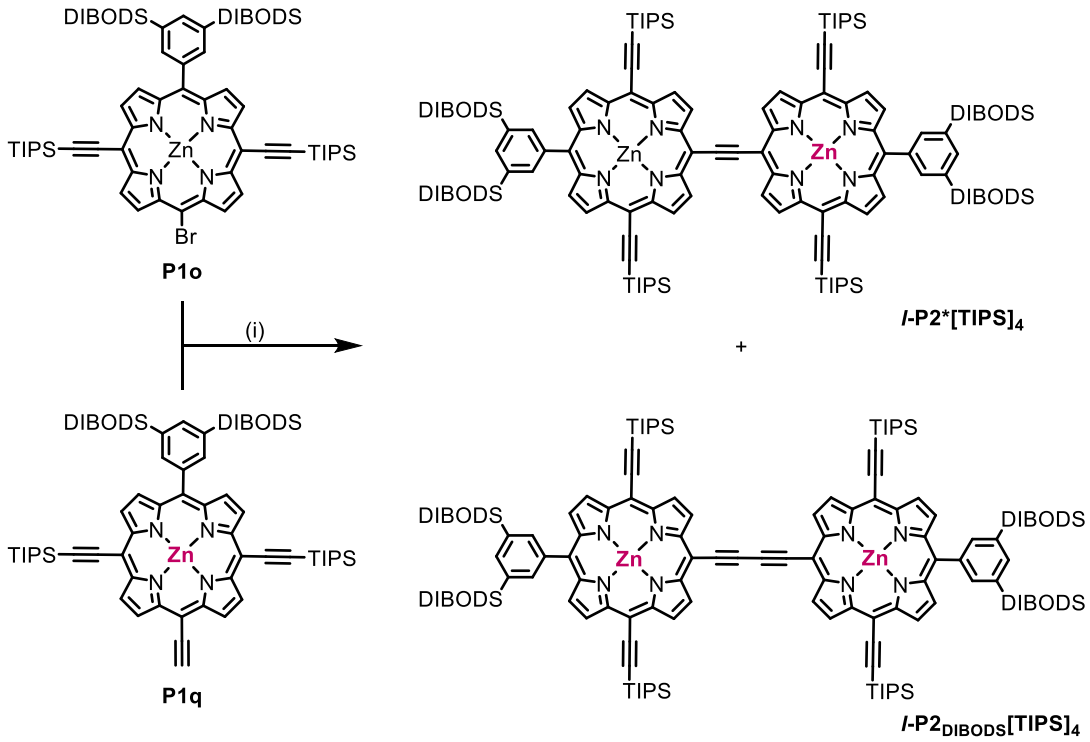

Scheme 5.7: (i) Pd_2dba_3, CuI, PPh_3, toluene, *N*,*N*-diisopropylamine, ***l*-P2*[TIPS]$_4$**; 86%, ***l*-P2$_{DIBODS}$[TIPS]$_4$**; <1%.

5.6.3 Synthesis of Mono-Acetylene Linked Porphyrin Trimer ***l*-P3$^{*C\text{-}2TMS}$**

To enable selective deprotection of the central monomer in the mono-acetylene linked porphyrin trimer, the TIPS acetylene protecting groups on **P1j** were removed (**P1k**) and the acetylenes were re-protected with TMS-substituents to give **P1r** (Scheme 5.8)

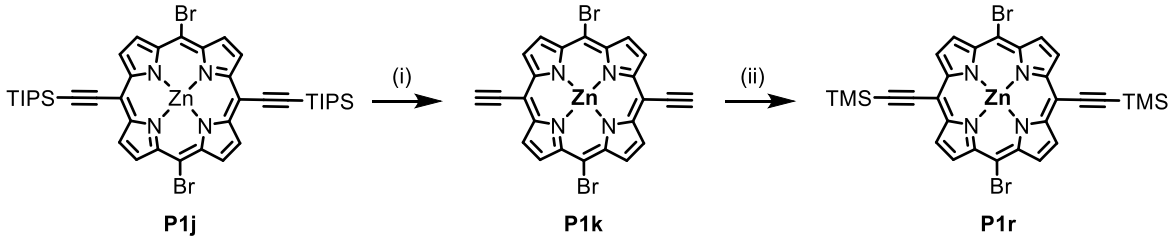

Scheme 5.8: (i) TBAF, CH_2Cl_2, 93%. (ii) LiHMDS, then TMS-chloride, THF, 53%. The zinc atom in **P1r** is black and bold according to the colour coding introduced in Figure 5.9.

Sonogashira cross-coupling of the porphyrin monomers **P1q** and **P1r** in a 3:1 ratio gave the mono-acetylenic porphyrin trimer ***l*-P3$^{*C\text{-}2TMS}$** in 96% yield from **P1r** (Scheme 5.9). As a side product, bis-acetylene porphyrin dimer was obtained *via* the homo-coupling of **P1q** (28% from **P1q**). This could be separated from ***l*-P3$^{*C\text{-}2TMS}$** *via* recycling GPC.

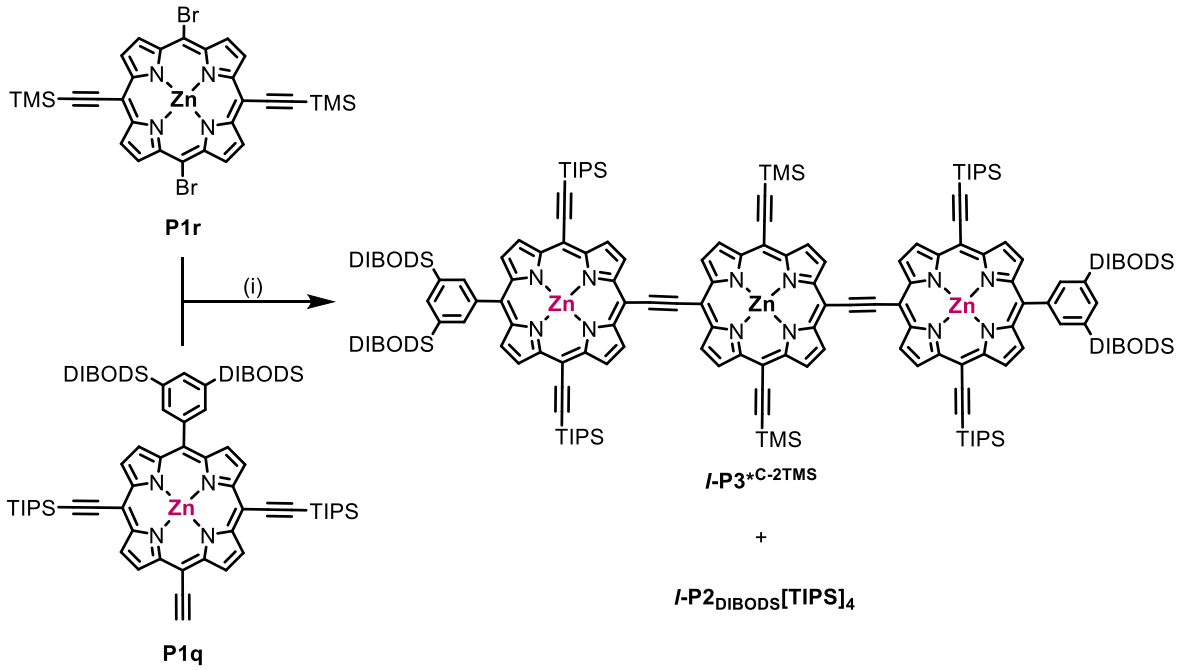

Scheme 5.9: (i) Pd_2dba_3, CuI, PPh_3, toluene, *N*,*N*-diisopropylamine, ***l*-P3*$^{C\text{-}2TMS}$** 96% from **P1r**; ***l*-P2$_{DIBODS}$[TIPS]$_4$**; 28% from **P1q**.

5.7 Synthesis and Properties of *t*-P12*·(T6)$_2$

5.7.1 Template-Directed Synthesis of ***t*-P12*·(T6)$_2$**

The TIPS acetylene protecting groups on ***l*-P2*[TIPS]$_4$** were removed with TBAF. Coupling of ***l*-P2*[acetylene]$_4$** in the presence of **T6** template gave ***t*-P12*·(T6)$_2$** in 7% yield after purification *via* recycling GPC (Scheme 5.10). The GPC trace shows that most higher molecular weight side-products are removed during the work-up (Figure 5.10).

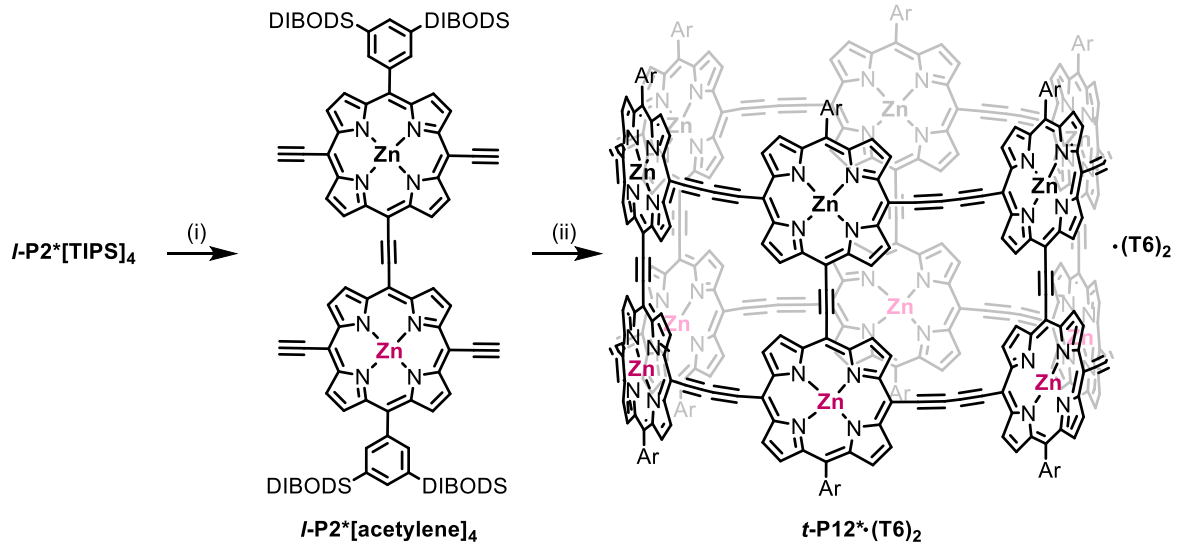

Scheme 5.10: (i) TBAF, CH_2Cl_2, 100%. (ii) **T6,** $Pd(PPh_3)_2Cl_2$, CuI, 1,4-benzoquinone, toluene, *N*,*N*-diisopropylamine, 7%.

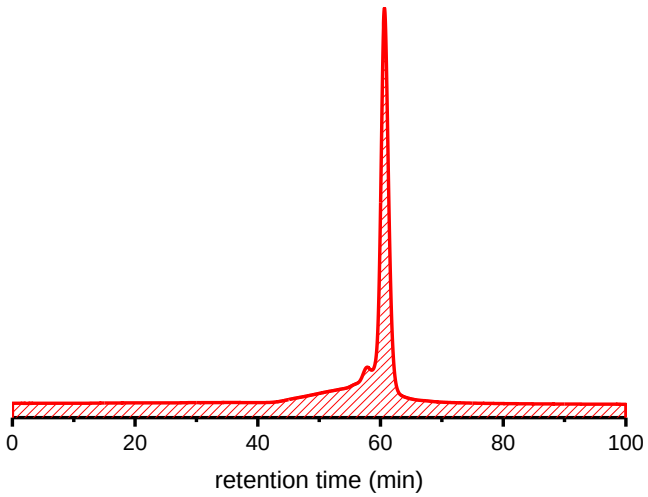

Figure 5.10: Recycling GPC trace (recorded at 400 nm, toluene/1% pyridine) of the ***t*-P12*·(T6)$_2$** reaction mixture, performed at 23 °C (6 h).

The synthesis of mono-acetylene linked 12-porphyrin nanotube proved to be challenging. The conditions used for the synthesis of bis-acetylene linked porphyrin nanotube ***t*-P12·(T6)$_2$** (see Chapter 3) resulted in a structure that characterised with broad peaks in the ^{1}H NMR spectrum. Extensive screening of the reaction conditions indicated that this reaction is particularly sensitive to the freshness of *N,N*-diisopropylamine and the reaction temperature.

The ^{1}H NMR spectrum of ***t*-P12*·(T6)$_2$** after the reaction has been performed at 65 °C with *N,N*-diisopropylamine which had been distilled a few weeks prior and stored over molecular sieves, compared to the reaction performed at the same temperature with freshly distilled *N,N*-diisopropylamine, shows relatively sharper signals in case of the latter (Figure 5.11). Furthermore, when the reaction was performed with freshly distilled *N,N*-diisopropylamine at 23 °C, further sharpening of the signals was observed (Figure 5.11). When the reaction was performed at 65 °C higher yields were obtained (up to 17%) and reaction times were shorter (2 h), however the only sharp ^{1}H NMR spectrum was acquired for the product of the reaction performed at 23 °C (with 6 h reaction time).

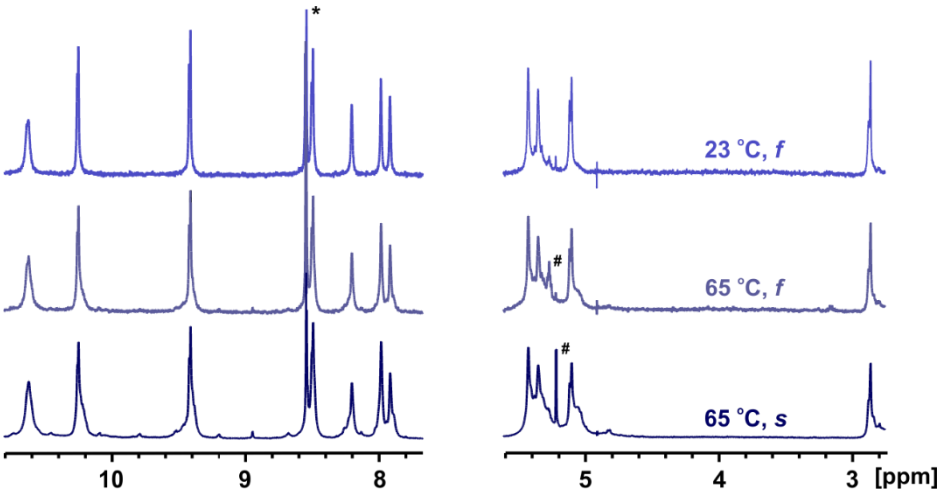

Figure 5.11: Region of the ^{1}H NMR spectra (400 MHz, $CDCl_3$ + 1% pyridine-d_5, 298K) of ***t*-P12*·(T6)$_2$** obtained after template-directed synthesis from ***l*-P2*[acetylene]$_4$** at 65 °C and 23 °C (***s*** = synthesis using *N*,*N*-diisopropylamine stored over molecular sieves, ***f*** = synthesis using freshly distilled *N*,*N*-diisopropylamine, * = pyridine residual signal, # = CH_2Cl_2 residual signal).

5.7.2 Characterisation of ***t*-P12*·(T6)$_2$**

Full assignment of the β-, aryl- and template proton NMR signals of ***t*-P12*·(T6)$_2$** was achieved *via* COSY and NOESY experiments (Figure 5.12 - Figure 5.15). The template protons **α**-**δ** were assigned using NOESY experiments in which **α**, the most strongly shielded template proton, shows strong NOESY correlations to the porphyrin β-protons **c**-**f** and to aryl proton **a** (Figure 5.13). Template proton **β** shows weak NOESY correlations to the same protons.

Assignment of the β-protons was achieved with a combination of COSY and NOESY experiments. NOESY correlations were found between *ortho*-aryl-proton **a** and **b**/**b'** and β-protons **c** and **d** (Figure 5.14). The substantial difference in chemical shifts allowed for the assignment of **d** (9.49 ppm) and **c** (8.57 ppm) since protons in close proximity to an acetylene moiety resonate relatively downfield. The stronger NOESY correlation of **a** and **b**/**b'** to **c** confirm this assignment.

Assignment of β-proton **d** allows for the assignment of proton **e** as there is a weak NOESY correlation between the two protons (Figure 5.14). Proton **e** subsequently shows a COSY correlation to proton **f** (Figure 5.15). This completes the assignment of the β-, aryl- and template proton signals of ***t*-P12*·(T6)$_2$** (Figure 5.12).

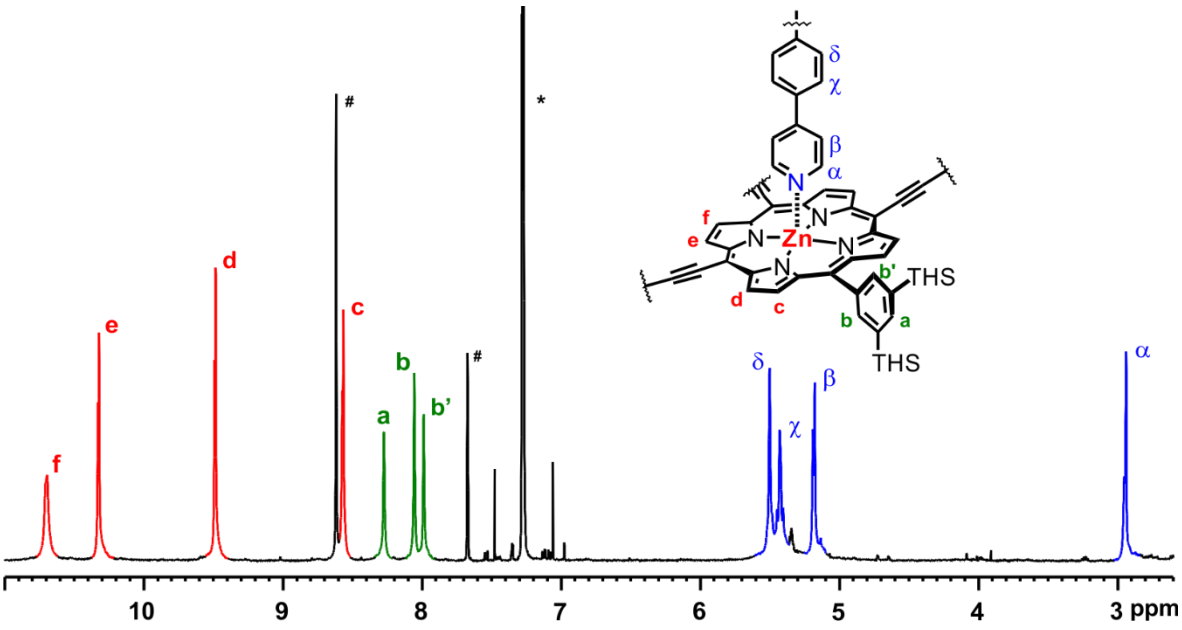

Figure 5.12: Region of the ^{1}H NMR spectrum (500 MHz, $CDCl_3$ + 1% pyridine-d_5, 298 K) of ***t*-P12*·(T6)$_2$** (# = pyridine residual signal, * = solvent residual signal). β-proton, aryl-proton and template-proton assignments were achieved *via* COSY and NOESY experiments.

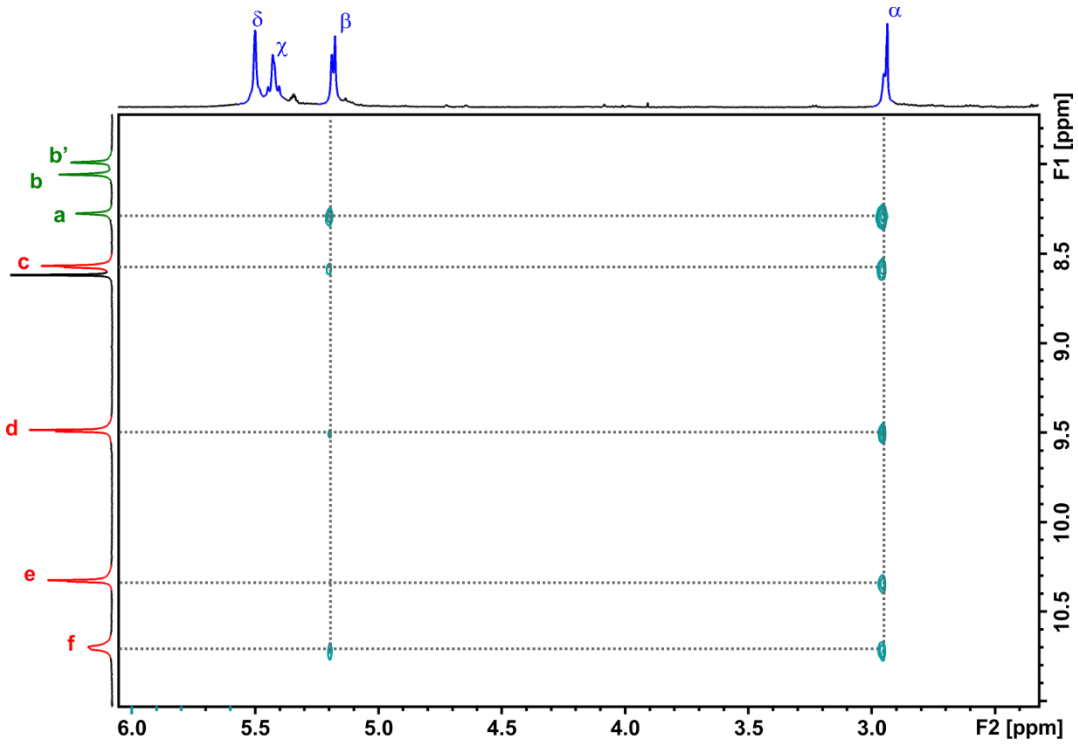

Figure 5.13: Region of the NOESY spectrum (500 MHz, $CDCl_3$ + 1% pyridine-d_5, 298 K) of ***t*-P12*·(T6)$_2$** with cross-peaks from template protons **α** and **β** to porphyrin protons **c**-**f** and **a**.

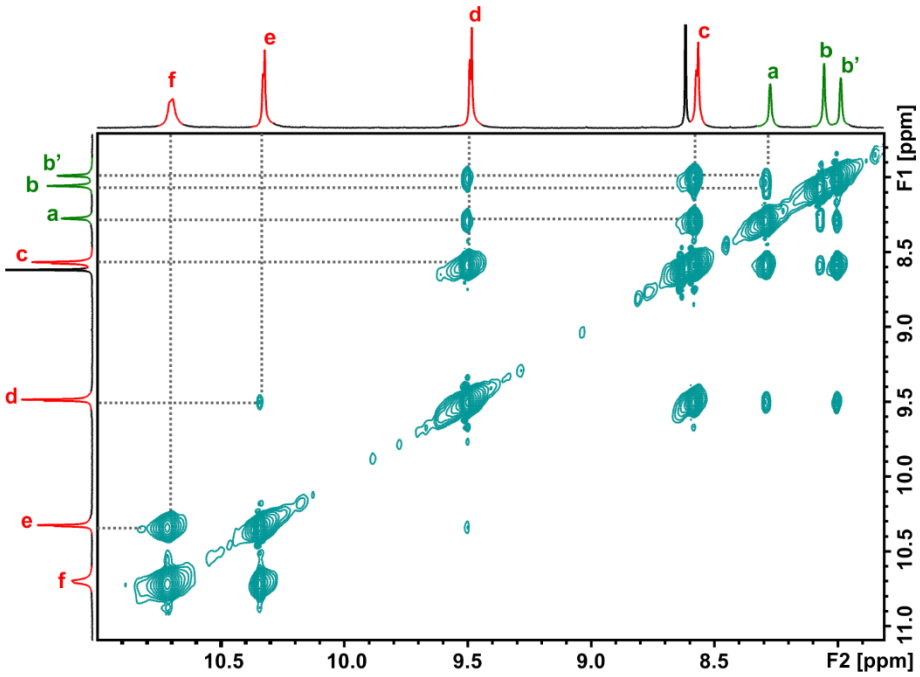

Figure 5.14: β-proton and aryl-proton region of the NOESY spectrum (500 MHz, $CDCl_3$ + 1% pyridine-d_5, 298 K) of ***t*-P12*·(T6)$_2$** with selected cross-peaks.

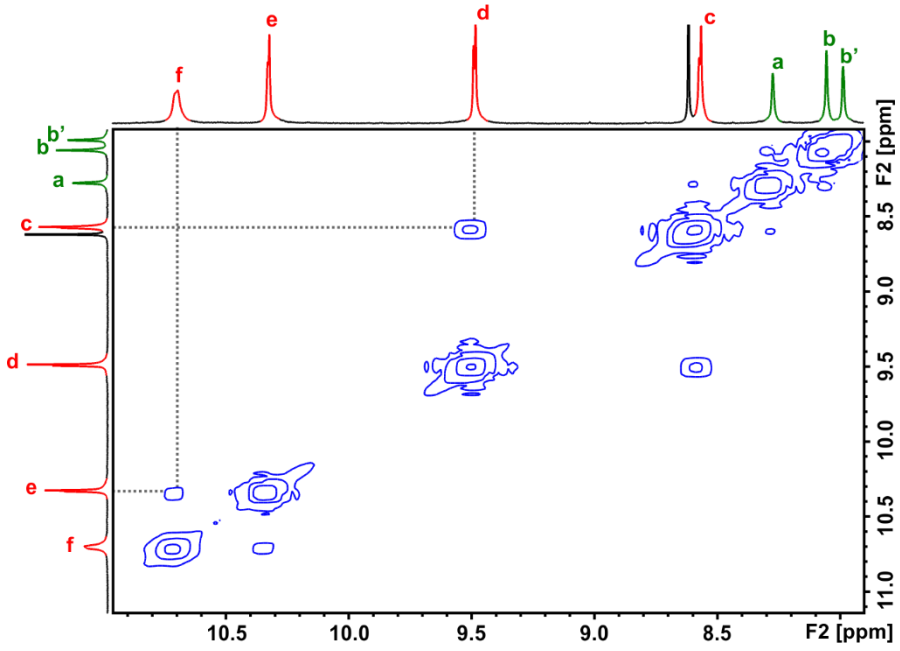

Figure 5.15: Region of the COSY spectrum (500 MHz, $CDCl_3$ + 1% pyridine-d_5, 298 K) of ***t*-P12*·(T6)$_2$** with assigned cross-peaks from **e** to **f** and from **d** to **c**.

The β-proton which is closest to the mono-acetylene link (**f**) resonates further downfield (at 10.7 ppm) than the analogous proton in the ***l*-P2*** precursor (10.4 ppm) and the analogous proton in the bis-acetylene 12-porphyrin nanotube (10.0 ppm; Chapter 3,

Figure 3.8). Proton **e** shows a similar relative downfield shift. This suggest that for ***t*-P12*·(T6)$_2$**, protons **f** and **e** are strongly deshielded by the ring currents from both porphyrins across the mono-acetylene link, which furthermore provides evidence of the (template enforced) co-planar conformation of the dimer-unit in this complex.

MALDI-ToF analysis shows three sharp peaks at m/z 17556, 16593 and 15565, corresponding to ***t*-P12*·(T6)$_2$** (Calculated m/z: 17551.91), ***t*-P12*·T6** and ***t*-P12***, respectively (Figure 5.16).

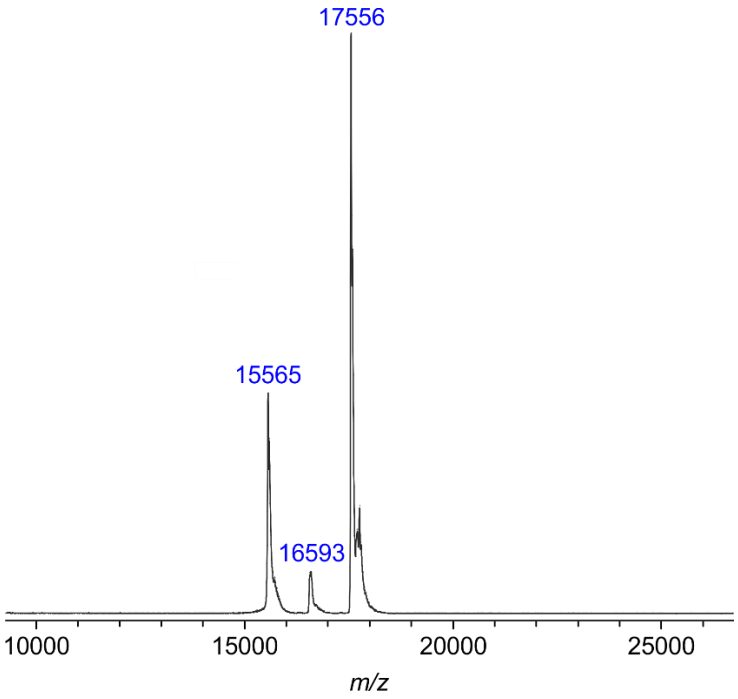

Figure 5.16: MALDI-ToF spectrum of ***t*-P12*·(T6)$_2$** (Matrix: DCTB).

5.7.3 Photophysical Properties of ***t*-P12*·(T6)$_2$**

The enhanced conjugation in ***t*-P12*·(T6)$_2$** relative to ***t*-P12·(T6)$_2$** is illustrated by a bathochromic shift in absorption of 40 nm (Figure 5.17, solid traces). To gain further insight in the photophysical properties of ***t*-P12*·(T6)$_2$**, the fluorescence emission and quantum yield were measured (Figure 5.17, pink dotted trace). The fluorescence quantum yield of ***t*-P12*·(T6)$_2$** (0.088%) is lower than that of ***t*-P12·(T6)$_2$** (0.22%, Figure 5.17, black dotted trace). This can partly be attributed to the stronger conjugation and hence smaller HOMO-LUMO gap in the first system. This would allow for more efficient non-radiative decay, a phenomenon generally summarised as the *Energy Gap Law*; the smaller the gap between ground and excited state, the more efficient non-radiative decay processes are, and hence the fluorescence quantum yield is reduced.[21–23] However, it is likely that the lower

fluorescence quantum yield of ***t*-P12*·(T6)$_2$** is a consequence of non-radiative decay pathways that are not yet understood.

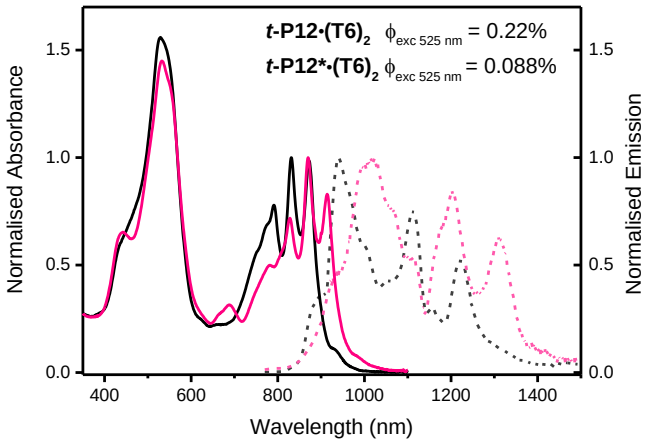

Figure 5.17: Normalised steady-state absorption (pink line) and fluorescence (pink dotted line) of ***t*-P12*·(T6)$_2$** and normalised steady-state absorption (black line) and fluorescence (black dotted line) of ***t*-P12·(T6)$_2$** (both λ_{exc} = 525 nm, measured in toluene at 298 K).

5.8 Synthesis and Properties of *t*-P18*·(T6)$_n$

5.8.1 Complexation of ***l*-P3*** *with* **T6**

We examined if the mono-acetylene linked porphyrin trimer would enable the template-directed synthesis of ***t*-P18*·(T6)$_3$** directly from ***l*-P3*** (instead of a pre-tube strategy described in Section 5.3.2). We anticipated ***l*-P3*** to form a tubular supramolecular complex with **T6** template as we expected it to favour perpendicular binding to the template (Figure 5.18) rather than a wrapping binding mode.[24]

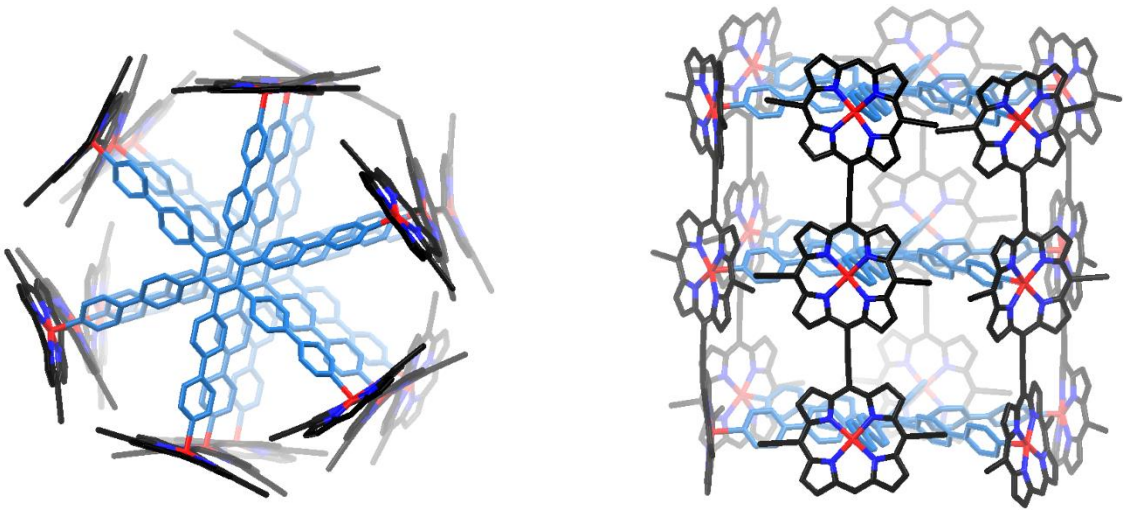

Figure 5.18: Calculated structure of **(*l*-P3*)$_6$·(T6)$_3$** with hydrogen atoms omitted (modified MM2 force field, aryl groups bearing solubilising side chains were omitted to simplify the calculation).

UV-vis-NIR titrations were performed to investigate the formation of the **(*l*-P3*)$_6$·(T6)$_3$** complex. A solution of **T6** template was titrated into a solution of fully deprotected ***l*-P3***. The titration curve shows a clear end-point at 0.5 **T6** to ***l*-P3*** ratio (Figure 5.19). This is in excellent agreement with the formation of a supramolecular tubular complex of three **T6** templates and six ***l*-P3*** moieties. The **T6**:***l*-P3*** ratio of 0.5 at the titration end-point is consistent with a 1:2 complex as well, however this would require a wrapping binding-mode of the porphyrin trimers around the **T6** template and this is geometrically unlikely.

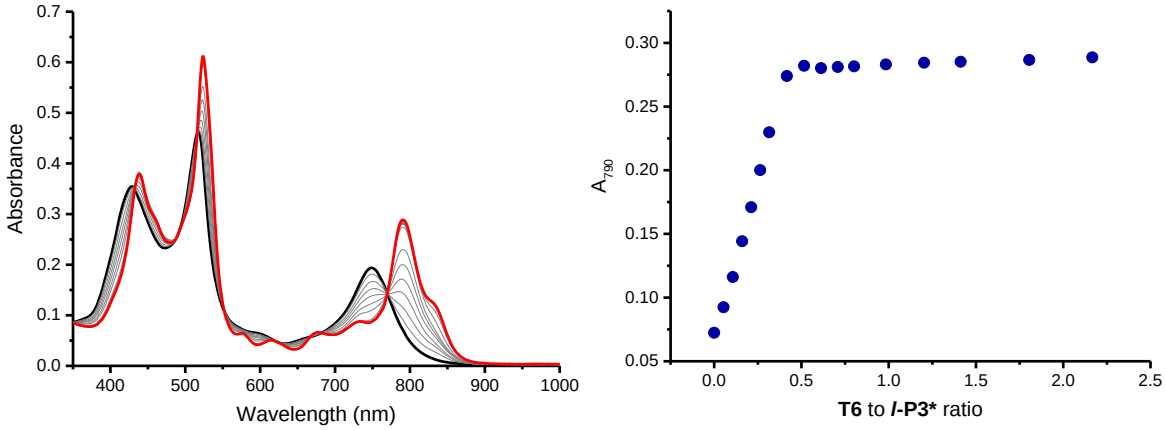

Figure 5.19: (left) UV-vis-NIR titration of ***l*-P3*[acetylene]$_6$** with **T6** (the black trace denotes the start of the titration; the red trace denotes the end of the titration, measured in $CHCl_3$ at 298 K). (right) Plotted absorption at 790 nm.

5.8.2 Direct Synthesis of ***t*-P18*·(T6)$_3$** *from* ***l*-P3***

Encouraged by the results from the UV-vis-NIR titration experiments, we examined the template-directed synthesis of ***t*-P18*·(T6)$_3$** *via* direct coupling of ***l*-P3*** in the presence of **T6** (Scheme 5.11).

Extensive reaction screening was performed to determine optimal reaction conditions, which were found to be coupling in $CHCl_3$ at 23 °C. The catalyst mixture was added as a solution in toluene and *N*,*N*-diisopropylamine such that the concentration of the latter would not exceed 2% v/v of the total reaction volume. Reaction progress was monitored by UV-vis-NIR spectroscopy. When no more spectroscopic changes were observed, the reaction mixture was passed through an Al_2O_3 plug and eluted with $CHCl_3$. The crude material was further purified by size-exclusion chromatography (THF/1% pyridine) and finally subjected to recycling GPC (THF/1% pyridine).

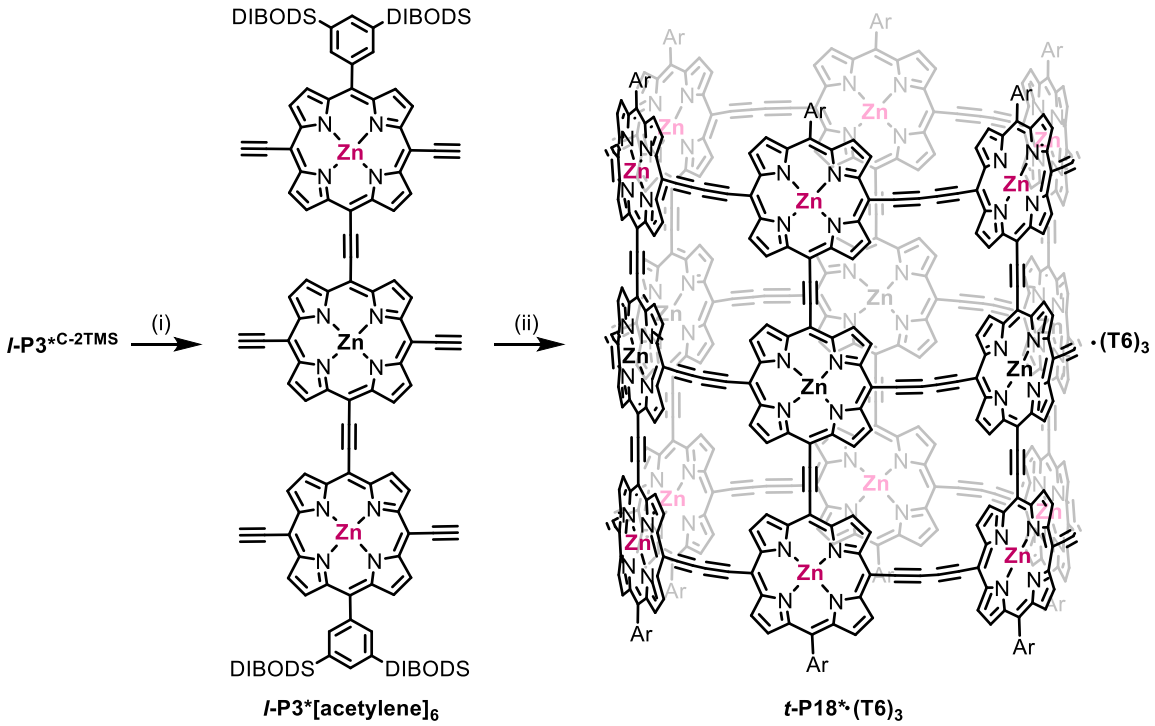

Scheme 5.11: (i) TBAF, CH_2Cl_2, pyridine, 98%. (ii) **T6,** $Pd(PPh_3)_2Cl_2$, CuI, 1,4-benzoquinone, $CHCl_3$, toluene, *N,N*-diisopropylamine, yield not determined.

The recycling GPC trace (Figure 5.20) shows that besides ***t*-P18*·(T6)$_3$**, a large amount of higher molecular weight material is formed. Unfavourable mismatched coupling of the linear precursor prevails, despite the presumed supramolecular pre-organisation of ***l*-P3*[acetylene]$_6$** in a tubular arrangement. The amount of polymerisation in this reaction was of such a high level, that it was impossible to isolate a characterisable amount of ***t*-P18*·(T6)$_3$** *via* this straight template-directed approach.

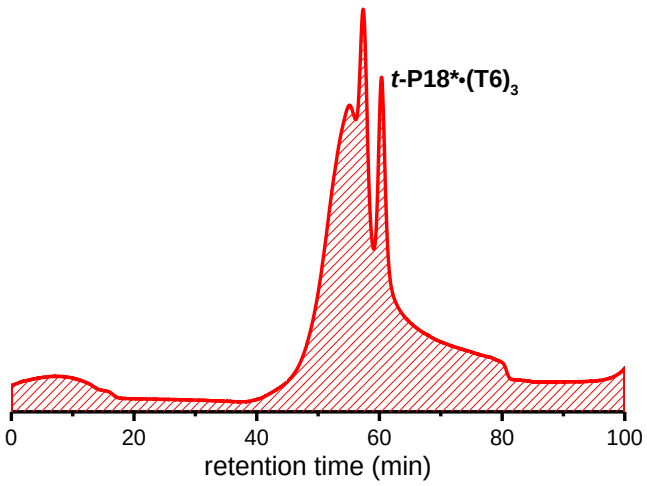

Figure 5.20: Recycling GPC trace (recorded at 590 nm, THF/1% pyridine) of the ***t*-P18*·(T6)$_3$** reaction mixture *via* template-directed synthesis from ***l*-P3*[acetylene]$_6$**.

5.8.3 Synthesis of ***t*-P18*·T6 pre-tube**

In the next step on our way to an 18-porphyrin nanotube, we set out to explore the synthesis of ***t*-P18*·(T6)$_3$** *via* the pre-tube approach. The TMS acetylene protecting groups installed at the central porphyrin of ***l*-P3$^{*C\text{-}2TMS}$** were selectively removed and subsequent coupling of ***l*-P3$^{*C\text{-}2acetylene}$** in the presence of **T6** gave ***t*-P18*·T6 pre-tube** in 18% yield after purification by recycling GPC (Scheme 5.12). This yield is significantly higher than ***t*-P18·T6 pre-tube** from ***l*-P3$^{C\text{-}2acetylene}$** (7%), presumably since there is no unfavourable wrapping around the template and hence the porphyrin trimer building blocks are better pre-arranged to form the desired complex.

***t*-P18*·T6 pre-tube** was analysed by ^{1}H NMR, UV-vis-NIR spectroscopy, and MALDI-ToF spectrometry. The ^{1}H NMR spectrum is relatively simple considering the size of the complex (Mw: 22982 Da) due to its D_{6h} symmetry (Figure 5.21). The β-protons across the mono-acetylene link (**f** and **g**), are strongly deshielded and resonate further downfield than the equivalent protons in the bis-acetylene linked 18-porphyrin pre-tube, as the ring currents of both porphyrins across the mono-acetylene linkage contribute to the deshielding of these protons.

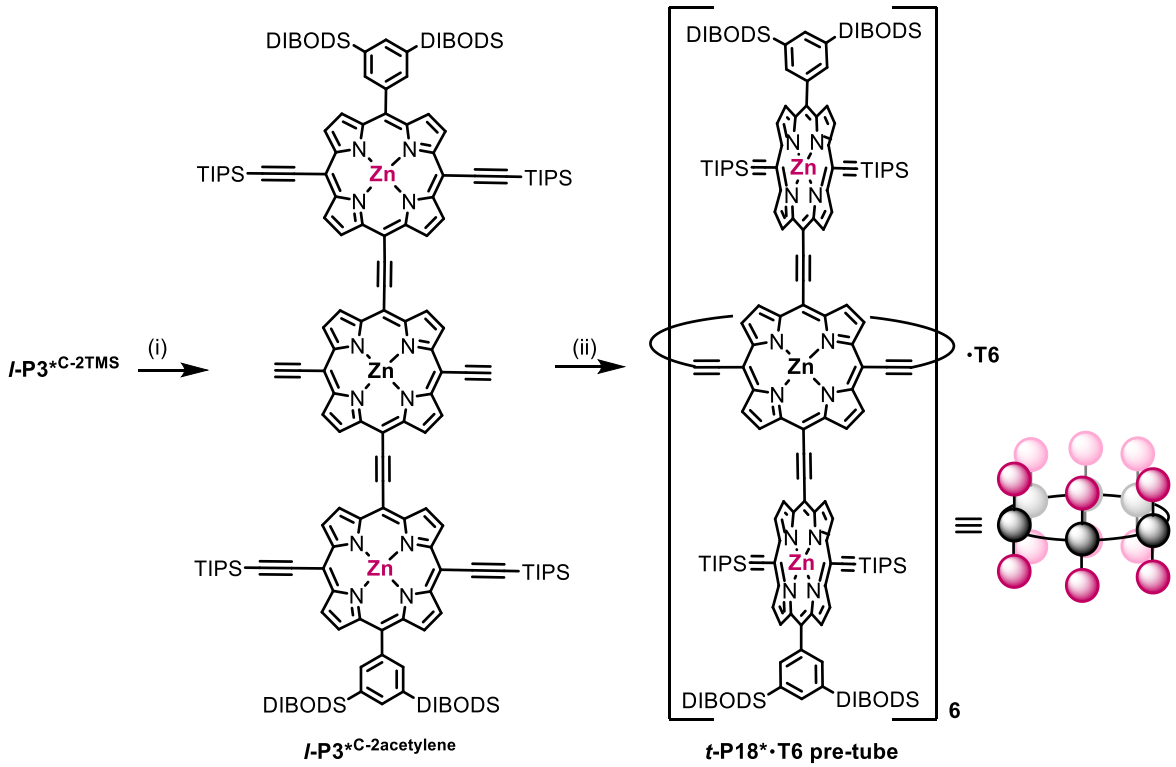

l-P3$^{*C\text{-}2TMS}$ *l*-P3$^{C\text{-}2acetylene}$ ***t*-P18*·T6 pre-tube**

Scheme 5.12: (i) K_2CO_3, THF, MeOH, pyridine, 90%. (ii) **T6,** $Pd(PPh_3)_2Cl_2$, CuI, 1,4-benzoquinone, $CHCl_3$, toluene, *N*,*N*-diisopropylamine, 18%.

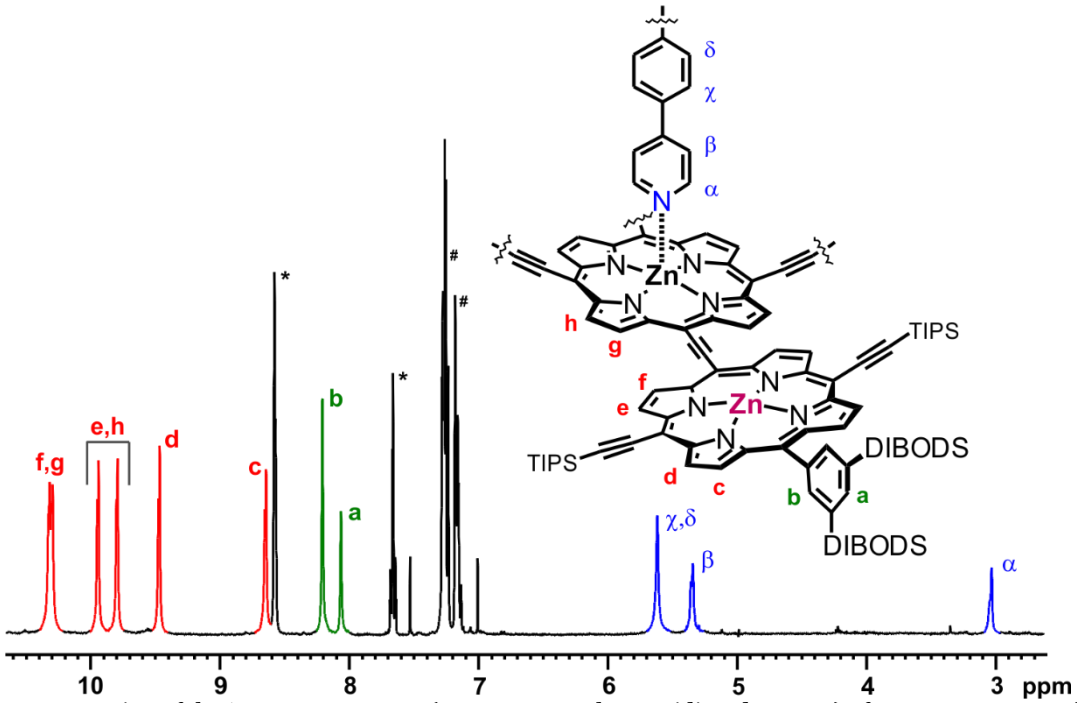

Figure 5.21: Region of the ^{1}H NMR spectrum (400 MHz, $CDCl_3$ + pyridine-d_5, 298 K) of ***t*-P18*·T6 pre-tube** (* = pyridine residual signal, # = toluene residual signal).

The UV-vis-NIR absorption spectrum of ***t*-P18*·T6 pre-tube** (Figure 5.22), shows features of both the trimer and ring-components, but is different than simply the sum of its parts. It is very similar to the UV-vis-NIR absorption spectrum of the bis-acetylene linked analogue; ***t*-P18·T6 pre-tube** (Figure 5.6). However, the enhanced conjugation in ***t*-P18*·T6 pre-tube**, induced by the mono-acetylene linkage, induces a relative bathochromic shift in absorption of 38 nm.

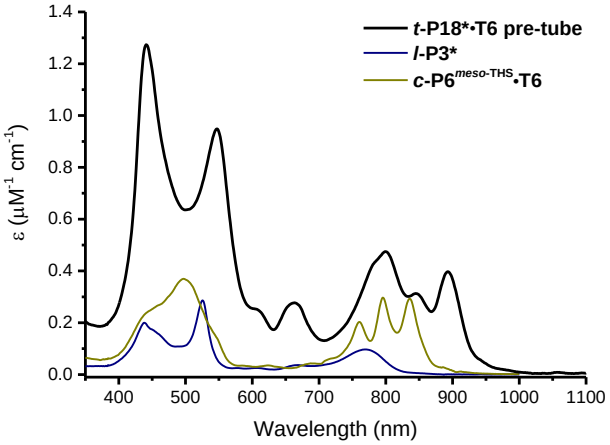

Figure 5.22: UV-vis-NIR absorption spectrum of ***t*-P18*·T6 pre-tube** (black trace), ***l*-P3*** (navy trace), and ***c*-P6$^{meso\text{-}THS}$·T6** (dark yellow trace) (all measured in $CHCl_3$ at 298 K).

The MALDI-ToF analysis shows two sharp peaks at m/z 22986 and 21986 corresponding to the ***t*-P18*·T6 pre-tube** complex (calculated for $C_{1440}H_{2052}N_{78}Si_{48}Zn_{18}$: 22982) and the pre-tube without **T6** template (Figure 5.23).

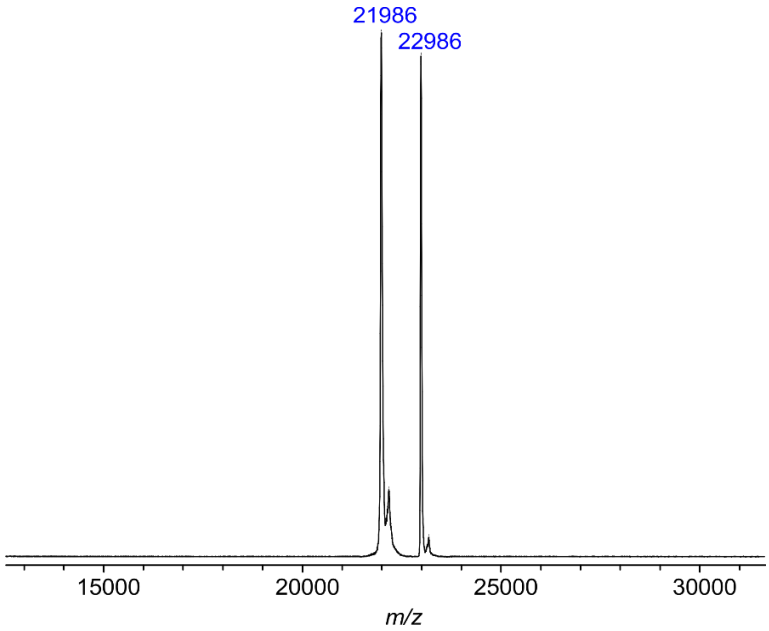

Figure 5.23: MALDI-ToF spectrum of ***t*-P18*·T6 pre-tube** (Matrix: DCTB).

5.8.4 Synthesis of ***t*-P18*·T6** *from* ***t*-P18*·T6 pre-tube**

Deprotection of the TIPS protecting groups of the acetylenes on the outer porphyrins of ***t*-P18*·T6 pre-tube** and subsequent coupling under palladium catalysed oxidative conditions gave the 18-porphyrin nanotube after purification by recycling GPC (Scheme 5.13).

Deprotection of ***t*-P18*·T6 pre-tube** was done carefully in a CH_2Cl_2/10% pyridine solution. The final coupling was performed under strongly diluted conditions (10 μM) compared to for example ***t*-P18*·T6 pre-tube** synthesis (0.25 mM) or template-directed synthesis of ***t*-P12*·(T6)$_2$** (0.75 mM). Furthermore, the final coupling was performed in a 10% pyridine solution in $CHCl_3$ and in the absence of **T6** template. Under these conditions, the amount of polymer formation due to cross-coupling between individual pre-tubes was significantly reduced. We suggest that aggregation of pre-tubes leads to cross-coupling. In the presence of **T6**, aggregation of the pre-tubes can easily occur due to their flat and exposed π-surface. In the absence of **T6** and presence of pyridine however, pyridine can coordinate to the zinc centres on the outer side of the tube, hindering the π-aggregation.

The reaction mixture was subjected to palladium catalysed oxidative conditions. Over the course of the reaction, the mixture turned from deep red to deep pink, indicative of porphyrin nanotube formation. Upon completion, the reaction mixture was passed through a short Al_2O_3 plug in toluene/1% pyridine to remove insoluble materials. The material was further purified by size-exclusion chromatography (THF/3% pyridine) and finally subjected to recycling GPC (THF/3% pyridine).

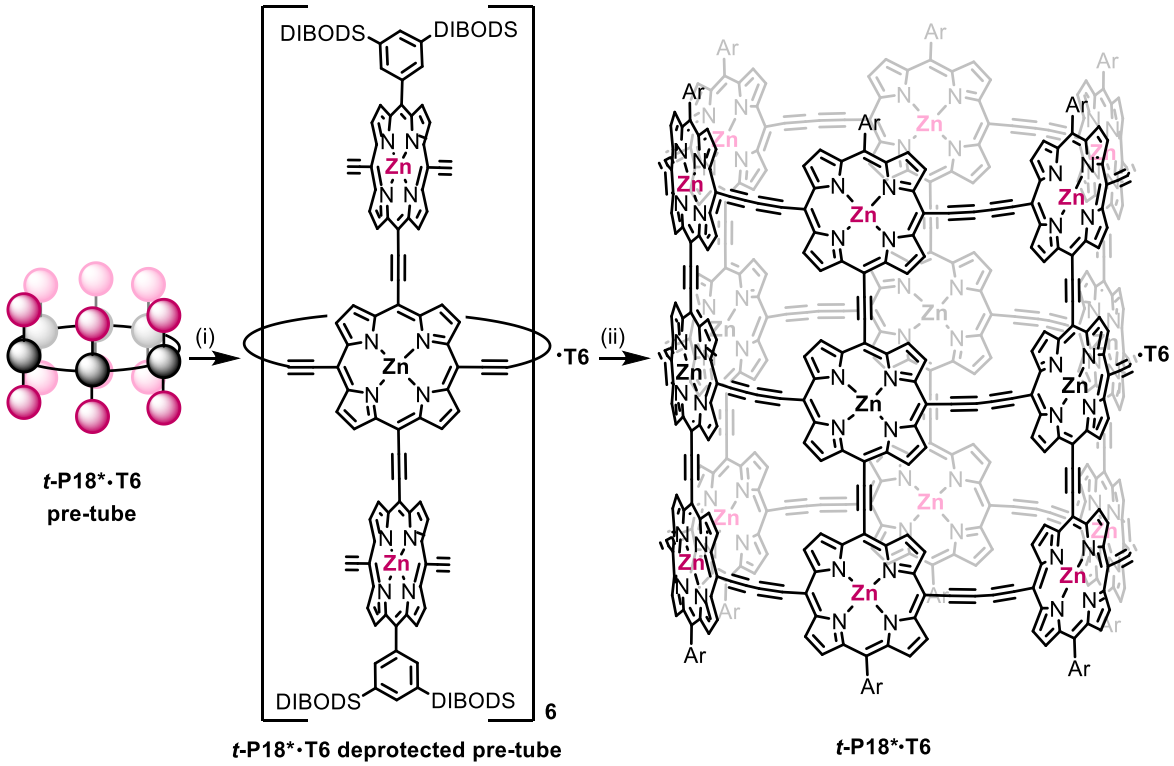

Scheme 5.13: (i) TBAF, toluene, pyridine, product not isolated. (ii) $Pd(PPh_3)_2Cl_2$, CuI, 1,4-benzoquinone, toluene, pyridine, *N*,*N*-diisopropylamine, yield not determined.

The recycling GPC trace (Figure 5.24) shows a relatively clean conversion of ***t*-P18*·T6 pre-tube** to ***t*-P18*·T6**. Slight streaking of the materials on the columns remained a problem, however, and two successive rounds of recycling GPC were required to isolate the target compound.

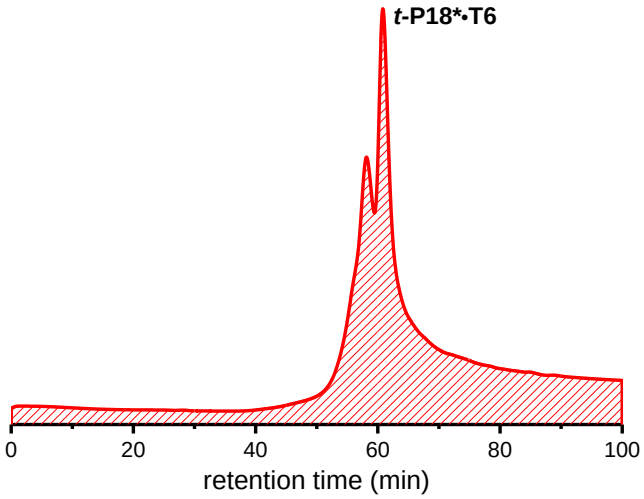

Figure 5.24: Recycling GPC trace (recorded at 500 nm, THF/3% pyridine) of the ***t*-P18*·T6** reaction mixture from the palladium catalysed coupling of deprotected ***t*-P18*·T6 pre-tube**.

5.8.5 Characterisation of ***t*-P18*·T6**

***t*-P18*·T6** was characterised by analytical GPC, MALDI-ToF spectrometry, UV-vis-NIR spectroscopy and ^{1}H NMR spectroscopy. The comparison of analytical GPC traces of ***t*-P18*·(T6)$_n$** prepared *via* template-directed synthesis from ***l*-P3*[acetylene]$_6$**, and from the stepwise synthesis *via* ***t*-P18*·T6 pre-tube**, shows that both strategies give the same final compound (30.3 min retention time). This can be identified as the target compound ***t*-P18*·(T6)$_n$**, referenced to the TIPS acetylene protected ***t*-P18*·T6 pre-tube** which exhibits a slightly shorter retention time (30.0 min), because of its higher molecular weight and larger hydrodynamic diameter (Figure 5.25).

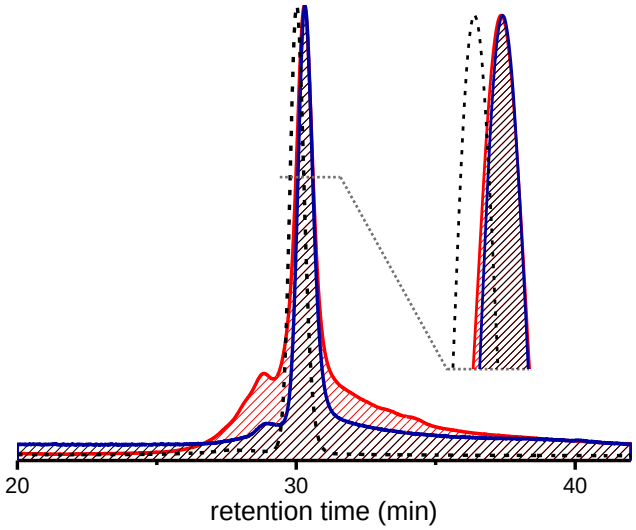

Figure 5.25: Analytical GPC traces (recorded at 500 nm) of; (red trace) ***t*-P18*·(T6)$_3$** prepared *via* template-directed synthesis from ***l*-P3*[acetylene]$_6$**. (blue trace) ***t*-P18*·T6** prepared in a stepwise synthesis *via* ***t*-P18*·T6 pre-tube**. (black dashed trace) ***t*-P18*·T6 pre-tube**.

***t*-P18*·T6** is prone to decomposition upon drying, hence the material was stored in solution (THF/pyridine). It was therefore not possible to determine the extinction coefficient of this compound. The (normalised) UV-vis-NIR absorption spectrum of ***t*-P18*·T6** shows an unusually broad and undefined Q band (Figure 5.26). The Soret and Q bands are slightly further red-shifted than those in the pre-cursor ***t*-P18*·T6 pre-tube** and the 12-porphyrin analogue; ***t*-P12*·(T6)$_2$**. This is an indication of efficient extension of the π-conjugated system in ***t*-P18*·T6**.

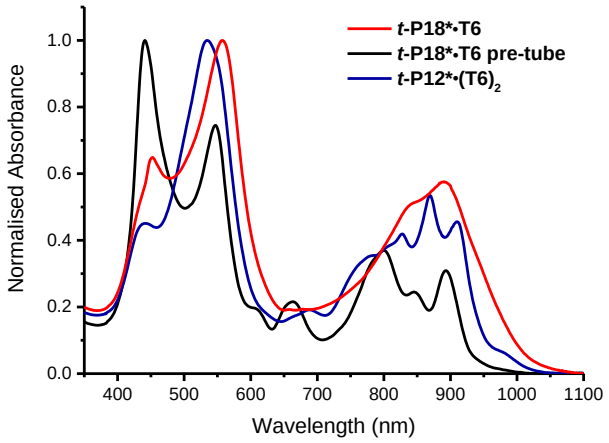

Figure 5.26: Normalised UV-vis-NIR absorption spectra of ***t*-P18*·T6** (red trace, measured in in $CHCl_3$ at 298 K), ***t*-P18*·T6 pre-tube** (black trace, measured in $CHCl_3$ at 298 K) and ***t*-P12*·(T6)$_2$** (blue trace, measured in toluene at 298 K).

MALDI-ToF analysis of ***t*-P18*·T6** shows a sharp single peak at m/z 18255 which corresponds to ***t*-P18*** in which the **T6** template has been lost, presumably due to the high laser power required (calculated m/z: 18208) (Figure 5.27).

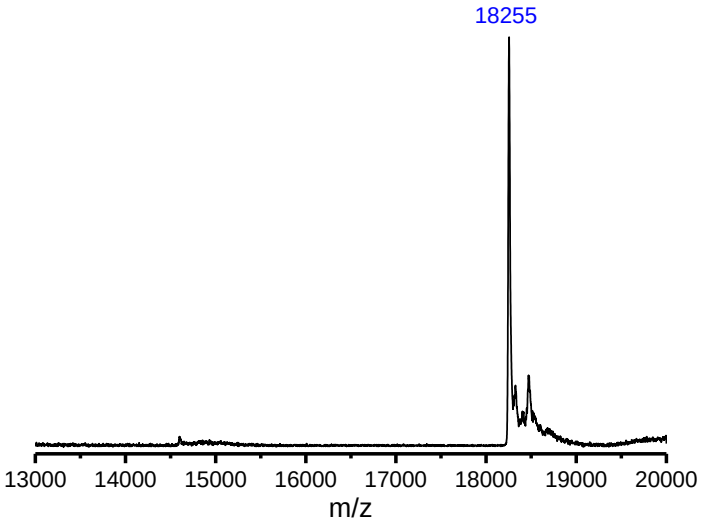

Figure 5.27: MALDI-ToF spectrum of ***t*-P18*** (Matrix: DCTB).

***t*-P18*·T6** gives rise to a broad ^{1}H NMR spectrum (Figure 5.28). However, in the aromatic region of the spectrum, signals for the β- and aryl-protons can be distinguished. The unresolved β-proton signals of ***t*-P18*·T6** resonate at a chemical shift that is similar to the β-protons in ***t*-P12*·(T6)$_2$**, and further downfield than the analogous protons in ***t*-P18*·T6 pre-tube**. Furthermore, a broad signal at 8.1-7.8 ppm can be distinguished which presumably corresponds to the aryl protons of the 18-porphyrin nanotube. A possible explanation for the broad ^{1}H NMR spectrum is the formation of π-π-stacked aggregates,[25] which typically causes broadening of the NMR spectrum.[26–28] Another explanation could be that the material exhibits unusual open-shell diradical character. This behaviour was recently observed for long rylene ribbons,[29] and is known to cause NMR broadening.[30,31] EPR measurements on ***t*-P18*·T6** could confirm the latter explanation and these experiments are under way.

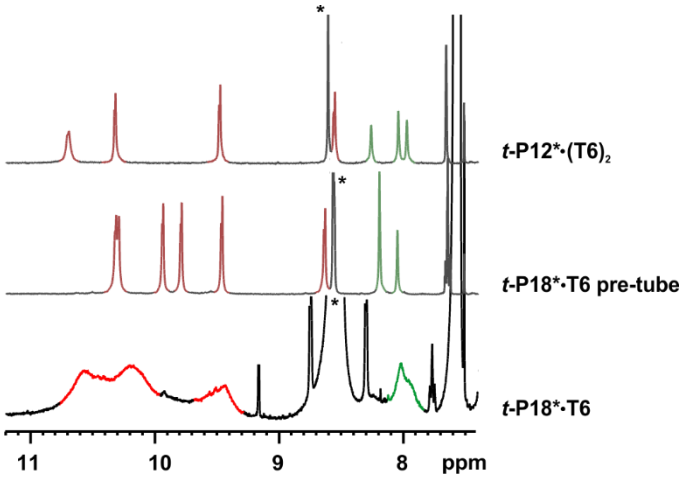

Figure 5.28: Region of the ^{1}H NMR spectra (400 MHz, $CDCl_3$ + 1% pyridine-d_5, 298K) of ***t*-P18*·T6**, ***t*-P18*·T6 pre-tube**, and ***t*-P12*·(T6)$_2$**. β-proton signals are labelled red, aryl-proton signals are labelled green (* = pyridine residual signal).

5.9 Conclusion

We developed a synthetic strategy to an 18-porphyrin nanotube. The first-generation design comprised the formation of an 18-porphyrin pre-tube. Subsequent deprotection of the outer porphyrin units followed by coupling under palladium catalysed oxidative conditions appear to have led to the formation of the target compound according to analytical GPC referenced to its precursor. However, low yields in the statistical coupling to form the porphyrin trimer building block, and in the formation of the 18-porphyrin pre-tube resulted in too little material to make this route a viable strategy towards an 18-porphyrin nanotube. These studies however provided valuable insights on the challenges that may arise when constructing increasingly long porphyrin nanotubes such as the requirement for a more powerful solubilising group, and the sensitivity of the pre-tube complex to drying.

To increase yields, we developed an alternative strategy comprising mono-acetylene linked porphyrin oligomers. The mono-acetylenic oligomers are unable to bind to the **T6** template in a wrapping binding mode, and hence adopt the desired perpendicular arrangement. Furthermore, we expected the mono-acetylenic connection to enhance electronic communication between the nanoring components of the porphyrin nanotube *via* increased conjugation.

This increased conjugation was established in the photophysical properties of a 12-porphyrin nanotube with mono-acetylenic linkages between the nanoring-components (***t*-P12*·(T6)$_2$**). Compared to its bis-acetylenic analogue ***t*-P12·(T6)$_2$**, ***t*-P12*·(T6)$_2$** displays a bathochromic shift in absorption of 40 nm as well as a decrease in fluorescence quantum yield. However, the yield of the template-directed synthesis of ***t*-P12*·(T6)$_2$** was lower than that of ***t*-P12·(T6)$_2$** and the former is sensitive to reaction temperature. The lower yield of the template-directed synthesis of ***t*-P12*·(T6)$_2$** is not surprising as the porphyrins across the mono-acetylene link are required to adopt a (close to) co-planar conformation. Previous studies indicated that this dimeric component preferably adapts a conformation with a dihedral angle of approximately 35°.[32,33] This alleviates the H-H clash across the mono-acetylenic link, while still allowing for substantial π-overlap.

Nanotube ***t*-P18*·(T6)$_n$** was prepared *via* two different synthetic strategies. We found that ***l*-P3*** coupled in the presence of **T6** forms ***t*-P18*·(T6)$_3$**, although mismatched coupling prevails, and only small amounts of the target compound are formed. The synthesis

of ***t*-P18*·T6** *via* a pre-tube approached proved to be more effective. The ***t*-P18*·T6 pre-tube** was obtained in 18% yield from ***l*-P3***, while the ***t*-P18·T6 pre-tube** was obtained in 7% yield from ***l*-P3**. This demonstrates how a change in synthetic strategy, as small as the removal of 4 carbon atoms from the essential precursor, can make a dramatic difference. The isolated 18-porphyrin nanotube contains one **T6** template, which resides at the centre of the porphyrin nanotube. Upon drying the material, higher molecular weight materials were formed, which renders it challenging to determine the yield of this reaction. Presumably, the nanotubes π-π-stack upon drying, leading to a close proximity of the acetylene moieties, potentially facilitating photochemical [2+2] cycloaddition, hence causing formation of higher molecular weight materials.

The successful formation of ***t*-P18*·T6** was confirmed by analytical GPC, UV-vis-NIR and MALDI-ToF analysis. While ^{1}H NMR spectroscopy reproducibly showed a broad and unresolved spectrum, the similarities in chemical shifts to relevant reference compounds provided further evidence that ***t*-P18*·T6** was successfully prepared. Suggested explanations for the broadening in NMR are the formation of π-π-stacked aggregates and the material exhibiting open-shell diradical character. We are currently examining the photophysical properties of this complex.

Porphyrin nanotube ***t*-P18*·T6** is to the best of our knowledge the largest π-conjugated molecular nanotube to date, with dimensions beyond that of many enzymes (3-7 nm globular diameter). The bottom-up synthetic approach to the monodisperse molecular nanotubes discussed in this thesis allows for various possible functionalisations and could enable access to tailor-build monodisperse fully conjugated nanotubes with tuneable properties. Considering the current inaccessibility of uniform-diameter single-chirality CNTs, the possibility to construct well-defined molecular analogues is of great interest.

5.10 Experimental Procedures

Porphyrin **P1**,[13,14] and porphyrin **P1b**[9,14] were prepared according to literature procedures.

5.10.1 Synthesis of Porphyrin Monomers

Magnesium 5,15-bis{[tri(propan-2-yl)silyl]ethynyl}porphyrin – P1g

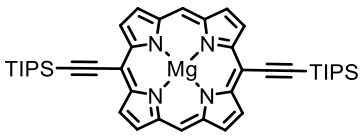

A solution of **P1** (248 mg, 0.37 mmol) and MgI_2 (515 mg, 1.8 mmol) in pyridine (30 mL) and Et_3N (1.5 mL) was heated to reflux overnight under nitrogen atmosphere, during which time the mixture became bright green. The volatiles were removed *in vacuo* and the residue was re-dissolved in CH_2Cl_2 and filtered through a SiO_2 plug (CH_2Cl_2 + 1% pyridine). Solvents were removed *in vacuo* to afford **P1g** as a 1:1 complex with pyridine (278 mg, 97%) as a dark purple solid with green lustre.

^{1}H NMR (400 MHz, $CDCl_3$, 298 K): δ_H 10.16 (s, 2H, *meso-H*), 9.82 (d, *J* = 4.3 Hz, 4H, *β-H*), 9.34 (d, *J* = 4.3 Hz, 4H, *β-H*), 1.54-1.47 (m, 42H).

MALDI-ToF m/z 692.35 (calculated for $C_{42}H_{52}MgN_4Si_2$: 692.36).

As lit.[14]

Magnesium 5,15-dibromo-10,20-bis{[tri(propan-2-yl)silyl]ethynyl}porphyrin – P1h

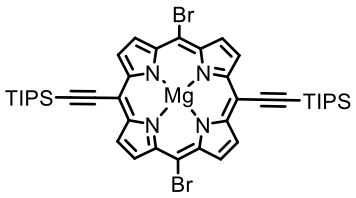

A solution of **P1g** (278 mg, 0.36 mmol) in dry $CHCl_3$ (35 mL) and pyridine (0.4 mL) was bubbled with N_2 before NBS (135 mg, 0.76 mmol) was added under magnetic stirring. The reaction progress was monitored by MALDI-ToF. After 1.5 h, MALDI-ToF showed the presence of mono- and di-brominated materials and additional NBS (43 mg) was added. Upon completion (after 5 h of total reaction time), the reaction was quenched with acetone (11 mL). The volatiles were removed *in vacuo* and the residue was purified by column chromatography (4:1 PE 40-60:CH_2Cl_2, + 1% pyridine) affording **P1h** (185 mg, 63%) as a dark blue solid with purple lustre.

^{1}H NMR (400 MHz, $CDCl_3$, 298 K): δ_H 9.65 (d, J = 4.5 Hz, 4H, *β-H*), 9.61 (d, J = 4.5 Hz, 4H, *β-H*), 1.51-1.45 (m, 42H, TIPS-*H*).

MALDI-ToF m/z 850.40 (calculated for $C_{42}H_{50}Br_2MgN_4Si_2$: 850.18).

As lit.[14]

5,15-dibromo-10,20-bis{[tri(propan-2-yl)silyl]ethynyl}porphyrin – P1i

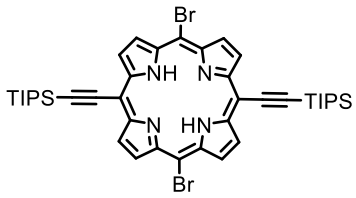

Trifluoroacetic acid (0.2 mL, 2.7 mmol) was added to a solution of **P1h** (502 mg, 0.54 mmol) in $CHCl_3$ (50 mL) under magnetic stirring. The reaction was monitored by TLC (10:1:1 PE 40-60:EtOAc:pyridine). Upon completion (after 10 min), the reaction was quenched by the addition of pyridine and immediately passed through a short SiO_2 plug ($CHCl_3$). Solvents were removed *in vacuo* to afford **P1i** (408 mg, 91%) as a purple solid with green lustre.

^{1}H NMR (400 MHz, $CDCl_3$, 298 K): δ_H 9.40 (d, J = 4.6 Hz, 4H, *β-H*), 9.32 (d, J = 4.6 Hz, 4H, *β-H*), 1.58-1.52 (m, 42H, TIPS-*H*), −4.0 (br s, 2H, N*H*).

MALDI-ToF m/z 828.48 (calculated for $C_{42}H_{52}Br_2N_4Si_2$: 828.21).

As lit.[14]

Zinc 5,15-dibromo-10,20-bis{[tri(propan-2-yl)silyl]ethynyl}porphyrin – P1j

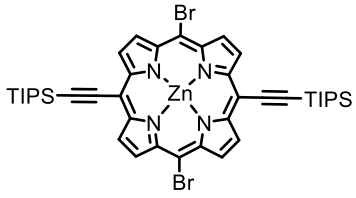

A solution of $Zn(OAc)_2{\cdot}2H_2O$ (220 mg, 1.00 mmol) in MeOH (1.8 mL) was added to a solution of **P1i** (166 mg, 0.20 mmol) in $CHCl_3$ (20 mL). The reaction mixture was heated under reflux for 2 h when TLC (2:1 PE 40-60:CH_2Cl_2) confirmed that insertion was completed. The solution was concentrated, and the material filtered through a short SiO_2 plug ($CHCl_3$). Solvents were removed *in vacuo* to afford **P1j** as a 1:1 complex with pyridine (179 mg, 100%) as a purple solid with green lustre.

^{1}H NMR (400 MHz, $CDCl_3$, 298 K): δ_H 9.63 (d, *J* = 4.6 Hz, 4H, *β-H*), 9.59 (d, *J* = 4.6 Hz, 4H, *β-H*), 1.52-1.45 (m, 42H, TIPS-*H*).

MALDI-ToF m/z 892.40 (calculated for $C_{42}H_{50}Br_2N_4Si_2Zn$: 892.12).

As lit.[14]

Zinc 5,15-dibromo-10,20-diethynylporphyrin – P1k

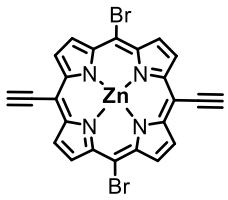

TBAF (1.0 M solution in THF, 0.51 mL, 0.51 mmol) was added to a solution of **P1j** (as a 1:1 complex with pyridine, 100 mg, 0.10 mmol) in CH_2Cl_2 (20 mL) and pyridine (2 mL). The reaction was stirred for 30 min before it was passed directly through a SiO_2 plug (CH_2Cl_2/5% pyridine). Solvents were removed *in vacuo* to afford **P1k** (62 mg,94%) as a purple solid.

Due to the poor solubility of the material, no ^{1}H NMR spectrum was recorded.

MALDI-ToF m/z 577.75 (calculated for $C_{24}H_{10}Br_2N_4Zn$: 577.85).

Zinc 5-[3,5-bis(trihexylsilyl)phenyl]-15-[(trimethylsilyl)ethynyl]-10,20-bis{[tri(propan-2-yl)silyl]ethynyl}porphyrin – P1l

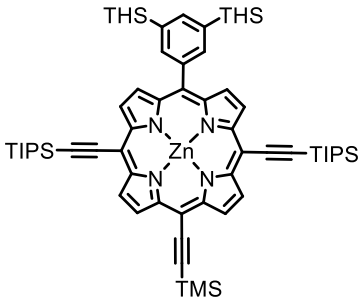

P1b (484 mg, 0.33 mmol), Pd_2dba_3 (30 mg, 33 μmol), CuI (6.3 mg, 33 μmol) and PPh_3 (17.3 mg, 66 μmol) were placed in a 50-mL two-necked flask. Toluene (20 mL) and *N,N*-diisopropylamine (10 mL) were added and the mixture was deoxygenated by 3 freeze-pump-thaw cycles. TMS-acetylene (68 μL, 0.49 mmol) was added and the reaction mixture was stirred overnight at room temperature. Solvents were removed *in vacuo* and the residue was purified by column chromatography (5:1 PE 40-60:CH_2Cl_2, + 1% pyridine) affording **P1l** (497 mg, 100%) as a purple solid.

^{1}H NMR (400 MHz, $CDCl_3$, 298 K): δ_H 9.71 (d, *J* = 4.5 Hz, 2H, *β-H*), 9.67 (d, *J* = 4.5 Hz, 2H, *β-H*), 9.60 (d, *J* = 4.6 Hz, 2H, *β-H*), 8.76 (d, *J* = 4.6 Hz, 2H, *β-H*), 8.16 (s, 2H, Ar-H_{ortho}), 7.96 (s, 1H, Ar-H_{para}), 1.53-1.41 (m, 54H), 1.41-1.33 (m, 12H), 1.33-1.25 (m, 24H), 0.95-0.89 (m, 12H), 0.89-0.83 (m, 18H), 0.64 (s, 9H, TMS-*H*).

MALDI-ToF m/z 1469.92, 1470.92 (95%) (calculated for $C_{89}H_{140}N_4Si_5Zn$: 1470.92).

As lit.[9]

Zinc 5-[3,5-bis(trihexylsilyl)phenyl]-15-ethynyl-10,20-bis{[tri(propan-2-yl)silyl]ethynyl}porphyrin – P1m

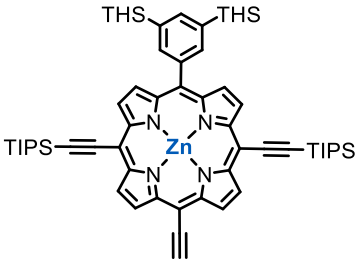

K_2CO_3 (39 mg, 0.28 mmol) was added to a solution of **P1l** (41.5 mg, 28.2 μmol) in THF (2 mL) and MeOH (2 mL). The suspension was stirred at 20 °C for 30 min before removal of the solvents *in vacuo*. The residue was taken up in CH_2Cl_2 (8 mL) and washed with H_2O (2 × 8 mL). The organic layer was dried over Na_2SO_4 and concentrated. The residue was subjected to column chromatography (6:1 PE 40-60:CH_2Cl_2 +1% pyridine) to afford **P1m** (32.1 mg, 82%) as a purple solid with green lustre.

^{1}H NMR (400 MHz, $CDCl_3$, 298 K): δ_H 9.74 (d, *J* = 4.6 Hz, 2H, *β-H*), 9.70 (d, *J* = 4.6 Hz, 2H, *β-H*), 9.64 (d, *J* = 4.6 Hz, 2H, *β-H*), 8.80 (d, *J* = 4.6 Hz, 2H, *β-H*), 8.17 (s, 2H, Ar-H_{ortho}), 7.97 (s, 1H, Ar-H_{para}), 4.16 (s, 1H, ≡-*H*), 1.54-1.42 (m, 54H), 1.42-1.34 (m, 12H), 1.34-1.26 (m, 24H), 0.96-0.89 (m, 12H), 0.89-0.84 (m, 18H).

MALDI-ToF m/z 1399.35 (calculated for $C_{86}H_{132}N_4Si_4Zn$: 1398.88).

As lit.[9]

5.10.2 Synthesis of Bis-Acetylene Linked Porphyrin Trimer

***l*-P3$_{THS}^{C-2Br}$**

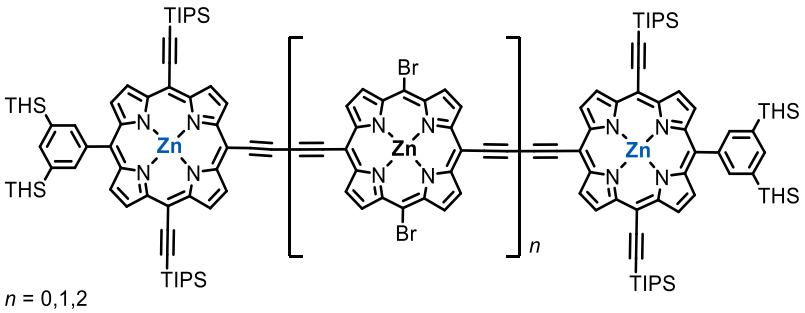

A solution was prepared of **P1m** (518 mg, 0.37 mmol) and **P1k** (~0.12 mmol, crude from deprotection) in dry toluene (15 mL), dry *N,N*-diisopropylamine (15 mL), and pyridine (7.5 mL). The mixture was bubbled with air and a catalyst mixture of $Pd(PPh_3)_2Cl_2$ (42 mg, 60 µmol), CuI (114 mg, 0.6 mmol) and 1,4-benzoquinone (260 mg, 2.4 mmol) in dry toluene (7 mL) and dry *N,N*-diisopropylamine (7 mL) was added. The mixture was stirred in the dark at room temperature overnight before the mixture was passed through a short SiO_2 plug (toluene/1% pyridine). The material was further purified by size-exclusion chromatography (BioBeads SX-1, toluene/1% pyridine) and finally subjected to recycling GPC (toluene/1% pyridine) to yield:

***l*-P2$_{THS}$[TIPS]$_4$ (n=0)** (365 mg, 92 µmol, 50% from **P1m**)

^{1}H NMR (400 MHz, $CDCl_3$, 298 K): δ_H 9.97 (d, J = 4.5 Hz, 4H, *β-H*), 9.85 (d, J = 4.5 Hz, 4H, *β-H*), 9.63 (d, J = 4.5 Hz, 4H, *β-H*), 8.78 (d, J = 4.5 Hz, 4H, *β-H*), 8.19 (s, 4H, Ar-H_{ortho}), 7.99 (s, 2H, Ar-H_{para}), 1.55-1.44 (m, 108H), 1.44-1.36 (m, 24H), 1.36-1.26 (m, 48H), 0.98-0.91 (m, 24H), 0.91-0.85 (m, 36H).

MALDI-ToF m/z 2800.76 (calculated for $C_{172}H_{262}N_8Si_8Zn_2$: 2794.75).

As lit.[9]

***l*-P3$_{THS}^{C-2Br}$ (n= 1)** (115 mg, 34 µmol, 28% from **P1k**)

^{1}H NMR (400 MHz, $CDCl_3$ + 1% pyridine-d_5, 298 K): δ_H 9.96 (d, J = 4.2 Hz, 4H, *β-*$H_{outer\text{-}P}$), 9.90 (d, J = 4.4, 4H, *β-*$H_{central\text{-}Br2P}$), 9.85 (d, J = 4.3 Hz, 4H, *β-*$H_{outer\text{-}P}$), 9.75 (d, J = 4.3 Hz, 4H, *β-*$H_{central\text{-}Br2P}$), 9.62 (d, J = 4.4 Hz, 4H *β-*$H_{outer\text{-}P}$), 8.78 (d, J = 4.4 Hz, 4H, *β-*$H_{outer\text{-}P}$), 8.19 (s, 4H, Ar-H_{ortho}), 7.98 (s, 2H, Ar-H_{para}), 1.53-1.43 (m, 108H), 1.43-1.34(m, 24H), 1.34-1.27 (m, 48H), 0.97-0.91 (m, 24H), 0.91-0.85 (m, 36H).

^{13}C NMR (100 MHz, $CDCl_3$ + 1% pyridine-d_5, 298 K): δ_C 153.5, 153.4, 152.8, 152.4, 150.3, 150.0, 140.7, 140.2, 136.1, 134.8, 134.1, 133.2, 132.5, 131.4, 130.8, 126.5, 123.7, 109.8, 107.9, 102.8, 101.4, 99.1, 98.4, 88.9, 87.6, 83.4, 82.1, 33.6, 31.7, 24.2, 22.8, 19.3, 14.3, 12.8, 12.1.

MALDI-ToF m/z 3375.93 (calculated for $C_{196}H_{270}Br_2N_{12}Si_8Zn_3$: 3370.59).

UV-vis-NIR ($CHCl_3$) λ_{max} (log ε): 461 (5.46), 474 (5.44), 502 (5.42), 603 (4.50), 658 (4.70), 746 (5.10).

***l*-P4$_{THS}^{C\text{-}4Br}$ (n=2)** (22 mg, 8 μmol, 13% from **P1k**)

^{1}H NMR (400 MHz, $CDCl_3$ + 1% pyridine-d_5, 298 K): δ_H 9.70 (d, *J* = 4.4 Hz, 4H, *β-H*), 9.64 (d, *J* = 3.5 Hz, 4H, *β-H*), 9.62-9.58 (m, 8H, *β-H*), 9.48 (d, *J* = 3.6 Hz, 4H, *β-H*), 9.40 (m, 8H, *β-H*), 8.90 (d, *J* = 4.5 Hz, 4H, *β-H*), 8.38 (s, 4H, Ar-H_{ortho}), 7.99 (s, 2H, Ar-H_{para}), 1.60-1.54 (m, 84H), 1.54-1.43 (m, 24H), 1.36-1.27 (m, 24H), 1.27-1.18 (m, 48H), 0.98-0.91 (m, 24H), 0.85-0.78 (m, 36H).

MALDI-ToF m/z 3951.99 (calculated for $C_{220}H_{279}Br_4N_{16}Si_8Zn_4$: 3952.43).

***l*-P3$_{THS}^{C\text{-}2CPDMS}$**

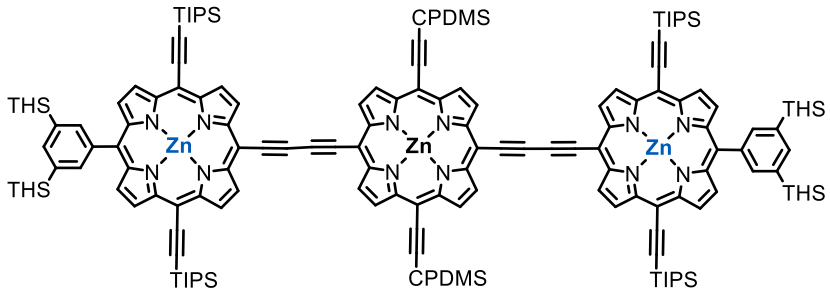

***l*-P3$_{THS}^{C\text{-}2Br}$** (116 mg, 34 μmol), Pd_2dba_3 (6.3 mg, 6.9 μmol), CuI (1.3 mg, 6.9 μmol) and PPh_3 (3.6 mg, 13 μmol) were placed in a 100-mL two-necked flask. Toluene (16 mL) and *N,N*-diisopropylamine (8 mL) were added and the mixture was deoxygenated by 3 freeze-pump-thaw cycles. Cyanopropyldimethylsilylacetylene (15.5 mg, 0.10 mmol) was added and the reaction mixture was stirred room temperature. The reaction was monitored by MALDI-ToF. After 2.5 h the reaction appeared to be complete by MALDI-ToF. Solvents were removed *in vacuo* and the residue was purified by column chromatography (1:1 PE 40-60:CH_2Cl_2, + 1% pyridine) to afford ***l*-P3$_{THS}^{C\text{-}2CPDMS}$** (117 mg, 97%) as a brown solid.

^{1}H NMR (400 MHz, $CDCl_3$ + 1% pyridine-d_5, 298 K): δ_H 9.95 (d, J = 4.5 Hz, 4H, β-$H_{outer\text{-}P}$), 9.93 (d, J = 4.5, 4H, β-$H_{central\text{-}P}$), 9.84 (d, J = 4.5 Hz, 4H, β-$H_{outer\text{-}P}$), 9.71 (d, J = 4.5 Hz, 4H, β-$H_{central\text{-}P}$), 9.62 (d, J = 4.5 Hz, 4H β-$H_{outer\text{-}P}$), 8.77 (d, J = 4.5 Hz, 4H, β-$H_{outer\text{-}P}$), 8.19 (s, 4H, Ar-H_{ortho}), 7.98 (s, 2H, Ar-H_{para}), 2.69 (t, J = 6.9 Hz, 4H, -CH_2-CN), 2.26 (m, 4H, -CH_2-$_{CPDMS}$), 1.55-1.43 (m, 108H), 1.43-1.35 (m, 24H), 1.34-1.24 (m, 48H), 0.97-0.90 (m, 28H), 0.91-0.83 (m, 36H), 0.72 (s, 12H, Si-CH_3).

IR: υ_{max}/cm^{-1} 2920, 2360 (C≡C), 2140 (C≡C).

MALDI-ToF m/z 3518.80 (calculated for $C_{212}H_{294}N_{14}Si_{10}Zn_3$: 3511.90).

5.10.3 Synthesis of ***t*-P18$_{THS}$·T6 pre-tube** *and* ***t*-P18$_{THS}$·(T6)$_3$**

l-P3$_{THS}^{C\text{-}2acetylene}$

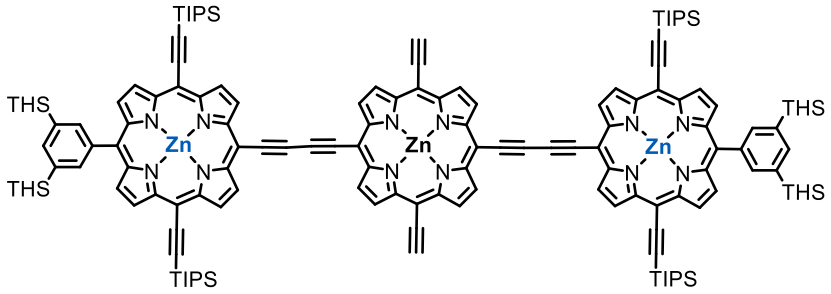

K_2CO_3 (8.3 mg, 60 µmol) was added to a solution of ***l*-P3$_{THS}^{C\text{-}2CPDMS}$** (14.1 mg, 4.0 µmol) in THF (1 mL) and MeOH (1 mL). The solution was stirred at room temperature for 30 min after which the mixture was passed through a SiO_2 plug (1:1 PE 40-60: CH_2Cl_2 + 1% pyridine). Solvents were removed *in vacuo* to afford ***l*-P3$_{THS}^{C\text{-}2acetylene}$** (13.3 mg, 100%) as a dark brown solid.

^{1}H NMR (400 MHz, $CDCl_3$ + 1% pyridine-d_5, 298 K): δ_H 9.96 (d, J = 4.4 Hz, 4H, β-$H_{outer\text{-}P}$), 9.91 (d, J = 4.4, 4H, β-$H_{central\text{-}P}$), 9.85 (d, J = 4.4 Hz, 4H, β-$H_{outer\text{-}P}$), 9.77 (d, J = 4.5 Hz, 4H, β-$H_{central\text{-}P}$), 9.62 (d, J = 4.5 Hz, 4H β-$H_{outer\text{-}P}$), 8.77 (d, J = 4.4 Hz, 4H, β-$H_{outer\text{-}P}$), 8.19 (s, 4H, Ar-H_{ortho}), 7.98 (s, 2H, Ar-H_{para}), 4.29 (s, 2H, ≡-H), 1.54-1.44 (m, 108H), 1.43-1.34 (m, 24H), 1.34-1.27 (m, 48H), 0.97-0.90 (m, 24H), 0.90-0.84 (m, 36H).

IR: υ_{max}/cm^{-1} 3312 (-C≡C-H stretch), 2920, 2360 (C≡C), 2140 (C≡C).

MALDI-ToF m/z 3265.99 (calculated for $C_{200}H_{272}N_{12}Si_8Zn_3$: 3261.77).

***t*-P18$_{THS}$·T6 pre-tube**

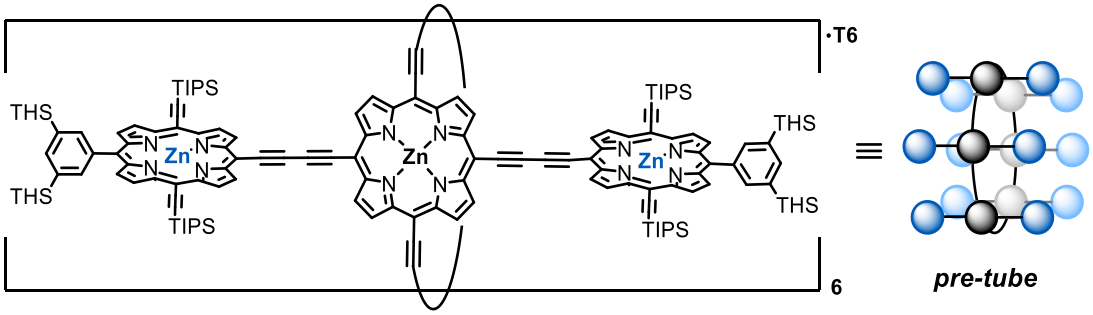

A solution of ***l*-P3$_{THS}^{C\text{-}2acetylene}$** (13.3 mg, 4 µmol) and **T6** (2.0 mg, 2 µmol) in $CHCl_3$ (4mL) was stirred for 30 min at room temperature. The solution was concentrated and the material re-dissolved in dry toluene (4 mL) and dry *N,N*-diisopropylamine (2 mL). The reaction mixture was heated to 65 °C and 300 µL of a catalyst mixture ($Pd(PPh_3)_2Cl_2$ (2.8 mg, 4.1 µmol), CuI (0.4 mg, 2 µmol), 1,4-benzoquinone (4.5 mg, 42 µmol) in dry toluene (1 mL) and dry *N,N*-diisopropylamine (0.5 mL)) was added. Heating was continued, and the reaction was monitored by UV-vis-NIR spectroscopy. After 3 h of reaction time additional 100 µL of a freshly prepared catalyst mixture was added. When no change in UV was observed any more (16 h) the reaction mixture was passed through a SiO_2 plug (toluene/1% pyridine). The material was further purified by size-exclusion chromatography (BioBeads SX-1, toluene/1% pyridine) and finally subjected to recycling GPC (toluene/1% pyridine) to afford ***t*-P18·T6 pre-tube** (0.9 mg, 7%) as a deep red solid.

^{1}H NMR (500 MHz, $CDCl_3$ + 1% pyridine-d_5, 298 K): δ_H 9.89 (m, 48H, *β-H*), 9.79 (d, *J* = 3.8 Hz, 24H, *β-H*), 9.71 (d, *J* = 4.1 Hz, 24H, *β-H*), 9.50 (d, *J* = 4.0 Hz, 24H, *β-H*), 8.67 (d, *J* = 4.0 Hz, 24H, *β-H*),8.12 (s, 24H, Ar-H_{ortho}), 7.95 (s, 12H, Ar-H_{para}), 5.81 (d, *J* = 9.0 Hz, 12H, T6.Ar-*H*), 5.74 (d, *J* = 8.8 Hz, 12H, T6.Ar-*H*), 5.35 (d, *J* = 6.1 Hz, 12H, T6.pyridyl-H_β), 2.82 (m, 12H, T6.pyridyl-H_α),1.51-1.41 (m, 108H), 1.41-1.32 (m, 108H), 1.32-1.23 (m, 576H), 1.06-0.98 (m, 288H), 0.94-0.87 (m, 144H), 0.87-0.79 (m, 216H).

MALDI-TOF m/z 20636 (calculated for $C_{1272}H_{1668}N_{78}Si_{48}Zn_{18}$: 20576.92).

UV-vis-NIR ($CHCl_3$) λ_{max} (log ε): 462 (5.86), 546 (5.52), 658 (5.21), 773 (5.26), 807 (5.17), 855 (5.24).

t-P18·(T6)$_3$ from *t*-P18$_{THS}$·T6 pre-tube

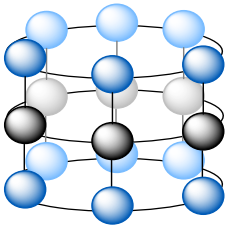

TBAF (1.0 M solution in THF, 5.3 µL, 5.3 µmol,) was added to a solution of ***t*-P18$_{THS}$·T6 pre-tube** (1.5 mg, 0.09 µmol) in toluene (1 mL) and pyridine (10 µL). The solution was stirred for 40 min after which it was passed through a short SiO_2 plug (toluene/1% pyridine). Deprotection was confirmed by MALDI-ToF analysis

MALDI-TOF m/z 15841 (**T6** is lost during the measurement; calculated for $C_{984}H_{1140}N_{72}Si_{24}Zn_{18}$: 15827).

To the obtained solution, dry toluene was added until a volume of 5 m was reached. $CHCl_3$ (2.5 mL) and **T6** (0.18 mg, 0.18 µmol) were added and the solution was stirred for 20 min to allow for complexation with **T6**. $CHCl_3$ was removed under reduced pressure and dry toluene (15 mL) and dry *N,N*-diisopropylamine (10 mL) were added. A catalyst solution of $Pd(PPh_3)_2Cl_2$ (2.5 mg, 3.6 µmol), CuI (3.4 mg, 18 µmol), 1,4-benzoquinone (3.9 mg, 36 µmol) in toluene (3 mL) and *N,N*-diisopropylamine (1.5 mL) was added and the reaction was monitored by UV-vis-NIR spectroscopy. After 2.5 h, freshly prepared catalyst mixture was added. When the reaction was judged complete (after 5 h of total reaction time), the material was slightly concentrated and passed through a short SiO_2 plug (toluene/1% *N,N*-diisopropylamine). The material was carefully concentrated and purified by size-exclusion chromatography (BioBeads SX-1, toluene/1% pyridine). Analysis by GPC (THF/1% pyridine) and MALDI-ToF indicated the formation ***t*-P18·(T6)$_3$**.

MALDI-TOF m/z 15908 (***t*-P18**; calculated for $C_{984}H_{1116}N_{72}Si_{24}Zn_{18}$: 15803), 16960 (***t*-P18·T6**; calculated for $C_{1056}H_{1164}N_{78}Si_{24}Zn_{18}$: 16800), 17859 (***t*-P18·(T6)$_2$**; calculated for $C_{1128}H_{1212}N_{84}Si_{24}Zn_{18}$: 17796), 18900 (***t*-P18·(T6)$_3$**; calculated for $C_{1200}H_{1260}N_{90}Si_{24}Zn_{18}$: 18794).

It was very challenging to measure a MALDI-ToF spectrum for this compound. The only spectrum obtained was of very poor resolution (peak widths 700-1000 m/z). In this case it was hence more informative that a pattern of 4 peaks is observed at **T6** template mass-intervals in roughly the right region, than the actual m/z values of the peaks. Since this approach to the 18-porphyrin nanotube was discontinued, no further attempts to measure MALDI-ToF of this particular compound were made.

5.10.4 Synthesis of Porphyrin Monomer – DIBODS Solubilising Group

Porphyrin **P1** was prepared according to literature procedures.[13,14]

(5-bromo-1,3-phenylene)bis[bis(2-methylpropyl)(octadecyl)silane] - Ar_{DIBODS}

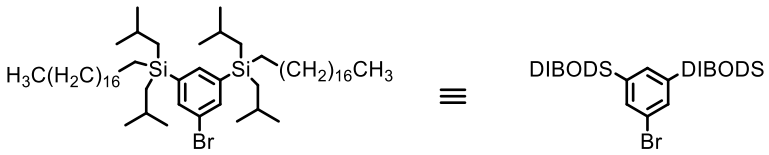

n-Butyl lithium (2.5 M solution in hexane, 6.48 mL, 16.2 mmol) was added dropwise by syringe to a stirring solution of 1,3,5-tribromobenzene (2.42 g, 7.7 mmol) in Et_2O (58 mL) at -78 °C, under N_2 atmosphere. The solution was stirred for 90 min before chlorodiisobutyloctadecylsilane (85% purity, 10 mL, 19 mmol) was added dropwise *via* a syringe. The solution was allowed to warm to room temperature. After stirring for another 90 min, the reaction mixture was washed with water, dried over $MgSO_4$ and filtered. The solution was concentrated and passed through a SiO_2 plug (PE 40-60). The solvent was removed to afford 5.8 g of a 3:1 mixture of **Ar_{DIBODS}** and 1,3,5-tris(diisobutyloctadecylsilyl)benzene. This crude product was dried under high vacuum and was used without further purification in the next step.

10-{3,5-bis[bis(2-methylpropyl)(octadecyl)silyl]phenyl}-5,15-bis{[tri(propan-2-yl)silyl]ethynyl}porphyrin – P1n[2H]

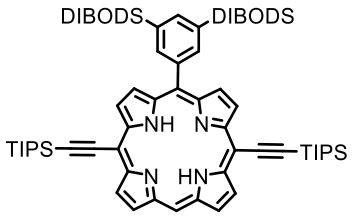

n-Butyl lithium (1.6 M solution in hexanes, 5.55 mL, 8.9 mmol) was added dropwise to a solution of **Ar_{DIBODS}** (5.4g, 8.9 mmol) in Et_2O (50 mL) at –78 °C under N_2 atmosphere. The mixture was allowed to warm to room temperature and stirred for 1 h. This solution was added dropwise to a solution of **P1** (917 mg, 1.37 mmol) in THF (50 mL). The mixture was stirred at room temperature overnight. Water (4.3 mL) was added, followed by DDQ (930 mg, 4.1 mmol). The reaction mixture was stirred for 20 min before Et_3N (1.8 mL) was added. Solvents were removed *in vacuo* and the residue was taken up in CH_2Cl_2 (350 mL) and washed with H_2O (4 × 200 mL). The organic layer was dried over $MgSO_4$ and concentrated. Column chromatography (10:1 to 7:1 PE 40-60:CH_2Cl_2) afforded **P1n[2H]** (1.33 g, 63 %) as a purple solid.

^{1}H NMR (400 MHz, $CDCl_3$, 298 K): δ_H 10.07 (s, 1H, *meso-H*), 9.73 (d, *J* = 4.6 Hz, 2H, *β-H*), 9.63 (d, *J* = 4.7 Hz, 2H, *β-H*), 9.28 (d, *J* = 4.6 Hz, 2H, *β-H*), 8.75 (d, *J* = 4.7 Hz, 2H, *β-H*), 8.23 (s, 2H, Ar-H_{ortho}), 8.06 (s, 1H, Ar-H_{para}), 1.99-1.88 (m, 4H), 1.57-1.42 (m, 42H), 1.40-1.25 (m, 68H), 1.01-0.97 (m, 24H), 0.97-0.92 (m, 8H), 0.89-0.84 (m, 6H), −2.37 (s, 2H, N*H*).

MALDI-ToF m/z 1535.96 (calculated for $C_{100}H_{166}N_4Si_4$:1536.22).

Zinc 10-{3,5-bis[bis(2-methylpropyl)(octadecyl)silyl]phenyl}-5,15-bis{[tri(propan-2-yl)silyl]ethynyl}porphyrin – P1n[Zn]

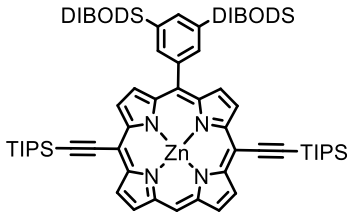

A solution of $Zn(OAc)_2{\cdot}2H_2O$ (0.81 g, 3.7 mmol) in MeOH (12 mL) was added to a solution of **P1n[2H]** (1.14 g, 0.74 mmol) in $CHCl_3$ (55 mL). The mixture was stirred at room temperature for 1 h before it was passed through a short SiO_2 plug (CH_2Cl_2/1% pyridine). Solvents were removed *in vacuo* to afford **P1n[Zn]** as a 1:1 complex with pyridine (1.27 g, 100%) as a purple solid with green lustre.

^{1}H NMR (400 MHz, $CDCl_3$, 298 K): δ_H 10.04 (s, 1H, *meso-H*), 9.81 (d, *J* = 4.4 Hz, 2H, *β-H*), 9.72 (d, *J* = 4.4 Hz, 2H, *β-H*), 9.31 (d, *J* = 4.4 Hz, 2H, *β-H*), 8.82 (d, *J* = 4.4 Hz, 2H, *β-H*), 8.24 (s, 2H, Ar-H_{ortho}), 8.06 (s, 1H, Ar-H_{para}), 2.03-1.92 (m, 4H), 1.58-1.45 (m, 42H, TIPS-*H*), 1.41-1.18 (m, 68H), 1.05-0.99 (m, 24H), 0.99-0.95 (m, 8H), 0.93-0.87 (m, 6H).

^{13}C NMR (100 MHz, $CDCl_3$, 298 K): δ_C 152.6 (2C), 152.4 (2C), 150.2 (2C), 149.9 (2C), 141.2 (C), 140.2 (2CH), 139.2 (CH), 135.3 (2C), 132.7 (2CH), 132.2 (2CH), 131.7 (2CH), 130.8 (2CH), 124.2 (C), 110.3 (2C), 107.1 (CH), 100.6 (2C), 97.4 (2C), 34.2, 32.1, 29.9, 29.8, 29.6, 29.5, 26.8, 26.7, 25.2 (4CH), 24.3, 23.9 ($4CH_2$), 22.9, 19.3 ($12CH_3$), 14.3 ($2CH_3$), 13.9, 12.1 (6CH).

MALDI-ToF m/z 1598.90 (calculated for $C_{100}H_{164}N_4Si_4Zn$: 1599.13).

Zinc 5-{3,5-bis[bis(2-methylpropyl)(octadecyl)silyl]phenyl}-15-bromo-10,20-bis{[tri(propan-2-yl)silyl]ethynyl}porphyrin – P1o

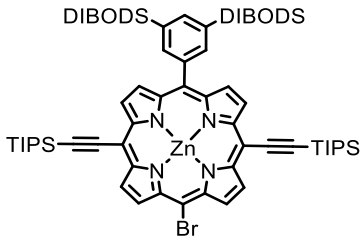

NBS (70 mg, 0.39 mmol) was added to a solution of **P1n[Zn]** (1:1 complex with pyridine, 653 mg, 0.39 mmol) in dry $CHCl_3$ (40 mL) and pyridine (4 mL). The mixture was stirred at room temperature and the reaction progress was monitored by TLC (starting material is fluorescent, while the product is not). Additional NBS (38 mg after 2.5 h, 10 mg after 3.5 h, and 24 mg after 4.5 h) was added until the reaction was complete. Solvents were removed *in vacuo* and the residue was purified by column chromatography (8:1 PE 40-60:CH_2Cl_2) affording **P1o** as a 1:1 complex with pyridine (357 mg, 52%) as a purple solid with green lustre.

^{1}H NMR (400 MHz, $CDCl_3$ + 1% pyridine-d_5, 298 K): δ_H 9.71 (d, J = 4.6 Hz, 2H, *β-H*), 9.66 (d, J = 4.6 Hz, 2H, *β-H*), 9.60 (d, J = 4.5 Hz, 2H, *β-H*), 8.70 (d, J = 4.6 Hz, 2H, *β-H*), 8.15 (s, 2H, Ar-H_{ortho}), 8.02 (s, 1H, Ar-H_{para}), 1.98-1.86 (m, 4H), 1.55-1.40 (m, 42H, TIPS-*H*), 1.38-1.14 (m, 68H), 1.00-0.95 (m, 24H), 0.95-0.90 (m, 8H), 0.90-0.82 (m, 6H).

^{13}C NMR (100 MHz, $CDCl_3$ + 1% pyridine-d_5, 298 K): δ_C 152.9 (2C), 152.8 (2C), 151.0 (2C), 149.7 (2C), 140.8 (C), 140.1 (2CH), 139.4 (CH), 135.5 (2C), 133.4 (2CH), 133.0 (2CH), 132.2 (2CH), 131.3 (2CH), 124.5 (C), 110.0 (2C), 106.1 (C), 101.8 (2C), 98.1 (2C), 34.2, 32.1, 29.9, 29.8, 29.6, 29.5, 26.8, 26.7, 25.2 (4CH), 24.3, 23.9 (4CH_2), 22.9, 19.3 (12CH_3), 14.3 (2CH_3), 13.9, 12.1 (6CH).

MALDI-ToF m/z 1678.92 (calculated for $C_{100}H_{163}BrN_4Si_4Zn$: 1679.04).

Zinc 5-{3,5-bis[bis(2-methylpropyl)(octadecyl)silyl]phenyl}-15-[(trimethylsilyl)ethynyl]-10,20-bis{[tri(propan-2-yl)silyl]ethynyl}porphyrin – P1p

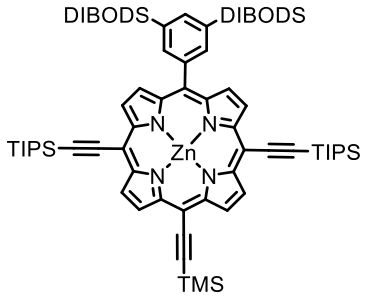

P1o (440 mg, 0.25 mmol), Pd_2dba_3 (23 mg, 25 μmol), CuI (4.8 mg, 21 μmol) and PPh_3 (13.1 mg, 50 μmol) were placed in a 100-mL two-necked flask. Toluene (15 mL) and *N,N*-diisopropylamine (7.5 mL) were added and the mixture was deoxygenated by 3 freeze-pump-thaw cycles. TMS-acetylene (52 μL, 0.38 mmol) was added and the reaction mixture was stirred overnight at room temperature. Solvents were removed *in vacuo* and the residue was purified by column chromatography (20:1 to 10:1 PE 40-60:CH_2Cl_2, + 1% pyridine) affording **P1p** (435 mg, 98%) as a blue solid with green lustre.

^{1}H NMR (400 MHz, $CDCl_3$ + 1% pyridine-d_5, 298 K): δ_H 9.70 (d, *J* = 4.5 Hz, 2H, *β-H*), 9.65 (d, *J* = 4.5 Hz, 2H, *β-H*), 9.58 (d, *J* = 4.5 Hz, 2H, *β-H*), 8.69 (d, *J* = 4.6 Hz, 2H, *β-H*), 8.16 (s, 2H, Ar-H_{ortho}), 8.02 (s, 1H, Ar-H_{para}), 1.99-1.86 (m, 4H), 1.56-1.40 (m, 42H), 1.39-1.15 (m, 68H), 1.02-0.95 (m, 24H), 0.95-0.90 (m, 8H), 0.90-0.83 (m, 6H), 0.63 (s, 9H, -Si-CH_3).

^{13}C NMR (100 MHz, $CDCl_3$ + 1% pyridine-d_5, 298 K): δ_C 152.7 (2C), 152.5 (2C), 152.4 (2C), 150.2 (2C), 140.8 (C), 140.1 (2CH), 139.3 (CH), 135.4 (2C), 132.9 (2CH), 131.9 (2CH), 131.6 (2CH), 130.7 (2CH), 125.7 (C), 109.9 (2C), 108.1 (C), 102.1 (2C), 100.6 (C), 100.4 (C), 97.9 (2C), 34.4, 32.1, 29.8 (broad), 29.6, 29.5, 26.8, 26.7, 26.1, 25.1 (4CH), 24.3, 23.9 ($4CH_2$), 22.8, 19.3 ($12CH_3$), 14.3 ($2CH_3$), 13.8, 12.1 (6CH), 0.6 ($3CH_3$).

MALDI-ToF m/z 1695.01 (calculated for $C_{105}H_{172}N_4Si_5Zn$: 1695.17).

Zinc 5-{3,5-bis[bis(2-methylpropyl)(octadecyl)silyl]phenyl}-15-ethynyl-10,20-bis{[tri(propan-2-yl)silyl]ethynyl}porphyrin – P1q

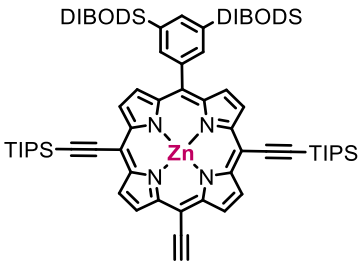

K_2CO_3 (352 mg, 2.5 mmol) was added to a solution of **P1p** (226 mg, 0.13 mmol (as a 1:1 complex with pyridine)) in THF (10 mL), MeOH (8 mL), and pyridine (0.1 mL). The suspension was stirred at room temperature for 30 min before the mixture was passed through a SiO_2 plug (2:1 PE 40-60:CH_2Cl_2 + 1% pyridine). Solvents were removed *in vacuo* to afford **P1q** (217 mg, 100%) as a purple solid with green lustre.

^{1}H NMR (400 MHz, $CDCl_3$ + 1% pyridine-d_5, 298 K): δ_H 9.71 (d, *J* = 4.5 Hz, 2H, *β-H*), 9.67 (d, *J* = 4.5 Hz, 2H, *β-H*), 9.59 (d, *J* = 4.5 Hz, 2H, *β-H*), 8.70 (d, *J* = 4.6 Hz, 2H, *β-H*), 8.16 (s, 2H, Ar-H_{ortho}), 8.02 (s, 1H, Ar-H_{para}), 4.14 (s, 1H, -≡-*H*), 1.99-1.87 (m, 4H), 1.54-1.40 (m, 42H), 1.38-1.14 (m, 68H), 1.01-0.95 (m, 24H), 0.95-0.91 (m, 8H), 0.89-0.84 (m, 6H).

^{13}C NMR (100 MHz, $CDCl_3$ + 1% pyridine-d_5, 298 K): δ_C 152.8 (2C), 152.6 (2C), 152.5 (2C), 150.2 (2C), 140.8 (C), 140.1 (2CH), 139.3 (CH), 135.4 (2C), 132.9 (2CH), 132.1 (2CH), 131.5 (2CH), 130.7 (2CH), 125.8 (C), 109.8 (2C), 102.1 (2C), 99.0 (C), 98.0 (2C), 86.5 (C), 83.1 (CH), 34.1, 32.1, 29.8 (broad), 29.5 (broad), 26.8, 26.7, 25.1 (4CH), 24.3, 23.9 ($4CH_2$), 22.8, 19.2 ($12CH_3$), 14.3 ($2CH_3$), 13.8, 12.1 (6CH).

MALDI-ToF m/z 1623.08 (calculated for $C_{102}H_{164}N_4Si_4Zn$: 1623.13).

5.10.5 Synthesis of Bis-Acetylene Linked Porphyrin Trimer (Ar = DIBODS)

***l*-P3$_{THS}^{C-2Br}$**

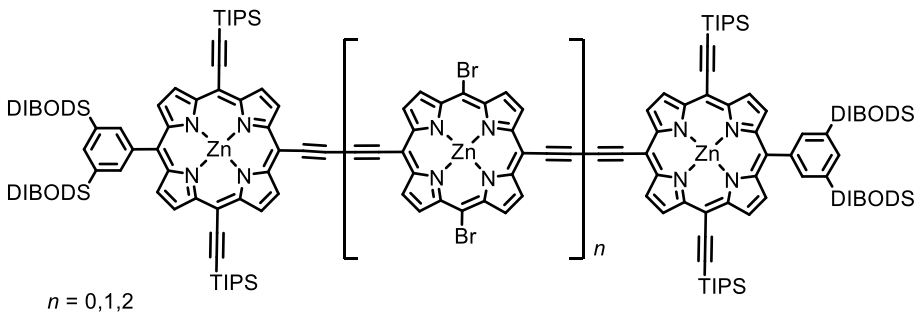

A solution was prepared of **P1q** (~0.245 mmol, crude from deprotection) and **P1k** (~82 µmol, crude from deprotection) in dry toluene (12 mL), dry *N,N*-diisopropylamine (12 mL), and pyridine (6 mL). A catalyst mixture of $Pd(PPh_3)_2Cl_2$ (28.8 mg, 41 µmol), CuI (78.0 mg, 0.41 mmol) and 1,4-benzoquinone (178 mg, 1.64 mmol) in dry toluene (5 mL) and dry *N,N*-diisopropylamine (5 mL) was added. The mixture was stirred in the dark at room temperature overnight before the mixture was passed through a short SiO_2 plug (toluene/5% pyridine). Solvents were removed *in vacuo* and the material was subsequently purified by size-exclusion chromatography (BioBeads SX-1, toluene/1% pyridine). Separation of the reaction products by recycling GPC (toluene/1% pyridine) yielded:

***l*-P2$_{DIBODS}$ (n=0)** (282 mg, 87 µmol, 71% from **P1q**)

^{1}H NMR (400 MHz, $CDCl_3$ + 1% pyridine-d_5, 298 K): δ_H 9.94 (d, *J* = 4.5 Hz, 4H, *β-H*), 9.82 (d, *J* = 4.5 Hz, 4H, *β-H*), 9.60 (d, *J* = 4.5 Hz, 4H, *β-H*), 8.75 (d, *J* = 4.5 Hz, 4H, *β-H*), 8.19 (s, 4H, Ar-H_{ortho}), 8.04 (s, 2H, Ar-H_{para}), 2.01-1.89 (m, 8H), 1.57-1.44 (m, 84H), 1.42-1.17 (m, 136H), 1.03-0.97 (m, 48H), 0.97-0.92 (m, 16H), 0.89-0.83 (m, 12H).

^{13}C NMR (125 MHz, $CDCl_3$ + 1% pyridine-d_5, 298 K): δ_C 153.4 (4C), 152.6 (4C), 152.2 (4C), 150.2 (4C), 140.7 (2C), 149.9 (4CH), 139.3 (2CH), 135.4 (2C), 133.0 (4CH), 132.4 (4CH), 131.5 (4CH), 130.7 (4CH), 126.3 (2C), 109.7 (4C), 102.6 (4C), 99.4 (2C), 98.2 (4C), 87.8 (2C), 81.9 (4C), 34.1, 32.0, 29.8 (broad), 29.5 (broad), 26.8, 26.7, 25.1 (8CH), 24.2, 23.8 ($8CH_2$), 22.8, 19.2 ($24CH_3$), 14.3 ($4CH_3$), 13.8, 12.0 (12CH).

MALDI-ToF m/z 3246.35 (calculated for $C_{204}H_{326}N_8Si_8Zn_2$: 3246.25).

UV-vis-NIR ($CHCl_3$) λ_{max} (log ε): 457 (5.39), 481 (5.28), 512 (5.37), 607 (4.41), 663 (4.68), 699 (4.77).

***l*-P3$_{DIBODS}^{C\text{-}2Br}$ (n= 1)** (56.5 mg, 15 µmol, 18% from **P1k**)

^{1}H NMR (400 MHz, $CDCl_3$ + 1% pyridine-d_5, 298 K): δ_H 9.98 (d, *J* = 4.5 Hz, 4H, *β-H*), 9.86 (d, *J* = 4.5 Hz, 4H, *β-H*), 9.85 (d, *J* = 4.5 Hz, 4H, *β-H*), 9.70 (d, *J* = 4.5 Hz, 4H, *β-H*), 9.62 (d, *J* = 4.5 Hz, 4H, *β-H*), 8.73 (d, *J* = 4.5 Hz, 4H, *β-H*), 8.21 (s, 4H, Ar-H_{ortho}), 8.06 (s, 2H, Ar-H_{para}), 2.02-1.90 (m, 8H), 1.59-1.44 (m, 84H), 1.42-1.17 (m, 136H), 1.03-0.98 (m, 48H), 0.98-0.94 (m, 16H), 0.90-0.85 (m, 12H).

^{13}C NMR (125 MHz, $CDCl_3$ + 1% pyridine-d_5, 298 K): δ_C 153.6, 153.5, 152.8, 152.3, 150.3, 150.1, 140.7, 140.0, 135.5, 134.1, 133.0, 132.5, 132.4, 131.4, 130.9, 126.5, 109.7, 107.8, 102.8, 101.6, 99.0, 98.5, 99.0, 87.5, 83.4, 81.9, 34.1, 32.0, 29.8 (broad), 29.5 (broad), 26.8, 26.7, 25.1, 24.3, 23.9, 22.8, 19.3, 14.2, 13.8, 12.1.

MALDI-ToF m/z 3823.41 (calculated for $C_{228}H_{334}Br_2N_{12}Si_8Zn_3$: 3823.09).

***l*-P4$_{DIBODS}^{C\text{-}4Br}$ (n=2)** (9.5 mg, 2.2 μmol, 5% from **P1k**)

^{1}H NMR (400 MHz, $CDCl_3$ + 1% pyridine-d_5, 298 K): δ_H 9.71 (d, *J* = 4.2 Hz, 4H, *β-H*), 9.68 (d, *J* = 4.4 Hz, 4H, *β-H*), 9.64 (d, *J* = 4.2 Hz, 4H, *β-H*), 9.60 (m, 8H, *β-H*), 9.42 (m, 8H, *β-H*), 8.82 (d, *J* = 4.4 Hz, 4H, *β-H*), 8.35 (s, 4H, Ar-H_{ortho}), 8.06 (s, 2H, Ar-H_{para}), 2.03-1.90 (m, 8H), 1.66-1.45 (m, 84H), 1.41-1.15 (m, 136H), 1.08-0.95 (m, 64H), 0.91-0.84 (m, 12H).

MALDI-ToF m/z 4399.57 (calculated for $C_{252}H_{342}Br_4N_{16}Si_8Zn_4$: 4400.93).

***l*-P3$_{DIBODS}^{C\text{-}2CPDMS}$**

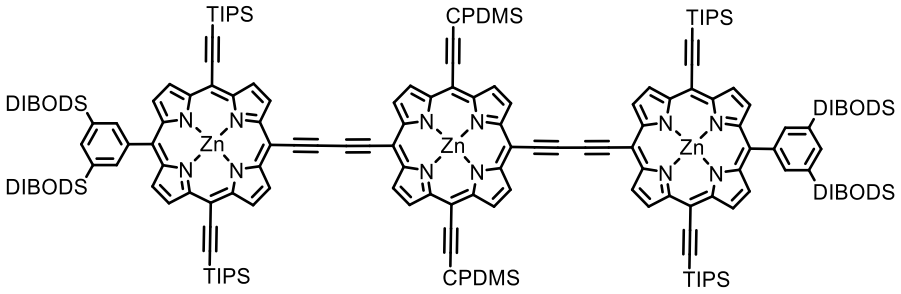

***l*-P3$_{DIBODS}^{C\text{-}2Br}$** (56.5 mg, 15 μmol), Pd_2dba_3 (2.7 mg, 3 μmol), CuI (0.6 mg, 3 μmol) and PPh_3 (1.6 mg, 6 μmol) were placed in a 50-mL two-necked flask. Toluene (8 mL) and *N,N*-diisopropylamine (4 mL) were added and the mixture was deoxygenated by 3 freeze-pump-thaw cycles. Cyanopropyldimethylsilylacetylene (7 mg, 45 μmol) was added and the reaction mixture was stirred overnight at room temperature. Solvents were removed *in vacuo* and the residue was purified by column chromatography (1:1 PE 40-60:CH_2Cl_2 + 1% pyridine) affording ***l*-P3$_{DIBODS}^{C\text{-}2CPDMS}$** (57 mg, 96%) as a chestnut solid.

^{1}H NMR (400 MHz, $CDCl_3$ + 1% d_5-pyridine , 298 K): δ_H 9.96 (d, *J* = 4.5 Hz, 4H, *β-H*), 9.93 (d, *J* = 4.5 Hz, 4H, *β-H*), 9.85 (d, *J* = 4.5 Hz, 4H, *β-H*), 9.71 (d, *J* = 4.5 Hz, 4H, *β-H*), 9.62 (d, *J* = 4.5 Hz, 4H, *β-H*), 8.73 (d, *J* = 4.5 Hz, 4H, *β-H*), 8.21 (s, 4H, Ar-H_{ortho}), 8.06 (s, 2H, Ar-H_{para}), 2.69 (t, *J* = 7.0 Hz, 4H, CH_2), 2.27 (m, 8H, CH_2), 2.02-1.90 (m, 8H), 1.59-1.46 (m, 84H), 1.43-1.20 (m, 136H), 1.04-0.99 (m, 48H), 0.99-0.94 (m, 16H), 0.90-0.85 (m, 12H), 0.72 (s, 12H, CH_3).

MALDI-ToF m/z 3957.15 (calculated for $C_{244}H_{358}N_{14}Si_{10}Zn_3$: 3964.40).

UV-vis-NIR ($CHCl_3$) λ_{max} (log ε): 460 (5.47), 519 (5.46), 601 (4.62), 656 (4.69), 739 (5.08).

5.10.6 Full Deprotection of ***l*-P3$_{\text{DIBODS}}^{\text{C-2CPDMS}}$** *and Coupling in the Presence of* **T6**

l-P3$_{\text{DIBODS}}$[acetylene]$_6$

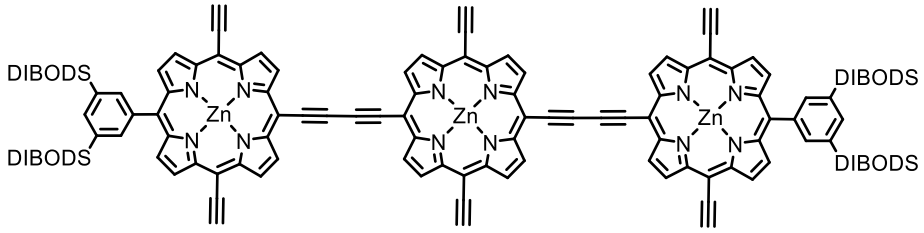

TBAF (1.0 M solution in THF, 0.16 mL, 0.16 mmol) was added to a solution of ***l*-P3$_{\text{DIBODS}}^{\text{C-2CPDMS}}$** (4.5 mg, 1.1 μmol) in CH_2Cl_2 (1 mL) and pyridine (0.01 mL). The solution was stirred at room temperature for 30 min and then directly passed through a SiO_2 plug (CH_2Cl_2/1% pyridine). Solvents were removed *in vacuo* to afford ***l*-P3$_{\text{DIBODS}}$[acetylene]$_6$** (3.5 mg, 100%) as a brown solid.

^{1}H NMR (400 MHz, $CDCl_3$ + 1% pyridine-d_5, 298 K): δ_H 9.95 (d, *J* = 4.5 Hz, 4H, *β-H*), 9.89 (d, *J* = 4.5 Hz, 4H, *β-H*), 9.76 (d, *J* = 4.5 Hz, 4H, *β-H*), 9.70 (d, *J* = 4.5 Hz, 4H, *β-H*), 9.59 (d, *J* = 4.5 Hz, 4H, *β-H*), 8.75 (d, *J* = 4.5 Hz, 4H, *β-H*), 8.23 (s, 4H, Ar-H_{ortho}), 8.06 (s, 2H, Ar-H_{para}), 4.27 (s, 2H, ≡-*H*), 4.17 (s, 4H, , ≡-*H*), 2.00-1.89 (m, 8H), 1.55-1.45 (m, 8H), 1.42-1.18 (m, 128 H), 1.04-0.98 (m, 48H), 0.98-0.93 (m, 16H), 0.91-0.84 (m, 12H).

Coupling of *l*-P3$_{\text{DIBODS}}$[acetylene]$_6$ in the presence of T6

Two different solvent/reaction temperature conditions were examined;
A solution of ***l*-P3$_{\text{DIBODS}}$[acetylene]$_6$** (3.5 mg, 1.1 μmol) and **T6** (1.7 mg, 1.7 μmol) in $CHCl_3$ (1.4 mL) was stirred for 10 min at room temperature when UV-vis-NIR spectroscopy confirmed formation of a complex. Half of the solution was concentrated and this material was re-dissolved in dry toluene (0.7 mL). Reaction A (in $CHCl_3$) was heated to 40 °C. Reaction B (in toluene) was heated to 65 °C. 0.5 mL of a catalyst mixture ($Pd(PPh_3)_2Cl_2$ (1.6 mg, 2.3 μmol), CuI (2.2 mg, 12 μmol), 1,4-benzoquinone (2.5 mg, 23 μmol) in dry toluene (0.85 mL) and dry *N,N*-diisopropylamine (0.15 mL)) was added to both A and B. Heating was continued and the reactions were monitored by UV-vis-NIR spectroscopy. After 2 h and 4 h of reaction time, an additional 0.25 mL of a freshly prepared catalyst mixture was added to A and B. When for both reactions no change in UV-vis-NIR was observed any more (after 5.5 h), the reaction mixtures were passed through a short Al_2O_3 plug (THF/1% pyridine). The materials were further purified by size-exclusion chromatography (BioBeads SX-1, THF/1% pyridine). At this point, most of the material had been lost as insoluble

compounds on either the Al_2O_3 plug or size-exclusion column. The remaining materials were analysed by analytical GPC (THF/1% pyridine) which showed a main component of unreacted ***l*-P3** as well as higher molecular weight materials.

5.10.7 Synthesis of ***l*-P2*[TIPS]$_4$** *and* ***l*-P3$^{*C\text{-}2TMS}$**

l-P2*[TIPS]$_4$

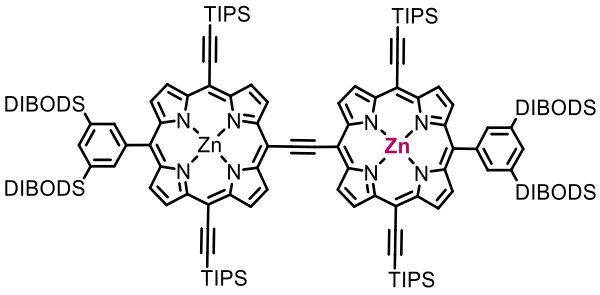

P1o (303 mg, 0.17 mmol) and **P1q** (98 mg, 57 μmol) were placed in a 100 mL two-necked flask in toluene (12 mL) and *N,N*-diisopropylamine (6 mL). In another 100 mL two-necked flask a catalyst mixture was prepared of Pd_2dba_3 (79 mg, 86 μmol), CuI (16.4 mg, 86 μmol) and PPh_3 (45 mg, 0.17 mmol) in toluene (12 mL) and *N,N*-diisopropylamine (6 mL). Both mixtures were deoxygenated by 3 freeze-pump-thaw cycles. The catalyst solution was added to the porphyrin mixture and the reaction mixture was stirred for 3 h. Solvents were removed *in vacuo* and the residue was purified by column chromatography (5:1 PE 40-60:CH_2Cl_2 + 1% pyridine). The mixture was purified by size-exclusion chromatography (BioBeads SX-1, toluene/1% pyridine) and finally subjected to recycling GPC (toluene/1% pyridine) to afford ***l*-P2*[TIPS]$_4$** (178 mg, 97% from **P1q**) as a green solid. Part of the excess porphyrin monomer **P1o** (59 mg, 34 μmol) was recovered. As a side product, 0.6 mg (<1% from **P1q**) of ***l*-P2$_{DIBODS}$[TIPS]$_4$** was obtained *via* the homo-coupling of **P1q**.

l-P2*[TIPS]$_4$

^{1}H NMR (400 MHz, $CDCl_3$ + 1% pyridine-d_5, 298 K): δ_H 10.39 (d, J = 4.5 Hz, 4H, *β-H*), 9.95 (d, J = 4.4 Hz, 4H, *β-H*), 9.65 (d, J = 4.5 Hz, 4H, *β-H*), 8.73 (d, J = 4.5 Hz, 4H, *β-H*), 8.22 (s, 4H, Ar-H_{ortho}), 8.05 (s, 2H, Ar-H_{para}), 2.02-1.90 (m, 8H), 1.59-1.46 (m, 84H), 1.42-1.18 (m, 136H), 1.04-0.98 (m, 48H), 0.98-0.94 (m, 16H), 0.88-0.83 (m, 12H).

^{13}C NMR (125 MHz, $CDCl_3$ + 1% pyridine-d_5, 298 K): δ_C 153.0 (4C), 152.7 (4C), 152.3 (4C), 150.5 (4C), 140.9 (2C), 140.1 (4CH), 139.3 (2CH), 135.5 (2C), 132.9 (4CH), 132.3 (4CH), 131.5 (4CH), 130.7 (4CH), 125.5 (2C), 110.0 (4C), 102.5 (4C), 102.3 (4C), 100.1

(2C), 98.1 (4C), 34.1, 32.0, 29.8 (broad), 29.5 (broad), 26.8, 26.7, 25.1 (8CH), 24.3, 23.9 ($8CH_2$), 22.8, 19.3 ($24CH_3$), 14.2 ($4CH_3$), 13.8, 12.1 (12CH).

MALDI-ToF m/z 3222.29 (calculated for $C_{202}H_{326}N_8Si_8Zn_2$: 3222.25).

UV-vis-NIR ($CHCl_3$) λ_{max} (log ε): 707 (4.69), 514 (5.40), 477 (5.00), 453 (5.24).

***l*-P2$_{DIBODS}$**

^{1}H NMR and **MALDI-ToF m/z** as above.

Zinc 5,15-dibromo-10,20-bis[(trimethylsilyl)ethynyl]porphyrin – P1r

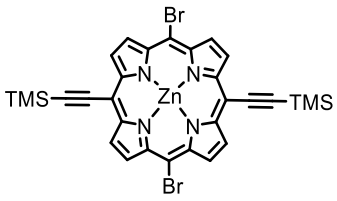

LiHMDS (1.0 M solution in THF, 0.2 mL, 0.2 mmol) was added to a solution of **P1k** (43.9 mg, 0.066 mmol) under N_2 atmosphere in THF (14 mL) under rapid stirring. The reaction was stirred for 10 min before TMS-chloride (37 μL, 0.29 mmol) was added and the reaction was monitored by TLC. After 2 h, a second batch of LiHMDS (1.0 M solution in THF, 0.1 mL, 0.1 mmol) and TMS-chloride (25 μL, 0.20 mmol) were added. Upon completion, $CHCl_3$:CH_2Cl_2 1:1 was added. The solution was washed with water and concentrated. Column chromatography (20:1:1 to 10:1:1 PE 40-60:EtOAc:pyridine to 10:1:1) afforded **P1r** (28.1, 53%) as a purple solid with green lustre.

^{1}H NMR (400 MHz, $CDCl_3$ +1% pyridine-d_5, 298 K): δ_H 9.55 (d, J = 4.6 Hz, 4H, *β-H*), 9.53 (d, J = 4.6 Hz, 4H, *β-H*), 0.64 (s, 18H, TMS-*H*).

^{13}C NMR (100 MHz, $CDCl_3$ +1% pyridine-d_5, 298 K): δ_C 152.77 (4C), 150.11 (4C), 133.60 (4CH), 132.48 (4CH), 107.65 (2C), 106.71 (2C), 101.89 (2C), 101.82 (2C), 0.49 (6CH3).

MALDI-ToF m/z 723.85 (calculated for $C_{30}H_{26}Br_2N_4Si_2Zn$: 723.93).

***l*-P3*C-2TMS**

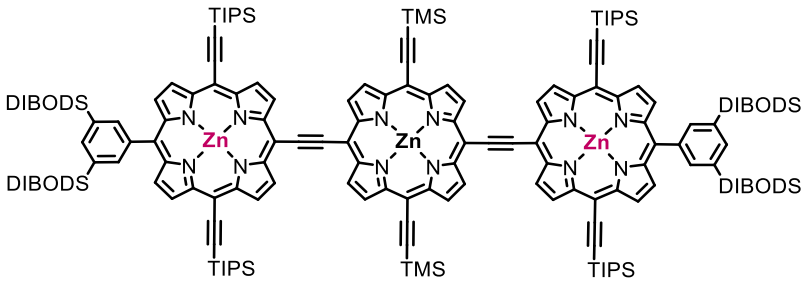

P1r (18.7 mg, 23 μmol - 1:1 complex with pyridine) and **P1q** (119 mg, 70 μmol - 1:1 complex with pyridine) were placed in a 100 mL two-necked flask in toluene (16 mL) and *N,N*-diisopropylamine (8 mL). In another 100 mL two-necked flask a catalyst mixture was prepared of Pd_2dba_3 (43 mg, 47 μmol), CuI (9 mg, 47 μmol) and PPh_3 (24 mg, 93 μmol) in toluene (7 mL) and *N,N*-diisopropylamine (3.5 mL). Both mixtures were deoxygenated by 3 freeze-pump-thaw cycles. The catalyst solution was added to the porphyrin mixture and the reaction mixture was stirred overnight at room temperature. Solvents were removed *in vacuo* and the residue was purified by column chromatography (3:1 PE 40-60:CH_2Cl_2 + 1% pyridine). The mixture was subsequently purified by size-exclusion chromatography (BioBeads SX-1, toluene/1% pyridine) and finally subjected to recycling GPC (toluene/1% pyridine) to afford ***l*-P3*C-2TMS** (85.4 mg, 96% from **P1r**) as a brown solid. As a side product ***l*-P2$_{DIBODS}$[TIPS]$_4$** (31.9 mg, 28% from **P1q**) of was obtained *via* the homo-coupling of **P1q**.

^{1}H NMR (500 MHz, $CDCl_3$ + 1% pyridine-d_5, 298 K): δ_H 10.42 (d, J = 4.4 Hz, 8H, *β-H*), 9.98 (d, J = 4.4 Hz, 4H, *β-H*), 9.95 (d, J = 4.4 Hz, 4H, *β-H*), 9.67 (d, J = 4.4 Hz, 4H, *β-H*), 8.76 (d, J = 4.4 Hz, 4H, *β-H*), 8.24 (s, 4H, Ar-H_{ortho}), 8.06 (s, 2H, Ar-H_{para}), 2.02-1.92 (m, 8H), 1.61-1.47 (m, 84H), 1.44-1.17 (m, 136H), 1.05-0.99 (m, 48H), 0.99-0.95 (m, 16H), 0.89-0.84 (m, 12H), 0.75 (s, 18H, Si-CH_3).

^{13}C NMR (125 MHz, $CDCl_3$ + 1% pyridine-d_5, 298 K): δ_C 152.9, 152.7, 152.3, 150.5, 140.7, 140.0, 139.3, 135.4, 133.0, 132.4, 131.6, 131.3, 130.9, 125.8, 109.0, 107.8, 104.3, 103.3, 102.6, 101.9, 101.1,99.9, 98.1, 34.1, 32.0, 29.8 (broad), 29.5 (broad), 26.8, 26.7, 25.1, 24.3, 23.8, 22.8, 19.3, 14.3, 13.8, 12.1, 0.0.

MALDI-ToF m/z 3810.17 (calculated for $C_{234}H_{325}N_{12}Si_{10}Zn_3$: 3810.35).

UV-vis-NIR ($CHCl_3$) λ_{max} (log ε): 438 (5.30), 526 (5.46), 669 (4.56), 770 (4.99).

***l*-P2$_{DIBODS}$**

^{1}H NMR and **MALDI-ToF m/z** as above.

5.10.8 Synthesis of ***t*-P12*·(T6)$_2$**

***l*-P2*[acetylene]$_4$**

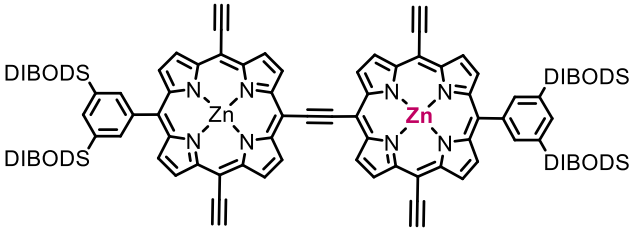

TBAF (1.0 M solution in THF, 0.12 mL, 0.12 mmol) was added to a solution of ***l*-P2*[TIPS]$_4$** (13 mg, 4.0 μmol) in CH_2Cl_2 (3 mL) and pyridine (0.1 mL). The solution was stirred at room temperature for 30 min and then passed through a SiO_2 plug (CH_2Cl_2/1% pyridine). Solvents were removed *in vacuo* to afford ***l*-P2*[acetylene]$_4$** (10.6 mg, 100%) as a green solid.

^{1}H NMR (400 MHz, $CDCl_3$ + 1% pyridine-d$_5$, 298 K): δ_H 10.43 (d, *J* = 4.5 Hz, 4H, *β-H*), 9.95 (d, *J* = 4.5 Hz, 4H, *β-H*), 9.66 (d, *J* = 4.5 Hz, 4H, *β-H*), 8.78 (d, *J* = 4.5 Hz, 4H, *β-H*), 8.24 (s, 4H, Ar-H_{ortho}), 8.07 (s, 2H, Ar-H_{para}), 4.24 (s, 4H, ≡*H*), 2.02-1.90 (m, 8H), 1.58-1.46 (m, 8H), 1.42-1.18 (m, 128H), 1.04-0.98 (m, 48H), 0.98-0.94 (m, 16H), 0.88-0.83 (m, 12H).

^{13}C NMR (100 MHz, $CDCl_3$ + 1% pyridine-d$_5$, 298 K): δ_C 153.2, 152.6, 152.3, 150.8, 140.7, 140.2, 135.6, 133.1, 132.3, 131.6, 131.0, 125.5, 102.3, 100.8, 86.6, 83.8, 34.1, 32.0, 29.9-29.7 (broad), 29.6, 29.5, 26.8, 26.7, 25.1, 24.3, 23.9, 22.8, 14.2, 13.8, 12.1.

MALDI-ToF m/z 2596.95 (calculated for $C_{166}H_{246}N_8Si_4Zn_2$: 2586.72).

***t*-P12*·(T6)$_2$**

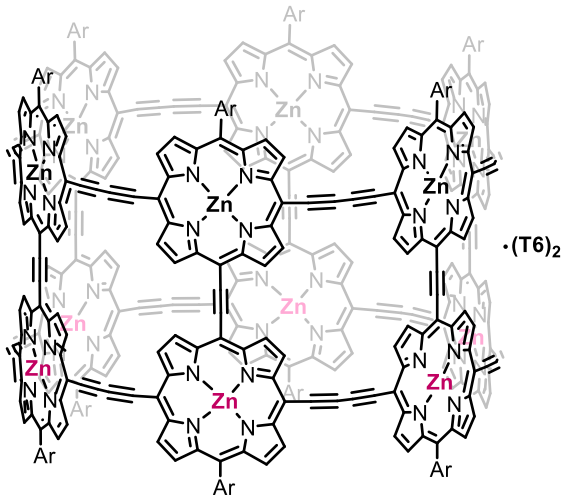

***l*-P2*[acetylene]$_4$** (9.2 mg, 3.5 μmol) was dissolved in $CHCl_3$ (3.5 mL) and **T6** (5.3 mg, 5.3 μmol) was added. The solution was stirred for 10 min after which UV-vis-NIR spectroscopy confirmed formation of the complex. The solution was concentrated and the residue re-dissolved in dry toluene (4.2 mL). The solution was stirred for 20 min before a catalyst mixture of $Pd(PPh_3)_2Cl_2$ (0.5 mg, 0.71 μmol), CuI (0.67 mg, 3.5 μmol) and 1,4-benzoquinone (0.77 mg, 7.1 μmol) in toluene (0.4 mL) and *N*,*N*-diisopropylamine (0.1 mL) was added. Additional catalyst was added after 2 h (½ eq catalyst), 3 h (1 eq catalyst) and 4.5 h (2 eq catalyst). After 6 h of total reaction time, UV-vis-NIR showed the reaction to be complete. The was filtered through a SiO_2 plug (CH_2Cl_2). The material was further purified by size-exclusion chromatography (BioBeads SX-1, toluene/1% pyridine) and finally subjected to recycling GPC (toluene/1% pyridine) to afford ***t*-P12*·(T6)$_2$** (0.68 mg, 7%) as a pink solid.

^{1}H NMR (500 MHz, $CDCl_3$ + 1% pyridine-d$_5$, 298 K): δ_H 10.69 (br s, 24H, *β-H*), 10.33 (d, *J* = 3.6 Hz, 24H, *β-H*), 9.49 (d, *J* = 4.1 Hz, 24H, *β-H*), 8.57 (d, *J* = 4.1 Hz, 24H, *β-H*), 8.27 (s, 12H, Ar-H_{para}), 8.05 (s, 12H, Ar-H_{ortho}), 7.99 (s, 12H, Ar-H_{ortho}), 5.50 (br s, 24H), 5.43 (m, 24H), 5.18 (d, *J* = 6.6 Hz, 24H), 2.94 (d, *J* = 6.6 Hz, 24H), 2.00-1.86 (m, 48H), 1.64-1.51 (m, 48H), 1.51–1.12 (m, 768H), 1.03–0.89 (m, 384H), 0.89–0.75 (m, 72H).

MALDI-ToF m/z 17556 (calculated for $C_{1140}H_{1548}N_{60}Si_{24}Zn_{12}$: 17551.91).

UV-vis-NIR (toluene) λ_{max} (log ε): 534 (5.92), 828 (5.55), 869 (5.65), 910 (5.59).

5.10.9 Synthesis of ***t*-P18*·T6 pre-tube** *and* ***t*-P18*·(T6)$_n$**

***l*-P3*[acetylene]$_6$**

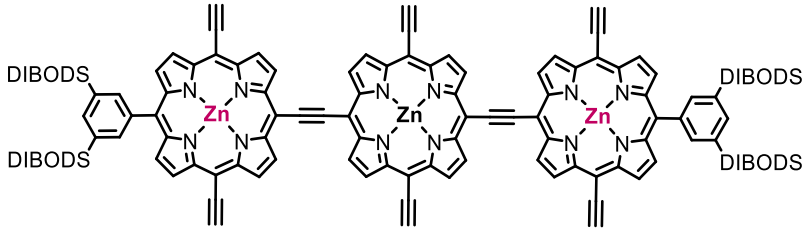

TBAF (1.0 M solution in THF, 0.16 mL, 0.16 mmol) was added to a solution of ***l*-P3*$^{C\text{-}2TMS}$** (20.4 mg, 5.3 μmol) in CH_2Cl_2 (5 mL) and pyridine (0.4 mL). The solution was stirred at room temperature for 30 min. and then directly passed through a SiO_2 plug (CH_2Cl_2/1% pyridine). Solvents were removed *in vacuo* to afford ***l*-P3*[acetylene]$_6$** (15.8 mg, 98%) as a brown solid.

^{1}H NMR (400 MHz, $CDCl_3$ + 1% pyridine-d$_5$, 298 K): δ_H 10.44 (d, *J* = 4.5 Hz, 4H, *β-H*), 10.37 (d, *J* = 4.5 Hz, 4H, *β-H*), 9.93 (d, *J* = 4.5 Hz, 4H, *β-H*), 9.86 (d, *J* = 4.5 Hz, 4H, *β-H*), 9.65 (d, *J* = 4.5 Hz, 4H, *β-H*), 8.78 (d, *J* = 4.5 Hz, 4H, *β-H*), 8.26 (s, 4H, Ar-H_{ortho}), 8.07 (s, 2H, Ar-H_{para}), 4.25 (s, 2H, ≡*H*), 4.22 (s, 4H, ≡*H*), 2.03-1.90 (m, 8H), 1.58-1.46 (m, 8H), 1.45-1.18 (m, 128H), 1.07-0.99 (m, 48H), 0.99-0.94 (m, 16H), 0.90-0.82 (m, 12H).

MALDI-ToF m/z 3039.20 (calculated for $C_{192}H_{256}N_{12}Si_4Zn_3$: 3039.74).

***l*-P3*$^{C\text{-}2acetylene}$**

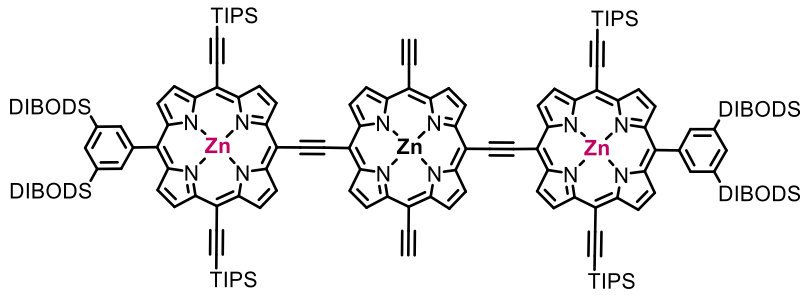

K_2CO_3 (23.8 mg, 0.17 mmol) was added to a solution of ***l*-P3*$^{C\text{-}2TMS}$** (32.9 mg, 8.6 μmol) in THF (5 mL), MeOH (4 mL), and pyridine (0.1 mL). The suspension was stirred at room temperature for 30 min before the mixture was passed through a SiO_2 plug (1:1 PE 40-60:CH_2Cl_2 + 1% pyridine). Solvents were removed *in vacuo* to afford ***l*-P3*$^{C\text{-}2acetylene}$** (28.4 mg, 90%) as a brown solid.

^{1}H NMR (400 MHz, $CDCl_3$ + 1% pyridine-d$_5$, 298 K): δ_H 10.43 (d, *J* = 4.4 Hz, 4H, *β-H*), 10.42 (d, *J* = 4.4 Hz, 4H, *β-H*), 9.98 (d, *J* = 4.5 Hz, 4H, *β-H*), 9.96 (d, *J* = 4.5 Hz, 4H,

β-H), 9.66 (d, *J* = 4.5 Hz, 4H, *β-H*), 8.75 (d, *J* = 4.5 Hz, 4H, *β-H*), 8.23 (s, 4H, Ar-H_{ortho}), 8.06 (s, 2H, Ar-H_{para}), 4.31 (s, 2H, ≡*H*), 2.03-1.92 (m, 8H), 1.61-1.47 (m, 84H), 1.44-1.17 (m, 136H), 1.05-0.99 (m, 48H), 0.99-0.95 (m, 16H), 0.89-0.82 (m, 12H).

MALDI-ToF m/z 3364.78 (calculated for $C_{228}H_{336}N_{12}Si_8Zn_3$: 3665.27).

***t*-P18*·(T6)$_3$** (directly from ***l*-P3*[acetylene]$_6$**)

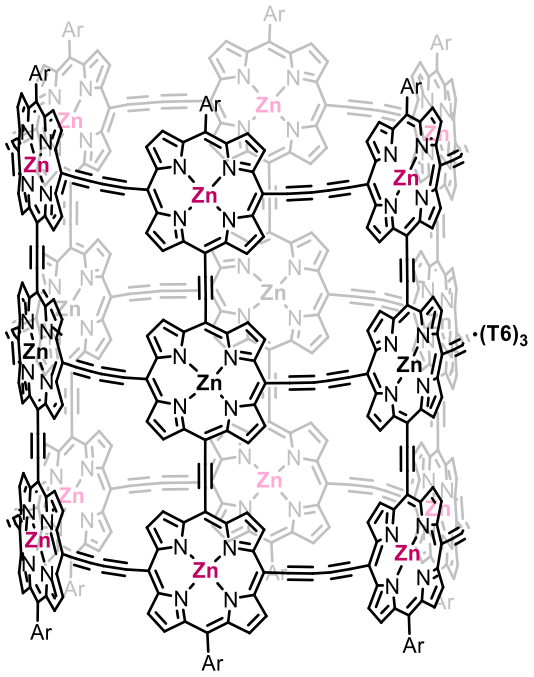

A solution of ***l*-P3*[acetylene]$_6$** (3.4 mg, 1.1 µmol) and **T6** (1.7 mg, 1.7 µmol) in $CHCl_3$ (6.5 mL) was stirred for 30 min at room temperature after which UV-vis-NIR spectroscopy confirmed formation of the complex. A catalyst mixture ($Pd(PPh_3)_2Cl_2$ (6.4 mg, 8.8 µmol), CuI (8.4 mg, 45 µmol), and 1,4-benzoquinone (9.6 mg, 90 µmol) in toluene (1.1 mL) and *N,N*-diisopropylamine (0.15 mL) was added. The reaction was monitored by UV-vis-NIR spectroscopy. After 3 h, 5.5 h, and 7 h, freshly prepared catalyst mixture was added. When no change in UV-vis-NIR was observed any more (7.5 h) the reaction mixture was directly passed through a short SiO_2 plug (CH_2Cl_2). The material was purified by size-exclusion chromatography (BioBeads SX-1, THF/1% pyridine) and finally subjected to recycling GPC (THF/1% pyridine). The formation of ***t*-P18*·(T6)$_3$** (which was obtained as a pink solution in THF/1% pyridine) was confirmed by analytical GPC. The isolated amount of material was insufficient to allow for analysis by ^{1}H NMR.

***t*-P18*·T6 pre-tube**

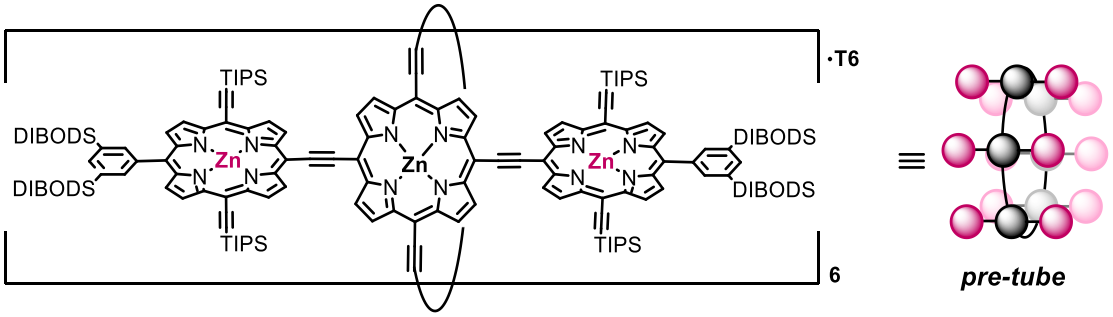

A solution of ***l*-P3*C-2acetylene** (23.8 mg, 6.5 μmol) and **T6** (3.2 mg, 3.25 μmol) in $CHCl_3$ (25 mL) was stirred for 20 min at room temperature after which UV-vis-NIR spectroscopy confirmed formation of the complex. The reaction mixture was heated to 40 °C and a catalyst mixture of $Pd(PPh_3)_2Cl_2$ (0.91 mg, 1.3 μmol), CuI (1.2 mg, 6.3 μmol), and 1,4-benzoquinone (1.4 mg, 13 μmol) in toluene (1 mL) and *N,N*-diisopropylamine (0.5 mL) was added. Heating was continued, and the reaction was monitored by UV-vis-NIR spectroscopy. After 2 h and 3.5 h an additional half equivalent of freshly prepared catalyst mixture was added. When no change in UV-vis-NIR was observed any more (6 h) the reaction mixture was directly passed through a short plug of basic Al_2O_3 (toluene/1% pyridine). After removal of the solvents *in vacuo*, the material was purified by size-exclusion chromatography (BioBeads SX-1, THF/1% pyridine) and finally subjected to recycling GPC (THF/1% pyridine) to afford ***t*-P18*·T6 pre-tube** (4.5 mg, 18%) as a dark red solid.

^{1}H NMR (400 MHz, $CDCl_3$ + 1% pyridine-d_5, 298 K): δ_H 10.32 (d, *J* = 3.9 Hz, 24H, *β-H*), 10.20 (d, *J* = 3.9 Hz, 24H, *β-H*), 9.95 (d, *J* = 3.9 Hz, 24H, *β-H*), 9.80 (d, *J* = 3.9 Hz, 24H, *β-H*), 9.47 (d, *J* = 4.0 Hz, 24H, *β-H*), 8.65 (d, *J* = 3.9 Hz, 24H, *β-H*), 8.21 (s, 24H, Ar-H_{ortho}), 8.06 (s, 12H, Ar-H_{para}), 5.62 (s, 24H), 5.35 (d, *J* = 5.6 Hz, 12H), 3.03 (br s, 12H), 2.03-1.91 (m, 48H), 1.61-1.48 (m, 48H), 1.48-1.15 (m, 1272H), 1.09-0.90 (m, 288H), 0.87-0.73 (m, 120H), 0.72-0.61 (m, 48H).

MALDI-ToF m/z 22986 (calculated for $C_{1440}H_{2052}N_{78}Si_{48}Zn_{18}$: 22982).

UV-vis-NIR ($CHCl_3$) λ_{max} (log ε): 441 (6.11), 547 (5.98), 663 (5.44), 800 (5.68), 845 (5.50), 893 (5.60).

***t*-P18*·T6** (from ***t*-P18*·T6 pre-tube**)

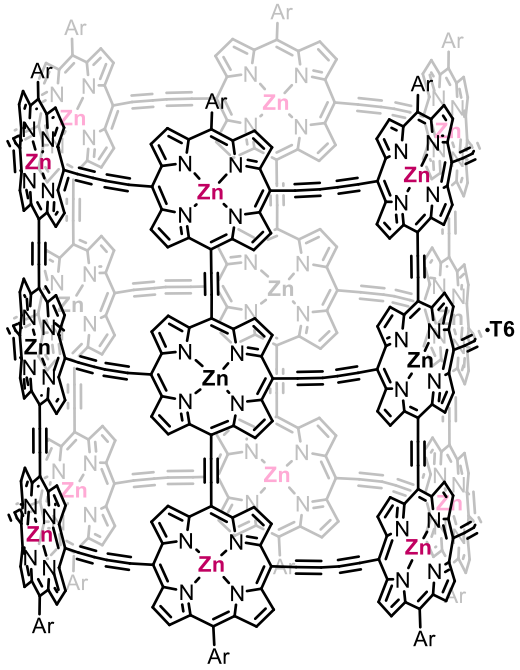

TBAF (1.0 M solution in THF, 43 µL, 43 µmol,) was added to a solution of ***t*-P18*·T6 pre-tube** (9.8 mg, 0.43, 0.43 µmol) in CH_2Cl_2 (4 mL) and pyridine (0.4 mL). The solution was stirred for 35 min after which it was passed through a short SiO_2 plug ($CHCl_3$/5% pyridine). The solvents were carefully removed *in vacuo*. Deprotection was confirmed by MALDI-ToF. The compound gives a broad ^{1}H NMR spectrum. This material was used without further purification in the next step in which a 100% conversion was assumed.

MALDI-ToF m/z 18283, 19286 (calculated for $C_{1152}H_{1524}N_{72}Si_{24}Zn_{18}$: 18232 and $C_{1224}H_{1572}N_{78}Si_{24}Zn_{18}$: 19229; deprotected ***t*-P18* pre-tube** without and with **T6,** resp.).

Deprotected ***t*-P18*·T6 pre-tube** was dissolved in $CHCl_3$ (120 mL) and pyridine (13 mL). A catalyst solution of $Pd(PPh_3)_2Cl_2$ (5.8 mg, 8.3 µmol), CuI (7.8 mg, 41 µmol), and 1,4-benzoquinone (8.8 mg, 81 µmol) in toluene (2.5 mL) and *N,N*-diisopropylamine (1.2 mL) was added and the reaction was monitored by UV-vis-NIR spectroscopy. After 2 h and 3.5 h, freshly prepared catalyst mixture was added. When the reaction was judged complete (after 4.5 h of total reaction time in which the solution had turned from deep red to deep pink), the material was passed through a short Al_2O_3 plug (toluene/1% pyridine). The material was purified by size-exclusion chromatography (BioBeads SX-1, THF/3% pyridine) and finally subjected to recycling GPC (THF/3% pyridine). The formation of ***t*-P18*·T6** (obtained as a pink solution in THF/3% pyridine) was confirmed by analytical GPC and MALDI-ToF. ^{1}H NMR was broad.

MALDI-ToF m/z 18255 (calculated for $C_{1152}H_{1524}N_{72}Si_{24}Zn_{18}$: 18208).

It was very challenging to measure a MALDI-ToF spectrum for these compounds. By the EPSRC UK National Mass Spectrometry Facility at Swansea University, no usable MALDI-ToF spectrum was obtained. Extensive efforts to measure a MALDI-ToF spectrum for these compounds by the author did give usable data, albeit with m/z values that are ~50 mass units off. As stand-alone proof for the formation of the 18-porphyrin nanotube these spectra are hence not sufficient. However, the author believes that in combination with the other evidence provided, these MALDI-ToF spectra support the conclusion that the target compound was successfully prepared.

5.11 References

(1) M. Hoffmann, C. J. Wilson, B. Odell, H. L. Anderson. 'Template-Directed Synthesis of a π-Conjugated Porphyrin Nanoring'. *Angew. Chem. Int. Ed.*, **2007**, *46*, 3122–3125.

(2) M. C. O'Sullivan, J. K. Sprafke, D. V Kondratuk, C. Rinfray, T. D. W. Claridge, A. Saywell, M. O. Blunt, J. N. O'Shea, P. H. Beton, M. Malfois, H. L. Anderson. 'Vernier Templating and Synthesis of a 12-Porphyrin Nano-Ring'. *Nature*, **2011**, *469*, 72–75.

(3) D. V. Kondratuk, L. M. A. Perdigão, A. M. S. Esmail, J. N. O'Shea, P. H. Beton, H. L. Anderson. 'Supramolecular Nesting of Cyclic Polymers'. *Nat. Chem.*, **2015**, *7*, 317–322.

(4) S. Liu, D. V. Kondratuk, S. A. L. Rousseaux, G. Gil-Ramírez, M. C. O'Sullivan, J. Cremers, T. D. W. Claridge, H. L. Anderson. 'Caterpillar Track Complexes in Template-Directed Synthesis and Correlated Molecular Motion'. *Angew. Chem. Int. Ed.*, **2015**, *54*, 5355–5359.

(5) S. A. L. Rousseaux, J. Q. Gong, R. Haver, B. Odell, T. D. W. Claridge, L. M. Herz, H. L. Anderson. 'Self-Assembly of Russian Doll Concentric Porphyrin Nanorings'. *J. Am. Chem. Soc.*, **2015**, *137*, 12713–12718.

(6) P. Parkinson, D. V. Kondratuk, C. Menelaou, J. Q. Gong, H. L. Anderson, L. M. Herz. 'Chromophores in Molecular Nanorings: When Is a Ring a Ring?'. *J. Phys. Chem. Lett.*, **2014**, *5*, 4356–4361.

(7) B. M. Wong. 'Optoelectronic Properties of Carbon Nanorings: Excitonic Effects from Time-Dependent Density Functional Theory'. *J. Phys. Chem. C*, **2009**, *113*, 21921–21927.

(8) T. Iwamoto, Y. Watanabe, Y. Sakamoto, T. Suzuki, S. Yamago. 'Selective and Random Syntheses of [N]cycloparaphenylenes (N = 8-13) and Size Dependence of Their Electronic Properties'. *J. Am. Chem. Soc.*, **2011**, *133*, 8354–8361.

(9) P. Neuhaus, A. Cnossen, J. Q. Gong, L. M. Herz, H. L. Anderson. 'A Molecular Nanotube with Three-Dimensional π-Conjugation'. *Angew. Chem. Int. Ed.*, **2015**, *54*, 7344 –7348.

(10) J. K. Sprafke, D. V. Kondratuk, M. Wykes, A. L. Thompson, M. Hoffmann, R. Drevinskas, W. H. Chen, C. K. Yong, J. Kärnbratt, J. E. Bullock, M. Malfois, M. R. Wasielewski, B. Albinsson, L. M. Herz, D. Zigmantas, D. Beljonne, H. L. Anderson. 'Belt-Shaped π-Systems: Relating Geometry to Electronic Structure in a Six-Porphyrin Nanoring'. *J. Am. Chem. Soc.*, **2011**, *133*, 17262–17273.

(11) D. V. Kondratuk, L. M. A. Perdigao, M. C. O'Sullivan, S. Svatek, G. Smith, J. N. O'Shea, P. H. Beton, H. L. Anderson. 'Two Vernier-Templated Routes to a 24-Porphyrin Nanoring'. *Angew. Chem. Int. Ed.*, **2012**, *51*, 6696–6699.

(12) P. Liu, P. Neuhaus, D. V. Kondratuk, T. S. Balaban, H. L. Anderson. 'Cyclodextrin-Templated Porphyrin Nanorings'. *Angew. Chem. Int. Ed.*, **2014**, *53*, 7770–7773.

(13) S. G. Wilson, H. L. Anderson. 'A Conjugated Triple Strand Porphyrin Array'. *Chem. Comm.*, **1999**, *1*, 1539–1540.

(14) T. E. O. Screen, K. B. Lawton, G. S. Wilson, N. Dolney, R. Ispasoiu, T. Goodson III, S. J. Martin, D. D. C. Bradley, H. L. Anderson. 'Synthesis and Third Order Nonlinear Optics of a New Soluble Conjugated Porphyrin Polymer'. *J. Mater. Chem.*, **2001**, *11*, 312–320.

(15) C. E. Tait, P. Neuhaus, M. D. Peeks, H. L. Anderson, C. R. Timmel. 'Transient EPR Reveals Triplet State Delocalization in a Series of Cyclic and Linear π-Conjugated Porphyrin Oligomers'. *J. Am. Chem. Soc.*, **2015**, *137*, 8284–8293.

(16) M. Hoffmann, J. Kärnbratt, M. H. Chang, L. M. Herz, B. Albinsson, H. L. Anderson. 'Enhanced π Conjugation Around a Porphyrin[6] Nanoring'. *Angew. Chem. Int. Ed.*, **2008**, *47*, 4993–4996.

(17) F. C. Grozema, C. Houarner-Rassin, P. Prins, L. D. A Siebbeles, H. L. Anderson. 'Supramolecular Control of Charge Transport in Molecular Wires'. *J. Am. Chem. Soc.*, **2007**, *129*, 13370–13371.

(18) L. Favereau, A. Cnossen, J. B. Kelber, J. Q. Gong, R. M. Oetterli, J. Cremers, L. M. Herz, H. L. Anderson. 'Six-Coordinate Zinc Porphyrins for Template-Directed Synthesis of Spiro-Fused Nanorings'. *J. Am. Chem. Soc.*, **2015**, *137*, 14256–14259.

(19) S. Richert, J. Cremers, I. Kuprov, M. D. Peeks, H. L. Anderson, C. R. Timmel. 'Constructive Quantum Interference in a Bis-Copper Six-Porphyrin Nanoring'. *Nat. Commun.*, **2017**, *8*, 14842–14846.

(20) M. Rickhaus, A. Vargas Jentzsch, L. Tejerina, I. Gruebner, M. Jirasek, T. D. W. Claridge, H. L. Anderson. 'Single-Acetylene Linked Porphyrin Nanorings'. *J. Am. Chem. Soc.*, **2017**, *139*, 16502–16505.

(21) M. Bixon, J. Jortner, J. Cortes, H. Heitele, M. E. Michel-Beyerle. 'Energy Gap Law for Nonradiative and Radiative Charge Transfer in Isolated and in Solvated Supermolecules'. *J. Phys. Chem.*, **1994**, *98*, 7289–7299.

(22) R. Englman, J. Jortner. 'The Energy Gap Law for Radiationless Transitions in Large Molecules'. *Mol. Phys.*, **1970**, *18*, 285–287.

(23) K. Kalyanasundaram. *Photochemistry of Polypyridine and Porphyrin Complexes*; Academic Press, **1992**.

(24) S. J. Lee, K. L. Mulfort, J. L. O'Donnell, X. Zuo, A. J. Goshe, P. J. Wesson, S. T. Nguyen, J. T. Hupp, D. M. Tiede. 'Supramolecular Porphyrinic Prisms: Coordinative Assembly and Solution Phase X-Ray Structural Characterization'. *Chem. Comm.*, **2006**, *3*, 4581–4583.

(25) M. Hutin, J. K. Sprafke, B. Odell, H. L. Anderson, T. D. W. Claridge. 'A Discrete Three-Layer Stack Aggregate of a Linear Porphyrin Tetramer: Solution-Phase Structure Elucidation by NMR and X-Ray Scattering'. *J. Am. Chem. Soc.*, **2013**, *135*, 12798–12807.

(26) S. Hiroto, A. Osuka. '*Meso*-Alkyl-Substituted *Meso-Meso* Linked Diporphyrins and *Meso*-Alkyl-Substituted *Meso-Meso*, B-B, B-B Triply Linked Diporphyrins'. *J. Org. Chem.*, **2005**, *70*, 4054–4058.

(27) D. Myśliwiec, B. Donnio, P. J. Chmielewski, B. Heinrich, M. Stepień. 'Peripherally Fused Porphyrins via the Scholl Reaction: Synthesis, Self-Assembly, and Mesomorphism'. *J. Am. Chem. Soc.*, **2012**, *134*, 4822–4833.

(28) H. L. Anderson. 'Conjugated Porphyrin Ladders'. *Inorg. Chem.*, **1994**, *33*, 972–981.

(29) W. Zeng, H. Phan, T. S. Herng, T. Y. Gopalakrishna, N. Aratani, Z. Zeng, H. Yamada, J. Ding, J. Wu. 'Rylene Ribbons with Unusual Diradical Character'. *Chem*, **2017**, *2*, 81–92.

(30) M. Abe. 'Diradicals'. *Chem. Rev.*, **2013**, *113*, 7011–7088.

(31) Z. Zeng, X. Shi, C. Chi, J. T. López Navarrete, J. Casado, J. Wu. 'Pro-Aromatic and Anti-Aromatic π-Conjugated Molecules: An Irresistible Wish to Be Diradicals'. *Chem. Soc. Rev.*, **2015**, *44*, 6578–6596.

(32) V. S. -Y. Lin, M. J. Therien. 'The Role of Porphyrin-to-Porphyrin Linkage Topology in the Extensive Modulation of the Absorptive and Emissive Properties of a Series of Ethynyl- and Butadiynyl-Bridged Bis- and Tris(Porphinato)Zinc Chromophores'. *Chem. – A Eur. J.*, **1995**, *1*, 645–651.

(33) L. Rintoul, S. R. Harper, D. P. Arnold. 'A Systematic Theoretical Study of the Electronic Structures of Porphyrin Dimers: DFT and TD-DFT Calculations on Diporphyrins Linked by Ethane, Ethene, Ethyne, Imine, and Azo Bridges'. *Phys. Chem. Chem. Phys.*, **2013**, *15*, 18951–18964.

6

Computational Studies on Large Porphyrin Nanostructures

Parts of this chapter were published in:

J. Cremers, R. Haver, M. Rickhaus, J. Q. Gong, L. Favereau, T. D. W. Claridge, L. M. H. Herz, H. L. A. Anderson. 'Template-Directed Synthesis of a Conjugated Zinc Porphyrin Nanoball'. *J. Am. Chem. Soc.,* **2018**, ASAP.

6.1 Abstract

This chapter describes Density Functional Theory (DFT) calculations on large π-conjugated porphyrin nanostructures. Size-dependent bandgap oscillations in bis-acetylene linked porphyrin nanotubes were examined, in analogy to recently published work by Allec and co-workers. Furthermore, the optimised geometry of ***t*-P12***, a 12-porphyrin nanotube with mono-acetylene linkages between the nanorings, showed a deformation from a perfect cylinder due to the dihedral angles adopted in the dimer-units. Finally, studies on porphyrin nanoballs with 10 and 14 porphyrin subunits are discussed. On the 14-porphyrin nanoball, TD-DFT studies provided insight into the electronic structure of this complex. The computed transitions are in good agreement with the experimental observations that after ultrafast relaxation, the exciton migrates over the entire chromophore.

6.2 Introduction

DFT made its appearance in the chemical literature in approximately 1990.[1] One of the pioneers of quantum mechanical modelling, Walter Kohn, received the 1996 Nobel prize in Chemistry for his contributions to DFT; using functionals of the electron density, the ground-state of a many-electron system can be described by 3 spatial coordinates. Later, Kohn and Sham split the description of the ground-state energy in a term of non-interaction electrons and a term describing all interactions of the individual electrons. The latter can be described by the exchange-correlation functional and is, to date, unknown. Numerous attempts of finding this functional have been made and the accuracy of DFT is crucially dependent on the chosen exchange-correlation functional. Although DFT had been popular for calculations in solid-state physics since 1970, it was at that time considered not accurate enough for calculations in quantum chemistry. With the improvements made by Kohn and others, it became possible to describe molecular geometries and ground-state energies.

DFT has been widely exploited by theoretical and experimental chemists alike, to address numerous questions in modern chemistry. In the publications referenced in this thesis alone, one in five include DFT studies on the reported compounds, complexes or materials. Examples of addressed questions include understanding the electronic properties,[2] analysis of conformational barriers,[3] and structure and stability confirmation of supramolecular complexes.[4,5]

In the Anderson group, DFT calculations have frequently been used to predict the properties of porphyrin nanostructures[6,7] or to support and/or explain experimental observations.[8,9] An example of the former is given in a recent study by Dr. Martin Peeks on the aromatic and antiaromatic ring currents in a molecular 6-porphyrin nanoring.[6] Nucleus-Independent Chemical Shift (NICS) calculations predicted the neutral and 12+ oxidation states to be non-aromatic, the 4+ oxidation state to be anti-aromatic and the 6+ oxidation state of the nanoring to be aromatic. These predictions were confirmed by ^{1}H NMR studies on these cations generated *via* chemical oxidation.

6.3 Methods

All DFT calculations in this section were conducted using Gaussian09/D.01 (ref.[10]) or Gaussian16/A.03 (ref.[11]). The B3LYP[12] density functional was used in conjunction with a 6-31G* basis set.[13–16] Grimme's D3 dispersion correction was used in geometry optimisations.[17] To simplify the calculations, truncated model compounds were used, in which the solubilising aryl groups were replaced by -H. Geometry optimisations were conducted in high symmetry where possible, to speed up calculations. The converged optimised structures were confirmed as minima by performing frequency calculations, which showed no imaginary frequencies. Orbitals are visualised with an isovalue of 0.008 a.u..

6.4 Bis-Acetylene Porphyrin Nanotubes

6.4.1 Size-Dependent Bandgap Oscillations in Porphyrin Nanotubes

In 2016, Allec and co-workers published a study on bandgap oscillations in various diameter porphyrin nanotubes.[18] Periodic DFT calculations were used to determine the electronic bandgap of (hypothetical) infinitely long porphyrin nanotubes with 2 to 36 porphyrin units around the nanoring component (P2-P32; see Figure 6.1 for a depiction of the P4 and P5 nanotubes).

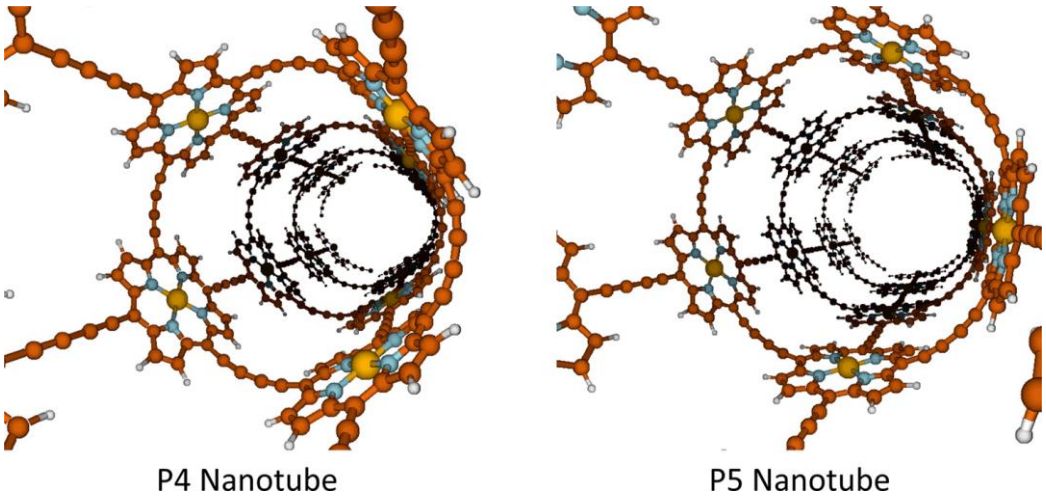

Figure 6.1: Optimised structures of the P4 (left) and P5 (right) nanotubes at the HSE06/DZP level of theory. Reprinted with permission from Ref. 18. Copyright 2016 American Chemical Society.

It was found that the HOMO-LUMO gaps (HLG, or bandgap) of these porphyrin nanotubes show a distinct odd-even effect: the even tubes have a smaller bandgap than the odd tubes. In contradiction to typical quantum confinement effects,[19,20] the bandgap of the even numbered porphyrin nanotubes increases with size. This effect ceases at large tube diameters, where the electronic states become essentially independent on the tube-diameter (Figure 6.2).

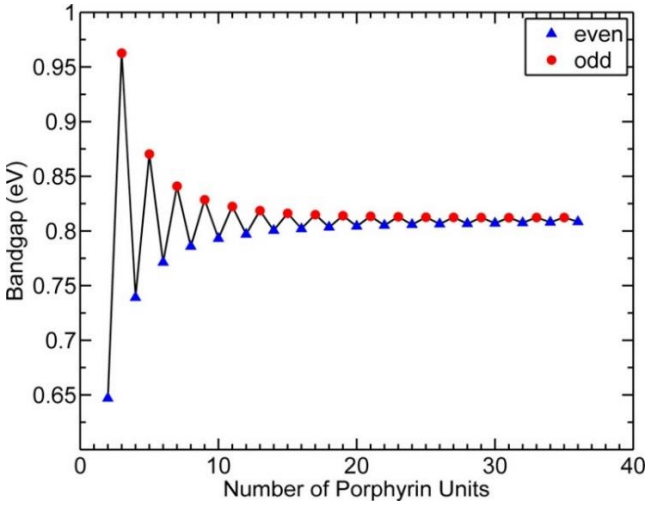

Figure 6.2: Electronic bandgaps for various porphyrin nanotubes as a function of the number of porphyrin units around the ring (obtained at the HSE06/DZP level of theory). Reprinted with permission from Ref. 18. Copyright 2016 American Chemical Society.

Orbital plots of the HOMO and LUMO of nanotubes with 5-porphyrin units (P5) and 6-porphyrin units (P6) around the ring component show that in both cases the HOMO is

delocalised over the entire π-conjugated system. The LUMO however is located only on the nanoring segment in the P6, while for the P5 there is electron density on the staves connecting the nanorings. Although Allec and co-workers generalise this phenomenon for all odd- and even-numbered porphyrin nanotubes, evidence for this statement was not provided.

We performed an analogous study on the bandgap oscillations by performing DFT calculations on discrete porphyrin nanotubes with 5, 6, 7, and 8 porphyrin units around the nanoring component and a length of 2 or 3 porphyrins. We chose these nanotubes specifically as they might be experimentally prepared *via* template-directed synthesis using previously reported templates.[21–23] The geometry optimised structures and frontier orbitals of ***t*-P10**, ***t*-P12**, ***t*-P14**, and ***t*-P16** are depicted in Figure 6.3 – Figure 6.6.

During the geometry optimisation of ***t*-P10**, D_{5h} symmetry was retained. The converged geometry resembles a perfect cylinder. The orbital delocalisation in ***t*-P10** is analogous to the delocalisation found by Allec and co-workers. The degenerate HOMO and LUMO orbitals are non-homogeneously delocalised over the π-conjugated system with complementary orbital densities between the HOMO/HOMO−1 and LUMO/LUMO+1 pairs (Figure 6.3, HOMO and LUMO depicted only). The HOMO shows electron density on all staves of the nanotube. The LUMO shows electron density on two staves of the nanotube, while there is none on the other three staves under the depicted density isovalue.

The optimised geometry and orbitals isosurfaces of ***t*-P12** are in excellent agreement with the previously published structure that was obtained at the BLYP/6-31G* level of theory.[9] While in the previous work the calculations were performed without symmetry constraints, in our calculation the nanotube retained D_{6h} symmetry (Figure 6.4).

D_{7h} symmetry was retained during the geometry optimisation of ***t*-P14** (Figure 6.5). The degenerate HOMOs and LUMOs of the perfectly cylindrical nanotube are, analogous to ***t*-P10**, complementary and non-homogeneously distributed. In contrast to the generalised odd-even LUMO distribution model as stated by Allec and co-workers, our discrete DFT calculations on ***t*-P14** do not show any delocalisation of the LUMO over the staves of the nanotube.

C_{8h} symmetry was retained during the geometry optimisation of ***t*-P16** (Figure 6.6). Similar to the optimised geometry and orbitals isosurfaces of ***t*-P12**, the 16-porphyrin nanotube resembles a perfect cylinder in which the HOMO shows electron density on the

entire chromophore system including the staves of the nanotube. The LUMO is localised on the ring-components with no electron density on the staves.

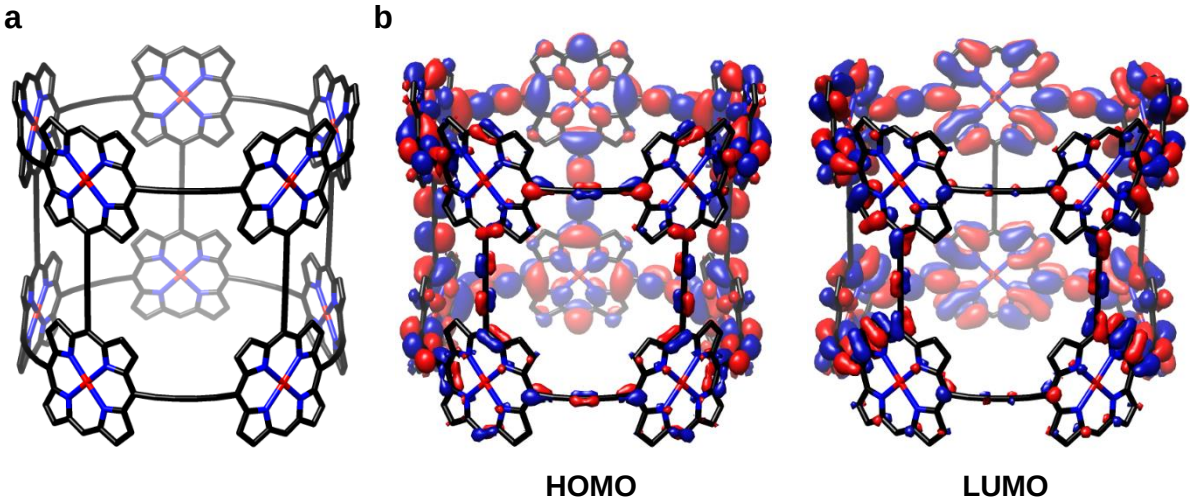

Figure 6.3: (a) Optimised geometry of ***t*-P10** calculated at the B3LYP/6-31G* level of theory. (b) HOMO and LUMO are degenerate with complementary non-homogeneous orbital distributions (degenerate pairs not shown) depicted with a density isovalue of 0.008 a.u.. Hydrogen atoms are omitted for clarity.

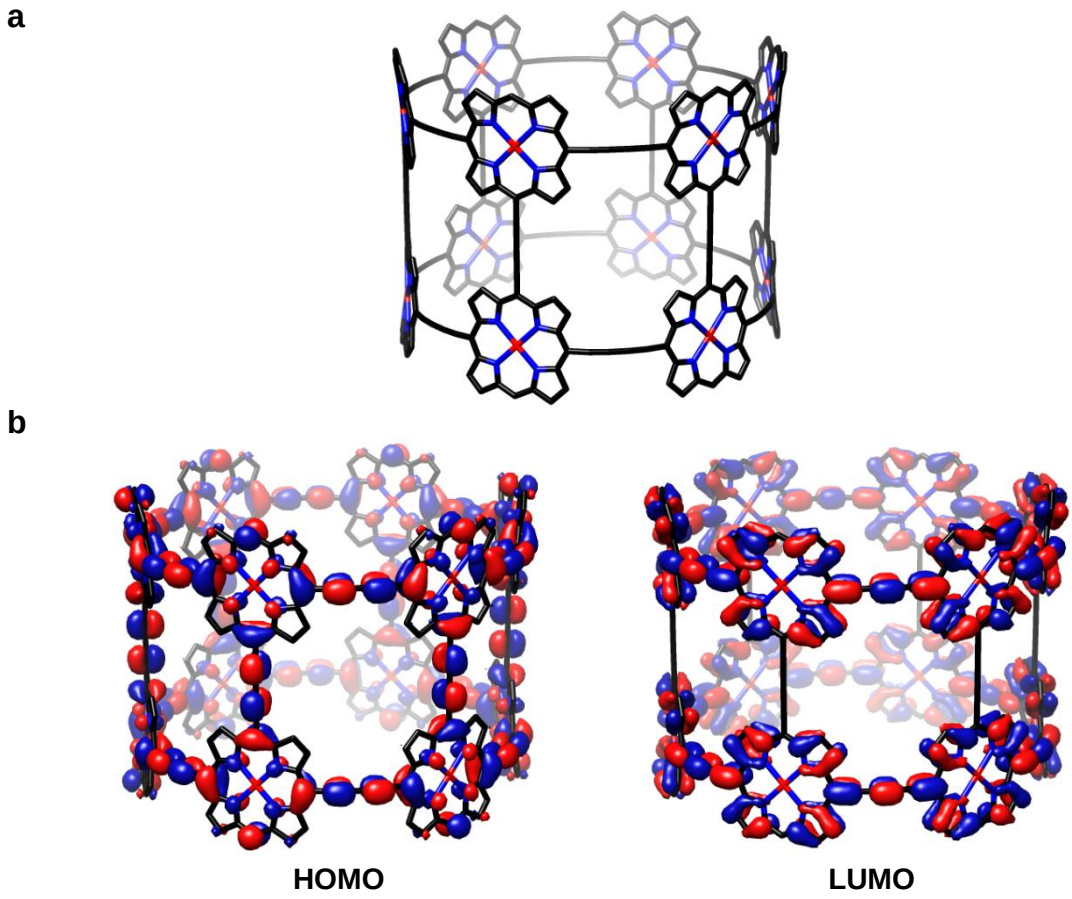

Figure 6.4: (a) Optimised geometry of ***t*-P12** calculated at the B3LYP/6-31G* level of theory. (b) HOMO and LUMO shown with a density isovalue of 0.008 a.u.. Hydrogen atoms are omitted for clarity.

a

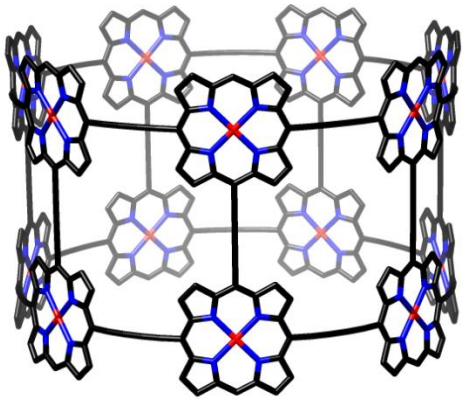

b

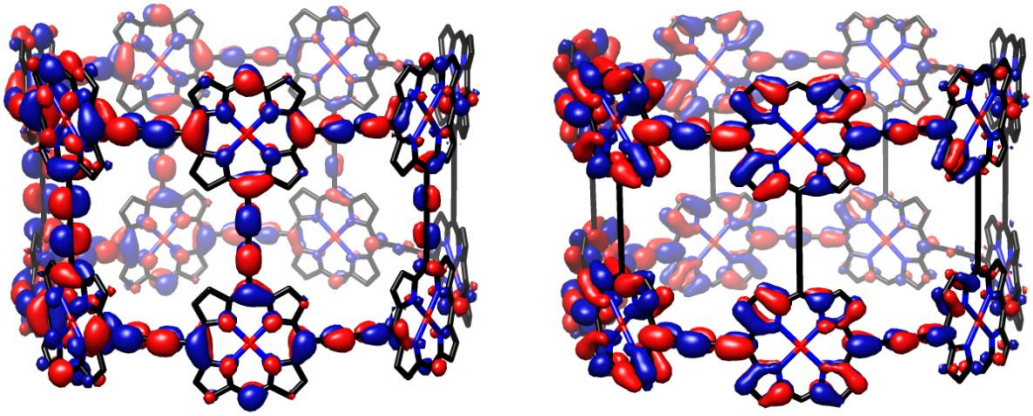

Figure 6.5: (a) Optimised geometry of ***t*-P14** calculated at the B3LYP/6-31G* level of theory. (b) HOMO and LUMO are degenerate with complementary non-homogeneous orbital distributions (degenerate pairs not shown) depicted with a density isovalue of 0.008 a.u.. Hydrogen atoms are omitted for clarity.

a

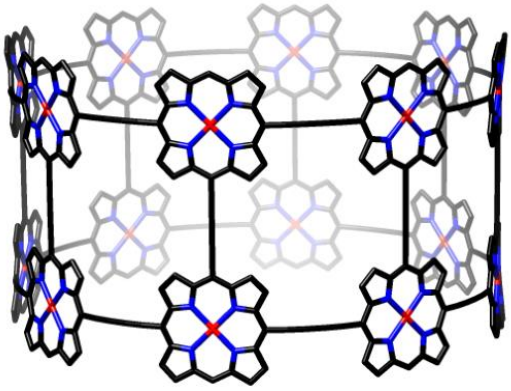

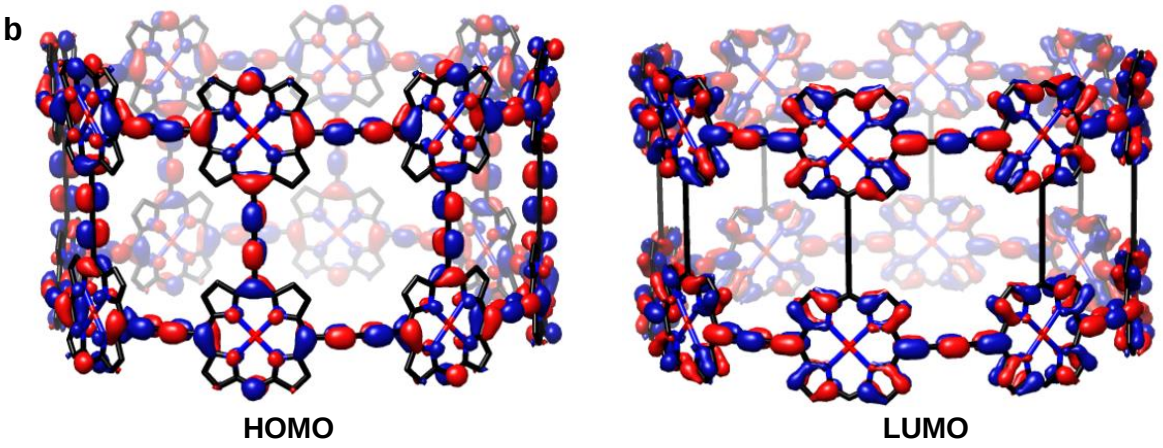

Figure 6.6: (a) Optimised geometry of ***t*-P16** calculated at the B3LYP/6-31G* level of theory. (b) HOMO and LUMO whosn with a density isovalue of 0.008 a.u.. Hydrogen atoms are omitted for clarity.

The bandgap oscillations for the nanotubes ***t*-P10**, ***t*-P12**, ***t*-P14** and ***t*-P16** are depicted in Figure 6.7, together with the bandgap for ***t*-P18**, a nanotube consisting of three conjoined rings. In agreement with the bandgap oscillations found by Allec and co-workers, the bandgap of the even-numbered porphyrin-nanotubes is smaller than that of the odd-numbered ones. In further agreement, we observe that the bandgap of the even-numbered porphyrin nanotubes increases with size and decreases with size for the odd-numbered tubes.

As an explanation for the origin of these bandgap oscillations, Allec and co-workers describe the nanoring components as having a continuous conjugated pathway of π-electrons. According to their approach, nanotubes containing an odd number of porphyrin units around the ring component satisfy Hückel's [4n+2] π-electron rule and are designated aromatic, while nanotubes containing an even number of porphyrin units around the ring component have [4n] π-electrons and are designated non-aromatic. Allec and co-workers therefore conclude that the electronic oscillations arise from a size-dependent alternation of aromatic and non-aromatic characteristics. However, such global ring current behaviour has not been observed for porphyrin nanorings in their neutral state, which rather possess local ring currents of the porphyrin components.[6]

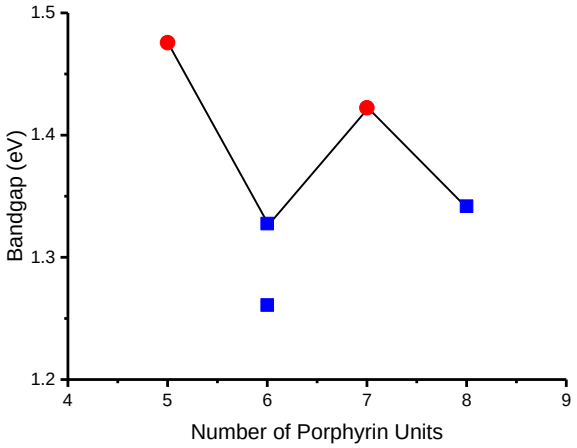

Figure 6.7: Electronic bandgaps for porphyrin nanotubes as a function of the number of porphyrin units around the ring (obtained at the B3LYP/6-31G* level of theory) with odd (red circles) and even (blue squares) number of porphyrin units around the ring segment. The three connected points are double layered porphyrin nanotubes, the free point is a three-layered porphyrin nanotube.

6.4.2 ***t*-P18**

In Chapter 5, synthetic efforts towards ***t*-P18·(T6)$_3$** were discussed. Although too little material was obtained to enable characterisation and further studies, we examined the geometry and molecular orbitals with DFT. The geometry optimisation of ***t*-P18** was performed in D_{6h} symmetry. The optimised structure shows an undistorted tubular geometry analogous to the converged structure of ***t*-P12**. The HOMO is delocalised over the entire conjugated system albeit with a higher coefficient on the central porphyrin nanoring. This effect is even more pronounced in the LUMO and fully reversed in the LUMO+1. The LUMO and LUMO+1 are practically degenerate and show negligible coefficients on the acetylene links between the conjoined rings (Figure 6.8).

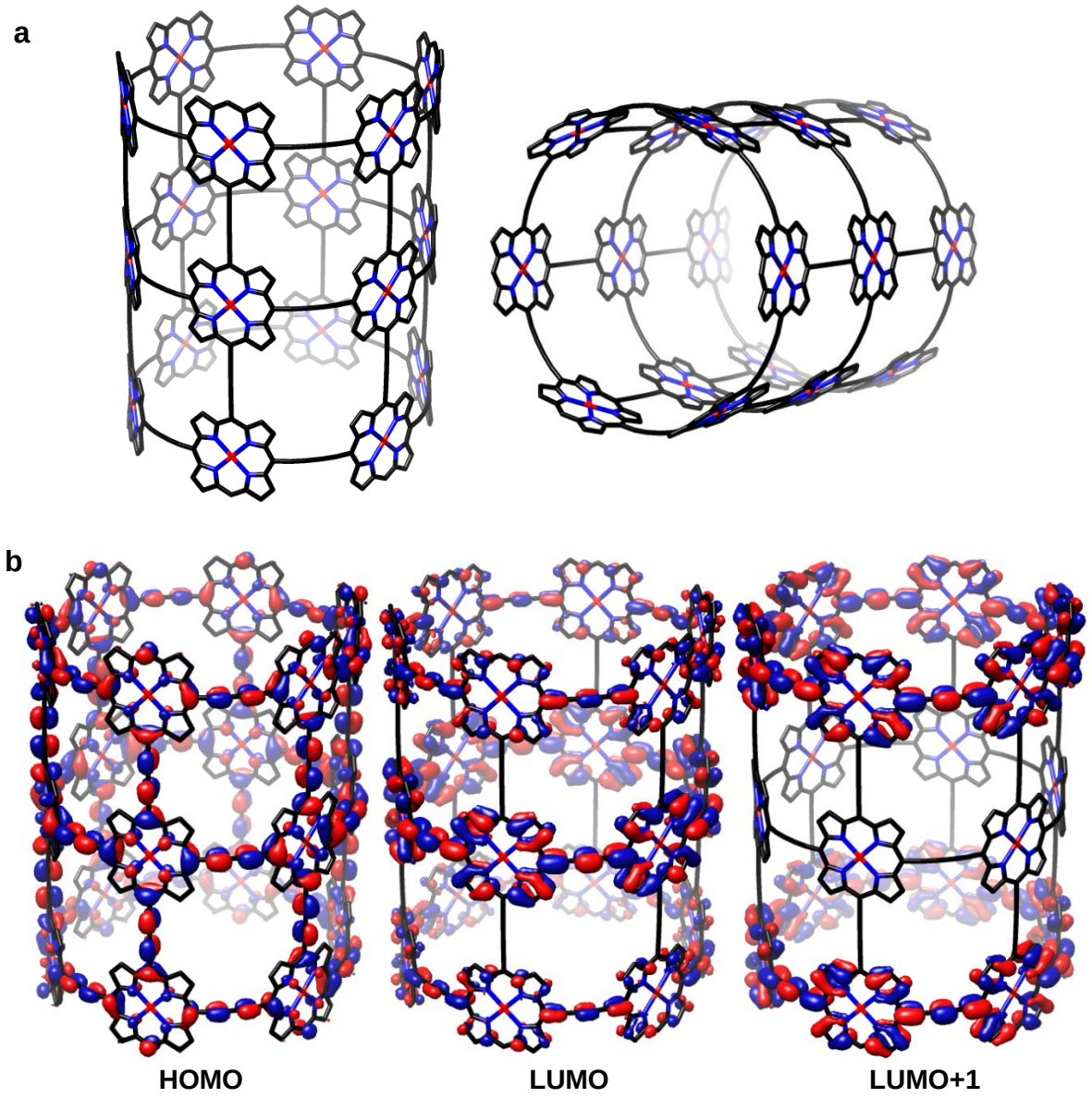

Figure 6.8: (a) Optimised geometry of ***t*-P18** calculated at the B3LYP/6-31G* level of theory. (b) HOMO, LUMO, and LUMO+1 shown with a density isovalue of 0.008 a.u.. Hydrogen atoms are omitted for clarity.

6.5 A Mono-Acetylene Porphyrin Nanotube – *t*-P12*

The geometry optimisation of ***t*-P12*** was performed in S_6 symmetry. Initially, the geometry optimisation was performed in D_{6h} symmetry and although the calculation converged, imaginary frequencies were found that indicated steric clash of the hydrogen atoms across the mono-acetylene link. Therefore, an optimisation was performed with constrained dihedral angles across the link. This constraint was subsequently removed and the geometry was optimised in S_6 symmetry, which was confirmed as minimum by a frequency calculation.

The top view of the optimised structure clearly shows the distortion of the nanotube, in which the porphyrins have adopted a twisted conformation with an average dihedral angle (measured on opposite β-carbon atoms across the mono-acetylene link) of 17.7° (Figure 6.9a). This conformation is adopted to avoid steric clash of the hydrogen atoms across the mono-acetylene link which, according to previous studies, prefers to adopt a twisted conformation with a dihedral angle of 35°.[24,25] Similarly to the HOMO and LUMO of ***t*-P12**, the HOMO of ***t*-P12*** is distributed over the entire π-system. The LUMO is localised over both rings, with negligible coefficients on the acetylene links between the rings (Figure 6.9b).

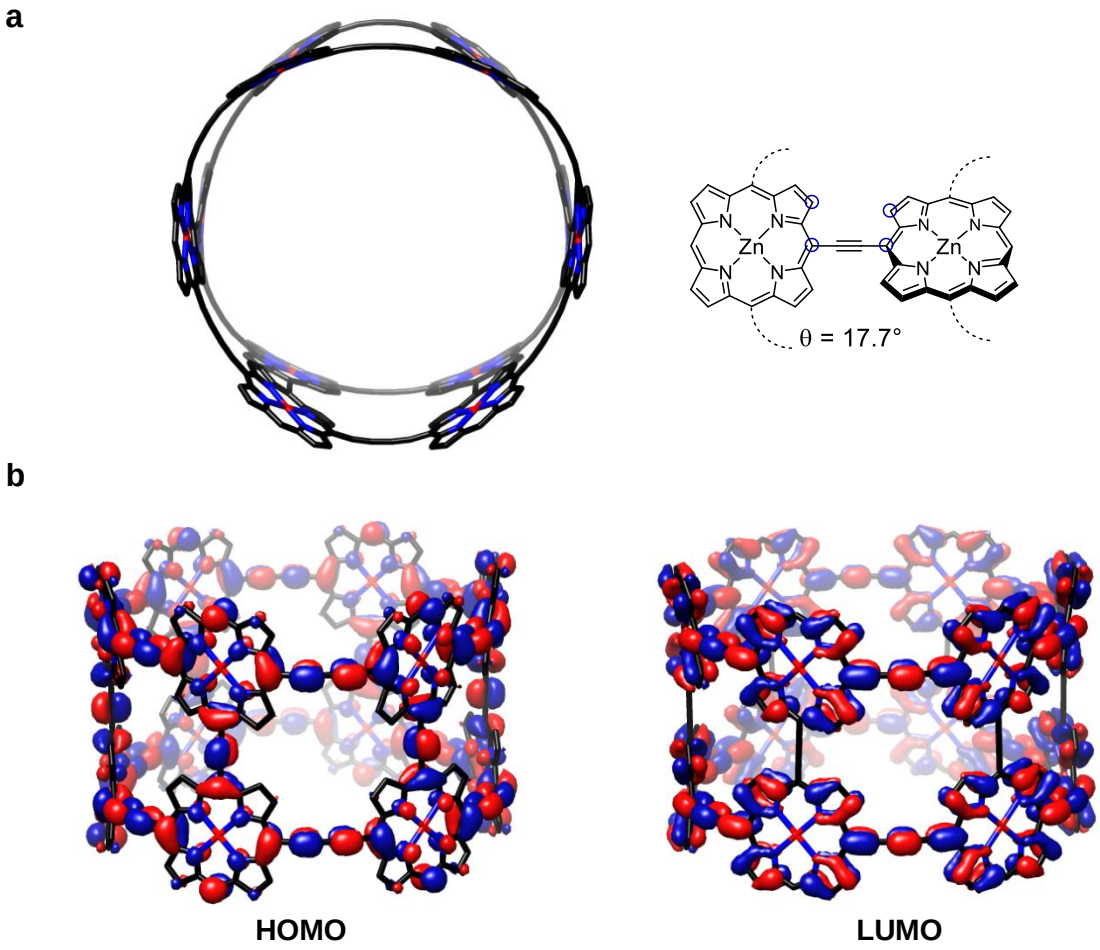

Figure 6.9: (a) Optimised geometry of ***t*-P12*** calculated at the B3LYP/6-31G* level of theory with a schematic depicting of the average dihedral angle across the mono-acetylenic link. (b) HOMO and LUMO shown with a density isovalue of 0.008 a.u.. Hydrogen atoms are omitted for clarity.

6.6 Porphyrin Nanoballs

A variety of porphyrin nanostructures with unusual photophysical properties have been synthesized in the Anderson group. As an intuitive next target after the previously reported porphyrin oligomers,[26] (fused) porphyrin nanorings,[23,27–29] and porphyrin nanotubes,[9] we explore the synthesis and properties of fully π-conjugated porphyrin nanoballs.[30]

The porphyrin nanoball with 10 porphyrin units has been prepared *via* template-directed synthesis combined with selective demetallation strategies to aid the assembly of two intersecting nanorings of 6 porphyrin units. Details on the synthesis of this fully D_{4h} symmetric porphyrin nanoball can be found in the DPhil Thesis of Jonathan Cremers, who performed most of the synthesis of this compound.

The porphyrin nanoball with 14 porphyrin units has been prepared *via* step-wise template-directed synthesis. This route starts from a 6-porphyrin nanoring with four terminal alkyne substituents. This ring is coupled to four porphyrin dimers, followed by a second template-directed step using four-legged template **T4**, to close the 10-porphyrin nanoring. Details on the synthesis of this prolate ellipsoid cage can be found in reference 30.

6.6.1 ***b*-P14**

The geometry optimisation of ***b*-P14** was performed in D_{2h} symmetry. The converged geometry resembles a prolate ellipsoidal cage (Figure 6.10a). The 6-porphyrin nanoring component is distorted from a perfect circle and rather resembles an ellipse with a Zn-Zn distance of 27.61 Å, as measured between the two spiro-porphyrins. Notably, when the optimisation was performed without symmetry constraints, the resulting optimised geometry has essentially D_{2h} symmetry (the root-mean-squared deviation in the position of atoms between the final geometry (C_1) and a re-symmetrised (D_{2h}) form is only about 0.001 Å). Furthermore, the computed energy and orbital energies are near identical for the geometries computed with and without symmetry constraints. The values depicted below are those obtained following D_{2h} symmetry.

The HOMO of the 14-porphyrin nanoball is delocalised over both the 6-porphyrin nanoring and 10-porphyrin nanoring components of this structure albeit with a higher electron density on the 6-porphyrin nanoring and in particular the spiro-porphyrins. The LUMO and LUMO+1 of ***b*-P14** have nearly identical energies (−3.23 eV and −3.22 eV,

respectively). They reside exclusively on either the 6-porphyrin nanoring and the 10-porphyrin nanoring component, respectively, with a homogeneous distribution around the respective [n]-porphyrin nanoring component (Figure 6.10b).

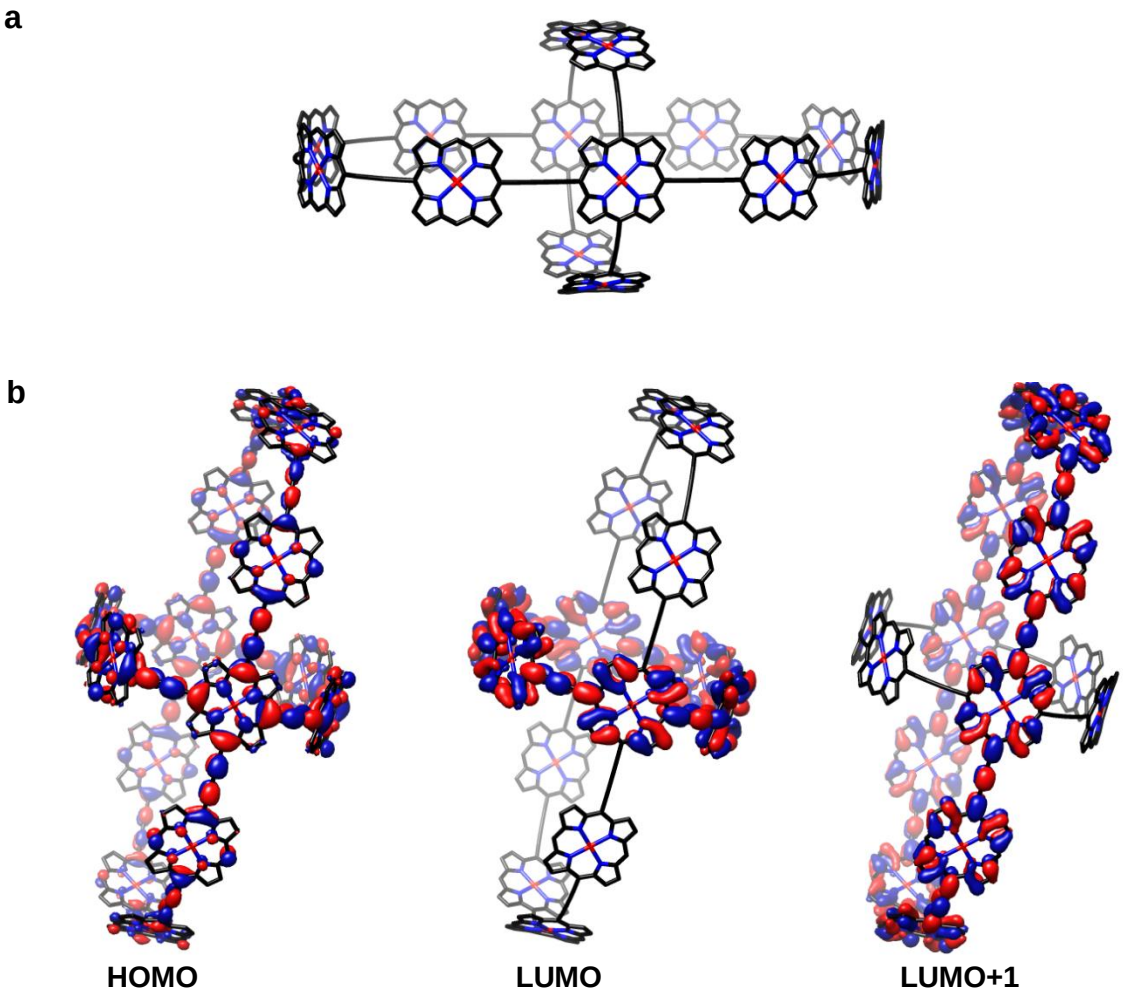

Figure 6.10: (a) Optimised geometry of ***b*-P14** calculated at the B3LYP/6-31G* level of theory. (b) HOMO, LUMO and LUMO+1 shown with a density isovalue of 0.008 a.u.. Hydrogen atoms are omitted for clarity.

Time-resolved photoluminescence (PL, fluorescence) spectroscopy enables the investigation of PL polarisation anisotropy dynamics and hence can address the relationship between molecular topology and exciton delocalisation dynamics. The PL anisotropy γ is calculated using

$$\gamma(t) = \frac{I_{\text{para}}(t) - I_{\text{perp}}(t)}{I_{\text{para}}(t) - 2I_{\text{perp}}(t)}$$

where I_{para} and I_{perp} are the PL intensities measured with detection polarised parallel and perpendicular to the excitation pulse polarisation, respectively.[31] Short, linear (porphyrin)

oligomers typically exhibit γ = 0.4, indicating that the exciton transition dipole does not reorient following excitation.[32,33] For a cyclic porphyrin structure with an exciton delocalised over the entire ring, an anisotropy value of γ = 0.1 is expected.[33,34] Molecules that support complete three-dimensional reorientation of the exciton transition dipole ought to display γ = 0. Finally, if the emission transition dipole moment is always oriented perpendicular to the polarization direction of the absorbing state, an anisotropy value of γ = −0.2 is anticipated.[9]

PL anisotropy studies on ***b*-P14** showed that there is an initial drop in anisotropy within the first 4 ps from γ = 0.1 to γ = 0.03 ± 0.01 which remains constant thereafter within the observation window of 20 ps after excitation (Figure 6.11). The almost complete loss of polarisation within the first 4 ps after excitation suggests that the exciton localises and migrates rapidly around the entire ball complex. Contributions from emission components polarised in both ring planes with perpendicular orientations result in an anisotropy value close to zero.[29] The delocalisation of the calculated HOMO and LUMO/LUMO+1 orbitals over the entire ball complex supports the observation that excitation can migrate between the two rings within the ball.

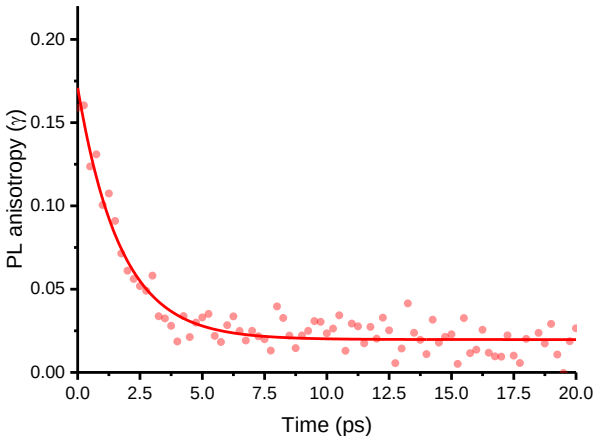

Figure 6.11: Fluorescence anisotropy dynamics of ***b*-P14**. Measurements were performed in toluene; the solution was excited at 820 nm and emission was detected at 950 nm.

Time-dependent DFT (TD-DFT) calculations were performed to provide better insight into the electronic structure of the 14-porphyrin nanoball. The vertical electronic excitations shown in Figure 6.12(left) reproduce the experimental trend in absorption energies in the Q band of ***b*-P14·T6·(T4)$_2$** (Figure 6.12(right)). It is worth noting that these TD-DFT calculations only consider the purely electronic <0,0> transition probabilities. As a result,

these calculations are unable to reproduce experiment for transitions which, despite being electric dipole forbidden, are vibronically allowed as a result of vibronic coupling.[35] The explicit calculation of a vibronic spectrum is possible using DFT, however is not feasible for molecules of this size.

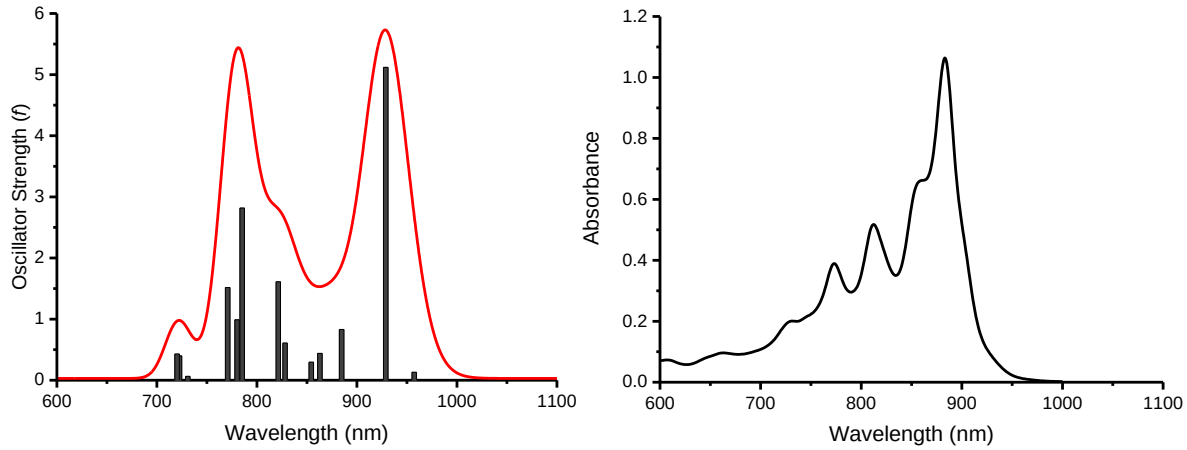

Figure 6.12: (left) (grey bars) Calculated (TD-B3LYP/6-31G*) wavelength vs. oscillator strength of the 14-porphyrin nanoball (red) simulated absorption spectrum assuming a Gaussian line-shape for each transition, with width 575 cm^{-1}. (right) Region of the UV-vis-NIR absorption spectrum of the ***b*-P14·T6·(T4)$_2$** complex ([0.7 μM], measured in toluene at 298 K).

Natural transition orbitals (NTOs)[36] provide a qualitative description of an electronic excitation and a visualisation of the natural orbital origin of the hole and electron involved in a transition.[37] A single transition may be described by multiple electron/hole NTO pairs. The relative contribution of each electron/hole pair is described by an eigenvalue (λ). NTOs of ***b*-P14** were calculated to offer further insight into the nature of the predominant transitions in the Q-band.

The NTO pair describing the predominant electronic transition (at 929 nm) shows that the electron is localised over the 10-porphyrin nanoring segment of the nanoball, while the hole is located on the entire chromophore system (Figure 6.13(top)). The predominant NTO of the electronically forbidden $S_0 \rightarrow S_1$ transition shows a similar distribution with the hole located over the entire chromophore system (Figure 6.13(bottom)). However, for this NTO pair, the electron is localised only over the 6-porphyrin nanoring. These calculations are in good agreement with the experimentally determined anisotropy of $\gamma = 0.03$ (Figure 6.11), which indicated that (after ultrafast relaxation) the exciton migrates rapidly between the two rings of the ball.

Hole	Electron	λ
$S_0 \rightarrow S_4$ (929 nm); f = 5.12		
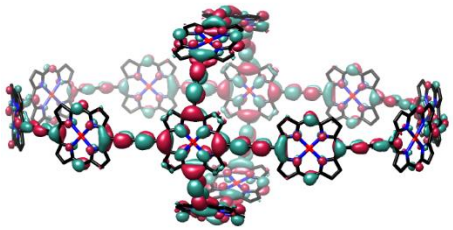	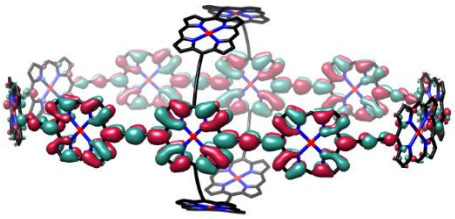	**0.703**
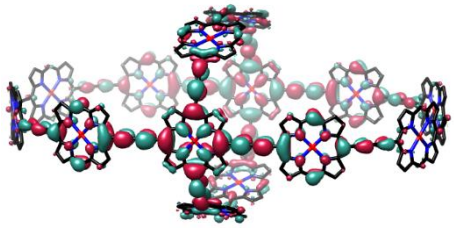	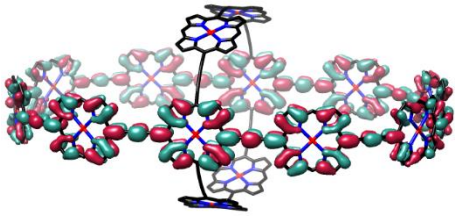	**0.260**
$S_0 \rightarrow S_1$ (1066 nm); f = 0 (electronically forbidden)		
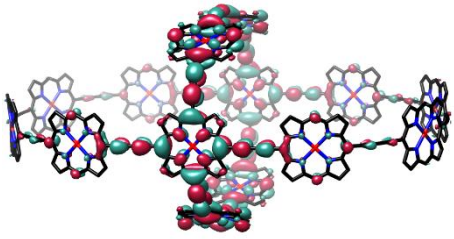	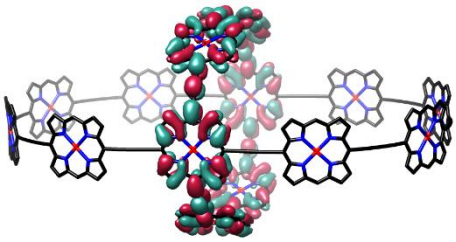	**0.912**

Figure 6.13: Natural transition orbitals (NTOs) calculated at the B3LYP/6-31G* level of theory for the predominant electronic transition **$S_0 \rightarrow S_4$** (929 nm) of ***b*-P14** (top NTO pairs) and the electronically forbidden $S_0 \rightarrow S_1$ transition (1066 nm). f denotes the calculated oscillator strengths. The eigenvalue associated with the NTO hole/electron pair is shown as λ.

6.6.2 ***b*-P10**

During the geometry optimisation of 10-porphyrin nanoball, ***b*-P10**, the structure retained D_{4h} symmetry. The converged geometry shows that the cyclicity of the 6-porphyrin nanoring components is kept. The HOMO is fully delocalised over both nanoring components. The LUMO was found to be degenerate and resides on either of the two rings (Figure 6.14). Since the HOMO and degenerate LUMOs are homogeneously delocalised over the three-dimensional symmetric chromophore system, an experimental time-dependent fluorescence anisotropy of zero is expected, as complete reorientation of the exciton

transition dipole should render $\gamma = 0$. The photophysical properties of this symmetric porphyrin nanoball are currently being examined.

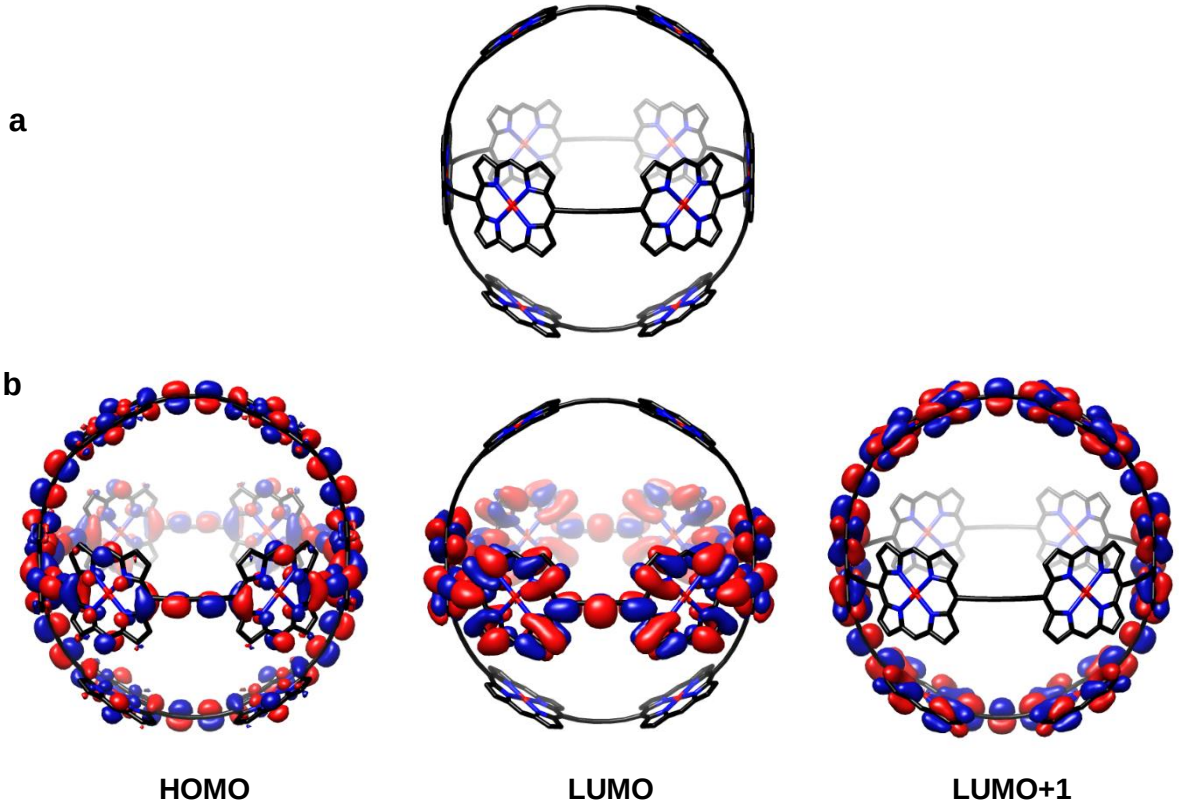

Figure 6.14: (a) Optimised geometry of ***b*-P10** calculated at the B3LYP/6-31G* level of theory. (b) HOMO, LUMO and LUMO+1 shown with a density isovalue of 0.008 a.u.. Hydrogen atoms are omitted for clarity.

6.7 Conclusion

Calculations on different-size infinite and discrete porphyrin nanotubes were performed by Allec and co-workers and our group, respectively. HOMO/LUMO orbital densities and bandgap oscillations were explored. One of the interesting features from both studies was the presence of LUMO density on the nanotube staves in ***t*-P10** (*i.e.* 5 porphyrin units around the nanoring segment). However, while Allec and co-workers generalise this phenomenon for porphyrin nanotubes with an odd number of porphyrin units around the nanoring component, we did not observe an analogous distribution in the next largest nanotube with an odd number of porphyrin units around the nanoring component; ***t*-P14**. The size-dependent bandgap oscillation could potentially be explored experimentally. This would likely require the nanotubes to be template-free, for which a synthetic method was discussed in Chapter 3. Although the synthesis of ***t*-P12** has been successful *via* two

different strategies (Chapter 3), attempts to prepare ***t*-P10** and ***t*-P14** *via* template-directed synthesis have so far been unsuccessful.

The optimised geometry of ***t*-P12***, a 12-porphyrin nanotube in which the conjoined 6-porphyrin nanorings are connected *via* mono-acetylene linkers (synthesis discussed in Chapter 5), shows a distorted geometry to alleviate steric congestion across the mono-acetylene link. This agrees with previous theoretical studies on mono-acetylene linked porphyrin dimers.

DFT calculations on a prolate ellipsoidal 14-porphyrin nanoball, ***b*-P14**, show the distribution of the HOMO over the entire ball and the practically degenerate LUMO/LUMO+1 over each of the two ring components. Experimental PL anisotropy measurements demonstrate almost complete loss of polarisation, suggesting that the exciton rapidly migrates around the ball complex. This observation was confirmed by TD-DFT calculations of the NTOs, where the predominant electronic transition shows that the hole is located on the entire 14-porphyrin system, while the electron is delocalised over the 10-porphyrin nanoring component. The NTO from the (electronically forbidden, vibronically allowed) $S_0 \rightarrow S_1$, shows a similar distribution of the hole, however, the electron is delocalised over the 10-porphyrin nanoring segment. This study nicely demonstrates how synthesis, photophysical studies and DFT calculations can complement each other and can create a complete picture of the excited state delocalisation of this unique porphyrin nanostructure.

6.8 References

(1) W. Koch, M. C. Holthausen. *A Chemist's Guide to Density Functional Theory*, Second Edition; Wiley-VCH Verlag GmbH, **1999**.

(2) R. Sekiguchi, K. Takahashi, J. Kawakami, A. Sakai, H. Ikeda, A. Ishikawa, K. Ohta, S. Ito. 'Preparation of a Cyclic Polyphenylene Array for a Zigzag-Type Carbon Nanotube Segment'. *J. Org. Chem.*, **2015**, *80*, 5092–5110.

(3) J. Xia, M. R. Golder, M. E. Foster, B. M. Wong, R. Jasti. 'Synthesis, Characterization, and Computational Studies of Cycloparaphenylene Dimers'. *J. Am. Chem. Soc.*, **2012**, *134*, 19709–19715.

(4) T. Kamada, N. Aratani, T. Ikeda, N. Shibata, Y. Higuchi, A. Wakamiya, S. Yamaguchi, K. S. Kim, Z. S. Yoon, D. Kim, A. Osuka. 'High Fidelity Self-Sorting Assembling of Meso-Cinchomeronimide Appended *Meso-Meso* Linked Zn(II) Diporphyrins'. *J. Am. Chem. Soc.*, **2006**, *128*, 7670–7678.

(5) T. Iwamoto, Z. Slanina, N. Mizorogi, J. Guo, T. Akasaka, S. Nagase, H. Takaya, N. Yasuda, T. Kato, S. Yamago. 'Partial Charge Transfer in the Shortest Possible Metallofullerene Peapod, La@C_{82}⊂[11]cycloparaphenylene'. *Chem. - Eur. J.*, **2014**, *20*, 14403–14409.

(6) M. D. Peeks, T. D. W. Claridge, H. L. Anderson. 'Aromatic and Antiaromatic Ring Currents in a Molecular Nanoring'. *Nature*, **2017**, *541*, 200–203.

(7) A. A. Kocherzhenko, S. Patwardhan, F. C. Grozema, H. L. Anderson, L. D. A. Siebbeles. 'Mechanism of Charge Transport along Zinc Porphyrin-Based Molecular Wires'. *J. Am. Chem. Soc.*, **2009**, *131*, 5522–5529.

(8) J. B. Kelber, N. A. Panjwani, D. Wu, R. Gómez-Bombarelli, B. W. Lovett, J. J. L. Morton, H. L. Anderson. 'Synthesis and Investigation of Donor–Porphyrin–Acceptor Triads with Long-Lived Photo-Induced Charge-Separate States'. *Chem. Sci.*, **2015**, *6*, 6468–6481.

(9) P. Neuhaus, A. Cnossen, J. Q. Gong, L. M. Herz, H. L. Anderson. 'A Molecular Nanotube with Three-Dimensional π-Conjugation'. *Angew. Chem. Int. Ed.*, **2015**, *54*, 7344 –7348.

(10) 'Gaussian09/D.01'. M. J. Frisch, G. W. Trucks, H. B. Schlegel, G. E. Scuseria, M. A. Robb, J. R. Cheeseman, G. Scalmani, V. Barone, G. A. Petersson, H. Nakatsuji, X. Li, M. Caricato, A. V. Marenich, J. Bloino, B. G. Janesko, R. Gomperts, B. Mennucci, H. P. Hratchian, J. V. Ortiz, A. F. Izmaylov, J. L. Sonnenberg, D. Williams-Young, F. Ding, F. Lipparini, F. Egidi, J. Goings, B. Peng, A. Petrone, T. Henderson, D. Ranasinghe, V. G. Zakrzewski, J. Gao, N. Rega, G. Zheng, W. Liang, M. Hada, M. Ehara, K. Toyota, R. Fukuda, J. Hasegawa, M. Ishida, T. Nakajima, Y. Honda, O. Kitao, H. Nakai, T. Vreven, K. Throssell, J. A. Montgomery, Jr., J. E. Peralta, F. Ogliaro, M. J. Bearpark, J. J. Heyd, E. N. Brothers, K. N. Kudin, V. N. Staroverov, T. A. Keith, R. Kobayashi, J. Normand, K. Raghavachari, A. P. Rendell, J. C. Burant, S. S. Iyengar, J. Tomasi, M. Cossi, J. M. Millam, M. Klene, C. Adamo, R. Cammi, J. W. Ochterski, R. L. Martin, K. Morokuma, O. Farkas, J. B. Foresman, and D. J. Fox, Gaussian 09, Revision D.01, software, Wallingford CT, **2009**.

(11) 'Gaussian16/A.03'. M. J. Frisch, G. W. Trucks, H. B. Schlegel, G. E. Scuseria, M. A. Robb, J. R. Cheeseman, G. Scalmani, V. Barone, G. A. Petersson, H. Nakatsuji, X. Li, M. Caricato, A. V. Marenich, J. Bloino, B. G. Janesko, R. Gomperts, B. Mennucci, H. P. Hratchian, J. V. Ortiz, A. F. Izmaylov, J. L. Sonnenberg, D. Williams-Young, F. Ding, F. Lipparini, F. Egidi, J. Goings, B. Peng, A. Petrone, T. Henderson, D.

Ranasinghe, V. G. Zakrzewski, J. Gao, N. Rega, G. Zheng, W. Liang, M. Hada, M. Ehara, K. Toyota, R. Fukuda, J. Hasegawa, M. Ishida, T. Nakajima, Y. Honda, O. Kitao, H. Nakai, T. Vreven, K. Throssell, J. A. Montgomery, Jr., J. E. Peralta, F. Ogliaro, M. J. Bearpark, J. J. Heyd, E. N. Brothers, K. N. Kudin, V. N. Staroverov, T. A. Keith, R. Kobayashi, J. Normand, K. Raghavachari, A. P. Rendell, J. C. Burant, S. S. Iyengar, J. Tomasi, M. Cossi, J. M. Millam, M. Klene, C. Adamo, R. Cammi, J. W. Ochterski, R. L. Martin, K. Morokuma, O. Farkas, J. B. Foresman, and D. J. Fox, Gaussian 16, Revision A.03,software, Wallingford CT, **2016**.

(12) A. D. Becke. 'Density-Functional thermochemistry.III. The Role of Exact Exchange'. *J. Chem. Phys.*, **1993**, *98*, 5648.

(13) R. Ditchfield, W. J. Hehre, J. A. Pople. 'Self-Consistent Molecular-Orbital Methods. IX. An Extended Gaussian-Type Basis for Molecular-Orbital Studies of Organic Molecules'. *J. Chem. Phys.*, **1971**, *54*, 724–728.

(14) W. J. Hehre, R. Ditchfield, J. A. Pople. 'Self—Consistent Molecular Orbital Methods. XII. Further Extensions of Gaussian—Type Basis Sets for Use in Molecular Orbital Studies of Organic Molecules'. *J. Chem. Phys.*, **1972**, *56*, 2257–2261.

(15) P. C. Hariharan, J. A. Pople. 'The Influence of Polarization Functions on Molecular Orbital Hydrogenation Energies'. *Theor. Chim. Acta*, **1973**, *28*, 213–222.

(16) V. A. Rassolov, J. A. Pople, M. A. Ratner, T. L. Windus. '6-31G* Basis Set for Atoms K through Zn'. *J. Chem. Phys.*, **1998**, *109*, 1223–1229.

(17) S. Grimme, J. Antony, S. Ehrlich, H. Krieg. 'A Consistent and Accurate Ab Initio Parametrization of Density Functional Dispersion Correction (DFT-D) for the 94 Elements H-Pu'. *J. Chem. Phys.*, **2010**, *132*, 154104–154122.

(18) S. I. Allec, N. V. Ilawe, B. M. Wong. 'Unusual Bandgap Oscillations in Template-Directed π-Conjugated Porphyrin Nanotubes'. *J. Phys. Chem. Lett.*, **2016**, *7*, 2362–2367.

(19) E. Roduner. 'Size Matters: Why Nanomaterials Are Different'. *Chem. Soc. Rev.*, **2006**, *35*, 583–592.

(20) S. Reich, C. Thomsen, J. Maultzsch. *Carbon Nanotubes*; Wiley-VCH Verlag GMBH & Co. KGaA, 2003.

(21) P. Liu, Y. Hisamune, M. D. Peeks, B. Odell, J. Q. Gong, L. M. Herz, H. L. Anderson. 'Synthesis of Five-Porphyrin Nanorings by Using Ferrocene and Corannulene Templates'. *Angew. Chem. Int. Ed.*, **2016**, *55*, 8358–8362.

(22) M. Hoffmann, J. Kärnbratt, M. H. Chang, L. M. Herz, B. Albinsson, H. L. Anderson. 'Enhanced π Conjugation Around a Porphyrin[6] Nanoring'. *Angew. Chem. Int. Ed.*, **2008**, *47*, 4993–4996.

(23) P. Liu, P. Neuhaus, D. V. Kondratuk, T. S. Balaban, H. L. Anderson. 'Cyclodextrin-Templated Porphyrin Nanorings'. *Angew. Chem. Int. Ed.*, **2014**, *53*, 7770–7773.

(24) V. S. -Y. Lin, M. J. Therien. 'The Role of Porphyrin-to-Porphyrin Linkage Topology in the Extensive Modulation of the Absorptive and Emissive Properties of a Series of Ethynyl- and Butadiynyl-Bridged Bis- and Tris(Porphinato)Zinc Chromophores'. *Chem. – A Eur. J.*, **1995**, *1*, 645–651.

(25) L. Rintoul, S. R. Harper, D. P. Arnold. 'A Systematic Theoretical Study of the Electronic Structures of Porphyrin Dimers: DFT and TD-DFT Calculations on Diporphyrins Linked by Ethane, Ethene, Ethyne, Imine, and Azo Bridges'. *Phys. Chem. Chem. Phys.*, **2013**, *15*, 18951–18964.

(26) H. L. Anderson. 'Building Molecular Wires from the Colours of Life: Conjugated Porphyrin Oligomers'. *Chem. Comm.*, **1999**, 2323–2330.

(27) M. C. O'Sullivan, J. K. Sprafke, D. V Kondratuk, C. Rinfray, T. D. W. Claridge, A. Saywell, M. O. Blunt, J. N. O'Shea, P. H. Beton, M. Malfois, H. L. Anderson. 'Vernier Templating and Synthesis of a 12-Porphyrin Nano-Ring'. *Nature*, **2011**, *469*, 72–75.

(28) D. V. Kondratuk, L. M. A. Perdigao, M. C. O'Sullivan, S. Svatek, G. Smith, J. N. O'Shea, P. H. Beton, H. L. Anderson. 'Two Vernier-Templated Routes to a 24-Porphyrin Nanoring'. *Angew. Chem. Int. Ed.*, **2012**, *51*, 6696–6699.

(29) L. Favereau, A. Cnossen, J. B. Kelber, J. Q. Gong, R. M. Oetterli, J. Cremers, L. M. Herz, H. L. Anderson. 'Six-Coordinate Zinc Porphyrins for Template-Directed Synthesis of Spiro-Fused Nanorings'. *J. Am. Chem. Soc.*, **2015**, *137*, 14256–14259.

(30) J. Cremers, R. Haver, M. Rickhaus, J. Q. Gong, L. Favereau, T. D. W. Claridge, L. M. H. Herz, H. L. A. Anderson. 'Template-Directed Synthesis of a Conjugated Zinc Porphyrin Nanoball'. *J. Am. Chem. Soc.,* **2018**, ASAP.

(31) M. H. Chang, M. Hoffmann, H. L. Anderson, L. M. Herz. 'Dynamics of Excited-State Conformational Relaxation and Electronic Delocalization in Conjugated Porphyrin Oligomers'. *J. Am. Chem. Soc.*, **2008**, *130*, 10171–10178.

(32) M. H. Chang, M. J. Frampton, H. L. Anderson, L. M. Herz. 'Intermolecular Interaction Effects on the Ultrafast Depolarization of the Optical Emission from Conjugated Polymers'. *Phys. Rev. Lett.*, **2007**, *98*, 1–4.

(33) P. Parkinson, D. V. Kondratuk, C. Menelaou, J. Q. Gong, H. L. Anderson, L. M. Herz. 'Chromophores in Molecular Nanorings: When Is a Ring a Ring?'. *J. Phys. Chem. Lett.*, **2014**, *5*, 4356–4361.

(34) C.-K. Yong, P. Parkinson, D. V. Kondratuk, W.-H. Chen, A. Stannard, A. Summerfield, J. K. Sprafke, M. C. O'Sullivan, P. H. Beton, H. L. Anderson, L. M. Herz. 'Ultrafast Delocalization of Excitation in Synthetic Light-Harvesting Nanorings'. *Chem. Sci.*, **2015**, *6*, 181–189.

(35) J. K. Sprafke, D. V. Kondratuk, M. Wykes, A. L. Thompson, M. Hoffmann, R. Drevinskas, W. H. Chen, C. K. Yong, J. Kärnbratt, J. E. Bullock, M. Malfois, M. R. Wasielewski, B. Albinsson, L. M. Herz, D. Zigmantas, D. Beljonne, H. L. Anderson. 'Belt-Shaped π-Systems: Relating Geometry to Electronic Structure in a Six-Porphyrin Nanoring'. *J. Am. Chem. Soc.*, **2011**, *133*, 17262–17273.

(36) R. L. Martin. 'Natural Transition Orbitals'. *J. Chem. Phys.*, **2003**, *118*, 4775–4777.

(37) M. D. Peeks, P. Neuhaus, H. L. Anderson. 'Experimental and Computational Evaluation of the Barrier to Torsional Rotation in a Butadiyne-Linked Porphyrin Dimer'. *Phys. Chem. Chem. Phys.*, **2016**, *18*, 5264–5274.